A coupled crystal plasticity - phase field formulation to describe microstructural evolution in polycrystalline aggregates during recrystallisation

Guillaume Abrivard

MINES
ParisTech

ED n°432 : Science des Métiers de l'Ingénieur

THESE

pour obtenir le grade de

DOCTEUR DE L'ECOLE NATIONALE SUPERIEURE DES MINES DE PARIS

Spécialité Sciences et Génie des Matériaux

présentée et soutenue publiquement par

Guillaume Abrivard

le 20 Novembre 2009

A Coupled Crystal Plasticity - Phase Field Formulation
To Describe Microstructural Evolution
In Polycrystalline Aggregates During Recrystallisation

Directeurs de thèse : *Esteban BUSSO*
Samuel FOREST

Jury

M. Ingo STEINBACH	President	Ruhr-Universität Bochum, Allemagne
M. Marc GEERS	Rapporteur	Eindhoven University of Technology, Pays-Bas
M. Thierry HOC	Rapporteur	Ecole Centrale de Lyon, France
M. Fionn DUNNE	Examinateur	University of Oxford, Royaume-Uni
M. Roland LOGE	Examinateur	MINES ParisTech, France
M. Benoît APPOLAIRE	Examinateur	Onera, France
M. Esteban BUSSO	Directeur de thèse	MINES ParisTech, France
M. Samuel FOREST	Directeur de thèse	MINES ParisTech, France

Abstract

During thermo-mechanical processing, the strain energy stored in the microstucture of an FCC polycrystalline aggregate is generally reduced by physical mechanisms which rely, at least partially, on mechanisms such as dislocation cell or grain boundary motion which occur during recovery, recrystallisation or grain growth. The aim of this work is to develop a constitutive framework capable of describing the microstructural evolution driven by grain boundary curvature and/or stored energy during recrystallisation and grain growth. As recrystallisation processes depend primarily on the nature of the microstructural state, an accurate prediction of such phenomena requires that the microstructural heterogeneities which develop just before recrystallisation be properly described. These heterogeneities may consist of structures such as dislocation cells and pile-ups, shear and twin bands. The microstructural characteristics present in a polycrystal aggregate just before the onset of thermal recrystallisation are first reproduced numerically. The constitutive behaviour of each grain in the aggregate is described using a dislocation mechanics-based crystallographic formulation which accounts for non-local effects through the introduction of geometrically necessary dislocations. The single crystal model is implemented into the finite element method using a finite-strain kinematics framework. Different measures of stored internal strain energy are determined based on the dislocation density distribution in the aggregate. The minimisation of stored and grain boundary energies provides the driving force for grain boundary motion. To describe the interface motion, a phase field model taking into account the stored energy distribution is formulated and implemented within a continuum mechanics framework. A weak coupling between the grain boundary kinematics and the crystal plasticity model is made through the dislocation densities and the grain orientations. Furthermore, the parameters of the free energy are calibrated based on published Read-Shockley boundary energy data. To validate the proposed model, a polycrystalline aluminium aggregate is first cold deformed under plan strain conditions and then annealed. The predicted recrystallised material volume fraction evolution with respect to time was found to have the same dependence on deformation level and temperature as that reported in the literature. The implications of such findings for future developments are discussed.

Remerciements

Cette thèse s'est déroulée au Centre des Matériaux de l'Ecole des Mines de Paris. Je tiens tout d'abord à remercier son directeur, M. Esteban Busso, de m'y avoir accueilli et de m'avoir offert un environnement propice à l'émulation.

Je remercie également les membres du jury qui ont examiné avec soin ce travail, en particulier, M. Marc Geers et M. Thierry Hoc pour les remarques attentives et pour avoir accepté la lourde tâche de rapporter ce travail, ainsi que M. Ingo Steinbach pour m'avoir fait l'honneur d'accepter la présidence de mon jury.

Ce travail a été financé dans le cadre du projet Européen Digimat en partenariat avec la NSF. Je tiens à remercier tous les acteurs de ce consortium, en particulier, les deux responsables de ce projet, M. Roland Logé et M. Anthony Rollett.

J'ai eu la chance de réaliser ce travail sous la direction de M. Esteban Busso et M. Samuel Forest. Leurs compétences et leurs qualités humaines ont été une source de motivation permanente pour moi. Je tiens, à nouveau, à remercier M. Esteban Busso qui m'a beaucoup apporté durant cette période et qui a su rester disponible malgré ses nombreuses responsabilités. Ses conseils avisés m'ont permis de tracer les grands axes de cette thèse et, sa confiance, de garder une grande autonomie dans la réalisation de mes travaux.

Je tiens à exprimer ma gratitude à M. Samuel Forest, qui m'a également beaucoup soutenu. Son indéfectible enthousiasme m'a aidé à traverser les moments de doutes inévitables au cours d'une thèse. La rigueur de son analyse constitue pour moi un modèle que je m'efforcerai de suivre. Il a de plus fait l'effort d'être présent au cours de ce travail et ce malgré ses très nombreuses activités, je lui en suis donc d'autant plus reconnaissant.

J'ai également pu bénéficier des conseils et du point de vue précieux de M. Benoit Appolaire. Ses qualités tant scientifiques qu'humaines, ont été pour moi un soutien inestimable.

Mes remerciements vont également à l'ensemble du groupe COCAS au sein duquel j'ai trouvé une ambiance de travail sympathique et stimulante et, en particulier, M. Georges Cailletaud, pour m'avoir aidé à faire mes premiers pas avec Zebulon.

Je souhaite aussi remercier collectivement les chercheurs permanents ou non avec qui j'ai travaillé et dont j'ai également pu disposer des savoirs durant ces années. Je tiens à associer à ces remerciements, M. André Pineau qui, par nos discussions autour d'un café, m'a permis de rester au contact de la réalité métallurgique et surtout, de partager ses connaissances passionnantes sur l'histoire angevine.

Je remercie vivement toutes les personnes du service administratif que je n'ose citer de peur d'oublier des noms, celles du service informatique pour m'avoir fourni les conditions de travail indispensables à l'avancement de mes travaux et, Odile du service documentation pour avoir complété ma bibliographie avec efficacité. Bien évidemment, je tiens à remercier, Liliane, pour son dévouement et son accueil chaleureux dans son bureau avant mes réunions avec Esteban.

Ces années de thèse auraient, sans aucun doute, été moins agréables sans la présence de l'ensemble des thésards et post-docs du CdM avec qui j'ai travaillé, discuté et rigolé. Je

Contents

Chapter -I-

Introduction

Contents

I.1 Aims

During metal forming, engineering properties of metallic alloys are affected by a combination of thermal/mechanical processes. For example, a series of deformation and recrystallisation processes is used to improve the deep drawing characteristics of aluminium sheet for beverage can fabrication, as shown in Figure I.1. Nevertheless, fracture toughness of high strength aluminium alloys is better for an unrecrystallised material than for a recrystallised material of comparable yield strength.

<div align="center">(a)   (b)</div>
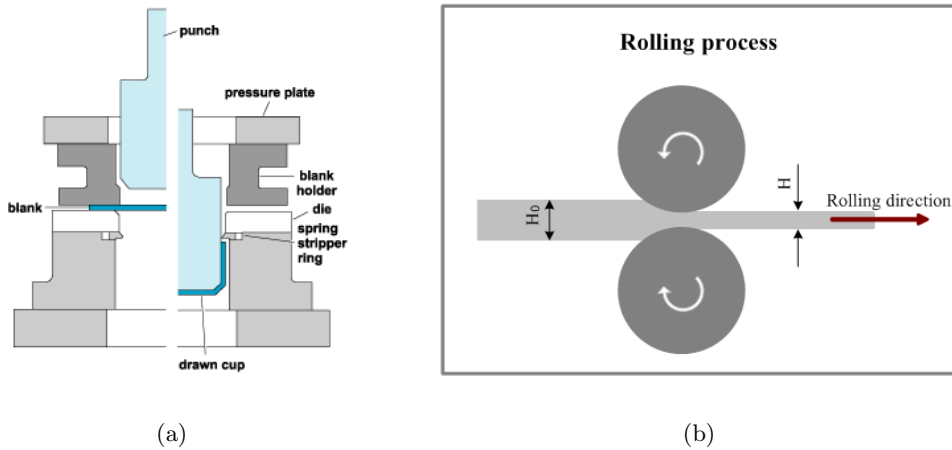
Figure I.1 : Schematics of (a) deep drawing, (b) sheet rolling

In a more general view, the physical phenomena induced by the thermo-mechanical processes infers complex microstructure changes which improve or not the final product properties. Among the physical phenomena responsible for microstructure changes, extensive care has been carried out on recrystallisation and related annealing phenomena. The typical recrystallisation process during heat treatment of a cold worked metal is referred to as static primary recrystallisation. Sometimes it is also referred to as discontinuous recrystallisation, since it proceeds locally and thus does not affect the entire volume concurrently. The term static recrystallisation is used to distinguish the thermal recrystallisation after cold work deformation under subsequent heat treatment, from the recrystallisation phenomena occurring concurrently with deformation at elevated temperatures, which is referred to as dynamic recrystallisation. The dynamic recrystallisation will not be discussed in this thesis. The static recrystallisation phenomena can be divided in two steps. First, the recrystallisation nuclei appear and grow in highly defective material as seen in Figure I.2. This is called the primary recrystallisation. After this first step leading to a microstructure made of small grains, the grain growth occurs to reduce the large grain boundary quantity.

Recrystallization processes depend on features that span scales from the polycrystalline topology to atomic arrangements around interfaces such as grain boundaries. Important factors over length scales of decreasing size include: (a) grain interactions, which set up stress fields that persist over grain dimensions, (b) stress variations within grains due to the presence of dislocation structures, which perturb the longer range field across the grain, (c) energies and mobilities of interfaces, which control their kinetics, and (d) particles and solutes, interacting with interfaces and modifying their kinetics.

Current industrial control of recrystallisation mainly focuses on control of texture for

(a) Deformed, t = 0 min

(b) t = 3 min

(c) t = 10 min

(d) t = 20 min
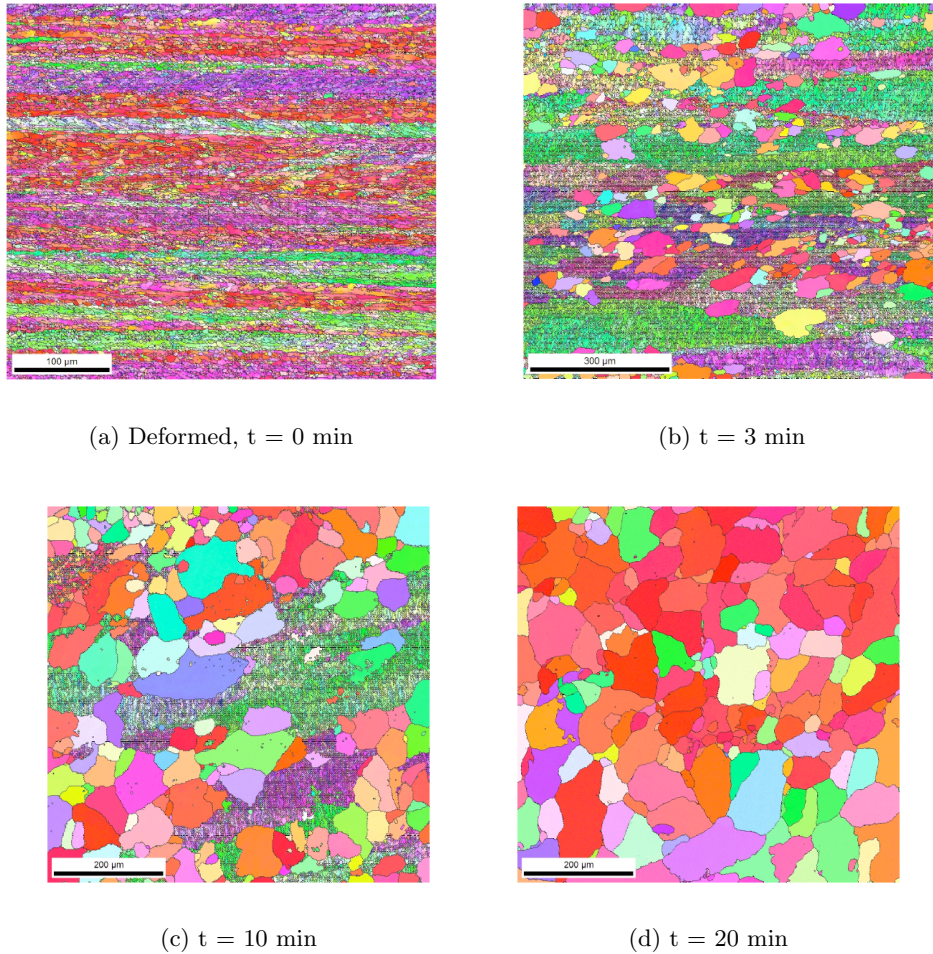
Figure I.2 : EBSD snapshots during recrystallisation phenomenon at 350°

formability, control of grain size and degree of recrystallisation for surface appearance and damage related properties. However, this method provides only quantitative measures and no qualitative understanding. Theories for recrystallisation that provide quantitatively correct predictions of crystallographic orientation, grain size distributions and mechanical properties have long been sought to model material processing from start to finish. Such a model requires a detailed understanding of both deformation and recrystallisation.

A large number of studies has been successful at predicting the mechanical behaviour of polycrystalline aggregates subjected to large deformations, including texture evolution. Ever since the work of Taylor, crystallographic models have tended to account for micro mechanical and physical aspects of deformation through appropriate microstructure evolution laws. On the other hand, extensive researches have been carried out on recrystallisation phenomenon. There have been several computational approaches to studying recrystallisation and grain growth in materials; the Monte Carlo method, phase field model, vertex dynamics and cellular automaton methods. A Few works have been done in order to couple the mechanical behaviour and the microstructure evolution. For instance, (Raabe and Becker, 2000) presents a two-dimensional approach for simulating primary static recrystallisation based on coupling a viscoplastic crystal plasticity finite-element model with a probabilistic kinetic cellular automaton. (Battaile *et al.*, 1999) proposed to simulate the microstructural evolution of

heavily deformed polycrystalline Cu by coupling a constitutive model for polycrystal plasticity with the Monte Carlo Potts model for grain growth. However, Monte Carlo and Cellular Automaton methods are both probabilistic techniques. Furthermore, in its standard form, CA does not allow for curvature as a driving force for grain boundary migration while the MC model does not result in a linear relationship between migration rate and stored energy. Recently, (Bernacki *et al.*, 2008) proposed a level set framework for the numerical modelling of primary static recrystallisation in a polycrystalline material which has been found promising. Nevertheless, contrary to level set method, phase-field method is a physically-based technic for simulating microstructural evolution. It has been applied to solidification, precipitate growth and coarsening, martensitic transformations and grain growth and, more recently, also to other solid-state phase transformations like the austenite to ferrite transformation in steels. Therefore, the aim of this work is to develop a coupled crystal plasticity-phase field formulation to describe the microstructural evolution in polycrystalline aggregates driven by grain boundary curvature and/or stored energy during recrystallisation and grain growth.

This thesis is part of a larger framework; the European project Digimat. The project entitled multiscale modelling of recrystallisation in metals based on a digital material framework has been done in collaboration with two US teams. The principal objectives are summarized below within 6 main sub-projects (the partners are cited with brackets):
• Development of a digital material framework (Mines Paris - ParisTech (CEMEF), Carnegie Mellon University)
• Modelling of the deformation of the microstructure (Mines Paris - ParisTech (CDM, CEMEF), Imperial College)
• Boundary interaction with dislocation and other defects through dislocation dynamics (Eotvos Lorend University, Princeton University)
• Atomistic arrangement with atomistic modelling (Princeton University)
• Modelling of recrystallisation (Mines Paris - ParisTech (CDM, CEMEF), Carnegie Mellon University)
• Experimental program (Eotvos Lorend University, Mines Paris - ParisTech (CDM, CEMEF), Imperial College)

I.2   Outline

As recrystallisation processes depend primarily on the nature of the microstructural state, an accurate prediction of such phenomena requires that the microstructural heterogeneities which develop just before recrystallisation be properly described. Therefore, chapter II contains a short review of existing models to describe the constitutive behaviour of the FCC polycrystalline aggregates. The single crystal elasto-viscoplastic model proposed by (Cheong and Busso, 2004) is detailed and will be used in the following sections. The constitutive behaviour of each grain in the aggregate is described using a non-local dislocation mechanics-based crystallographic formulation and finite-strain kinematics. The associated finite element implementation with an implicit integration is explained.

Chapter III proposed to study the possibilities and the limits of the elasto-viscoplastic model to describe the deformation behaviour of Al polycrystals. First, main deformation features in aluminium are reviewed. Then, the elasto-viscoplastic model is calibrated on single crystal and then validated on polycrystal aggregates with different grains sizes with data available in the literature. The model is utilized to reproduce numerically the microstructural characteristics present in a polycrystal aggregate just before the onset of

thermal recrystallisation during a channel die compression test. Channel-die compression tests are used to achieve plane strain compression, corresponding to the idealized conditions of sheet rolling. Non-local effects through the introduction of geometrically necessary dislocations (GND) are analysed.

During thermo-mechanical processing, energy stored in the microstructure of an FCC polycrystalline aggregate through dislocations accumulation is the main driving force in recrystallisation phenomena. Previous work in this area has focused on investigating the influence of strain gradients on the macroscopic behaviour of polycrystal aggregates, rather than on the stored energy distributions. Therefore, the objective of this work is to investigate the stored energy and dislocation density distributions found at the onset of recrystallisation. In chapter IV, different measures of stored internal energy based on the dislocation density distribution in the aggregate obtained from elasto-viscoplastic model the are proposed. The partition of plastic work into heat and stored energy are examined in single crystals and in polycrystalline aggregates.

In order to describe the interface motion, grain boundary properties are outlined in chapter V. Since the minimisation of stored and grain boundary energies provides the driving force for grain boundary motion, a phase field model taking into account the stored energy distribution is formulated and implemented within the continuum framework. The parameters of the free energy are calibrated based on published Read-Shockley boundary energy data.

Chapter VI studies the model abilities to predict grain boundary motion during grain growth and recrystallisation. General aspects of recrystallisation and grain growth are recalled. Driving forces due to curvature and due to stored energy are studied separately in order to see the effect on grain boundary velocity. First, misorientation and temperature effects are reported in curved bicrystals where curvature is considered as the only driving force for grain boundary motion. A particular attention is carried out on triple and quadruple junctions evolution. Topology and kinetics of a polycrystal aggregate during grain growth are scrutinized. Then, bicrystal velocity with flat grain boundary and stored energy difference between grains are examined. To compare their amount, stored energy and curvature are introduced as competing driving forces in curved grain. Since, in materials having high stacking fault energy such as Al, the sources of nuclei are the existing subgrains or cells in the deformed microstructure, a simple case of recrystallisation without the introduction of the 'classical' nuclei is detailed. Finally, a weak coupling is proposed between the phase field and the single crystal models.

I.3   Notations

Type	Notation
$\mathbf{b}$	Burger vector
a,b,c,d,e	phase field free energy coefficients
C^e	flow rule parameter
C^s	flow rule parameter
e	internal energy density
η	crystal order at the macroscopic scale
E_d	stored energy based on dislocaion density
E_p	stored energy based on plastic work
E_t	stored energy based on thermodynamic consideration
$\mathbf{E}^e$	Green-Lagrangian strain tensor
$\mathbf{F}$	otal deformation gradient tensor
$\mathbf{F}^0$	Helmhotz free energy of activation
$\mathbf{F}^e$	elastic part of deformation gradient tensor
$\mathbf{F}^p$	plastic part of deformation gradient tensor
$\dot{\mathbf{F}}$	total deformation gradient tensor rate
γ_{gb}	grain boundary energy
γ_{SFE}	stacking fault energy
$\dot{\gamma}^\alpha$	crystallographic slip rate on slip system α
$h^{\alpha\beta}$	dislocation interaction matrix
μ	shear modulus
$\mathbf{L}$	spatial velocity gradient
$\mathbf{L}^p$	plastic part of spatial velocity gradient
L	anisotropic elasticity tensor
M	grain boundary mobility
M^α	Schmid factor
$\mathbf{m}^\alpha$	slip system direction
$\mathbf{n}^\alpha$	normal to the slip plane
ν	poisson coefficient
P	grain boundary driving force
$\mathbf{P}^\alpha$	generalised schmid tensor
Q	activation energy for grain boundary energy
θ	grain orientation
$\mathbf{T}$	second Piola-Kirchoff stress tensor
r	averaging spacing between dislocation
R	universal gas constant
ρ_α	dislocation density on the slip system α
ρ_G^α	geomtrically dislocation density on the slip system α
ρ_S^α	statistically dislocation density on the slip system α

$\rho_S^\alpha e$	edge statiscally dislocation density on the slip system α
$\rho_S^\alpha s$	screw statiscally dislocation density on the slip system α
ρ_T^α	total dislocation density on the slip system α
σ	Cauchy stress tensor
s	entropy energy density
S^α	slip resistance on the crystallographic slip system α
T	absolute temperature
τ	shear stress
τ^α	shear modulus in the slip system α
$\hat{\tau}_0$	lattice friction at 0K
U	Helmholtz free energy density
v	grain boundary velocity
$\dot{\omega}^p$	plastic power per unit volume

References

Battaile C.C., Buchheit T.E., Holm E.A., Wellman G.W., and Neilsen M.K. (1999). *Coupled simulations of mechanical deformation and microstructural evolution using polycrystal plasticity and Monte Carlo Potts models.* In : Multiscale modelling of materials, vol. 538, pp 269–273. Materials Research Society.

Bernacki M., Chastel Y., Coupez T., and Loge R. E. (2008). *Level set framework for the numerical modelling of primary recrystallization in polycrystalline materials.* Scripta Materialia, vol. 58 n° 12, pp 1129–1132.

Cheong K.S. and Busso E.P. (2004). *Discrete dislocation density modelling of single phase FCC polycrystal aggregates.* Acta Materialia, vol. 52 n° 19, pp 5665–5675.

Raabe D. and Becker R.C. (2000). *Coupling of a crystal plasticity finite-element model with a probabilistic cellular automaton for simulating primary static recrystallization in aluminium.* Modelling and simulation in materials science and engineering, vol. 8 n° 4, pp 445–462. Symposium on the Modelling of Texture and Anisotropic Properties in Steel and Aluminium Industries for Optimum Materials Performance, Rosemont, IL, Oct 11-15, 1998.

Chapter -II-

Constitutive Behaviour of the FCC Polycrystalline Aggregates

Contents

As recrystallisation processes depend on the nature of the deformed state, a first step of an accurate modelling of recrystallisation involves a prediction of the microstructural heterogeneities which develop within grains just before recrystallisation takes place. The deformation process (tension, wire extrusion, extrusion, compression, torsion, shear, rolling...) and, the nature of the material play, an important role in the nature of the deformation state. In this work, the deformation state of cold deformed FCC metals with medium to high stacking fault energy (SFE) is studied. A range of materials and their SFE data which fall into this category are shown in Table II.1. Therefore, chapter II contains a short review of existing models to describe the constitutive behaviour of the FCC polycrystalline aggregates. The single crystal elasto-viscoplastic formulation in a finite-strain kinematics framework proposed by (Cheong and Busso, 2004) is detailed and extended to include non-local effect. The finite element implementation associated to the model with an implicit integration is exposed.

Table II.1 : Stacking fault energy of metals (Murr, 1975)

Metal	γ_{SFE} (mJm^{-2})	Metal	γ_{SFE} (mJm^{-2})
Aluminium	166	Zinc	140
Copper	78	Magnesium	125
Silver	22	Zirconium	240
Gold	45	304 stainless steel	21
Nickel	128	Cobalt (FCC)	15

II.1 Introduction

II.1.1 Crystallographic Slip Systems

Metals of high or moderate stacking fault energy such as aluminium alloys and copper deform by slip. Therefore, in continuum mechanics, an accurate prediction of the deformed state requires the modelling of the behaviour of the material by a crystallographic formulation. For FCC crystals, in general at low temperatures, slip takes place on most densely packed planes {111} and in the most densely packed directions <110>. Therefore, crystallographic is assumed to occur on the 12 octahedral {111}<110> slip systems. The Schmid and Boas slip system labelling convention is used to identify the individual slip systems in Table II.2. For each slip system α, the unit vectors, $\mathbf{m}^\alpha$ and $\mathbf{n}^\alpha$, representing, the slip direction and the normal to the slip plane, respectively.

II.1.2 Characteristics of Cold Deformed Microstructure

When an aggregate made of a large number of grains with an assumed random crystallographic orientation plastically deforms, deformation is essentially inhomogeneous even under simple loading conditions, as the interaction between neighbouring grains leads to the formation of a complex microstructure. During metal-forming processes, crystals generally change orientations. As a result, a general state of anisotropy appears at the macroscopic scale, and, at lower scales, regions of different orientations develop within the original grain. The texture development during deformation has an impact on the formability and mechanical properties of alloys while the grain subdivision or fragmentation due to misorientation within the grain, plays a dominant role in recrystallisation phenomena and, in particular the

Table II.2 : Schmid-Boas slip system notation of the octahedral slip system family

Notation : α	$\mathbf{b} \equiv \mathbf{m}^\alpha$	$\mathbf{n}^\alpha$
A2	$[\bar{1}11]$	$(0\bar{1}1)$
A3	$[\bar{1}11]$	(101)
A6	$[\bar{1}11]$	(110)
B2	$[111]$	$(0\bar{1}1)$
B4	$[111]$	$(\bar{1}01)$
B5	$[111]$	$(\bar{1}10)$
C1	$[\bar{1}\bar{1}1]$	(011)
C3	$[\bar{1}\bar{1}1]$	(101)
C5	$[\bar{1}\bar{1}1]$	$(\bar{1}10)$
D1	$[1\bar{1}1]$	(011)
D4	$[1\bar{1}1]$	$(\bar{1}01)$
D6	$[1\bar{1}1]$	(110)

nucleation phenomena. Therefore, numerous studies have been carried out to control the crystallographic textures in order to improve product performance (Kalidindi *et al.*, 1992, Becker and Panchanadeeswaran, 1995, Zhao *et al.*, 2004). Furthermore, considerable work has also focused on the description of the nature of the deformed state, especially intragranular misorientations, (Hughes and Hansen, 1997, Merriman *et al.*, 2008) and their prediction (Seefeldt *et al.*, 2001, Butler and Hu, 1989). It is now known that there is a wide range of length scales, from nanometres to millimetres, at which the microstructure is heterogeneous during deformation.

Figure II.1 summarises the main features of the deformed state according to their length-scale. The shear bands in Figure II.2 a, are non-crystallographic and may extend through several grains. The deformation or transition bands in Figure II.2 b are the consequences of subdivision within grain into large regions of different orientations. At a lower scale, the deformed polycrystalline aggregate is made of cells or subgrains. These cell structures are essentially low-angle grain boundaries which subdivide each grain to produce inhomogeneities at the intragranular level. This is the result of having a non-uniform dislocation distribution where each boundary contains a rich density of entangled dislocations, separated by regions which are almost dislocation free, see Figure II.3.

II.1.3 Representative Volume Element Definition

A polycrystalline aggregate is a heterogeneous material where the mechanical properties vary over a characteristic distance (cell size, deformation band, grain). The volume element needs to have the proper size, small enough to be macroscopically considered as a material point and large enough to represent the macroscopic material properties, see Figure II.4. In general, homogeneous or periodic boundary conditions are prescribed to the volume element to satisfy the averaging procedure. In this case, two polycrystalline aggregates with a change of microstructure have the same macroscopic mechanical properties. Such a volume element is called a representative volume element (RVE). Several studies have been carried out to find the minimum RVE size for specific mechanical properties. A first approach of the size of RVE
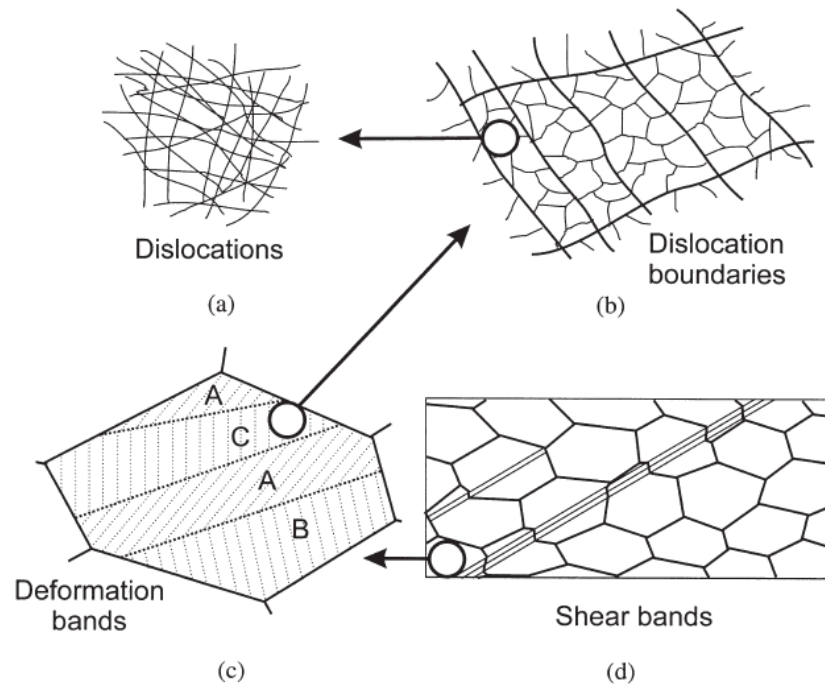
Figure II.1 : The hierarchy of microstructure in a polycrystalline metal deforming by slip. The various features are shown at increasing scales: (a) dislocations, (b) dislocation boundaries, (c) deformation and transition bands within a grain, (d) specimen and grain-scale shear bands (Humphreys and Hatherly, 2004)
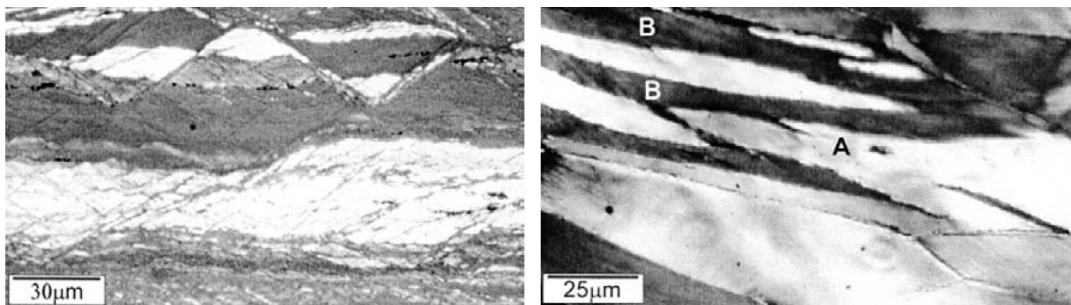
Figure II.2 : (a) Shear bands in Al-Zn-Mg alloy cold rolled 90%, (b) deformation bands (B) in a grain (A) in Al-1%Mg (Humphreys and Hatherly, 2004)
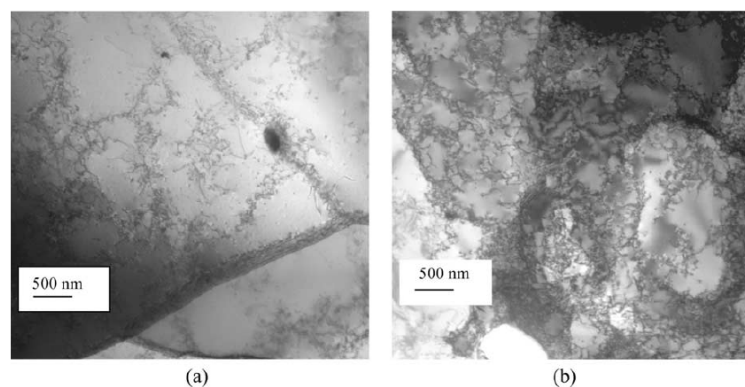
Figure II.3 : TEM bright field images of an Al alloy (5005) deformed at (a) 2% and (b) 10% (Trivedi *et al.*, 2004)
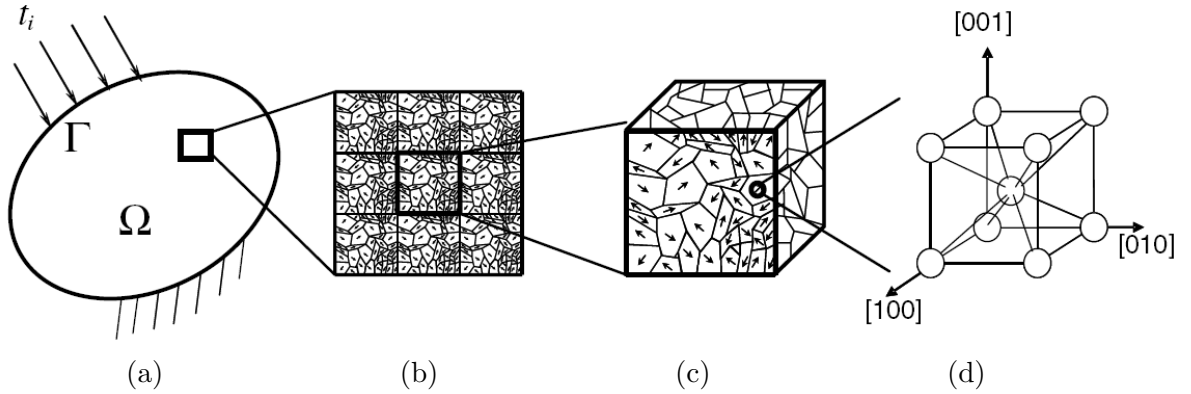
Figure II.4 : Macro continuum and micro polycrystal structures: (a) macro continuum, (b) micro structure, (c) RVE, (d) crystal lattice (Nakamachi *et al.*, 2007)

for polycrystals can be found in (Quilici *et al.*, 1998). (Ren and Zheng, 2002) showed that the minimum RVE size for the effective shear modulus G has a roughly linear dependence upon the degree of anisotropy of single crystals with a minimum RVE size of 20 or less for all cubic materials. (Kanit *et al.*, 2003) considered the RVE size as a function of five parameters: the studied physical property, the contrast of properties, the volume fractions of components, the wanted relative precision for the estimate of the effective property and the number of executions of the microstructure associated with computations that one is ready to carry out.

The polycrystalline aggregate considered as a RVE ensures the reproducibility of the macroscopic behaviour. However, a good description of the grain morphology is required to predict an accurate localisation, for instance, of strain to study nucleation or stress driven fracture problems. Polycrystalline aggregates contain a large number of grains of various shapes and one of the main difficulties is to discretise the microstructure. Most of the characterisation techniques rely on grain-surface observations such as orientation imaging microscopy (OIM). The main drawbacks of the measurements is the destruction of the sample to obtain a 3D characterisation of the aggregate. New methodologies such as X-ray microtomography (Madi *et al.*, 2007) and synchrotron hard X-ray (Baruchel *et al.*, 2008), allow the full characterisation of the aggregate. The meshing of the aggregates obtained by experimental techniques imply some difficulties due to the non-convexity of the grains. One of the simplest method is to consider the grain shape as cuboidal in order to get the main deformed features and the macroscopic stress-strain response of the aggregates. On the other hand, more realistic three-dimensional grain morphologies have been produced containing a large number of random grains generated using Voronoi polyhdra model (Barbe *et al.*, 2001a), while dodecahedral-shaped crystals have been used to built up realistic polycrystals (Mika and Dawson, 1998).

II.1.4 Mechanical Behaviour Transition: From Single Crystal to Polycrystalline Aggregate

Numerous models have been developed to describe the transition from the mechanical behaviour of a single crystal to that of a polycrystalline. The main approaches are described in this section, namely:
• Taylor Type
• Self-Consistent
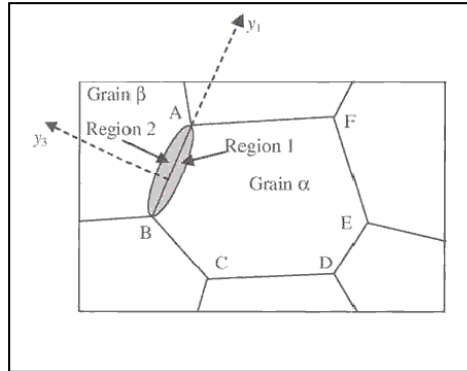
Figure II.5 : Schematic representative microstructure (Van Houtte *et al.*, 2005)

• Finite Element
• Fast Fourier Transformation

II.1.4.1   Taylor Type Models

One of the first models proposed to take the texture of the material into account was that proposed by Taylor (Taylor, 1938). It is still used to study the constitutive response of polycrystalline aggregates due its low numerical cost. It is capable of accurately predicting the macroscopic stress-strain response and texture evolution of FCC polycrystals with medium to high stacking fault energies through an averaging procedure. It provides an upper-bound solution by ensuring the compatibility between individual grains within an aggregate. The compatibility condition is satisfied by assuming that the strains are the same in all grains and equal to the macroscopic strain. However, grain interactions are ignored and as a result it is not able to describe the features of the deformed state.

To improve the deformation behaviour of polycrystalline aggregates, other models such as relaxed-constraint (Honeff and Mecking, 1981, Kocks and Chandra, 1982) and multi-grains relaxed-constraint models (Van Houtte *et al.*, 2002) have been developed. Relaxed-constraint models satisfy selected compatibility relations and ignore some intergranular equilibrium components. The deformation of individual grains is partly relaxed based on geometrical considerations. In multi-grains relaxed-constraint models, such as the ALAMEL model (Van Houtte *et al.*, 2005), the local gradient deformation tensor is not constant within the grain and the approach accounts the interaction of a cluster of two grains, see Figure II.5.

II.1.4.2   Self-Consistent Models

In contrast with relaxed-constraint models, the self-consistent models satisfy both compatibility and equilibrium between grains in average sense (Eshelby, 1957). The constitutive laws are solved by different methods: incremental formulation (Hill, 1965), first order methods (Molinari *et al.*, 1987), second order methods (Ponte Castaneda, 1996) etc. The self-consistent scheme has been extended to elasto-plastic behaviour in a small deformation framework (Hill, 1965), in a large strain framework (Nemat-Nasser and Obata, 1986), to elasto-viscoplastic behaviour (Weng, 1982) and to viscoplastic behaviour (Lebensohn and Tomé, 1993).
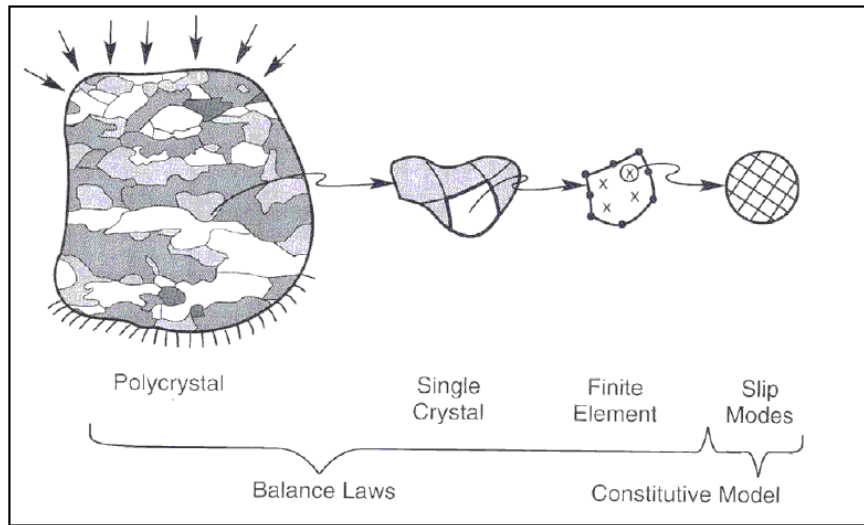
Figure II.6 : Finite element modelling of a polycrystal (Kocks *et al.*, 2000)

II.1.4.3   Finite Element Methods

Both Taylor type and self-consistent models assume that individual grains deform homogeneously which makes impossible the prediction of grain nucleation during recrystallisation. Finite element models are able to describe non-homogeneous deformation at both the intragranular and intergranular levels. When using finite-element (FE) to model polycrystalline aggregates, the constitutive response at each integration points of a finite-element is determined using a single crystal constitutive model. In this approach, the transition from the constitutive response of each crystal to the response of a polycrystalline aggregate is shown in Figure II.6. Typically, the single crystal accounts for deformation and for the associated lattice rotations through crystallographic slip. The distinct advantage of finite-element models compared to the other polycrystal plasticity models is that morphological effects such as grain size, shape and topology can be accounted for.

II.1.4.4   Fast Fourier Transformation (FFT)

The FTT method has been used to describe the mechanical behaviour of polycrystalline aggregates with periodic boundary conditions (Lebensohn, 2001). (Lebensohn, 2001) showed that the FTT method is numerically less costly than the finite element method for problems of same size. However, the limits of the method are in the required periodic boundary conditions.

II.1.5   Constitutive Law

II.1.5.1   Dislocations Interaction

The idea of a dislocation as a 1D crystal defect was first proposed in the 1930s to explain the lower shear strength measured in crystalline materials than theoretical estimates based on atomic bonding considerations (Frankel, 1926). It was predicted that defects had to exist to explain the reduction of the mechanical strength. A breakthrough arrived when the concept of an edge dislocation was introduced to explain this discrepancy (Orowan, 1934, Polanyi, 1934, Taylor, 1934). The screw dislocation was later introduced by (Burgers, 1939). It assumes that each dislocation moves when the shear stress,τ, reaches
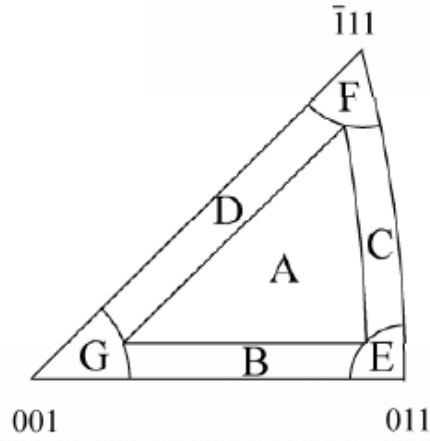
Figure II.7 : Inverse pole figure showing the number of active slip systems; A:1, B:2, C:2, D:2, E:4, F:6, G:8

a specific value necessary to overcome obstacles such as other dislocations, solute atoms or precipitates, grain boundaries, or the periodic lattice friction. It is the interaction of potentially mobile dislocations which determines the flow rate and the yield strength. For single-phase metals, forest dislocations (usually defined as dislocations on other slip systems threading the slip plane of a moving dislocation) constitute the main resistance to dislocation motion. Considering forest dislocations as the only obstacles and since the shear strain and stress fields around a dislocation are proportional to $1/r$, where r is the distance from the dislocation core, the shear stress requires to move per unit length of dislocation past another of opposite sign is,

$$\tau \propto \frac{\mu b^2}{2\pi r} \tag{II.1}$$

where μ being the shear modulus. The average spacing r between dislocations is inversely proportional to $\rho^{1/2}$ based on the assumption that there exists a regular arrangement of dislocations in space. This situation was first describe by (Orowan, 1940) which suggested that

$$\tau \propto \mu b^2 \rho^{1/2} \tag{II.2}$$

The dislocations move, in general, along specific directions, defined as slip systems, see Section II.1.1. The number of activated slip systems in which dislocation motion occurs is determined by Schmid Law,

$$\tau^\alpha = M^\alpha \sigma \tag{II.3}$$

where τ^α is the shear stress in the slip system α, M^α is the Schmid factor and σ is the applied stress. During a tensile test in the direction $\mathbf{t}$, the Schmid factor is defined as $M^\alpha = (\mathbf{n}^\alpha.\mathbf{t})(\mathbf{m}^\alpha.\mathbf{t})$ where $\mathbf{n}^\alpha$ and $\mathbf{m}^\alpha$ are, respectively, the unit vector normal to the slip plane and parallel to the slip direction. For instance, eight slip systems are active for tensile loading along the [001] direction, six systems are active for a uniaxial tensile loading along the [111] direction..., see Figure II.7

The Orowan relationship has been modified to describe the slip resistance on the crystallographic slip system, α,

$$S^\alpha \propto \mu b \sqrt{\sum_{\beta=1}^{N} h^{\alpha\beta} \rho^\beta} \tag{II.4}$$

Here, ρ^{β} is the crystallographic dislocation density on an arbitrary slip system β, while $\delta^{\alpha\beta}$ is a dislocation interaction matrix detailing the possible reactions between dislocations on different slip systems. Typically, the $h^{\alpha\beta}$ matrix contains two coefficients, one for the diagonal terms representing the self hardening interaction strength between dislocations on the same slip system, and another for the off-diagonal terms to describe the latent-hardening interaction strength between dislocations on dissimilar slip systems. The nature of each interaction depends on the character of the dislocation and leads to a complex interplay between the dislocations. Evidence of latent-hardening anisotropy during single slip obtained in latent hardening experiments (Kocks and Brown, 1966, Franciosi *et al.*, 1980) and dislocation dynamic works (Devincre *et al.*,) showed that each element of the interaction matrix describes the cross-interaction between dislocations on two different slip systems.

II.1.5.2 Rate Dependent Flow Rule

The strain-rate is determined almost entirely by the waiting time of the density ρ of mobile dislocations at pinning obstacles with a mean velocity $\bar{v}$ (Orowan, 1940) :

$$\dot{\gamma} = \rho b \bar{v} \tag{II.5}$$

At steady state, ρ is a function of the shear stress and temperature only. For this case, Eq.II.2 gives:

$$\rho = \alpha \left(\frac{\tau}{\mu b}\right)^2 \tag{II.6}$$

where μ is the shear modulus. The rate dependent Viscoplastic flow rule is based on the thermally activated motion of dislocations. The mean velocity of a dislocation segment, $\bar{v}$, is given by the following kinetic equation (Frost and Ashby, 1982):

$$\bar{\nu} = \beta b \nu \exp - \frac{\Delta G(\tau)}{kT} \tag{II.7}$$

where β is a dimensionless parameter, b is the magnitude of the Burgers' vector, and ν is a frequency. The quantity $\Delta G(\tau)$ depends on the distribution of obstacles and on the pattern of internal stresses. Assuming that random obstacles are seldom box-shaped, (Kocks, 1977) described the quantity $\Delta G(\tau)$ by the general equation:

$$\Delta G(\tau) = F_0 \left(1 - \left\langle \frac{\tau}{\hat{\tau}} \right\rangle^p\right)^q \tag{II.8}$$

Here, F_0 is an activation energy which depends on obstacle type. The quantity $\hat{\tau}$ is the "athermal flow strength", the shear strength in the absence of thermal energy. The parameters p and q define the shape of the energy-barrier profile. The quantities p, q and F_0 are bounded:

$$0 \le p \le 1 \tag{II.9}$$

$$1 \le q \le 2 \tag{II.10}$$

$$0.2 \le \frac{F_0}{\mu b^3} \le 2 \tag{II.11}$$

Combining Eqs.II.5, II.6, II.7 and II.8, the rate-equation for discrete-obstacle controlled plasticity becomes

$$\dot{\gamma} = \dot{\gamma}_0 exp \left[- \frac{F_0}{kT} \left(1 - \left\langle \frac{\tau}{\hat{\tau}} \right\rangle^p\right)^q \right] \tag{II.12}$$

where $\dot{\gamma}_0$ is a constant. The kinetic equation for each slip system rate, $\dot{\gamma}^{\alpha}$, represents the flow characteristics on an arbitrary slip system α, and can be derived from Eq.II.12:

$$\dot{\gamma}^{\alpha} = \dot{\gamma}_0 exp \left[- \frac{F_0}{kT} \left(1 - \left\langle \frac{\tau^{\alpha}}{\hat{\tau}} \right\rangle^p\right)^q \right] \tag{II.13}$$
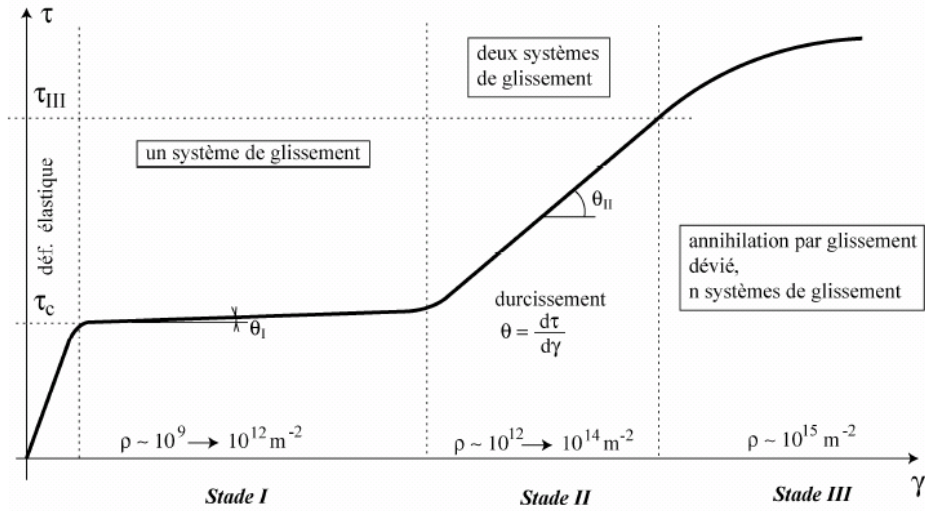
Figure II.8 : Generalised flow curve for FCC single crystals

The majority of most physics based flow rules used in single crystal models are based on this theory (Busso, 1990, Balasubramanian and Anand, 2002, Ma and Roters, 2004).

More phenomenological viscoplastic flow rule have been developed. (Cailletaud, 1992) proposed a single crystal model containing isotropic and kinematic hardening by means of the two internal variables, r^α and x^α for each slip system while in physically-based flow rule, dislocation densities are, in general, the internal variables, see details in the following section.

$$\dot{\gamma}^\alpha = \langle \frac{|\tau^\alpha - x^\alpha| - r^\alpha}{K} \rangle \tag{II.14}$$

II.1.5.3 Hardening Description

For more accurate modelling of deformation behaviour in single and polycrystals, an accurate understanding of the material hardening behaviour is necessary. Hardening phenomena is due to the obstacles that dislocations overcome during their motion in the microstructure. In single-phase alloy, the main obstacles are other dislocations. For most single crystals, three stages of plastic deformation are observed in the flow curve, see Figure II.8. Stage I of the plastic deformation is characterised by the easy-glide of dislocations of the primary slip system, predominantly edge dislocations. The low-hardening of Stage I is due to the activation of only one slip system. The linear Stage II is due to forest hardening, and its slope increases with the number of active slip systems. Dislocation structures observed in Stage II consist mainly of rectangular dislocation networks extended parallel to the primary glide plane. The dislocation density is further increased in Stage III. A cell structure is observed, which consists of dense dislocation networks surrounding regions nearly free of dislocations. The subsequent decrease in strain hardening rate stems from dynamic recovery.

For FCC polycrystals, four deformation stages are observed, see Figure II.9 a. The three first stages correspond to those described in the single crystal case under simple shear. On the flow curve of polycrystals, the Stage I is hardly observed. The work hardening rate decreases with increasing stress and strain at small to medium deformations (Stage III regime), whereas at large stresses and strains the strain hardening rate is almost constant
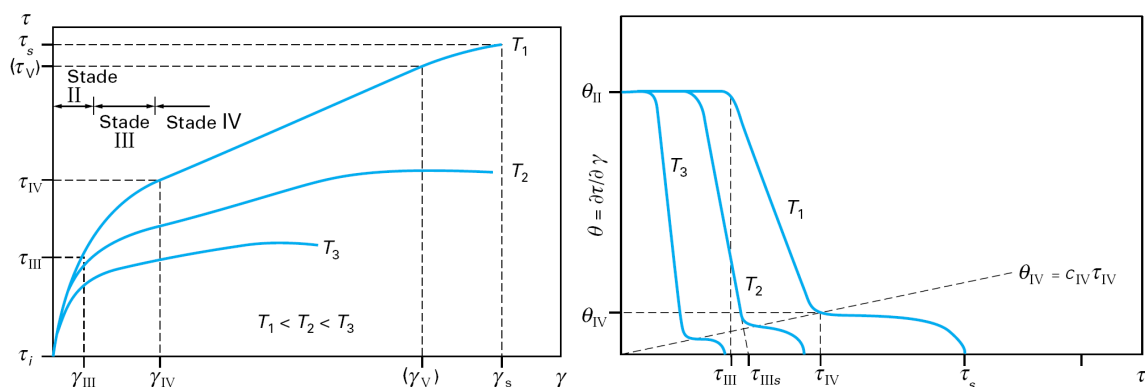
Figure II.9 : Schematic (a) hardening rate curve for FCC polycrystals and (b) hardening curve for FCC polycrystals (Driver and Chenal, 2000)

(Stage IV regime), see Figure II.9 b. Currently, there is not a single theory which can explain Stage IV, even though several theories have been proposed (Prinz and Argon, 1984, Rollet *et al.*, 1987, Argon and Haasen, 1993, Hughes and Hansen, 2000).

Two main kinds of models have been developed to describe the hardening behaviour in crystal plasticity: models with phenomenological internal state variables and models with dislocation densities as internal state variables. For instance, in the first category, see (Busso, 1990, Kumar and Yang, 1999) use slip resistances as state variables. (Cailletaud, 1988) transferred macroscopic laws to the single crystal scale and showed a good ability for predicting cyclic behaviour. These models have a distinct disadvantage in that the material state cannot be directly observed and the validation of these quantities would require difficult latent hardening experiments to be conducted (Bassani and Wu, 1991). For more detailed modelling of deformation behaviour in single and polycrystals, an appropriate description has to be based on microstructural state variables which are affected by the deformation history of the material. Therefore, models which rely on an internal-state variable approach are developed based on the understanding of microstructural evolution and the interaction of dislocations with short and long-range obstacles. Polycrystals plasticity models developed to describe cell-forming polycrystalline aggregates at large strains typically use dislocation cell walls and cell interiors (Estrin *et al.*, 1998) as well as boundaries which separate cell walls (Peeters *et al.*, 2000) as internal state variables. (Zikry and Kao, 1996) defined a constitutive formulation where mobile and immobile dislocation densities are used as the internal state variables. Similarly, (Roters *et al.*, 2000) defined mobile and immobile dislocations in cell interiors and immobile dislocations inside cell walls to be the internal state variables. Defining dislocations in cell interiors and in cell walls enables to specify different mobility for each dislocation type. Alternatively, dislocation can be also discretised into edge and screw dislocations. When dislocations intersect, jogs and kinks are formed. A kink is a step in the dislocation line in the slip plane where the dislocation moves while a jog is a step in dislocation line onto another slip plane. Kinks form on edge dislocations after intersection, are always glissile and consequently do not affect the subsequent glide of dislocation. In contrast, jogs with edge character formed in screw dislocations cannot glide since the glide plane for the jog is different from that for the main dislocation line. The jog is pinned and the dislocation is said to be sessile. In this case, motion can only occur by the dislocation line moving out of its existing glide plane, this is known as non-conservative motion. Here, the length of the dislocation line is not conserved. Therefore, the mobility of screw dislocations is markedly lower than that of an edge dislocation since its movement is
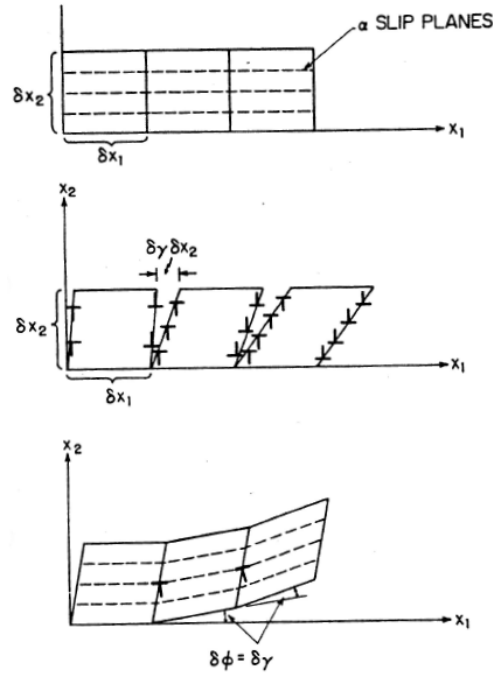
Figure II.10 : Crystal under a shear gradient (Ashby, 1970)

more severely impeded. (Arsenlis and Parks, 2002, Cheong and Busso, 2004) used edge and screw dislocations densities as internal state variables and assigned them different mobilities.

II.1.6 Incorporation of Strain Gradient Concepts

Size-dependent effects have been observed in a wide range of experiments. The more typical examples are the grain size dependence of initial yielding and work-hardening in polycrystalline aggregates, a behaviour known as the Hall-Petch effect (Hall, 1951, Petch, 1953, Hansen, 1977). In these examples, for a given strain, the smaller the grain size, the harder the material response is. A phenomenological expression of the Hall-Petch effect is

$$\sigma(\epsilon) = \sigma_0(\epsilon) + kd^{-1/2} \tag{II.15}$$

where d is the grain size, σ_0 is the friction stress and k is the Hall-Petch factor. The length-scale dependency results from the presence of strain gradients due to lattice incompatibilities associated with inhomogeneous plastic deformation. When strain gradients are of the order of the dominant microstructural length scale (small grain size), the macroscopic stress-strain response is affected. (Nye, 1953) was the first to give a measure of the plastic deformation incompatibility through the Nye's tensor which will be defined later in the section. In order to better understand the interplay and mechanism of dislocations in macroscopic hardening, (Ashby, 1970) considered that dislocations can be composed of statistically-stored dislocations (SSDs) and geometrically necessary dislocations (GNDs). The SSDs are considered to be inherently present in a homogeneously deforming material, where they accumulate in numbers by randomly impeding and trapping other moving dislocations. On the other hand, GNDs are considered to be 'necessary' in order to accommodate lattice incompatibilities in regions where deformation is inhomogeneous, resulting in the curvature of the crystal lattice. Therefore, GNDs are essentially localised in grain boundaries where the lattice discontinuity is found.

Figure II.10 illustrates the formation of GNDs (Ashby, 1970). A crystal split in several
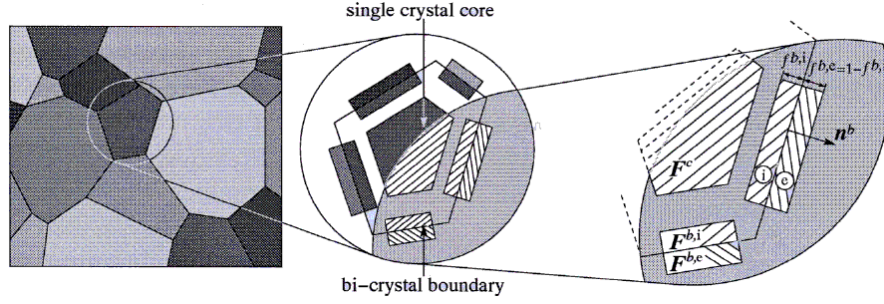
Figure II.11 : From a polycrystal assembly, each crystal is decomposed into constituent parts, representing its core and its boundaries (Evers *et al.*, 2002)

blocks is under shear gradient. Dislocations of the same type but opposite sign annihilate. The dislocations excess resulting from this annihilation process, is proportional to the slip gradient with respect to x,

$$\rho_G = \frac{1}{b}\frac{\partial \gamma}{\partial x} \tag{II.16}$$

Classical crystal plasticity models are enhanced to take into account the length-scale dependency. (Weng, 1983) proposed to link the threshold stress on each slip system and the grain size d by introducing explicitly the Hall-Petch relation in the self-consistent theory for plastic deformation of metals developed in (Weng, 1982). However, this approach is questionable since that the Hall-Petch relation is only a macroscopic relation. As mentioned in II.1.4.1, the first Taylor-type models assume deformation uniformity within grains and across grain boundaries, violating the stress equilibrium condition at the interfaces. (Evers *et al.*, 2002) proposed an alternative intermediate model whereby each grain is fictitiously subdivided into a core and several grain boundary fractions. The crystal interior is modelled by one single crystal volume element, whereas several bi-crystal volume elements represent the grain boundaries, see Figure II.11. The average plastic deformation discrepancy between the core and the interior bi-crystal parts represents heterogeneous intragranular deformations accommodated by GNDs. From the measure of plastic deformation incompatibility given by Nye's dislocation tensor (Nye, 1953), defined as the curl of the plastic part of the deformation gradient (curl of $\mathbf{F}^p$) by (Dai and Parks, 1997), the GNDs density are estimated and included in the slip resistance.

In the single crystal framework, (Fleck and Hutchinson, 1997, Shu and Fleck, 1999), (Gurtin, 2002) proposed a second gradient theory including a higher order stress tensor. The length scale arises from the curvature of the crystal lattice controlled by the deformation gradients. Higher order theories such as Cosserat media have also been developed in a single crystal framework incorporating coupled stress to take into account the length scale dependency (Forest *et al.*, 2001). Although motivated from concepts in dislocation theory, an approach to describe strain gradient effects without additive higher order stresses has been developed by (Acharya *et al.*, 2003, Busso *et al.*, 2000, Arsenlis and Parks, 1999). These non-local theories rely on an internal state variable approach to determine the macroscopic response of the material whereby strain gradient effects are introduced directly into the evolutionary laws of the state variables. The strain gradient effects are incorporated by determining the GND population using Nye's tensor, which gives a measure of the plastic deformation incompatibility. Physically, Nye's tensor can be interpreted as a measure for the closure failure of Burger's circuit enclosing an infinitesimal surface, where the inner product

of Nye's tensor Λ with the unit normal vector $\mathbf{n}$ of surface S is integrated over that surface,

$$G = \int_S \Lambda.\mathbf{n}dS \qquad (II.17)$$

That closure failure is equivalent to a cumulative Burger's vector G, and is related to the density and character of GNDs piercing the enclosed surface. Strain gradient theories based on the Nye's tensor show good agreement with experimental work (Dai and Parks, 1997, Busso and McClintock, 1996, Acharya and Beaudoin, 2000). Contrary to the second gradient and Cosserat theories, they are relatively easy to implement numerically and do not require higher order stresses and additional boundary conditions.

II.2 Single Crystal Constitutive Equation

The single crystal model based on dislocation mechanics used here was proposed by (Busso and Cheong, 2001). After its initial implementation in the finite element code Abaqus, it has been successfully used in a series of studies (Cheong and Busso, 2004, Cheong *et al.*, 2005, Cheong and Busso, 2006). In the model, dislocations are discretised into edge and screw components with intrinsically different relative mobilities and are subject to different dynamic recovery processes. The individual roles played by each dislocation type in contributing to the overall deformation behaviour, are distinguished. Furthermore, discretising the dislocations into edges and screws enables to take into account their different energy per unit length of dislocation line in the strain energy formulation.

II.2.1 Finite Strain Formulation

The foundations of the constitutive model for single crystal elasto-plastic finite strain kinematics used here, follow the approach proposed by (Mandel, 1973). The basic feature is the distinction between two physical mechanisms, represented by the multiplicative decomposition of the total deformation gradient tensor $\mathbf{F}$, see Figure II.12. The total deformation gradient can be multiplicatively decomposed into $\mathbf{F^p}$, associated with crystallographic slip, and $\mathbf{F^e}$ which describes the stretching and the rotation of the crystal lattice

$$\mathbf{F} = \mathbf{F^e}\mathbf{F^p} \qquad (II.18)$$

As the deformation history is important, it is essential to express the total deformation gradient $\mathbf{F}$ in rate-form

$$\dot{\mathbf{F}} = \mathbf{LF}, \qquad (II.19)$$

where $\dot{\mathbf{F}}$ is the rate of the total deformation gradient and $\mathbf{L}$ is the spatial velocity gradient. From eqs. II.18 and II.19, $\mathbf{L}$ can be additively decomposed into its elastic $\mathbf{L}^e$ and plastic $\mathbf{L}^p$ counterparts,

$$\mathbf{L} = \dot{\mathbf{F}}^e\mathbf{F}^{e-1} + \mathbf{F}^e\dot{\mathbf{F}}^p\mathbf{F}^{p-1}\mathbf{F}^{e-1} = \mathbf{L}^e + \mathbf{F}^e\mathbf{L}^p\mathbf{F}^{e-1}. \qquad (II.20)$$

The plastic flow is assumed to be the result of crystallographic slip. $\mathbf{L}^p$ is the sum of crystallographic slip rates on N number of activated slip systems (Asaro and Rice, 1977)

$$\mathbf{L}^p = \sum_{\alpha=1}^{N} \dot{\gamma}^{\alpha}\mathbf{P}^{\alpha} \qquad (II.21)$$
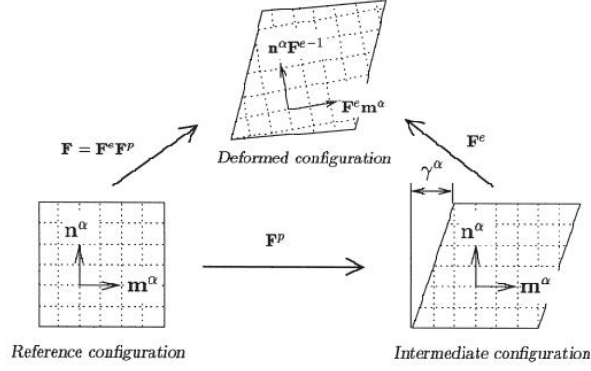
Figure II.12 : Single crystal kinematics showing the decomposition of the total deformation gradient **F** into a plastic part **F$^{\mathbf{p}}$** due to crystallographic slip and an elastic part associated with lattice strains and rotation. The crystallographic axes are represented by slip direction **m**$^{\alpha}$ and slip plane normal **n**$^{\alpha}$.

where $\dot{\gamma}^{\alpha}$ is the crystallographic slip rate of an arbitrary α slip system, **P**$^{\alpha}$ is the dyadic product of the crystallographic slip direction vector **m**$^{\alpha}$ and slip plane normal unit vector **n**$^{\alpha}$ in the reference configuration :

$$\mathbf{P}^{\alpha} = \mathbf{m}^{\alpha} \otimes \mathbf{n}^{\alpha} \tag{II.22}$$

The time rate of change of the plastic deformation gradient, $\dot{\mathbf{F}}^{p}$, is defined by :

$$\dot{\mathbf{F}}^{p} = \mathbf{L}^{p}\mathbf{F}^{p} \tag{II.23}$$

Let us consider a hyperelastic behaviour. It relies on Green-Lagrangian strain tensor with respect to the intermediate configuration:

$$\mathbf{E}^{e} = \frac{1}{2}(\mathbf{F}^{eT}\mathbf{F}^{\mathbf{e}} - \mathbf{I}) \tag{II.24}$$

The term **T** defined as the second Piola-Kirchoff stress pushed forward to the intermediate configuration is the work conjugate stress measure to the Green-Lagrange strain tensor **E**^{e}, (Meissonnier *et al.*, 2001). **T** and σ, the Cauchy stress tensor, are related through,

$$\mathbf{T} = (det\mathbf{F}^{e})\mathbf{F}^{e-1}\sigma\mathbf{F}^{e-T} \tag{II.25}$$

Since **T** is the work conjugate stress measure related to the Green-Lagrange strain tensor **E**^{e}, a hyperelastic constitutive law referred to the intermediate configuration is used to describe the mechanical response of the single crystal, thus allowing a total stress-strain relationship to be derivable from the Helmholtz free energy density U of the lattice per unit reference volume,

$$\mathbf{T} = \frac{\partial U}{\partial \mathbf{E}^{e}} \tag{II.26}$$

Differentiating Eq. II.26 with respect to **E**^{e} yields a fourth order tensor κ,

$$\frac{\partial \mathbf{T}}{\partial \mathbf{E}^{e}} = \kappa \tag{II.27}$$

where

$$\kappa = \frac{\partial^{2}U}{\partial \mathbf{E}^{e2}} \tag{II.28}$$

In most crystalline metals, the elastic deformation range is infinitesimal when compared to the plastic strains. Therefore, κ can be approximated by the fourth order anisotropic elasticity tensor $\mathcal{L}$ and the final constitutive law from Eq. II.26 becomes,

$$\mathbf{T} \approx \mathcal{L} : \mathbf{E}^e \tag{II.29}$$

With the single crystal kinematics established, it is now necessary to link it to the evolution of the dislocation density state variables through the crystallographic slip rates $\dot{\gamma}^\alpha$ introduced in eq. II.21

II.2.2 Dislocation Mechanics-based Crystallographic Formulation

II.2.2.1 Kinetics of Inelastic Flow

The associated flow rule governing the kinetics of inelastic flow is rate-dependent since the flow rate due to dislocation motion (Orowan, 1940) is inherently rate dependent even at low-temperatures. The obstacles to dislocation motion can be broadly classified to be either short or long-ranged types. As described in Section II.1.5.2, short-range obstacles are thermally activated and can be interpreted as representing local barriers which can be overcome by thermal fluctuations alone. The long-range obstacles are considered to be athermal in nature as they present themselves as energy barriers which can be overcome by thermal activation. Here, the kinetic equation used for the crystallographic slip rate describes the flow characteristics on an arbitrary slip system α, for a given temperature, structure and applied stress taking into account the thermal and athermal components (Busso, 1990, Busso and McClintock, 1996). From eq. II.13 and extrapolating the slip resistance and lattice stress at 0K, the kinetic equation for the crystallographic slip rate $\dot{\gamma}^\alpha$ has the following expression:

$$\dot{\gamma}^\alpha = \dot{\gamma}_0 \exp\left[-\frac{F_0}{kT} \left\{ 1 - \left\langle \frac{|\tau^\alpha| - S_0^\alpha \mu/\mu_0}{\widehat{\tau}_0 \mu/\mu_0} \right\rangle^p \right\}^q \right] sign(\tau^\alpha) \tag{II.30}$$

F_0 is defined as the Helmholtz free energy of activation, which is the total free energy needed to overcome short-range obstacles without the aid of an applied shear stress. The term $\widehat{\tau}_0$ represents the lattice friction at 0 K and S_0^α is the total athermal slip resistance to dislocation motion. The shear moduli ratio at T, μ and at 0 K, μ_0 are introduced to extrapolate the lattice friction stress and the slip resistance at $T(K)$. The constants p and q are parameters defining the shape of the energy-barrier profile. The term $sign(\tau^\alpha)$ accounts for positive and negative slip on the slip system.

For a slip system α, the plastic power per unit volume, $\dot{\omega}^p$, is defined through the relation,

$$\dot{\omega}^p = \sum_\alpha^N \tau^\alpha \dot{\gamma}^\alpha \tag{II.31}$$

Making reference to the intermediate configuration, an alternative definition can be obtained in terms of $\mathbf{E}^e$ and $\mathbf{T}$,

$$\dot{\omega}^p = \mathbf{F}^{eT}\mathbf{F}^e\mathbf{T} : \mathbf{L}^p \tag{II.32}$$

The resolved shear stress τ^α can be approximated (for small elastic stretches) as

$$\tau^\alpha \approx \mathbf{T} : \mathbf{P}^\alpha \tag{II.33}$$

The crystallographic slip only occurs when the effective driving stress is greater than zero.

II.2.2.2 Evolution of Dislocation Densities

Recalling the definition of Ashby (1970) postulated that the total dislocation density in a metal can be classified into two categories, statistically stored dislocations (SSDs) and geometrically necessary dislocations (GNDs). The GNDs are distinguished from the SSDs as they are only present in regions of non-homogeneous plastic deformation to accommodate geometric incompatibilities or strain-gradients within. Therefore, the total dislocation density can be additively decomposed into statistically-stored and geometrically necessary parts,

$$\rho_T^\alpha = \rho_S^\alpha + \rho_G^\alpha \tag{II.34}$$

Both categories contribute to the total athermal slip resistance S_T^α defined as,

$$S_T^\alpha = \sqrt{(S_S^\alpha)^2 + (S_G^\alpha)^2} \tag{II.35}$$

with,

$$S_S^\alpha = \lambda_S \mu b_S^\alpha \sqrt{\sum_{\beta=1}^N h^{\alpha\beta} \rho_S^\beta} \tag{II.36}$$

$$S_G^\alpha = \lambda_G \mu b_G^\alpha \sqrt{\sum_{\beta=1}^N h^{\alpha\beta} \rho_G^\beta} \tag{II.37}$$

Here, μ is the shear modulus while λ_S and λ_G are statistical coefficients which accounts for the deviation from regular spatial arrangements of the SSD and GND populations, respectively. The terms b_S^α and b_G^α are their corresponding Burgers vector magnitude. In what follows, it will be assumed for simplicity that $\lambda = \lambda_S = \lambda_G$ and $b = b_S^\alpha = b_G^\alpha$. Furthermore, $h_S^{\alpha\beta}$ and $h_G^{\alpha\beta}$ are the respective SSD and GND dislocation interaction matrices.

$$h_k^{\alpha\beta} = \omega_{k1} + (1 - \omega_{k2})\delta^{\alpha\beta} \quad for \quad k = S, G \tag{II.38}$$

Here, ω_{k1} and ω_{k2} are the interaction coefficients and $\delta_{\alpha\beta}$ is the Kronecker Delta.

Both categories are additively separated into pure edge and screw types,

$$\rho_S^\alpha = \rho_{Se}^\alpha + \rho_{Ss}^\alpha \tag{II.39}$$

$$\rho_G^\alpha = \rho_{Gen}^\alpha + \rho_{Get}^\alpha + \rho_{Gs}^\alpha \tag{II.40}$$

ρ_{Se}^α and ρ_{Ss}^α represent the statistical edge and screw dislocation density components. The subscripts en and et refer to edge components resolved along the slip direction $\mathbf{m}^\alpha$ and perpendicular to it, $\mathbf{t}^\alpha = \mathbf{m}^\alpha \times \mathbf{n}^\alpha$. Edge and screw dislocations act as obstacles to dislocation motion in the form of forest dislocations. As ρ_e^α and ρ_s^α represent edge dislocations density and screw dislocations density respectively. They contribute to the athermal slip resistance in the following way:

$$S_S^\alpha = \lambda \mu b^\alpha \sqrt{\sum_{\beta=1}^N h^{\alpha\beta} \rho_e^\beta + \rho_s^\beta} \tag{II.41}$$

The statistically stored dislocations densities evolution equations are formulated as balance equations between dislocation generation and dislocation annihilation. The generation or multiplication of SSDs is due mainly to the resistance to dislocation motion posed by forest dislocation acting as random obstacles, forcing the moving dislocation to percolate through a combination of dislocation bowing and expansion. Dislocation generation is assumed to
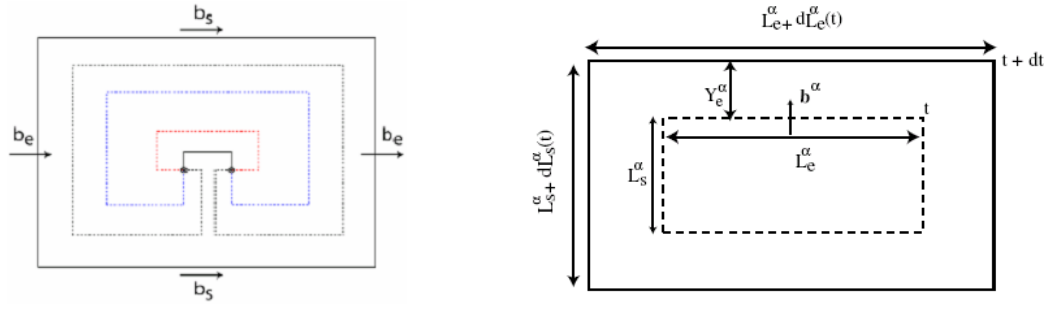
Figure II.13 : Dislocation multiplication - schematic diagram of an idealised expanding dislocation loop during a time interval dt (Cheong and Busso, 2004)
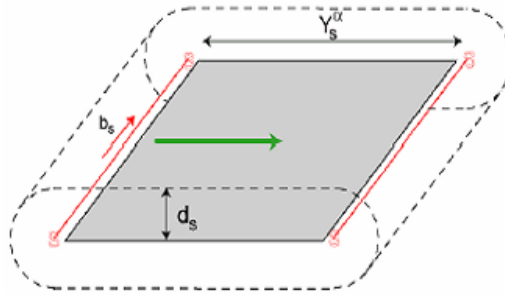
Figure II.14 : Dislocation annihilation - Schematic diagram of the annihilation region for a screw dislocation after a time interval dt (Cheong and Busso, 2004)

be associated with the expansion of dislocation loops originating from existing Franck-Read type sources. Figure II.2.2.2 shows an idealised, expanding dislocation loop on a arbitrary active slip system α during a time dt. The loop is assumed to be rectangular, with straight edge and screw sides of lengths L_e^α and L_s^α, respectively. Here, Y_e^α is the mean free path of the edge dislocation segment, defined to be the distance travelled by the segment before its motion is arrested by forest dislocations. Derivation with respect to time yields the rate of generation of edge dislocation density,

$$\dot{\rho}_{e,gen}^\alpha = \frac{C_e}{b^\alpha Y_e^\alpha}\dot{\gamma}^\alpha \tag{II.42}$$

and similarly for the generation of screw dislocations,

$$\dot{\rho}_{s,gen}^\alpha = \frac{C_s}{b^\alpha Y_s^\alpha}\dot{\gamma}^\alpha \tag{II.43}$$

C_e and C_s are parameters which scale the magnitudes of the slip rate contributions from the edge and screw segments, respectively.

Mutual annihilation between parallel dislocations of the same character but opposite signs is assumed to be the predominant annihilation mechanism. An annihilation event occurs when two dislocations are drawn towards each other by their attractive forces in order to reduce their line energies. Through this combination process, the opposing dislocations mutually annihilate. The probability of such an event occurring is determined by the cross sectional area for annihilation, see Figure II.2.2.2. Such a region is illustrated by the dash line around a gliding screw dislocation, which moves from the position at time "t" to "t+dt".
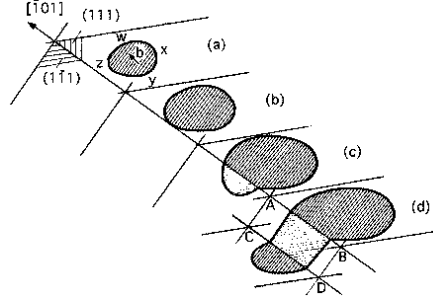
Figure II.15 : Cross-slip in FCC crystal: a screw dislocation at z can glide in either the
(111) or the ($1\bar{1}1$) close-packed planes.

The symbol d_s represents the critical distance for mutual annihilation between two anti-
parallel screw dislocations to take place (Kubin *et al.*, 2009). Since screw dislocations have
the ability to cross-slip even at low temperatures, Figure II.3, they will inevitably encounter
more annihilation events than edge dislocations and the critical distance is larger. The screw
dislocation density annihilation rate is:

$$\dot{\rho}^\alpha_{s,ann} = \frac{C_s}{b_\alpha}\left[\frac{\pi d_s^2}{Y_s^\alpha} + 2d_s\right]\rho_s^\alpha\dot{\gamma}^\alpha \tag{II.44}$$

The edge dislocation density annihilation rate is different because of their inability to cross-
slip:

$$\dot{\rho}^\alpha_{e,ann} = \frac{C_s}{b_\alpha}\left[2d_s\right]\rho_s^\alpha\dot{\gamma}^\alpha \tag{II.45}$$

To express the previous laws in terms of dislocations densities, Y_e^α and Y_s^α can be linked to
the mean obstacle spacing l_m^α, where the dominant obstacles for a pure single crystal are the
forest dislocations.

$$Y_i^\alpha = \frac{l_m^\alpha}{K_i}; \quad i = e, s \tag{II.46}$$

The mean dislocation spacing is linked to the total dislocation density as in
(Basinski and Basinski, 1979),

$$l_m^\alpha = \frac{1}{\sqrt{\sum_{\beta=1}^N \rho_T^\beta}} \tag{II.47}$$

From eqs. II.42 to II.47, the dislocation density evolution equations are formulated as balance
equations between dislocation generation and dislocation annihilation.

$$\dot{\rho}_e^\alpha = \frac{C_e}{b^\alpha}\left[K_e\sqrt{\sum_{\beta=1}^N \rho_T^\beta} - 2d_e\rho_e^\alpha\right]|\dot{\gamma}^\alpha| \tag{II.48}$$

$$\dot{\rho}_s^\alpha = \frac{C_s}{b^\alpha}\left[K_s\sqrt{\sum_{\beta=1}^N \rho_T^\beta} - \rho_s^\alpha\left(\pi d_s^2 K_s\sqrt{\sum_{\beta=1}^N \rho_T^\beta} + 2d_s\right)\right]|\dot{\gamma}^\alpha| \tag{II.49}$$

II.3   Polycrystal : Non-local Effects

The strain gradient theory here follows the work of (Busso *et al.*, 2000), where the evolution
of the GND structure is linked to local slip rate gradients. During plastic deformation of
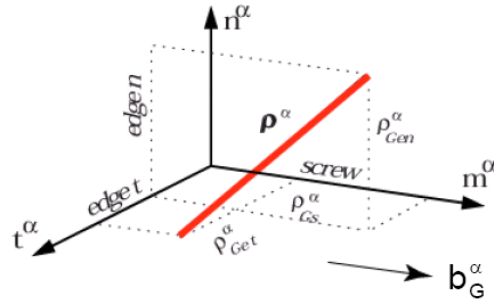
Figure II.16 : Local orthogonal coordinate system of reference for a generic geometrically necessary dislocation line in an arbitrary slip system α

crystalline materials, GNDs accommodate orientation gradients within single crystals in the material. This dislocation structure is necessary to maintain lattice continuity. By definition, the density of the GNDs is related to the net Burgers' vector of all dislocations piercing an infinitesimal surface (S) with normal $\mathbf{n}$, and enclosed counterclockwise by a circuit (G) in the intermediate configuration associated with $\mathbf{F}^p$. The resulting discontinuity G on completion of a Burgers' circuit around the path can then be defined through Nye's dislocation density tensor Λ (Nye, 1953) using Stoke's Theorem,

$$G = -\int_{\Gamma} \mathbf{F}^p dX = \int_{S} \Lambda.\mathbf{n}dS, \quad \text{where} \quad \Lambda = \text{curl}\{\mathbf{F}^p\} = \nabla \times \mathbf{F}^p \tag{II.50}$$

The evolution of GNDs can be then obtained by differentiating Eq. II.50 with respect to time. Here,

$$G = \int_{S} \dot{\Lambda}.\mathbf{n}dS = \int_{S} \sum_{\alpha} \dot{\Lambda}^{\alpha}.\mathbf{n}dS, \quad \text{where} \quad \dot{\Lambda}^{\alpha} = \text{curl}\{(\dot{\gamma}^{\alpha}\mathbf{m}^{\alpha} \otimes \mathbf{n}^{\alpha})\mathbf{F}^p\} \tag{II.51}$$

Considering that there exists a vectorial field of GNDs for every slip system, the GNDs can be represented by a generic GND line vector $\rho_{\mathbf{G}}^{\alpha}$ with Burger's vector $\mathbf{b}$. This dislocation line vector can be further discretised into its edge and screw components by solving along axes of the coordinate system defined in terms of the slip directions $\mathbf{m}^{\alpha}$, its slip plane normal $\mathbf{n}^{\alpha}$ and a third orthogonal direction $\mathbf{t}^{\alpha} = \mathbf{m}^{\alpha} \times \mathbf{n}^{\alpha}$

$$\rho_{\mathbf{G}}^{\alpha} = \rho_{Gs}^{\alpha}\mathbf{m}^{\alpha} + \rho_{Gen}^{\alpha}\mathbf{n}^{\alpha} + \rho_{Get}^{\alpha}\mathbf{t}^{\alpha} \tag{II.52}$$

Here, ρ_{Gs}^{α} refers to its screw component parallel to $\mathbf{m}^{\alpha}$ while ρ_{Gen}^{α} and ρ_{Get}^{α} are the edge components parallel to $\mathbf{n}^{\alpha}$ and $\mathbf{t}^{\alpha}$, respectively. The Burgers' vector discontinuity associated to the density of the GNDs crossing a unit area (S) with normal r is given by

$$G = \int_{S} (\mathbf{b}_{G}^{\alpha} \otimes \rho_{G}^{\alpha}).\mathbf{n}dS \tag{II.53}$$

Differentiating eq. II.53, a second expression of the rate of $\mathcal{G}$ is obtained

$$\dot{G} = \int_{S} (\mathbf{b}_{G}^{\alpha} \otimes \dot{\rho}_{G}^{\alpha}).\mathbf{n}dS \tag{II.54}$$

By equating eqs. II.51 and II.53, the final expression for the GND evolution written in tensorial form is

$$\dot{\rho}_{G_{sw}}^{\alpha}(\mathbf{b}_{G}^{\alpha} \otimes \mathbf{m}^{\alpha}) + \dot{\rho}_{G_{et}}^{\alpha}(\mathbf{b}_{G}^{\alpha} \otimes \mathbf{t}^{\alpha}) + \dot{\rho}_{G_{en}}^{\alpha}(\mathbf{b}_{G}^{\alpha} \otimes \mathbf{n}^{\alpha}) = curl\{(\dot{\gamma}^{\alpha}\mathbf{m}^{\alpha} \otimes \mathbf{n}^{\alpha})\mathbf{F}^p\} \tag{II.55}$$

II.4   Methodology: Finite Element Implementation

Two integration methods are generally used to solve highly non-linear constitutive equations; explicit or implicit integration. In an implicit integration, an iterative approach is employed in solving the non-linear equations to achieve convergence. In the case of the explicit FE method, the equations can be solved directly to determine the solution without iteration. (Harewood and McHugh, 2007) developed a rate-dependent crystal plasticity algorithm using the explicit FE package, ABAQUS/explicit. The subroutine and an equivalent implicit version were used in a series of comparative boundary value problem analysis. They recognised the advantages that the explicit method has in solving certain loading conditions; however, the implicit procedures are best suited for quasi-static computations allowing larger time steps. In the FE Zebulon code (Besson *et al.*, 1998), the implicit integration method is used to solve the global mechanical equations. However, an explicit local integration or implicit local integration will be employed.

II.4.1   Local Integration Methods

Two local integration methods have been used for this model: an explicit Runge-Kutta method, and an implicit mid-point method resolved by a Newton-Raphson local convergence loop (Besson *et al.*, 2001a). For both methods, the following set of variables of integration is defined, taking into account the number of slip systems N:

$$\mathcal{V}_{int} = \{\mathbf{E_e}, (\gamma^\alpha, \rho_{Ss}^\alpha, \rho_{Se}^\alpha, \alpha = 1..N)\} \tag{II.56}$$

For the Runge-Kutta method, the rate of each variable has just to be prescribed. In the implicit case, residuals have to be defined. Therefore, only local implicit integration will be detailed in this work.

II.4.2   Finite Strain Formalism in a Local Implicit Integration Scheme

An implicit time integration procedure using a Newton-type algorithm is employed to determine the material state variables. Given a list of known variables at the beginning of the time increment, $\mathbf{F}_n$, $\mathbf{F}_n^p$, $\rho_{Se,n}^\alpha$ and $\rho_{Ss,n}^\alpha$, together with an estimate of the total deformation gradient, $\mathbf{F}_{n+1}$. a finite strain formalism in a local implicit integration scheme proposed in (Musienko, 2005) is used to calculate the material state variables at the next iteration.

The time rate of change of the plastic deformation gradient, $\dot{\underset{\sim}{\mathbf{F}}}^p$, is defined by:

$$\dot{\mathbf{F}}^p = \mathbf{L}^p \mathbf{F}^p \tag{II.57}$$

Integrating Eq. II.57, we have the following integration scheme:

$$\mathbf{F}_{n+1}^p = \mathbf{F}_n^p \exp(\mathbf{L}^p \Delta t) = \mathbf{F}_n^p \exp(\Delta\gamma^\alpha \mathbf{P}_{n+1}^\alpha) \tag{II.58}$$

Let us consider:

$$\mathbf{F}^* = \mathbf{F}_{n+1} \mathbf{F}_n^{p-1} \tag{II.59}$$

Also, by definition:

$$\mathbf{F}_{n+1}^e = \mathbf{F}_{n+1} \mathbf{F}_{n+1}^{p-1} \tag{II.60}$$

We then obtain,

$$\mathbf{F}^* = \mathbf{F}_{n+1}^e \exp(\Delta\gamma^\alpha \mathbf{P}^\alpha) \approx \mathbf{F}_{n+1}^e (\mathbf{I} + \Delta\gamma^\alpha \mathbf{P}_{n+1}^\alpha) \tag{II.61}$$

In order to write a relation in term of the elastic strain, we obtain

$$\mathbf{F}^{*T}\mathbf{F}^* = (\mathbf{I} + \Delta\gamma^\alpha \mathbf{P}_{n+1}^\alpha)^T \mathbf{F}_{n+1}^{eT} \mathbf{F}_{n+1}^e (\mathbf{I} + \Delta\gamma^\alpha \mathbf{P}_{n+1}^\alpha) \tag{II.62}$$

Eq. II.62 is developed at the first order:

$$\mathbf{F}^{*T}\mathbf{F}^* = \mathbf{F}_{n+1}^{eT} \mathbf{F}_{n+1}^e + 2\Delta\gamma^\alpha (\mathbf{P}_{n+1}^\alpha \mathbf{C}_{n+1}^e) \tag{II.63}$$

Using the expression of the Lagrangian strain, an equation with elastic and plastic parts can be found. There,

$$\mathbf{E}^* = \mathbf{E}_{n+1}^e + \Delta\gamma^\alpha (\mathbf{P}_{n+1}^\alpha \mathbf{C}_{n+1}^e) \tag{II.64}$$

II.4.3 Theta Method (θ-method)

Let us consider $\mathcal{V}_{int}^t$, N-dimensional vector containing the variables to be minimised and its increment on the time step Δt, $\Delta\mathcal{V}_{int}$, its estimation at $t + \theta\Delta t$, $\mathcal{V}_{int}^\theta$ is

$$\mathcal{V}_{int}^\theta = \mathcal{V}_{int}^t + \theta\Delta\mathcal{V}_{int} \tag{II.65}$$

where $0 \le \theta \le < 1$. A generalised form of the problem at $t + \theta\Delta t$ can be written as

$$\mathcal{F}(\mathcal{V}_{int}^\theta, \Delta\mathcal{V}_{int}) = \mathcal{F}_0 \tag{II.66}$$

The reduced form of eq. II.66 at the kth iteration is

$$\mathcal{R}^k = \mathcal{F}^k - \mathcal{F}_0 \tag{II.67}$$

where $\mathcal{F}^k$ is the evaluation of $\mathcal{F}$ at kth iteration. The Newton-Raphson expression for the (k+1)th iteration is. Thus,

$$\Delta\mathcal{V}_{int}^{k+1} = \Delta\mathcal{V}_{int}^k - [\mathcal{J}_\theta^{k+1}]^{-1}\mathcal{R}^k. \tag{II.68}$$

where $\mathcal{J}_\theta^{k+1}$ is the jacobian matrix. The dimension of $\mathcal{V}_{int}$ for the single crystal model with 12 slip systems is 42. Thus,

$$\mathcal{V}_{int} = \{\mathbf{E_e}, (\gamma^\alpha, \rho_{Ss}^\alpha, \rho_{Se}^\alpha, \alpha = 1..12)\} \tag{II.69}$$

The method provides the most robust integration schemes for $\theta = 1$. The residual system for $\theta = 1$ is written as

$$\mathcal{R}^k = \begin{bmatrix} r_{E_e} \\ r_{\gamma^\alpha} \\ r_{\rho_{Se}^\alpha} \\ r_{\rho_{Ss}^\alpha} \end{bmatrix}$$

where

$$r_E = -\mathbf{E}^* + \mathbf{E}_{n+1}^e + \sum_{\alpha=1}^{N} \Delta\gamma^\alpha (\mathbf{N}_{n+1}^\alpha \mathbf{C}_{n+1}^e) \tag{II.70}$$

$$r_{\gamma^\alpha} = \Delta\gamma^\alpha - \dot{\gamma}_0 \exp\left[-\frac{F_0}{kT}\left\{ 1 - \left\langle \frac{|\tau_{n+1}^\alpha| - S_{n+1}^\alpha}{\widehat{\tau}} \right\rangle^p \right\}^q \right] sign(\tau^\alpha)\Delta t \tag{II.71}$$

$$r_{\rho_{Se}^\alpha} = \Delta\rho_{Se}^\alpha - \frac{C_e}{b^\alpha}\left[K_e \sqrt{\sum_{\beta=1}^{N} \rho_{T_{n+1}}^\beta} - 2d_e\rho_{Se_{n+1}}^\alpha \right]\Delta\gamma^\alpha sign(\tau^\alpha) \tag{II.72}$$

$$r_{\rho_{Ss}^\alpha} = \Delta\rho_{Ss}^\alpha - \frac{C_s}{b^\alpha}\left[K_s \sqrt{\sum_{\beta=1}^{N} \rho_{T_{n+1}}^\beta} - \rho_{Ss_{n+1}}^\alpha \left(\pi d_s^2 K_s \sqrt{\sum_{\beta=1}^{N} \rho_{T_{n+1}}^\beta} + 2d_s \right) \right]\Delta\gamma^\alpha sign(\tau^\alpha) \tag{II.73}$$

In what follows, the expressions of the Jacobian operator are written for the crystal plasticity model previous described. The Jacobian matrix, $\mathcal{J}^k$, contains the partial derivatives of the residuals, $\mathcal{R}^k$, with respect to the unknowns:

$$\mathcal{J}_\theta^k = \begin{bmatrix} \frac{\partial r_e}{\partial \Delta \mathbf{E}^e} & \frac{\partial r_e}{\partial \Delta \gamma^\alpha} & \frac{\partial r_e}{\partial \Delta \rho_{Se}^\alpha} & \frac{\partial r_e}{\partial \Delta \rho_{Ss}^\alpha} \\ \frac{\partial r_{\gamma^\alpha}}{\partial \Delta \mathbf{E}^e} & \frac{\partial r_{\gamma^\alpha}}{\partial \Delta \gamma^\gamma} & \frac{\partial r_{\gamma^\alpha}}{\partial \Delta \rho_{Se}^\gamma} & \frac{\partial r_{\gamma^\alpha}}{\partial \Delta \rho_{Ss}^\gamma} \\ \frac{\partial r_{\rho_{Se}^\alpha}}{\partial \Delta \mathbf{E}^e} & \frac{\partial r_{\rho_{Se}^\alpha}}{\partial \Delta \gamma^\gamma} & \frac{\partial r_{\rho_{Se}^\alpha}}{\partial \Delta \rho_{Se}^\gamma} & \frac{\partial r_{\rho_{Se}^\alpha}}{\partial \Delta \rho_{Ss}^\gamma} \\ \frac{\partial r_{\rho_{Ss}^\alpha}}{\partial \Delta \mathbf{E}^e} & \frac{\partial r_{\rho_{Ss}^\alpha}}{\partial \Delta \gamma^\gamma} & \frac{\partial r_{\rho_{Ss}^\alpha}}{\partial \Delta \rho_{Se}^\gamma} & \frac{\partial r_{\rho_{Ss}^\alpha}}{\partial \Delta \rho_{Se}^\gamma} \end{bmatrix}$$

II.4.4 An Algorithm For the Evaluation of the Tangent Operator

In the same way as for the resolution of the local non-linear equations, a consistent tangent matrix is required to solve the global equation with a fully implicit method, namely $\frac{\partial \sigma}{\partial \mathbf{E}^{tot}}$. (Simo and Hughes, 1997) developed an algorithm which is briefly described. Once convergence has been achieved, one finds

$$\begin{bmatrix} d\Delta \mathbf{E}^e \\ d\Delta \gamma^\alpha \\ d\Delta \rho_{Se}^\alpha \\ d\Delta \rho_{Ss}^\alpha \end{bmatrix} = \left[\mathcal{J}_\theta^{k+1} \right]^{-1} \cdot \begin{bmatrix} d\Delta \mathbf{E}^{tot} \\ 0 \\ 0 \\ 0 \end{bmatrix}$$

so that the top left subcomponent of the inverted Jacobian matrix $\left[\mathcal{J}_\theta^{k+1} \right]_e^{-1}$ relates the variation of $\Delta \mathbf{E}^e$ with respect to the variation of $\Delta \mathbf{E}^{tot}$:

$$\left[\mathcal{J}_\theta^{k+1} \right]_e^{-1} = \frac{\partial \Delta \mathbf{E}^e}{\partial \Delta \mathbf{E}^{tot}} \tag{II.74}$$

The elastic constitutive equations can then be used to evaluate the partial derivatives of $\Delta \sigma$ with respect to $\Delta \mathbf{E}^{tot}$. Therefore, the non-linear tangent matrix consistent with the $\Delta \mathbf{E}^{tot}$ integration algorithm is (Simo and Hughes, 1997):

$$\mathbf{D} = \frac{\partial \Delta \sigma}{\partial \Delta \mathbf{E}^{tot}} = \mathbf{C} \left[\mathcal{J}_\theta^{k+1} \right]_e^{-1} \tag{II.75}$$

A more detailed description of the formulation can be found in (Besson *et al.*, 2001a).

II.4.5 Determination of Slip-Rate Gradients for Non-Local Constitutive Behaviour

As explained in a previous section, the strain gradient formulation is incorporated through the introduction of GND densities which evolve according to the spatial slip-rate gradients defined by (Busso *et al.*, 2000),

$$\mathbf{b}_G^\alpha (\dot{\rho}_{G_{sw}}^\alpha \mathbf{m}^\alpha + \dot{\rho}_{G_{et}}^\alpha \mathbf{t}^\alpha) + (\dot{\rho}_{G_{en}}^\alpha \mathbf{n}^\alpha) = \text{curl}\{\dot{\gamma}^\alpha \mathbf{n}^\alpha \mathbf{F}^p\} = \text{curl}\{A\} \tag{II.76}$$

In order to determine the evolution of the GNDs, the quantity curl$\{A\}$ has to be calculated. Given that the spatial variation of the quantity $\{A\}$ is necessary to estimate its curl, a spatial interpolation needs to be done at each Gauss point with its neighbours. A post-processing method is used to evaluate the gradients. Firstly, the quantity $\{A\}$ is calculated after each each time step. Then, the quantity $\{A\}$ at each integration points is extrapolated

at the nodes using the shape functions of the element. Subsequently, the spatial gradients $\{A\}$ at each integration point are obtained directly from the spatial derivatives of the shape functions and interpolated back to the integration points. In contrast to the method used by (Busso *et al.*, 2000), the shape functions employed to extrapolate the variable are the same in all the FE resolution. Once the quantity $curl\{A\}$ is estimated, it is used in the next iteration to explicitly updated the GNDs using a forward Euler scheme,

$$\rho_{G_i,n+1}^{\alpha} = \rho_{G_i,n}^{\alpha} + \Delta t \dot{\rho}_{G_i,n}^{\alpha} \tag{II.77}$$

In view of the fact that the GNDs are explicitly updated, the accuracy of the solution is ensured only if a sufficiently small time step is used.

II.5 Conclusions

The deformation state of cold deformed pure FCC metals with medium to high stacking fault energy is briefly reviewed so as to underline its intergranular and intragranular heterogeneities. Among the different methods used to describe the mechanical behaviour of polycrystalline aggregate in continuum mechanics, finite element models have been opted for their ability to describe non-homogeneous deformation at both intragranular and intergranular levels. The single crystal model proposed by (Cheong and Busso, 2004) have been preferred for its distinction between screw and edge dislocation densities. Since the grain size change during recrystallization and grain growth, non-local effects have been introduced through geometrically necessary dislocations. An implicit integration scheme of the single crystal model in a finite strain formalism has been detailed for its implementation in the FE code Zebulon.

References

ACHARYA A., BASSANI J.L., AND BEAUDOIN A. (2003). *Geometrically necessary dislocations, hardening, and a simple gradient theory of crystal plasticity.* Scripta Materialia, vol. 48 n° 2, pp 167–172.

ACHARYA A. AND BEAUDOIN A.J. (2000). *Grain-size effect in viscoplastic polycrystals at moderate strains.* Journal of the Mechanics and Physics of Solids, vol. 48 n° 10, pp 2213–2230.

ARGON A.S. AND HAASEN P. (1993). *A new mechanism of work-hardening in the late stages of large-strain plastic-flow in fcc and diamond cubic-crystals.* Acta Metallurgica, vol. 41 n° 11, pp 3289–3306.

ARSENLIS A. AND PARKS D.M. (1999). *Crystallographic aspects of geometrically-necessary and statistically-stored dislocation density.* Acta Materialia, vol. 47 n° 5, pp 1597–1611.

ARSENLIS A. AND PARKS D.M. (2002). *Modeling the evolution of crystallographic dislocation density in crystal plasticity.* Journal of the Mechanics and Physics of Solids, vol. 50 n° 9, pp 1979–2009.

ASARO R.J. AND RICE J.R. (1977). *Strain localization in ductile single-crystals.* Journal of the Mechanics and Physics of Solids, vol. 25 n° 5, pp 309–338.

ASHBY M.F. (1970). *The deformation of plastically non-homogeneous materials.* Philosophical Magazine, vol. 21, pp 399–424.

BALASUBRAMANIAN S. AND ANAND L. (2002). *Elasto-viscoplastic constitutive equations for polycrystalline fcc materials at low homologous temperatures.* Journal of the Mechanics and Physics of Solids, vol. 50 n° 1, pp 101–126.

BARBE F., DECKER L., JEULIN D., AND CAILLETAUD G. (2001a). *Intergranular and intragranular behavior of polycrystalline aggregates. Part 1: F.E. model.* International Journal of Plasticity, vol. 17, pp 513–536.

BARUCHEL J., BLEUET P., BRAVIN A., COAN P., LIMA E., MADSEN A., LUDWIG W., PERNOT P., AND SUSINI J. (2008). *Advances in synchrotron hard X-ray based imaging.* Comptes Rendus Physique, vol. 9, pp 624–641.

BASINSKI S.J. AND BASINSKI Z.S. (1979). *Plastic deformation and work hardening in Dislocations in Solids.* In : Volume 4 : Dislocation in metallurgy (ed. Nabarro F. R. N.), pp 261–362. North-Holland Publishers.

BASSANI J.L. AND WU T.Y. (1991). *Latent hardening in single-crystals.2. Analytical characterization and predictions.* Proceedings of the Royal Society of London A, vol. 435 n° 1893, pp 21–41.

BECKER R. AND PANCHANADEESWARAN S. (1995). *Effects of grain interactions on deformation and local texture in polycrystals.* Acta Metallurgica, vol. 43, pp 2701–2719.

BESSON J., CAILLETAUD G., CHABOCHE J.-L., AND FOREST S. (2001a). *Mécanique non–linéaire des matériaux.* Hermes.

BESSON J., LE RICHE R., FOERCH R., AND CAILLETAUD G. (1998). *Object–Oriented Programming Applied to the Finite Element Method. Part II: Application to Material Behaviors.* Revue Européenne des éléments finis, vol. 7, pp 567–588.

BURGERS J.M. (1939). *Some considerations on the fields of stress connected with dislocation in a regular crystal lattice I.* Proceedings of the Koninklijke Nederlandse Akad. Wetenschappen, vol. 42, pp 293–325.

BUSSO E.P. (1990). *Cyclic deformation of monocrystalline nickel aluminide and high temperature coatings.* Thèse de Doctorat, MIT.

BUSSO E.P. AND CHEONG K.S. (2001). *Length scale effects on the macroscopic behaviour of single and polycrystalline FCC crystals.* Journal de Physique IV, vol. 11 n° PR5, pp 161–170. (5th European Mechanics of Materials Conference, Delft, Netherlands, Mar 05-08, 2001).

BUSSO E.P. AND McCLINTOCK F.A. (1996). *A dislocation mechanics-based crystallographic model of a B2-type intermetallic alloy.* International Journal of Plasticity, vol. 12 n° 1, pp 1–28.

BUSSO E.P., MEISSONNIER F.T., AND O'DOWD N.P. (2000). *Gradient-dependent deformation of two-phase single crystals.* Journal of the Mechanics and Physics of Solids, vol. 48 n° 11, pp 2333–2361.

BUTLER J.F. AND HU H. (1989). *Channel die compression of aluminum single-crystals.* Materials science and engineering a-structural materials properties microstructure and processing, vol. 114, pp L29–L33.

CAILLETAUD G. (1988). *Micromechanical approach of polycrystalline behavior.* Revue de Physique Appliquée, vol. 23 n° 4, pp 353–365.

CAILLETAUD G. (1992). *A micromechanical approach to inelastic behaviour of metals.* International Journal of Plasticity, vol. 8, pp 55–73.

CHEONG K.S. AND BUSSO E.P. (2004). *Discrete dislocation density modelling of single phase FCC polycrystal aggregates.* Acta Materialia, vol. 52 n° 19, pp 5665–5675.

CHEONG K.S. AND BUSSO E.P. (2006). *Effects of lattice misorientations on strain heterogeneities in FCC polycrystals.* Journal of the Mechanics and Physics of Solids, vol. 54 n° 4, pp 671–689.

CHEONG K.S., BUSSO E.P., AND ARSENLIS A. (2005). *A study of microstructural length scale effects on the behaviour of FCC polycrystals using strain gradient concepts.* International Journal of Plasticity, vol. 21 n° 9, pp 1797–1814.

DAI H. AND PARKS D. (1997). *Geometrically-necessary dislocation density and scaledependent crystal plasticity.* In : Proceedings of Plasticity '97, pp 17–18. Neat Press, ed. A.S. Khan.

DEVINCRE B., HOC T., AND KUBIN L.P. *Collinear interactions of dislocations and slip systems.* Materials Science and Engineering A, vol. 400.

DRIVER J. AND CHENAL B. (2000). *Écrouissage d'alliages d'aluminium.* Technical report, Les techniques de l'ingénieur M230.

ESHELBY J.D. (1957). *The determination of the elastic field of an ellipsoidal inclusion and related problems.* Proc. Roy. Soc. London, vol. A 241, pp 376–396.

ESTRIN Y., TOTH L.S., MOLINARI A., AND BRECHET Y. (1998). *A dislocation-based model for all hardening stages in large strain deformation.* Acta Materialia, vol. 46 n° 15, pp 5509–5522.

EVERS L.P., PARKS D.M., BREKELMANS W.A.M., AND GEERS M.G.D. (2002). *Crystal plasticity model with enhanced hardening by geometrically necessary dislocation accumulation.* Journal of the Mechanics and Physics of Solids, vol. 50 n° 11, pp 2403–2424.

FLECK N.A. AND HUTCHINSON J.W. (1997). *Strain gradient plasticity.* Advances in Applied Mechanics, vol. 33, pp 295–361.

FOREST S., BOUBIDI P., AND SIEVERT R. (2001). *Strain localization patterns at a crack tip in generalized single crystal plasticity.* Scripta Materialia, vol. 44 n° 6, pp 953–958.

FRANCIOSI P., BERVEILLER M., AND ZAOUI A. (1980). *Latent hardening in copper and aluminium single crystals.* Acta Metallurgica, vol. 28, pp 273–283.

FRANKEL J. (1926). *Zur theorie der elastizitätsgrenze und der festigkeit kristallinischer körper.* Zeitschrift fur Physik, vol. 37, pp 572–609.

FROST H.J. AND ASHBY M.F. (1982). *Deformation-mechanism maps.* Pergamon Press.

GURTIN M.E. (2002). *A gradient theory of single-crystal viscoplasticity that accounts for geometrically necessary dislocations.* Journal of the Mechanics and Physics of Solids, vol. 50 n° 1, pp 5–32.

HALL E.0. (1951). *The deformation and ageing of mild steel.* Proceedings of the Physical Soc., vol. 64, pp 747–753.

HANSEN N. (1977). *Effect of grain-size and strain on tensile flow-stress of aluminium at room-temperature.* Acta Metallurgica, vol. 25 n° 8, pp 863–869.

HAREWOOD F. J. AND MCHUGH P. E. (2007). *Comparison of the implicit and explicit finite element methods using crystal plasticity.* Comput. Mat. Sci., vol. 39 n° 2, pp 481–494.

HILL R. (1965). *Continuum micro-mechanics of elastoplastic polycrystals.* Journal of the Mechanics and Physics of Solids, vol. 13, pp 89–101.

HONEFF H. AND MECKING H. (1981). *Analysis of the deformation texture at different rolling conditions.* In : S. Nagamashi (Ed.), Proceedings of the 6th International Conference on Textures of Materials, pp 347–355. The Iron and Steel Institute of Japan.

HUGHES D.A. AND HANSEN N. (1997). *High angle boundaries formed by grain subdivision mechanisms.* Acta Materialia, vol. 45 n° 9, pp 3871–3886.

HUGHES D.A. AND HANSEN N; (2000). *Microstructure and strength of nickel at large strains.* Acta Materialia, vol. 48 n° 11, pp 2985–3004.

HUMPHREYS F.J. AND HATHERLY M. (2004). *Recrystallization and Related Annealing Phenomena.* Pergamon.

KALIDINDI S.R., BRONKHORST C.A., AND ANAND L. (1992). *Crystallographic texture evolution in bulk deformation processing of FCC metals.* Journal of the Mechanics and Physics of Solids, vol. 40, pp 537–569.

KANIT T., FOREST S., GALLIET I., MOUNOURY V., AND JEULIN D. (2003). *Determination of the size of the representative volume element for random composites: statistical and numerical approach.* International Journal of Solids and Structures, vol. 40, pp 3647–3679.

KOCKS U.F. (1977). *The theory of an obstacle-controlled yield strength-Report after an international workshop.* Mat. Sci. and Eng., vol. 27, pp 291–298.

KOCKS U.F. AND BROWN T.J. (1966). *Latent hardening in aluminum.* Acta Metallurgica, vol. 14, pp 87–98.

KOCKS U.F. AND CHANDRA H. (1982). *Slip geometry in partially constrained deformation.* Acta Metallurgica, vol. 30, pp 695.

KOCKS U.F., TOMÉ C.N., AND WENK H.R. (2000). *Texture and anisotropy.* Cambridge University Press.

KUBIN L., HOC T., AND DEVINCRE B. (2009). *Dynamic recovery and its orientation dependence in face-centered cubic crystals.* Acta Materialia, vol. 57 n° 8, pp 2567–2575.

KUMAR A.V. AND YANG C.H. (1999). *Study of work hardening models for single crystals using three dimensional finite element analysis.* International Journal of Plasticity, vol. 15 n° 7, pp 737–754.

LEBENSOHN R.A. (2001). *N-site modeling of a 3D viscoplastic polycrystal using Fast Fourier transform.* vol. 49, pp 2723–2737.

LEBENSOHN R.A. AND TOMÉ C.N. (1993). *A self-consistent anisotropic approach for the simulation of plastic deformation and texture development of polycrystals: application to zirconium alloys.* Acta Metallurgica et Materialia, vol. 41, pp 2611–2624.

MA A. AND ROTERS F. (2004). *A constitutive model for fcc single crystals based on dislocation densities and its application to uniaxial compression of aluminium single crystals.* Acta Materialia, vol. 52 n° 12, pp 3603–3612.

MADI K., FOREST S., BOUSSUGE M., GAILLIÈGUE S., LATASTE E., BUFFIÈRE J.-Y., BERNARD D., AND JEULIN D. (2007). *Finite element simulations of the deformation of fused-cast refractories based on X-ray computed tomography.* Comput. Mat. Sci., vol. 39, pp 224–229.

MANDEL J. (1973). *Equations constitutives et directeurs dans les milieux plastiques et viscoplastiques.* International Journal of Solids and Structures, vol. 9, pp 725–740.

MEISSONNIER F.T., BUSSO E.P., AND O'DOWD N.P. (2001). *Finite element implementation of a generalised non-local rate-dependent crystallographic formulation for finite strains.* International Journal of Plasticity, vol. 17 n° 4, pp 601–640. (7th International Symposium on Plasticity and Its Current Applications, Cancun, Mexico, Jan, 1999).

MERRIMAN C.C., FIELD D.P., AND TRIVEDI P. (2008). *Orientation dependence of dislocation structure evolution during cold rolling of aluminum.* Materials Science and Engineering A, vol. 494, pp 28–35.

MIKA D.P. AND DAWSON P.R. (1998). *Effects of grain interaction on deformation in polycrystals.* Materials Science and Engineering A, vol. 257, pp 62–76.

MOLINARI A., CANOVA G.R., AND AZHI S. (1987). *A self-consistent approach of the large deformation polycrystal viscoplasticity.* Acta Metallurgica, vol. 35, pp 2983–2994.

MURR L.E. (1975). *Interfacial phenomena in metals and alloys.* Addison-Wesley.

MUSIENKO A. (2005). *Plasticité cristalline en présence de grandes déformations et d'endommagement.* Thèse de Doctorat, Ecole des Mines de Paris.

NAKAMACHI E., TAM N.N., AND MORIMOTO H. (2007). *Multi-scale finite element analyses of sheet metals by using SEM-EBSD measured crystallographic RVE models.* International Journal of Plasticity, vol. 23, pp 450–489.

NEMAT-NASSER S. AND OBATA M. (1986). *Rate-dependent, finite elasto-plastic deformation of polycrystals.* Proceedings of the royal society of London A, vol. 407, pp 343–375.

NYE J. (1953). *Some geometrical relations in dislocated crystals.* Acta Metallurgica, vol. 1, pp 153–162.

OROWAN E.. (1934). *Zur kristallplastizitat III. uber den mechanismus des gleitvorganges.* Zeitschrift fur Physik, vol. 89, pp 634–659.

OROWAN E. (1940). *Problems of plastic gliding.* Proceedings of the Physical Soc., vol. A 52, pp 8–22.

PEETERS B., KALIDINDI S.R., VAN HOUTTE P., AND AERNOUDT E. (2000). *A crystal plasticity based work-hardening/softening model for b.c.c. metals under changing strain paths.* Acta Materialia, vol. 48 n° 9, pp 2123–2133.

PETCH N.J. (1953). *The cleavage strength of polycrystals.* J. Iron and Steel Inst., vol. 174, pp 25–28.

POLANYI M. (1934). *Gitterstorung die einem kristall plastisch machen konnte.* Zeitschrift fur Physik, vol. 89, pp 660–664.

PONTE CASTANEDA P. (1996). *Exact second order estimates for the effective mechanical properties of non linear composite materials.* Journal of the Mechanics and Physics of Solids, vol. 44, pp 827–862.

PRINZ F.B. AND ARGON A.S. (1984). *The evolution of plastic resistance in large strain plastic-flow of single-phase subgrain forming metals.* Acta Metallurgica, vol. 32 n° 7, pp 1021–1028.

QUILICI S., FOREST S., AND CAILLETAUD G. (1998). *On size effects in torsion of multi- and polycrystalline specimens.* Journal de Physique IV, vol. 8, pp 39–48.

REN Z.-Y. AND ZHENG Q.-S. (2002). *A Quantitative study of minimum sizes of representative volume elements of cubic polycrystals-numerical experiments.* Journal of the Mechanics and Physics of Solids, vol. 50, pp 881–893.

ROLLET A.D., KOCKS U.F., STOUT M.G., EMBURY J.D., AND DOHERTY R.D. (1987). *Modelling of large strain work-hardening.* Journal of Metals, vol. 39 n° 7, pp A22.

ROTERS F., RAABE D., AND GOTTSTEIN G. (2000). *Work hardening in heterogeneous alloys - A microstructural approach based on three internal state variables.* Acta Materialia, vol. 48 n° 17, pp 4181–4189.

SEEFELDT M., DELANNAY L., PEETERS B., AERNOUDT E., AND VAN HOUTTE P. (2001). *Modelling the initial stage of grain subdivision with the help of a coupled substructure and texture evolution algorithm.* actamater, vol. 49, pp 2129–2143.

SHU J.Y. AND FLECK N.A. (1999). *Strain gradient crystal plasticity: size-dependent deformation of bicrystals.* Journal of the Mechanics and Physics of Solids, vol. 47 n° 2, pp 297–324.

SIMO J. AND HUGHES T. (1997). *Computational Inelasticity.* Springer Verlag.

TAYLOR G.I. (1934). *The mechanism of plastic deformation of crystals Part I - Theoritical.* Proc. Roy. Soc. London, vol. A 145, pp 362–387.

TAYLOR G.I. (1938). *Plastic strain in metals.* Journal of the Institute of Metals, vol. 62, pp 307–324.

TRIVEDI P., FIELD D.P., AND WEILAND H. (2004). *Alloying effects on dislocation substructure evolution of aluminum alloys.* International Journal of Plasticity, vol. 20, pp 459–476.

VAN HOUTTE P., DELANNAY L., AND KALIDINDI S.R. (2002). *Comparison of two grain interaction models for polycrystal plasticity and deformation texture prediction.* International Journal of Plasticity, vol. 18, pp 359–377.

VAN HOUTTE P., LI S., SEEFELDT M., AND DELANNAY L. (2005). *Deformation texture prediction : from the Taylor model to the Advanced Lamel Model.* International Journal of Plasticity, vol. 21, pp 589–624.

WENG G.J. (1982). *A unified self-consistent theory for the plastic-creep deformation of metals.* Journal of Applied Mechanics, vol. 49, pp 728–734.

WENG G.J. (1983). *A micromechanical theory of grain-size dependence in metal plasticity.* Journal of the Mechanics and Physics of Solids, vol. 31 n° 3, pp 193–203.

ZHAO Z., MAO W., ROTERS F., AND RAABE D. (2004). *A texture optimization study for minimum earing in aluminium by use of a texture component crystal plasticity finite element method.* actamat, vol. 52, pp 1003–1012.

ZIKRY M.A. AND KAO M. (1996). *Dislocation based multiple-slip crystalline constitutive formulation for finite-strain plasticity.* Scripta Materialia, vol. 34 n° 7, pp 1115–1121.

Chapter -III-

Deformation Behaviour of Al Polycrystals

Contents

III.1   Introduction

Aluminium alloys and pure aluminium have been widely studied for 70 years, (Burgers and Snoek, 1935, Crussard *et al.*, 1950). Aluminium alloys are often used to form sheet metal by common manufacturing processes such as cold rolling, see Figure III.1. For instance, beverage cans are closed by rolling, and steel food cans are strengthened by rolling ribs into their sides. Rolling mills are also commonly used to precisely reduce the thickness of strip and sheet metals. In cold strip rolling, the width of the strip is much greater than its thickness, so the spread of the width is much less than the deformation in the rolling direction. Therefore, the deformation process is usually regarded as a problem of plain strain compression. To enable more accurately controlled deformation, channel-die compression device, equivalent to plane strain conditions, are employed instead of a laboratory rolling mill (Sue and Havner, 1984, Butler and Hu, 1989, Becker *et al.*, 1991, Driver *et al.*, 1994), see Figure III.1. The deformation textures deformed by rolling and by channel-die compression are largely similar, but significant differences develop with increasing thickness reduction (Hammelrath *et al.*, 1991). Thus, in the chapter, experimental and numerical samples will be tested under channel die compression up to 60% height reduction.
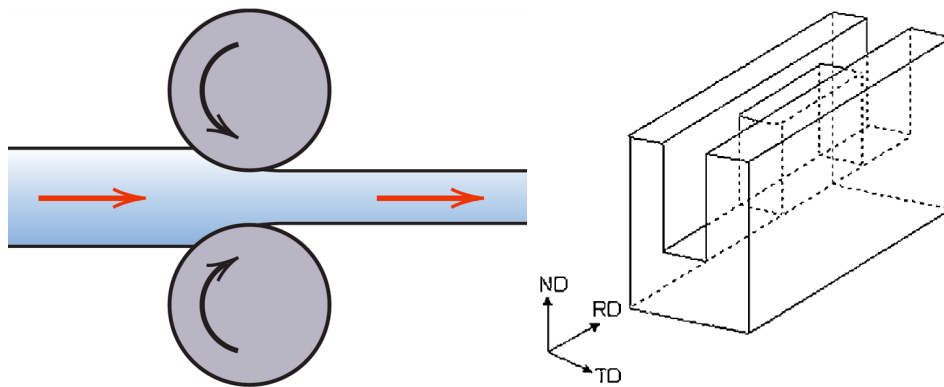
Figure III.1 : Schematic (a) rolling process and (b) a channel die compression test

III.1.1   Rolling Texture

Deformation processes in polycrystalline metals are always accompanied by a change of crystallographic orientation of each grain, which is often referred to as texture evolution. Most of the texture data available in the literature refers to IPF and ODF data. These analyses reveal the presence of texture components characteristic of metal forming process used, see Figure III.1. For instance, the {100} and {111} pole figures for 95% cold rolled aluminium are shown in Figure III.2.

III.1.2   Single Crystal - Rotation Path

The orientation changes that take place during deformation are not random. They are a consequence of the fact that deformation occurs on the most favourably oriented slip or twinning systems and it follows that the deformed metal acquires a preferred orientation or texture. For example, the response to plane strain compression of various orientations have been studied by various researchers (Akef and Driver, 1991, Becker *et al.*, 1991, Butler and Hu, 1989, Driver *et al.*, 1994, Theyssier *et al.*, 1995). Most crystal orientations, in channel die compression test, are accompanied by greater spread along the TD than ND and RD directions, see Figure III.2(b). However, the deformation

Table III.1 : Aluminium alloys characteristic texture components (Driver and Chenal, 2000)

Tableau 3 – Composantes principales des textures cristallographiques d'alliages d'aluminium								
Mode de déformation	**Indices de Miller**		**Angles d'Euler, φ_1 , Φ , φ_2**					
Tréfilage selon DA	fibres <111> et <100> // DA							
Compression uniaxiale selon DC	fibre <110> // DC							
Laminage	« Cu » {112} <11$\bar{1}$>		– 90	35,3	45			
	« S$_1$ » {123} <41$\bar{2}$> à « S$_3$ » {123} <63$\bar{4}$>		– 47	37	27	à	– 59	37	27
	« Laiton » {011} <21$\bar{1}$>		– 35,3	45	0			
	« Goss » {011} <100>		0	45	0			
Cisaillement	{001} <110>		45	0	0			
Extrusion plane	fibre {113} <33$\bar{2}$> +/– 30° DT		– 90	25	45			
Torsion à froid	{hkℓ} <110> + {111} <uvw>							
Torsion à chaud	{001} <110> + {112} <110>		45	0	0 ;	0	35	45
Recristallisation après laminage	« cube » {001} <100> ; « R » – S ;		0	0	0 ;	– 50	35	27 ;
	« cube tourné DT » {$\bar{1}$03} <301>		90	18	0			

(a)   (b)
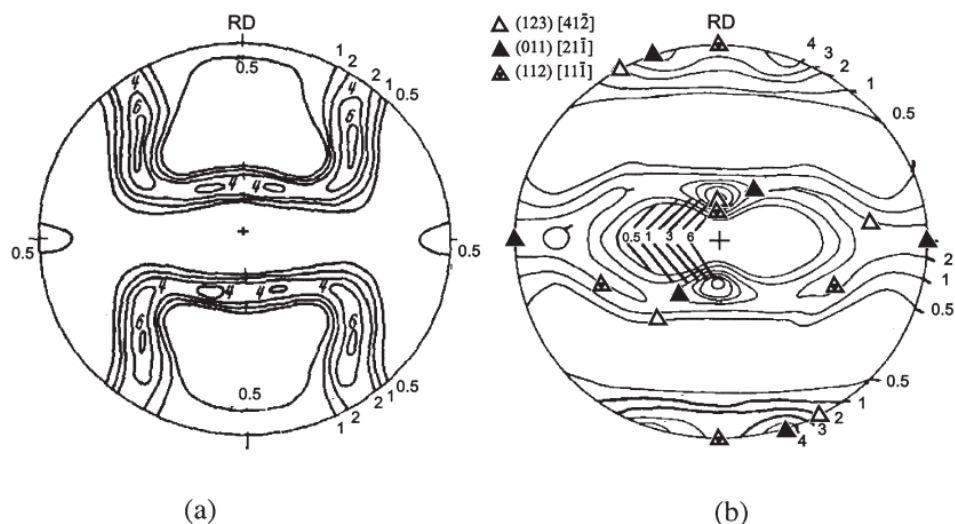
Figure III.2 : Pole figures of 95% cold rolled aluminium; (a) {100} pole figure; (b) {111} pole figure showing positions of several ideal orientations (Grewen and Huber,)
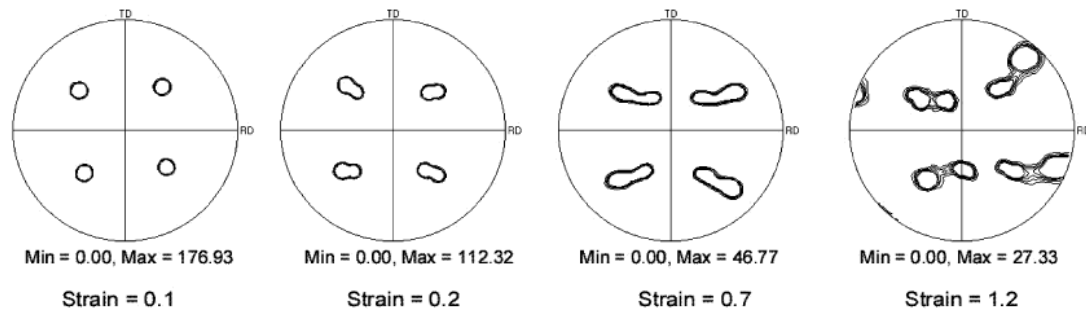
Figure III.3 : (111) pole figures of the deformation texture produced after plane strain compression of cube oriented crystals at room temperature measured using EBSD (Stanford *et al.*, 2003b)

texture of a deformed single crystal is generally distinguished as being either stable or unstable (Maurice *et al.*, 1992). The rolling texture components such as Copper {112}111, Brass {110}112, S {123}412 and Goss {110}001 are stable orientations and undergo minimal macroscopic lattice rotations with only a few degrees from the starting orientation. The disorientation axes are either close to the transverse direction, TD ({112}111, {110}112) or near random as in the {123}412 orientation (Godfrey *et al.*, 1998b, Godfrey *et al.*, 1998a). Unstable orientations undergo much greater lattice rotations during deformation and often break up into deformation bands. Examples are typical recrystallisation components, Cube {100}001 (Akef and Driver, 1991), see Figure III.3.

### III.1.3   Inter et Intragranular Misorientations

#### III.1.3.1   Deformation Bands

During plastic deformation of polycrystalline materials, individual grains are sometimes subdivided into areas rotating independently of one another to accommodate the imposed strain.   The reason for such grain fragmentation is that the number and selection of simultaneously acting slip systems differs between neighbouring areas within a grain. This leads to differences in lattice rotations between neighbouring areas within a grain and depends on the initial lattice orientation of the grain and its interaction with neighbouring grains. The deformation bands are most clearly observed in single crystals, bicrystals and very coarse grain polycrystals are separated by transition bands in the TD/RD plan (Liu *et al.*, 1998).

III.1.3.2   Dislocation Cells

In alloys with a high stacking fault energy and low solute content, such as dilute aluminium alloys, the microstructures after deformation at ambient or elevated temperatures can usually be described as a cellular or subgrain structure. Dislocation structure evolution during cold deformation of FCC polycrystals has been extensively investigated over the past couple of decades with primary emphasis on a qualitative description of the evolving structures and their relation to mechanical properties. As deformation increases in a material, grains begin to break into substructures. These substructures are characterized by two different types of boundaries: incidental dislocation boundaries (IDB) and geometrically necessary boundaries (GNB), see Figure III.4. The GNBs surround groups of cells in elongated cell blocks, itself surrounding regions that are almost dislocations free. This duplex structure persists throughout Stage II-IV. With increasing strain, the average GNB misorientation increases while the cell size decreases and the cell walls collapse into sub-boundaries, micro-
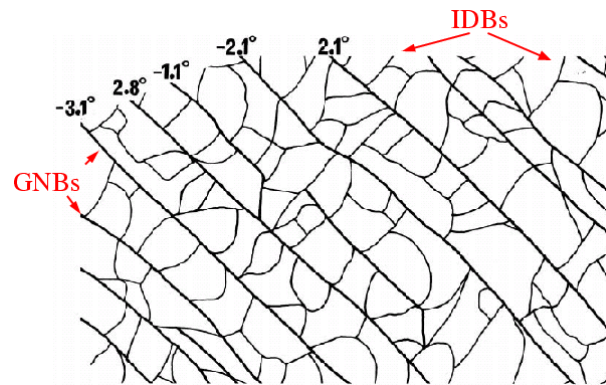
Figure III.4 : Schematics of cell-block boundaries and ordinary cell boundaries (Liu *et al.*, 1998)
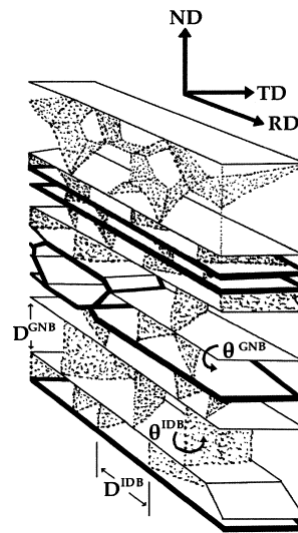
Figure III.5 : Schematic three dimensional drawing of the deformed microstructure. Sheets of extended GNBs with stippled low angle IDBs bridging between them. High angle GNBs are represented by thick lines and medium angle by medium thick lines (Hughes and Hansen, 2000)

shear bands appear and finally the cell and micro-band structures evolve into a lamellar structure. GNBs tend to be aligned at about 40° to the rolling direction RD (Liu *et al.*, 1998).

These two boundary types form differently. IDBs do so by the random trappings of glide dislocations and GNBs form between regions with one or more different operating slip systems to accommodate the accompanying difference in lattice rotations. These boundaries contain both statistically stored dislocations which do not contribute significantly to a net lattice rotation, and essentially in GNBs, excess dislocations which are geometrically necessary dislocations, contribute to the net lattice rotation (Merriman *et al.*, 2008). The GNBs which accommodate the lattice mismatch, will acquire much larger misorientation angles at a higher rate with increasing strain than IDBs. Those heterogeneities of the microstructure widely characterised by 2D techniques consist of nearly two-dimensional morphologies, see Figure III.5. The dislocation cells have been mainly characterised by transmission electron microscopy (TEM) (Ananthan *et al.*, 1991, Hughes and Hansen, 1997, Liu *et al.*, 1998), see
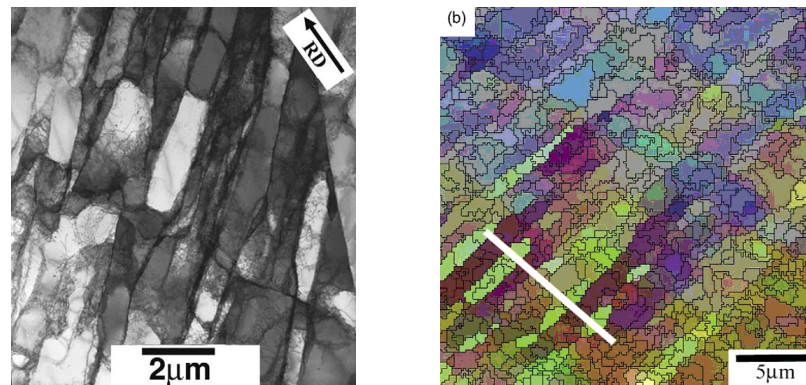
Figure III.6 : (a) transmission electron micrograph showing substructures after 20% rolling and (b) EBSD relative Euler orientation map showing substructures after 20%*rolling* with 0.5° boundaries superimposed (Hurley and Humphreys, 2003)
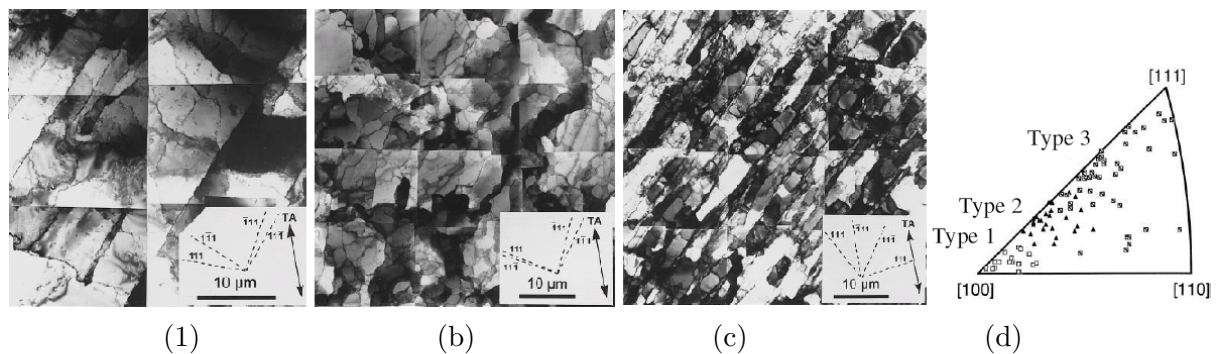
Figure III.7 : TEM micrograph of (a) Type 1, (b) Type 2, (c) Type 3 microstructures and (d) Inverse pole figure showing the tensile axis orientation of grains embedded in polycrystalline specimens strained up to 14%

Figure III.6 a, and more recently by scanning electron microscopy and high resolution electron backscatter diffraction (EBSD) (Driver *et al.*, 1994, Wilkinson, 2001, Hurley *et al.*, 2003), see Figure III.6 b. The use of EBSD enables more quantitative but less qualitative measurements than with the TEM (Winther *et al.*, 2004). The main measurable structural parameters with respect to the cell blocks are the spacing of dislocation boundaries and misorientation angles.

Grain orientations are known to have a strong influence on the dislocation substructures of plastically deformed metals, with obvious implications for work-hardening rates, stored energies, and recrystallisation. Consequently, the relations between deformation microstructures and crystal orientation, particularly of FCC metals, have been the subject of several investigations. Observations of cell block structures in deformed polycrystals under tension have revealed that the boundary plane for GNBs varies with location of the crystal orientation of the tensile axis within a standard stereographic triangle (Huang and Hansen, 1997). In Figure III.7, Type 1 represents microstructures subdivided by extended, crystallographic dislocation boundaries, defining cell blocks which contain ordinary cells while Type 3 represents microstructures with extended, non-crystallographic dislocation boundaries. A boundary is defined as crystallographic when is parallel to within 5° with a slip plane, whereas non-crystallographic boundaries make a larger angle with a slip plane. Type 2 depicts microstructures subdivided by ordinary dislocation boundaries defining a three dimensional cell structure (Hansen and Huang, 1998).

Table III.2 : Flow rule parameters for Al

$\widehat{\tau}_0(\text{MPa})$	p	q	$\dot{\gamma}_0(s^{-1})$	$F_0(\text{J})$
8.0	0.141	1.1	1.73×10^6	3.00×10^{-19}

Table III.3 : Single crystal model parameters for Al

	C_i	$K_i/b^\alpha(mm^{-1})$	$d_i(nm)$	$Y_i^\alpha(\mu m)$
Edge	0.5	55×10^3	7.0	162
Screw	0.5	110×10^3	35.0	81
$\mu = 45.0$ GPa	$\lambda = 0.3$	$b^\alpha = 0.286$ nm	$\omega_1 = 1.5$	$\omega_2 = 1.2$

III.2 Calibration of the Single Crystal Model

The material constants for Al come from published values (Cheong *et al.*, 2005). The anisotropic elasticity tensor for cubic crystals is defined by three independent parameters, C_{11}, C_{12} and C_{44}. All three parameters are temperature-dependent and each have been approximated by a polynomial relation (Simmons and Wang, 1971) in GPA units.

$$
\begin{aligned}
C_{11} &= 123.32 + (6.70 \times 10^{-8})\theta^3 - (1.13 \times 10^{-4})\theta^2 - (7.88 \times 10^{-3})\theta & \text{(III.1)} \\
C_{12} &= 70.65 + (4.41 \times 10^{-8})\theta^3 - (7.55 \times 10^{-5})\theta^2 - (4.00 \times 10^{-3})\theta & \text{(III.2)} \\
C_{44} &= 31.21 + (7.05 \times 10^{-9})\theta^3 - (1.22 \times 10^{-5})\theta^2 - (8.33 \times 10^{-3})\theta & \text{(III.3)} \\
\mu &= 29.16 + (9.00 \times 10^{-9})\theta^3 - (2.00 \times 10^{-5})\theta^2 - (73.00 \times 10^{-4})\theta & \text{(III.4)}
\end{aligned}
$$

The flow rule defined by Eq. II.30 contains a total of five parameters ($\dot{\gamma}_0$, F_0, $\widehat{\tau}_0$, p, q) which have been determined by (Balasubramanian and Anand, 2002). The hardening-recovery laws defined by Eqs. II.48 and II.49 contain six parameters (C_e, C_s, K_e, K_s, d_e, d_s) which have been identified by (Cheong *et al.*, 2005) from experimental data previously obtained by (Hosford *et al.*, 1971). The flow rule parameters are listed in Table III.2 and the single crystal model parameters in Table III.2.

In order to verify the validity of the calibrated parameters, finite-element (FE) calculations of single crystals under uniaxial tensile loading are performed in Zebulon (Besson *et al.*, 1998) using a FE mesh of identical dimensions to that of (Hosford *et al.*, 1971). As shown in Figure III.8, the mesh consists of $44 \times 4 \times 4$ elements. Quadratic brick elements with reduced integration (C3D2r) are used. Boundary conditions are described in Figure III.8. Nodes on each side of the opposite top and bottom faces are constrained from moving laterally to reproduce the grip constraints. As measured in (Hosford *et al.*, 1971), initial misalignment of 0.5° in the Al single crystals from the [100], [111] and [112] ideal orientations is introduced in the simulations carried out, see Tab. III.2. A true strain rate of $7.5 \times 10^{-5}s^{-1}$ was applied at a temperature of 273K. FE calculation performed by Abaqus (Cheong *et al.*, 2005) and Zebulon are shown in the form of stress-strain curves in Figure III.9. Curves obtained by both FE codes are identical and are in good agreement with experimental data.
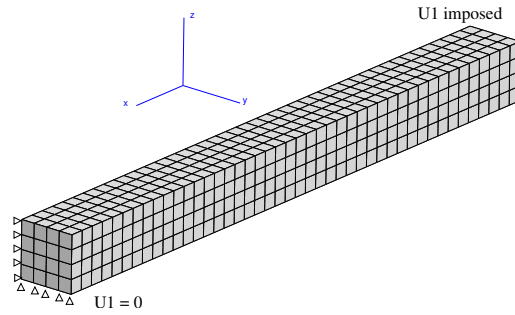
Figure III.8 : Specimen geometry and FE mesh used to simulate uniaxial tensile tests

Table III.4 : Euler angles (Bunge notation) with 0.5° misorientation from the tensile axis

Orientation	ϕ_1 (deg.)	θ (deg.)	ϕ_2 (deg.)
[111]	54.8	135.01	180.0
[100]	0.4	10.0	0.0
[112]	61.1	69.7	281.0
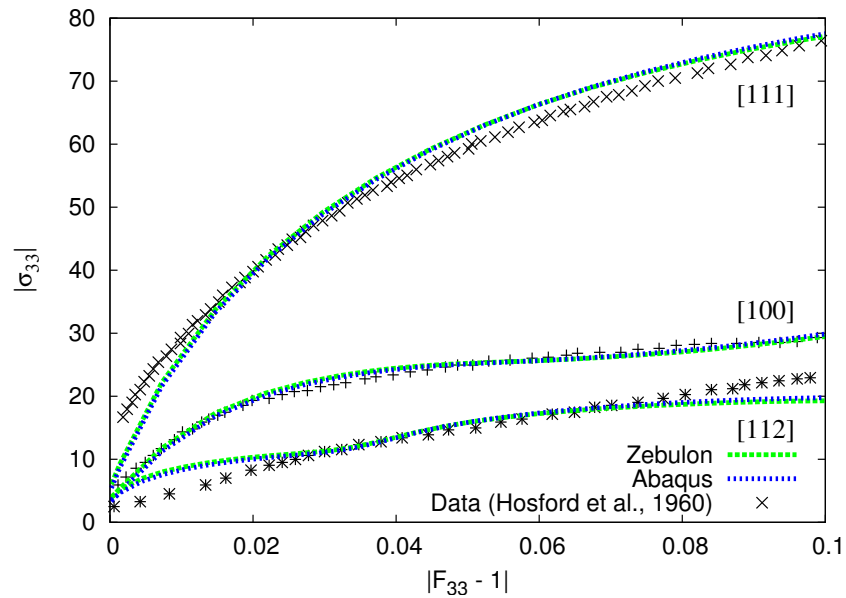
Figure III.9 : Comparison of true-stress true-strain prediction along [100], [111] and [112] with experiment data at 273°K

(a) (b)
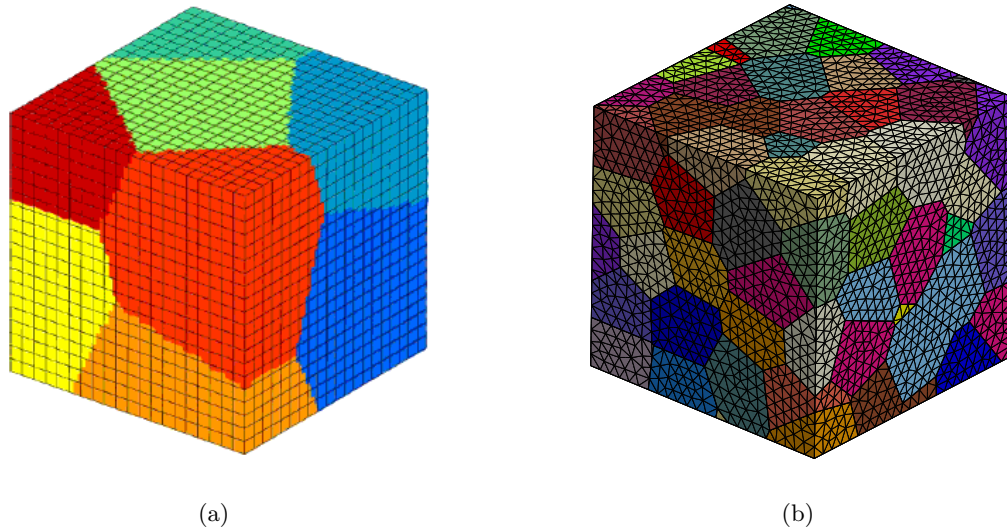
Figure III.10 : Microstructure generated using Voronoi tessellation: (a) regular mesh and (b) 'free' mesh (Osipov, 2007)

III.3 Single Crystal Model Validation for a Polycrystal

III.3.1 Impact of GNDs on Deformation Heterogeneities

This section reports the differences in the deformed features predicted by the introduction or not of the GNDs in the model. The RVE used to describe Al polycrystalline aggregates have an initial cubic geometry with different grain shape, see Figure III.10. The polycrystalline aggregate is obtained from a digital microstructure generated from mathematical models based on Poisson's distribution of the grains nuclei. This kind of aggregate generated by Voronoi tessellation has been extensively used in ((Barbe *et al.*, 2001a, Barbe *et al.*, 2001b, Kanit *et al.*, 2003, Zeghadi, 2005, Osipov, 2007) for different applications. Voronoi tessellation allows to obtain a grain morphology closed to the experimentally observed grain shape. The mesh generation procedure adopted in the present work introduces tetrahedra which are generated in two successive operations, skin construction and 2.5D mesh generation (Laug and Borouchaki, 2003), followed by the generation of the solid elements (George, 1997). This method avoids step phenomenon at grain boundaries as illustrated in Figure III.10. Furthermore, as each element belongs to only one grain, numerical singularities arising from behaviour discrepancies in the same element are avoided (Osipov, 2007). The mesh with 100 randomly-oriented grains is made of 97693 10-nodded isoparametric tetrahedral elements. Grains are defined by group of elements with randomly assigned orientations, as illustrated by the {111} pole figures shown in Figure III.12.

The boundary conditions are described in Figure III.11. A true strain rate of $0.7 \times 10^{-4}s^{-1}$ was applied on the top surface at a temperature of 273K. Parallel computations have been carried out to resolve the resulting non linear system. The FE code Zebulon used is fully parallelised (Feyel, 1998). The algorithm is based on a subdomain decomposition method called FETI (Finite Element Tearing and Interconnecting method (Fahrat and Roux, 1991)). After the decomposition of the structure into subdomains, the sub-problems into each domain are solved independently and an iterative scheme is employed to obtain the solution of the global problem, and to merge the results of all subdomains.

(a)
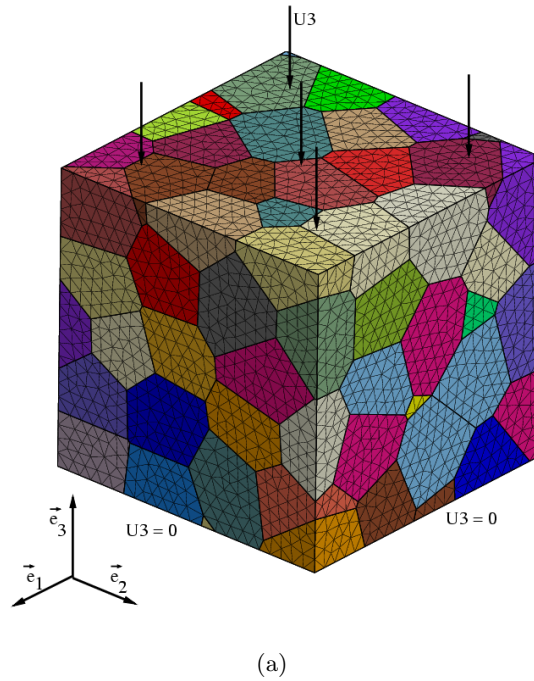
Figure III.11 : Polycrystalline Aggregate used to simulate uniaxial compression test

(a)　　　　　　　　(b)　　　　　　　　(c)
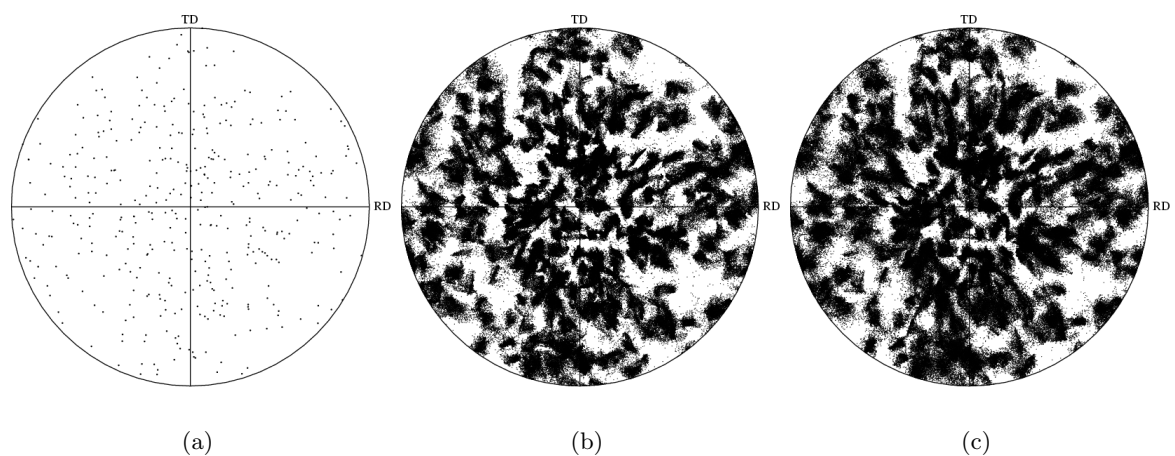
Figure III.12 : {111} Pole figures of (a) randomly assigned grain orientations, (b) after 10% height reduction and (c) after 10% height reduction when GNDs are included in the polycrystal

(a) with only SSDs (b) with SSDs and GNDs
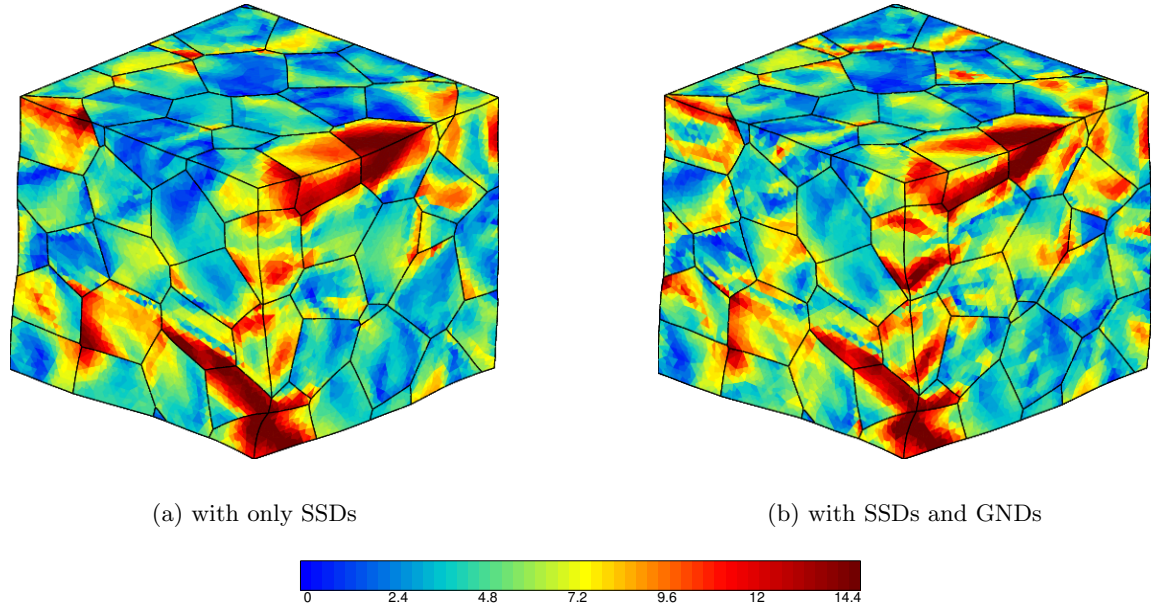
Figure III.13 : Accumulated grain rotations distribution after 10% height reduction

As seen in Figure III.12(a), no initial misorientation mosaicity has been assumed inside each grain. Figure III.12(b) shows the pole figures $\{111\}$ after 10% deformation. The spread of orientations seen in the figures underlines the misorientation development, which results in a significant increase of GNDs to accommodate these misorientations. However, the orientations spread in the pole figure where GNDs are accounted for seems more significant those observed where only SSDs are taken into account. In order to quantify grain rotation, the accumulated rotations distributions, defined by $\beta = \arccos(\frac{Tr(R_e)-1}{2})$ obtained from the polar decomposition of the elastic part of the gradient tensor, $F_e = R_e U_e$, where R_e is the elastic lattice rotation and U_e are the elastic lattice stretching, are shown on Figure III.13. In both cases, rotations inside grain are inhomogeneous. However, the rotation heterogeneities are stronger when GND hardening is accounted for. Rotations are mainly localised at aggregate edges and in lesser extent at grain boundaries. In addition to the misorientation development, grains undergo lattice rotations as illustrated in Figure III.14, where only a small fraction of polycrystalline aggregates kept the initial orientation. Figure III.13 shows similar rotation distributions while the average grain rotation increases with the introduction of GNDs.

The accumulated plastic strain distribution for both aggregates shown on Figure III.15 reveals heterogeneous areas with peaks in corners and edges. In contrast to the accumulative plastic strain, the Von Mises stress distribution is localized at grain boundaries as shown in Figure III.16, especially when GNDs are introduced. Figure III.17 shows the total dislocation density distribution. The accumulation of dislocations at the grain boundary is strengthened by GNDs introduction due the significant quantity of GNDs necessary to accommodate the lattice incompatibilities.

III.3.2 Representative Volume Element of Aggregates

In this section, grain morphology dependency is investigates. Two RVEs are used to describe Al polycrystalline aggregates. Both have an initial cubic geometry with different grain shapes,
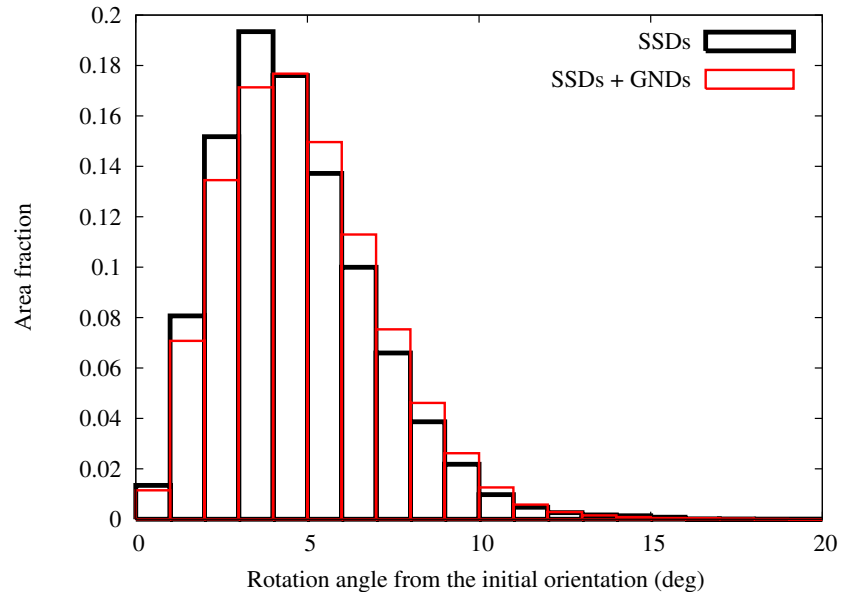
(a)

Figure III.14 : Statistics of the accumulated grain rotations after 10% deformation

(a) with only SSDs

(b) with SSDs and GNDs
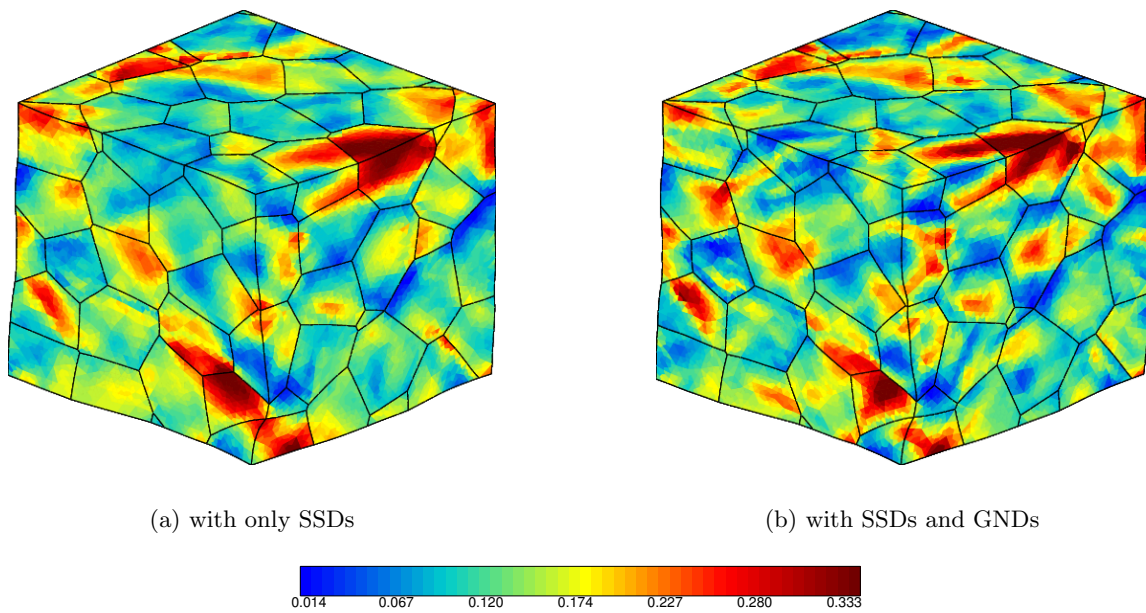
Figure III.15 : Accumulated plastic strain distributions after 10% height reduction

(a) with only SSDs

(b) with SSDs and GNDs
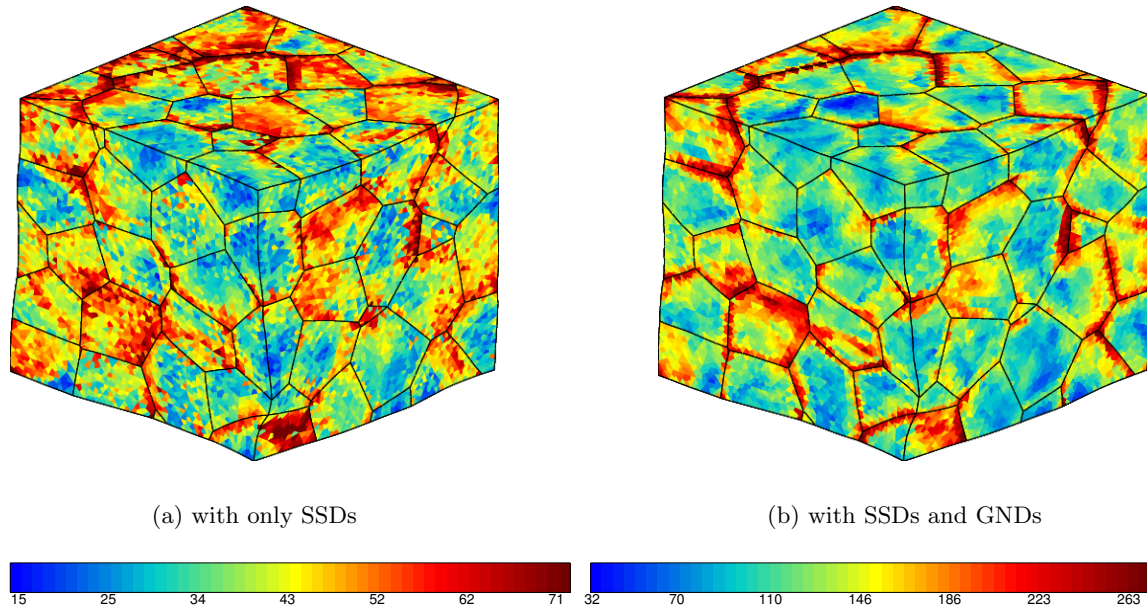
Figure III.16 : Von Mises stress distribution after 10% height reduction

(a) with only SSDs

(b) with SSDs and GNDs
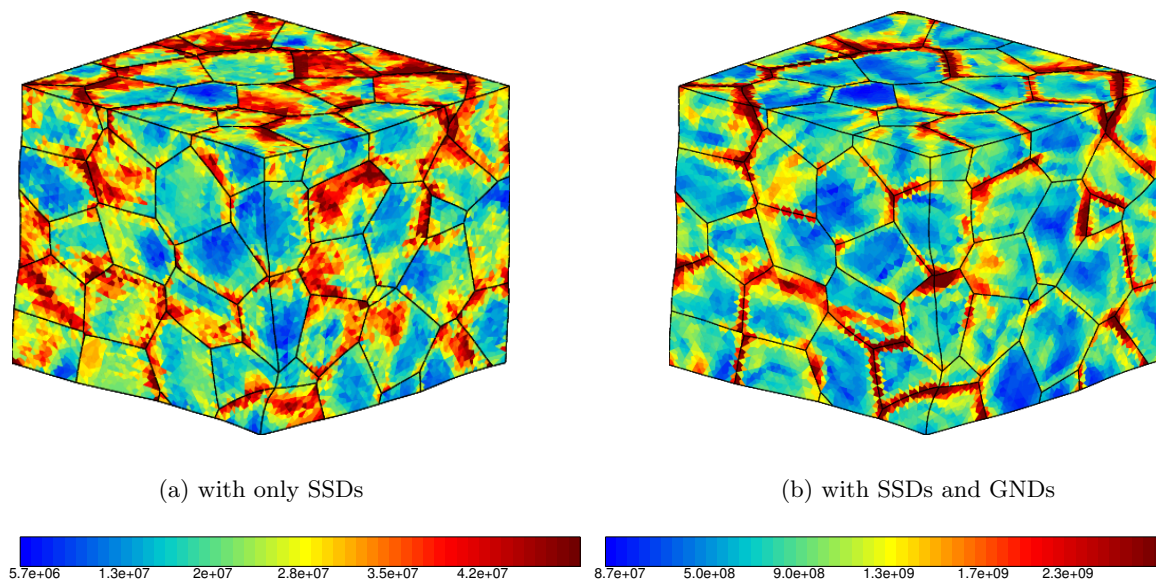
Figure III.17 : Distribution of all dislocation densities after 10% height reduction

(a)   (b)
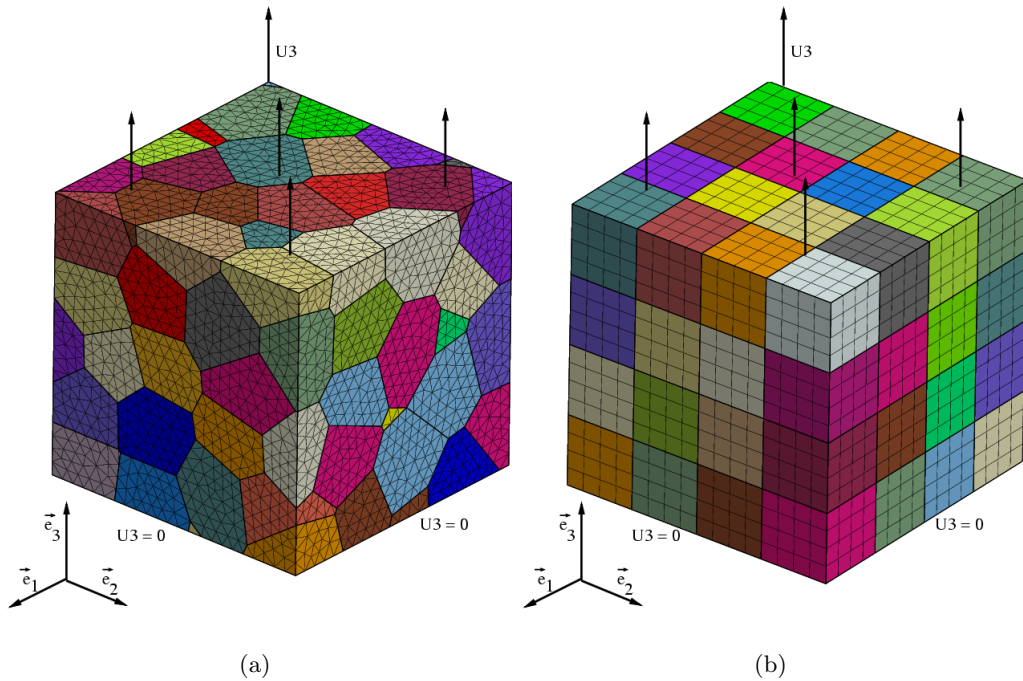
Figure III.18 : Polycrystalline aggregates used to simulate uniaxial tensile tests with (a) a free mesh and Voronoi tessellation, and with a (b), regular mesh

see Figure III.18. In both cases, grains are defined by groups of elements with randomly assigned orientations.

Boundary conditions are described in Figure III.18. A true strain rate of $0.7 \times 10^{-4} s^{-1}$ was applied at a temperature of 273K on the top surface. No initial misorientation has been assumed inside each grain. The resulting stress-strain response can be seen in Figure III.19 for both polycrystals. From this figure, it can be seen that the macroscopic stress-strain response is hardly affected by the grain morphology. The accumulated plastic strain distribution for both aggregates is given in Figure III.20. It consists of heterogeneous areas with peaks at the corners and edges of the RVE.

The predicted accumulated grain rotation is shown in Figure III.21. As underlined previously, rotations are heterogeneous inside each grain giving a misorientation development. Only a small fraction of the grains keep their initial orientation as seen in Figure III.22. Grain rotation is higher in the 64 grains aggregate cases due to a higher fraction of grains belonging to the free surfaces and thus not constrained by other grains to rotate.

In Figure III.19, both polycrystalline aggregates predicted similar stress-strain curves. Cuboidal grain shape aggregates are appropriate to predict macroscopic behaviour while the Voronoi shapes provides a more accurate local stress-strain state. We also notice the tetrahedral elements did not enhance the local heterogeneities compared to the cubic elements.

III.3.3   Grain Size Effect

The effect of grain size on the tensile behaviour and ductility of aluminium has been investigated at room temperature. The polycrystal responses predicted for three grain
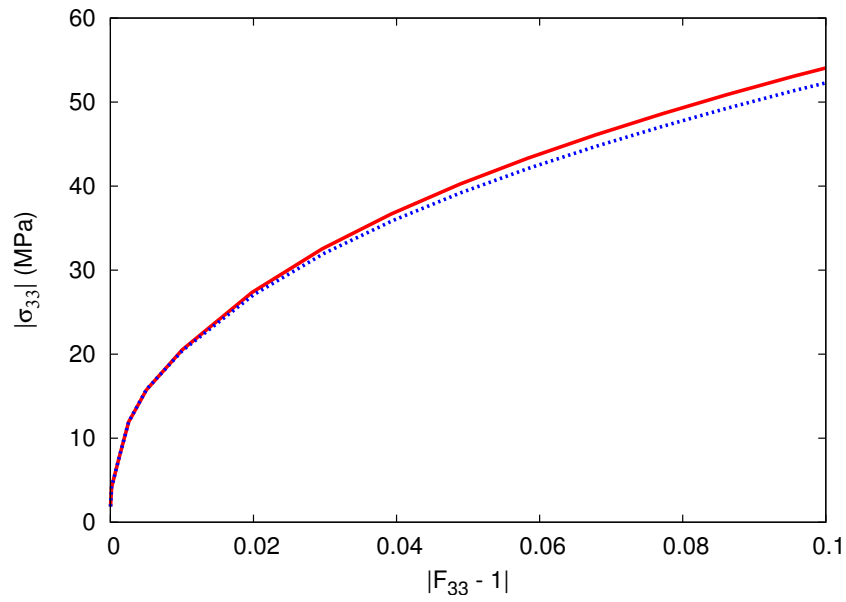
Figure III.19 : Predicted stress-strain responses of both polycrystalline aggregates
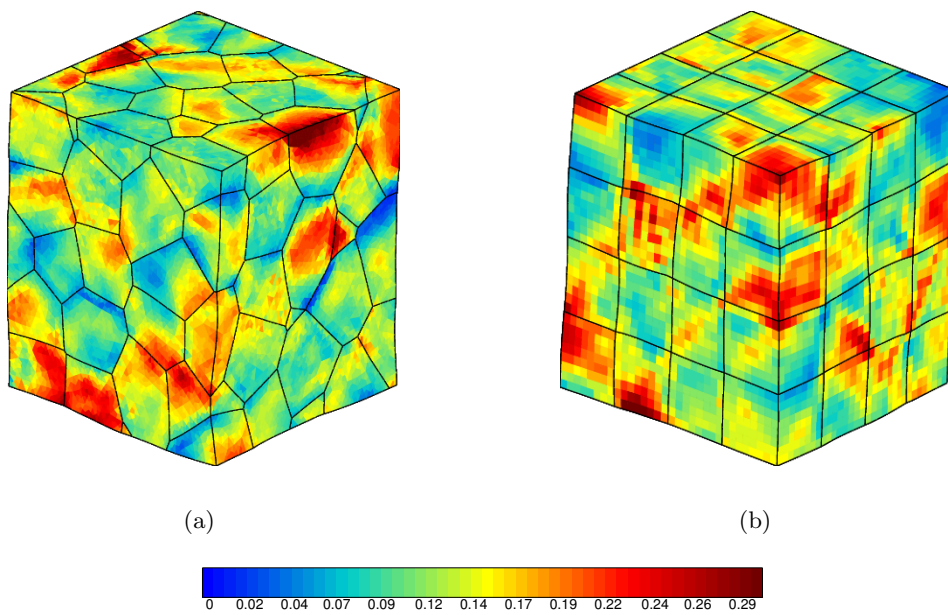
Figure III.20 : Accumulated plastic strain distribution after 10% height reduction

(a)   (b)
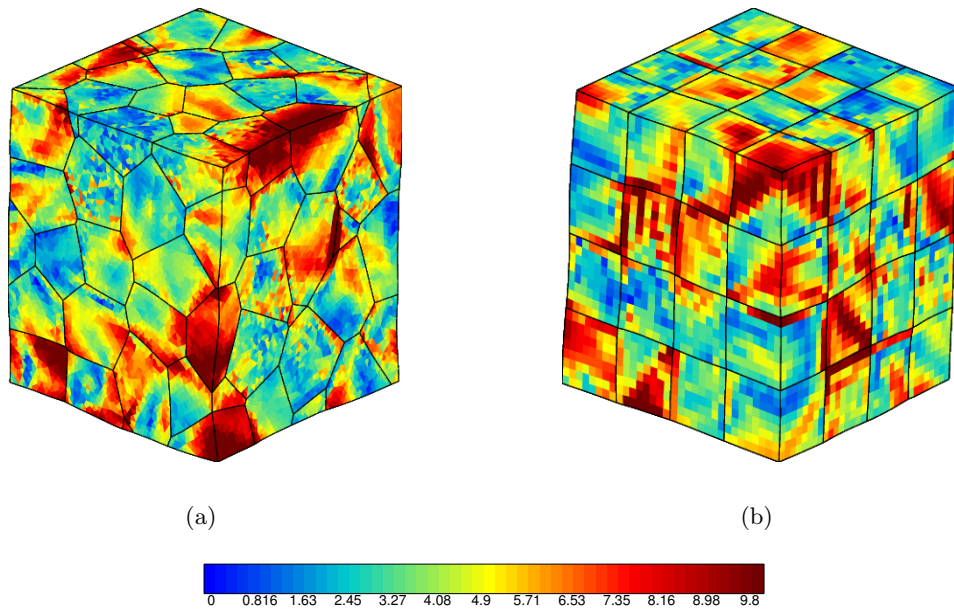
**Figure III.21** : Grain rotation distribution after 10% height reduction
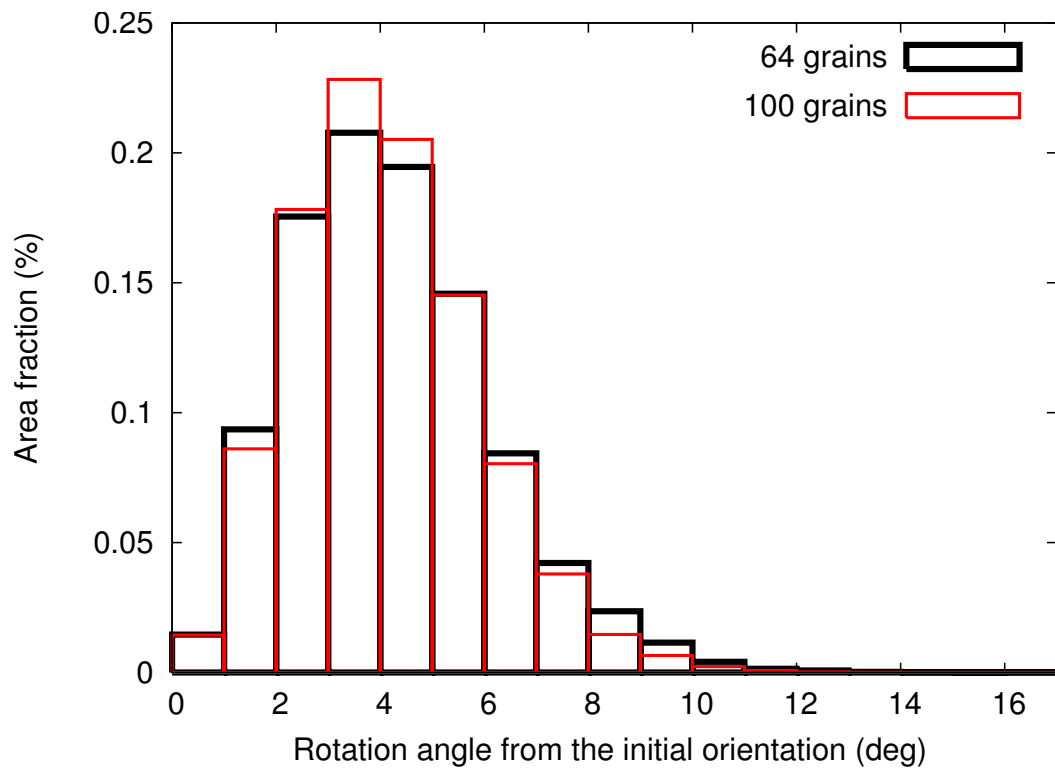
**Figure III.22** : Predicted grain rotations after 10% height reduction
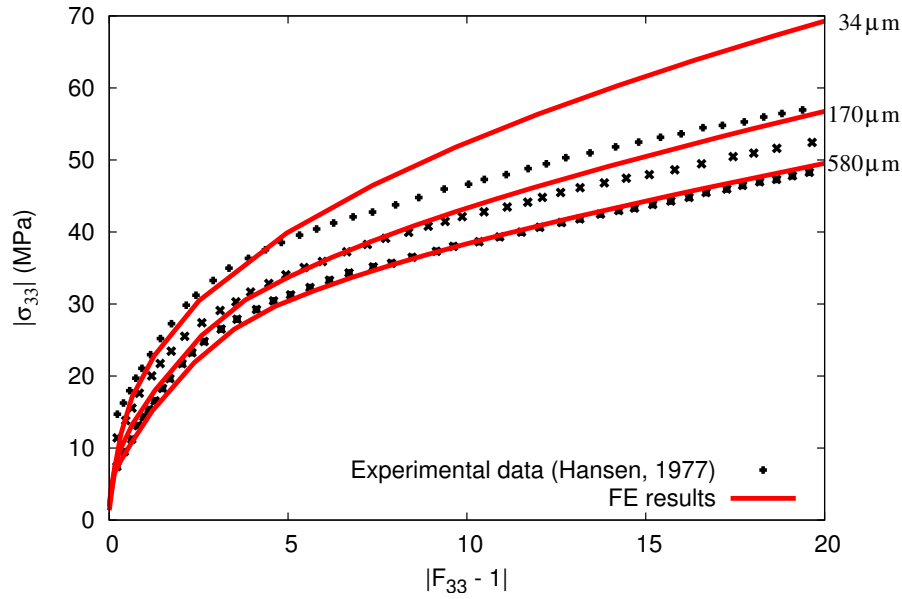
Figure III.23 : Comparison between the predicted macroscopic response of the 64-grains polycrystal with the experimental Al polycrystalline true stress-strain curves by (Hansen, 1977) for D = 34, 170 and 580 μm

sizes (34, 170 and 580 μm) are compared against the experimental data in Figure III.23. It is observed that a reduction in the initial grain size from $580 \mu m$ to $34 \mu m$ strengthens the polycrystal. The 580 μm grain size polycrystal response is in good agreement with experimental results while the hardening is too high for the both other grain sizes. For each grain size, the build up of strain gradients lead to the accumulation of GNDs during deformation affecting significantly the hardening behavior of polycrystalline aggregates.

It was found that the grain size dependence of the flow stress, σ, follows a modified Hall-Petch equation of the type,

$$\sigma = \sigma_0(\varepsilon) + k(\varepsilon)D^{-1/2} \tag{III.5}$$

where σ_0 and $k(\varepsilon)$ depends on the strain level. A linear interpolation of the FE results for different grain sizes is done on the Hall-Petch relation, see Figure III.24. The stress variation with grain size follows the Hall-Petch relation, however, the parameter k is overestimated.

III.4 Predictions

III.4.1 Channel Die Compression Test

In the present experiments, a channel die is used to simulate cold rolling of aluminum for deformation smaller than 50%, see Figure III.25. The die imposes a nominally plane strain deformation gradient on the metal similar to that experienced by the aluminum passing through a rolling mill. In this test, the walls of the channel suppress the lateral flow and develop heterogeneous lateral stresses at the walls which vary with crystal orientation. A Teflon film was placed between the samples and the die walls to prevent galling. The studied samples have been elaborated at ELTE (Budapest University), have been deformed by channel die compression up to 15% and 30% strain at room temperature at Mines de Saint-Etienne and have been observed at CdM.
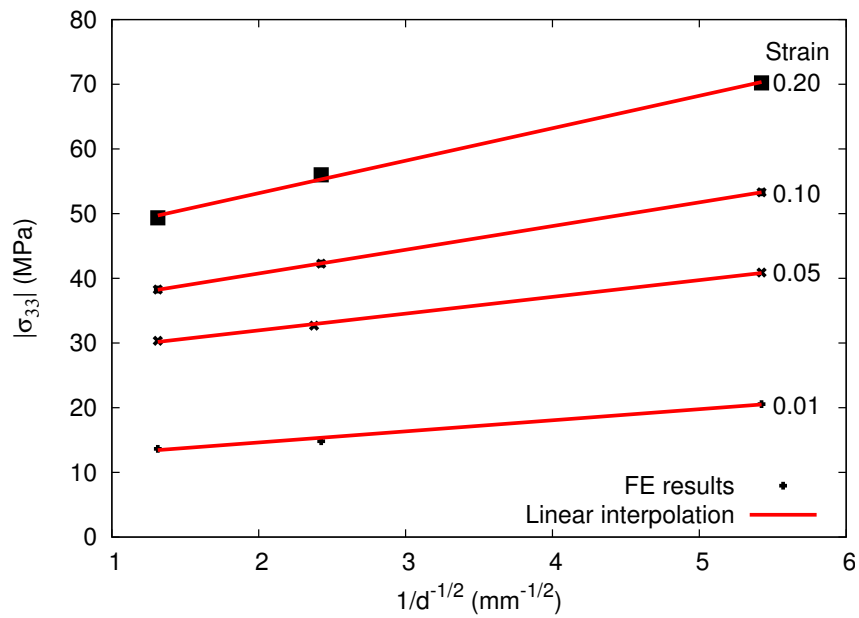
Figure III.24 : Flow stress dependency on grain size at various strain levels with the fitted Hall-Petch relation
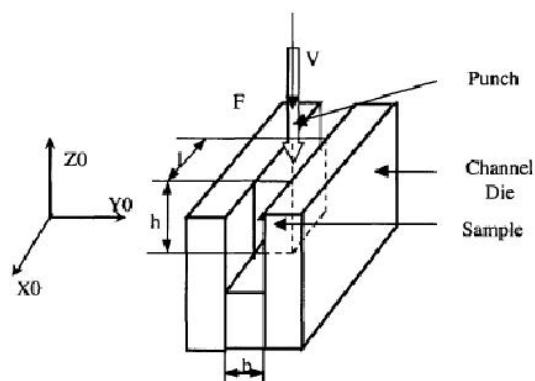
Figure III.25 : Schematic channel die compression test
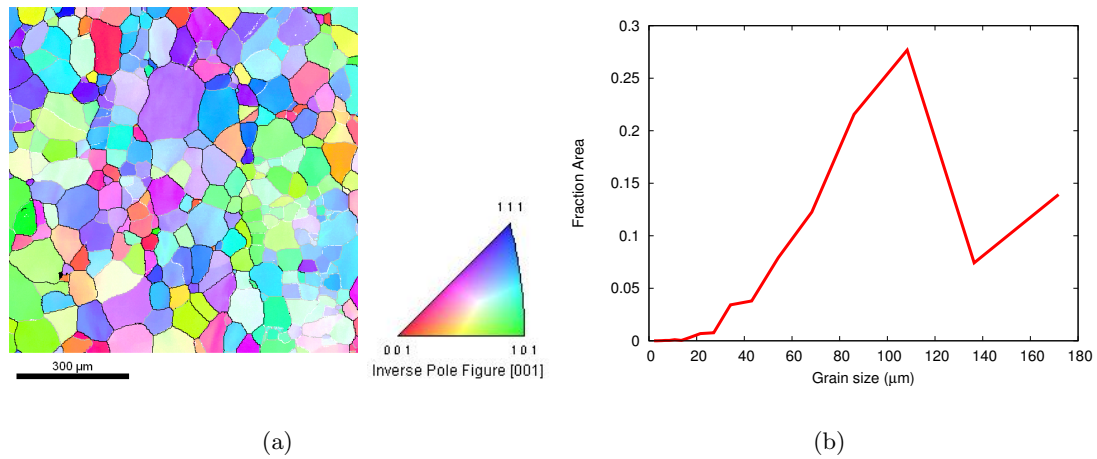
Figure III.26 : (a) Inverse pole figure [001] of undeformed sample and (b) initial sample grain size
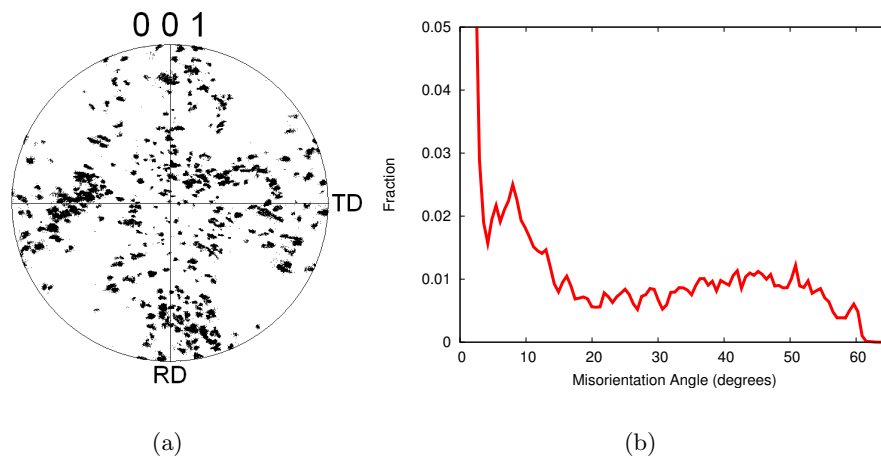
Figure III.27 : (a) Pole figure [001] of the undeformed sample, (b) and initial misorientation distribution

III.4.1.1   Materials Study

In this study, the material is an $Al - 0.5\%Mg$. In order to characterise the microstructure, EBSD measurements have been carried out on the undeformed sample. In Figure III.26, the inverse pole figure map constructed from the EBSD measurements shows a non uniform grain size distribution from $20\mu m$ to $300\mu m$ with an approximately isotropic texture in Figure III.28. However, an initial orientation spread is observed in the pole figure with the fuzzy points describing each grain orientation. In order to confirm this observation, a misorientation diagram has been added to Figure III.28 (b). A peak is noticed for misorientations lower than $3°$ and a smallest one for misorientations around $45°$ as established by (Mackenzie, 1964) for isotropic texture. Therefore, the commonly used assumption that each grain in a polycrystalline aggregate can be uniquely described by a single lattice orientation is debatable.

With a large initial grain size (around $100\mu m$), the aluminium alloy, which is a material

(a)   (b)
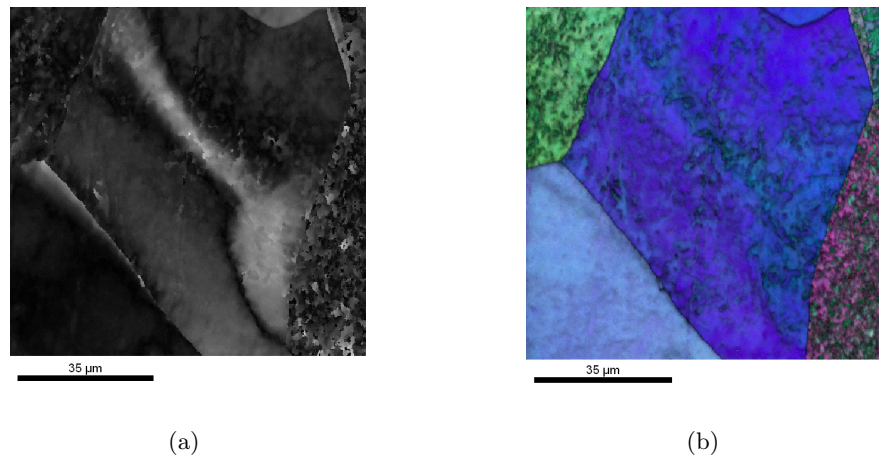
Figure III.28 : (a) Orientation deviation from the reference orientation and (b) inverse pole figure [001] map with index quality of EBSD measures

with a high stacking fault energy, seems suitable for subgrain structure development.

III.4.1.2   Substructures Measurements

Grain fragmentation, local orientation gradients and substructures are characterised using electron scanning backscatter diffraction (EBSD) in a field emission gun scanning electron microscope (FEGSEM) for the samples deformed by channel die compression. To avoid the problems associated with frictional conditions on the surfaces, the scanned region was an internal interface corresponding to the ND-TD plane. The sectioned surfaces were prepared by a fine metallographic polish after deformation. The orientation maps were made with a step size of $0.2\mu m$. A small step size enables a detailed analysis of the deformation band distributions and their associated orientation spreads together with an analysis of the substructure development (via the spatial distributions of low-angle boundaries).

Two random areas from a 15% deformed sample has been scanned. Since the grain size varies from $20\mu m$ to $300\mu m$, in the first area, four grains are observed while in the second, only one grain is scanned. In Figure III.28, the orientation map reveals an inhomogeneities. The centered grain breaks into a macroscopic deformation band strongly disoriented by rotation. The crystal lattice undergoes major rotations inside the grain. In order to analyse more accurately the lattice rotation inside the grains, misorientation lines are plotted from point to points in Figure III.29. In Grain 1, no global orientation gradient is observed along the line. The red line in grain one highlights rapid change of orientation ($3°$) approximately every $4\mu m$ and, between each peak, the orientation is constant. This is the typical characteristic of cell structure. In Grain 2, a global orientation gradient is observed with no localisation in line. Line 3 exhibits a deformation band around $5\mu m$, $15°$ disoriented from the orientation. Grain 4 demonstrates only a weak tendency to lattice rotation while in Grain 5, orientation change localisation occurs along the misorientation line. It was found that heterogeneities depend strongly on the initial grain orientation.

EBSD measurements on the second area are shown in Figure III.30. The three lines across the grain exhibit similar profile with a rapid change of orientation about$6°$. For these specific orientations, an average cell size of about 2.6 μm has been measured. (Hughes, 2001) found a

(a)

(b) line 1

(c) line 2

(d) line 3

(e) line 4

(f) line 5
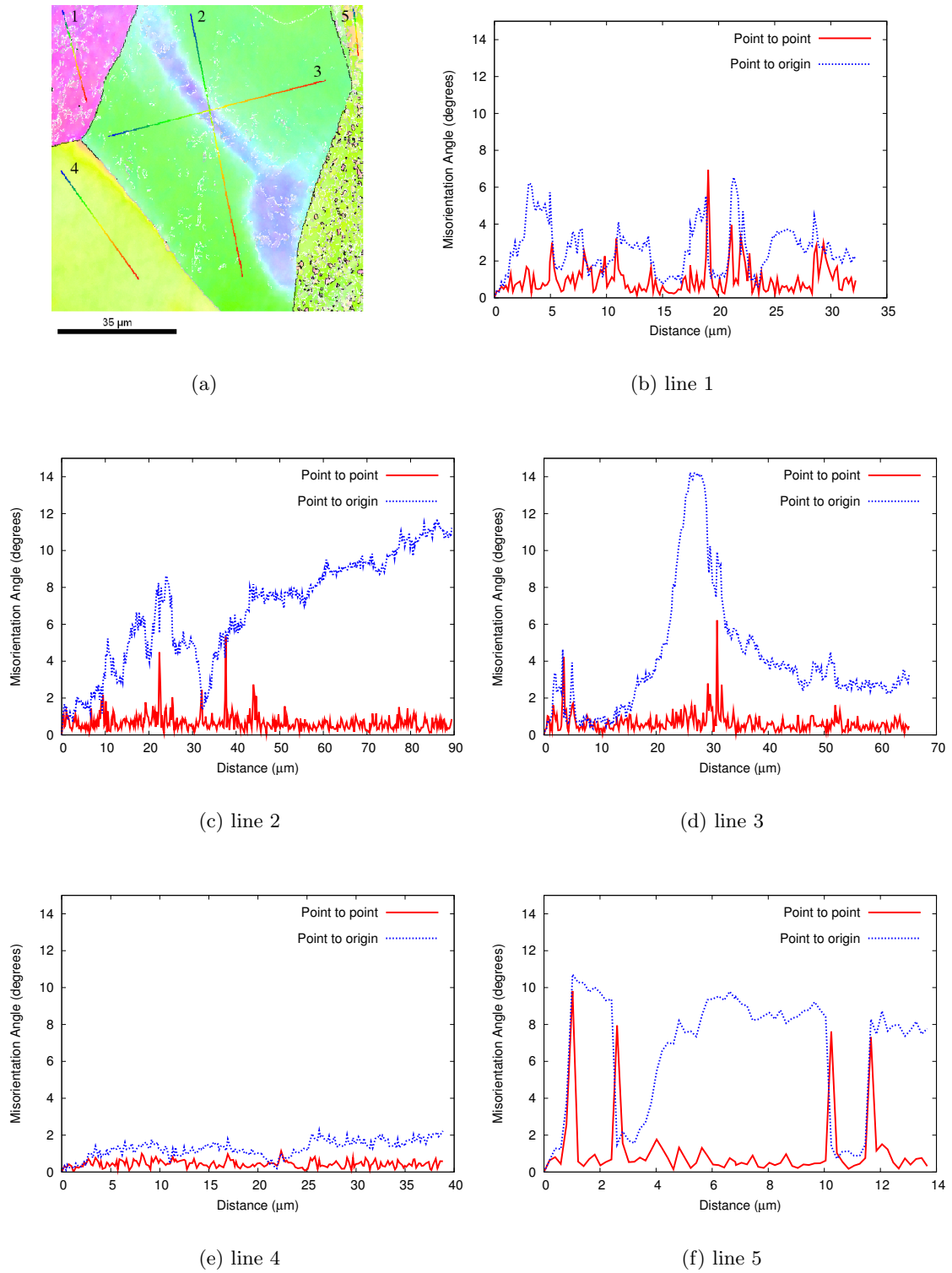
Figure III.29 : (a) Inverse [010] pole figure after 15% deformation and (b, c, d, e, f) misorientations across grains

(a)

(b) line 1

(c) line 2

(d) line 3
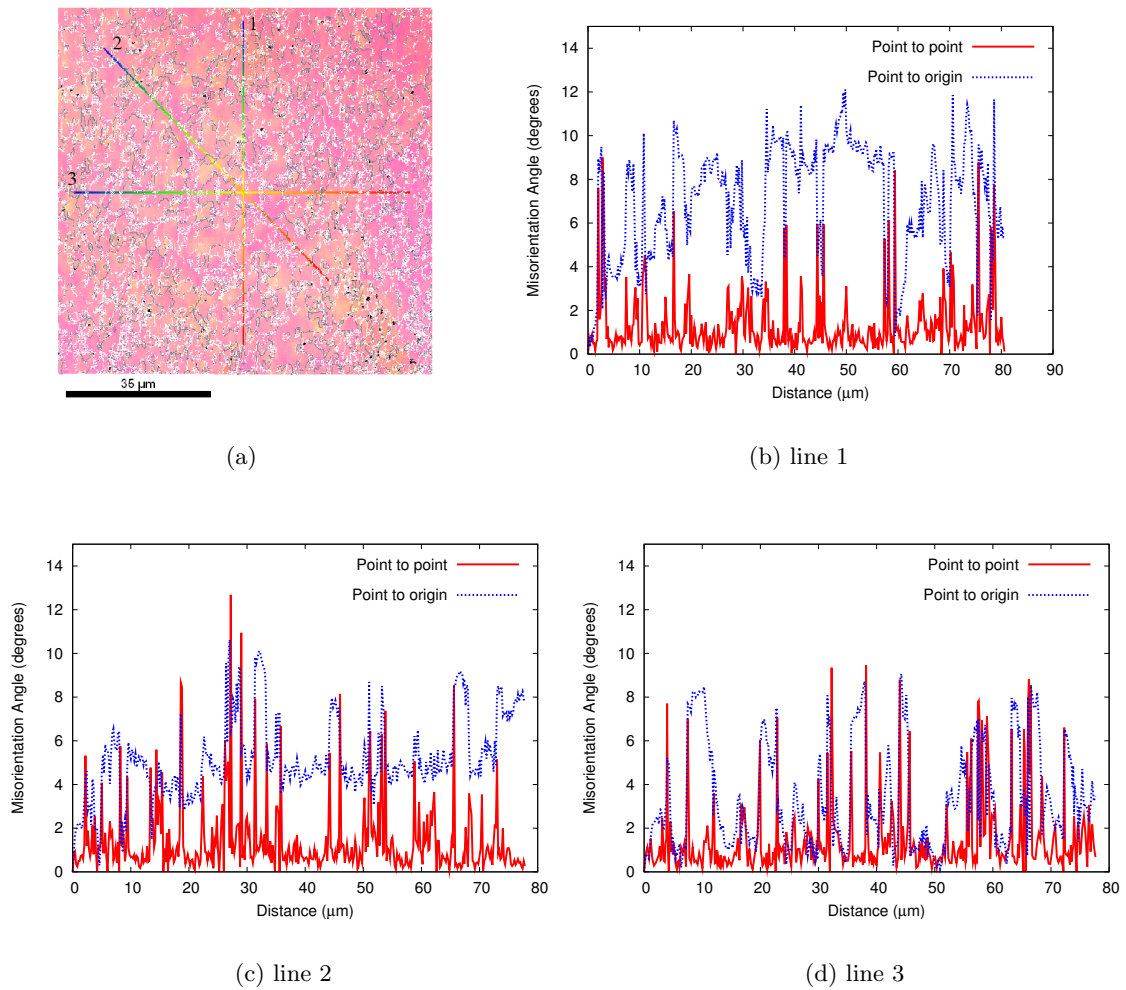
Figure III.30 : (a) Inverse pole figure [010] of a 15% deformed sample and (b, c, d) misorientations across grains

value about 1.5 μm from TEM measurements while (Liu *et al.*, 1998) found a value of about 2.2 μm for cold rolled pure aluminium.

One random area after 30% deformation sample has been scanned. No rapid change of orientation has been observed across the misorientation lines 2 and 3 but rather large orientation gradients. A significant misorientation is observed in line 3. However, no substructure formation has been observed contrary to the 15% deformed sample. Subgrains formation was found to occur for some specific grains orientations.

As it is well known, the initial orientation of the crystallites and the configuration of the active slip systems clearly govern the different paths of the crystal lattice rotation. This observation can explain the absence of cell structures for some grain orientations. It is also known that additional solute prevent cell formation. For example solute additions like Mg additions to Al that increase the friction stress result in deformation microstructures with a more uniform distribution of dislocations (Hughes, 2001). Another reason can be linked to the sample preparation where the mechanical and, chemical polishing may not have been suitable.

(a)

(b) line 1

(c) line 2

(d) line 3
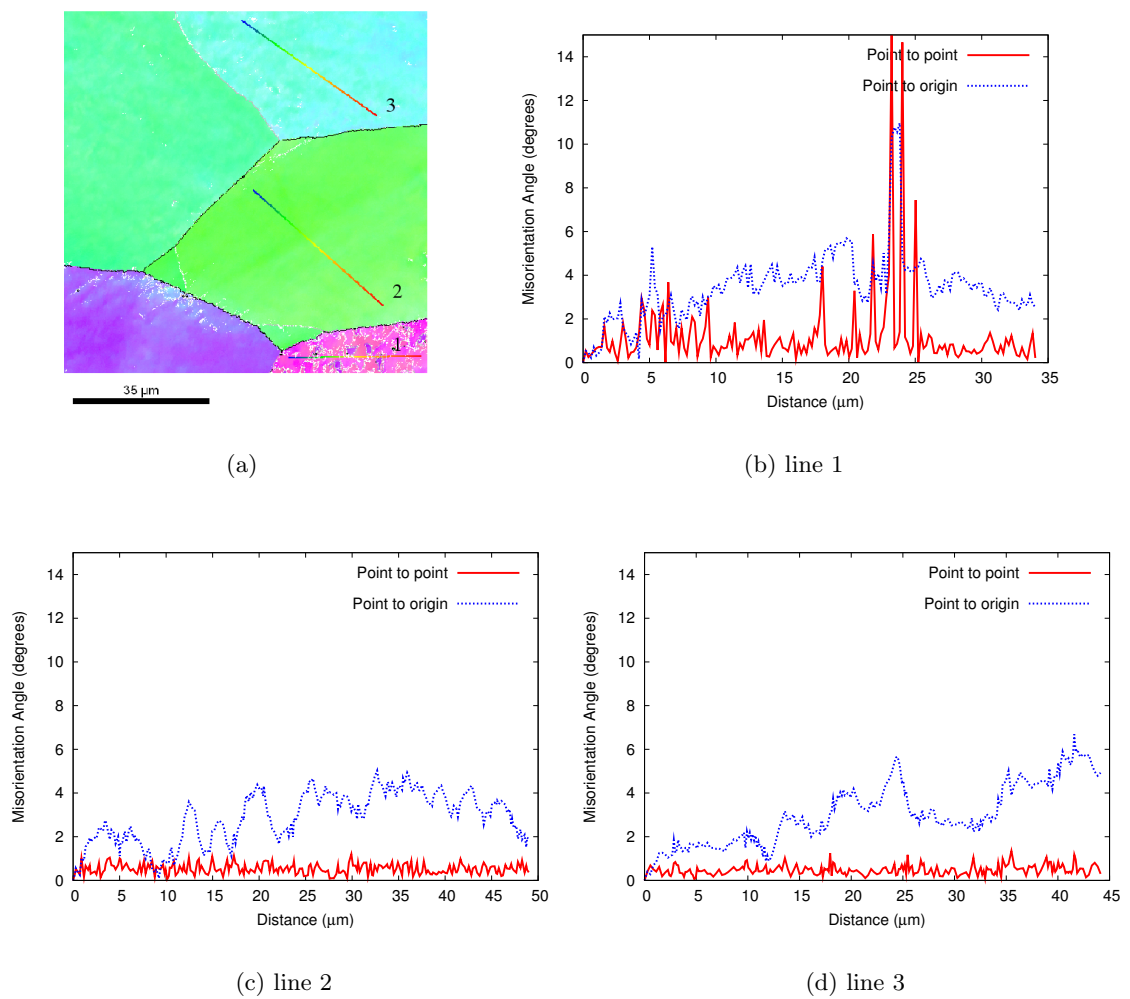
Figure III.31 : (a) Inverse pole figure [010] of 30% deformed sample and (b, c, d) Misorientations across grains

(a) 1263 nodes   (b) 8895 nodes   (c) 20161 nodes   (d) 45443 nodes
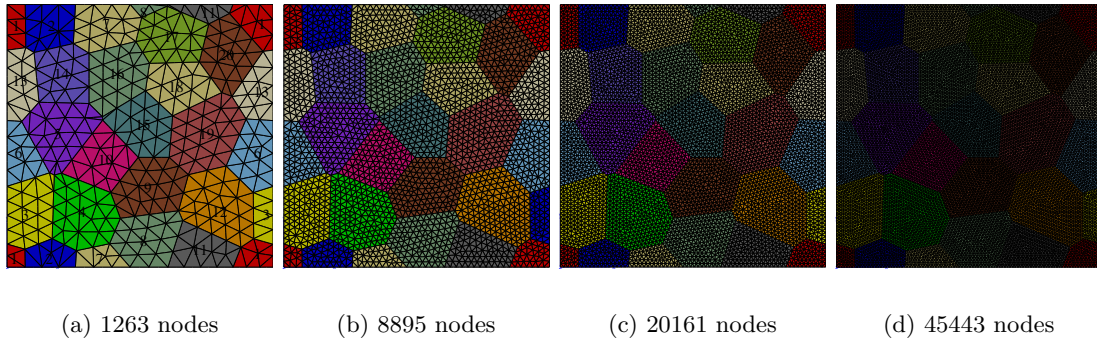
Figure III.32 : Polycrystal aggregate consisting of 20 grains with mesh refinement

Once the main features of the deformed state have been measured by EBSD, abilities of the FE model to predict them are studied in the next section.

III.4.2 Mesh Size Effect on Polycrystal Response

The presumption that 2D plane strain compression is essentially equivalent to 3D plane strain compression by comparing the stress-strain curve and the deformation textures which have been validated by (Erieau, 2004) on IF steel. Although IF steel is a BCC material, we assumed the same conclusions for aluminium (FCC material). Therefore, 2D plane strain compression can be used to simulate channel die compression test.

Since GNBs arises (by definition in the model equation) from the different activity of the slip systems on either side of the boundary leading to a creation of misorientations, the goal of the present investigation thorough mesh refinement is to investigate in-grain subdivision and inter-grain misorientations leading to the geometrically necessary boundaries (GNB). The polycrystal material used in this simulation has been assumed to have a random distribution of grain orientations with different mesh sizes, 1263 nodes, 8895 nodes, 20161 nodes and 45443 nodes, see Figure III.32. The initial texture can be seen in Figure III.33. The polycrystal model in Figure III.32, is generated using Voronoi tessellation algorithms. In this preliminary study, only 20 grains are considered with a grain around $100\mu m$ which gives 1 elements, respectively, equal to $28.0\mu m$, $14.0\mu m$, $10.0\mu m$, $6.6\mu m$ and $4.5\mu m$. A 30% height reduction plane strain compression is imposed on the aggregate. Boundary conditions are applied such that the sample deforms by compression along x2 (ND). The numerical results of the aggregate deformed under plane strain compression are discussed in the next section.

Figure III.34 shows the effect of mesh refinement on the average strain-stress response of the aggregate with GNDs introduction. The response increase with mesh refinement. It can be seen that the predictions exhibit mesh sensitivity as soon as plastic deformation occurs. This effect has been underlined in (Cheong *et al.*, 2005) for Cu polycrystal from grain less than 30 μm during tensile loadings. As GNDs build-ups are associated with gradients of slip developing at adjacent grain boundaries, the mesh-sensitive response must be linked to a significant increase in the number of GNDs relative to the SSD population. Thus mesh sensitivity is expected to increase as the grain size decreases with more slip gradients, and hence more GNDs, are generated.

Figures III.36 show the cumulated plastic deformation maps. The map of the deformed polycrystal give the grain shape changes but also an insight into the more localized

(a)   (b)
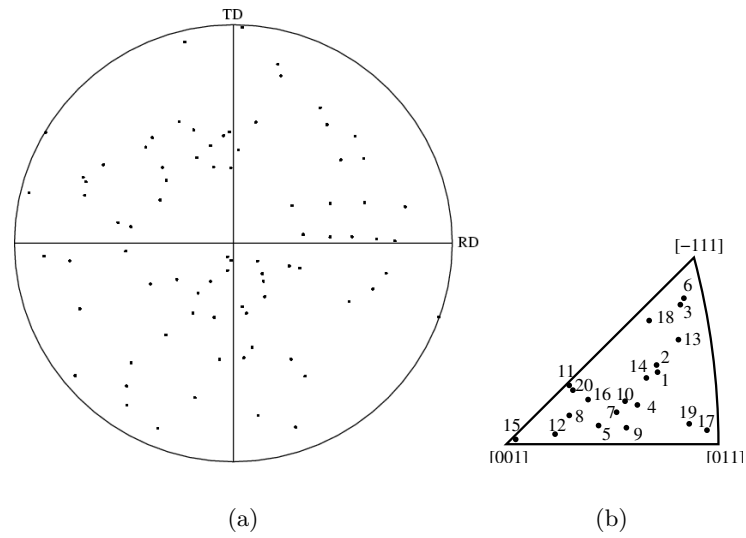
Figure III.33 : {111} pole figure and {001} inverse pole figure with corresponding grain orientation
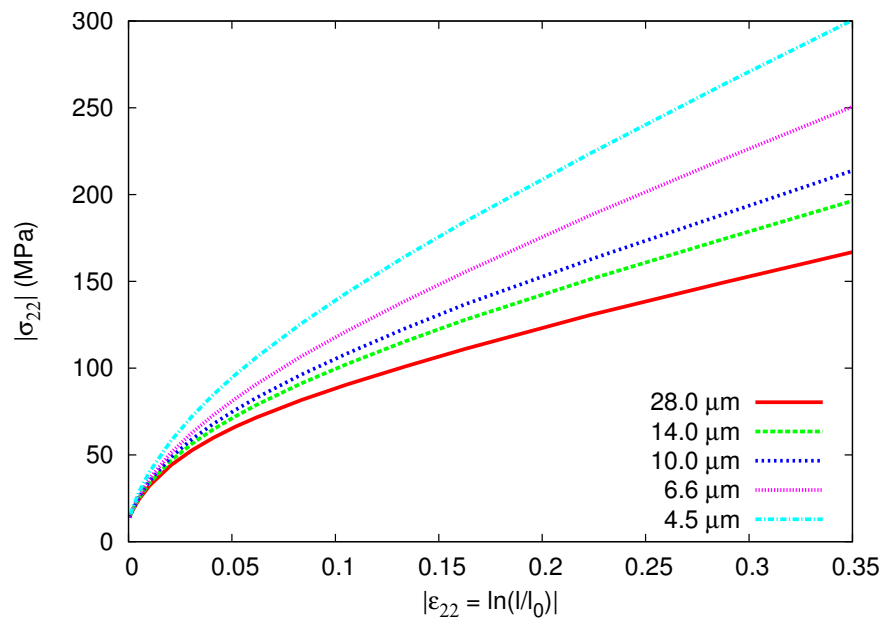
Figure III.34 : Effect of mesh refinement for 20-grain polycrystal on strain-stress response

(a)
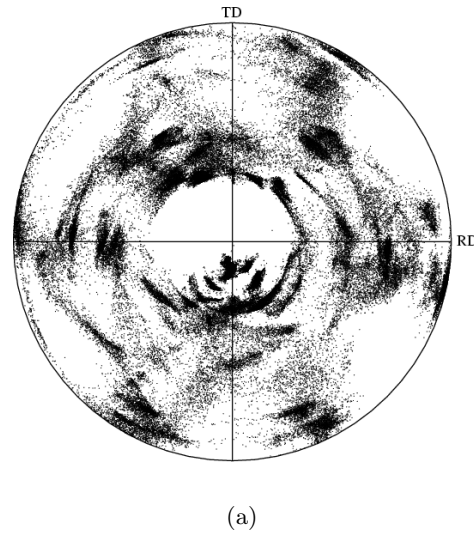
Figure III.35 : {111} pole figure of 60% height reduction aggregates

deformation heterogeneities. Grains are observed to break up into macroscopic deformation bands aligned to shear directions (40° towards the rolling direction, x1). With mesh refinement, this process leads finally to the formation of a micro-band structure as straight dense dislocation walls running parallel to each other along preferred directions. They are especially highlight in macroscopic bands observed in the first figure. This results in the multiplication of GNDs inside grains. Since GNDs accommodate lattice incompatibilities in regions where deformation is inhomogeneous, resulting in the curvature of the crystal lattice, Figure III.37 shows the cumulative lattice rotation from the initial orientation. The rotation bands are localized in the same grains that the deformation bands. Only one grain is almost free of heterogeneities, grain 15, where its orientation is closed to [001] directions. In order to quantify the grain rotation, the total rotation for the initial rotation are plotted in Figure III.38. For the coarsest mesh, the grain rotations are mainly between 5° and 20°. With mesh refinement, the rotation spreads in the small rotations as many as in large rotations. The mesh refinement increases the lattice orientation heterogeneities. Another method to establish the lattice heterogeneities consist in observing the accumulated slip. As seen in Figure III.39, slip activation is heterogeneous inside grain which means lattice rotation occurs inside grains.

As well known, boundary conditions affected the macroscopic behavior of the polycrystalline aggregates and the grain heterogeneities. The grains closed to the boundary may exhibit different features. In order to verify this assertion, same previous conditions are applied for a 46 grains polycrystalline aggregate. The mesh size is identical to the called mesh 3. Figure III.40 shows the macroscopic response which is similar for both polycrystalline aggregates. Same macroscopic and microscopic bands are observed in both case. Similar features have been observed in both cases.

However, since the micro-bands size is limited to the element size and stress-strain response is diverging with mesh refinement, the predicted micro-bands appear more as numerical singularities than as physical heterogeneities.

(a) 1263 nodes

(b) 8895 nodes

(c) 20161 nodes

(d) 45443 nodes
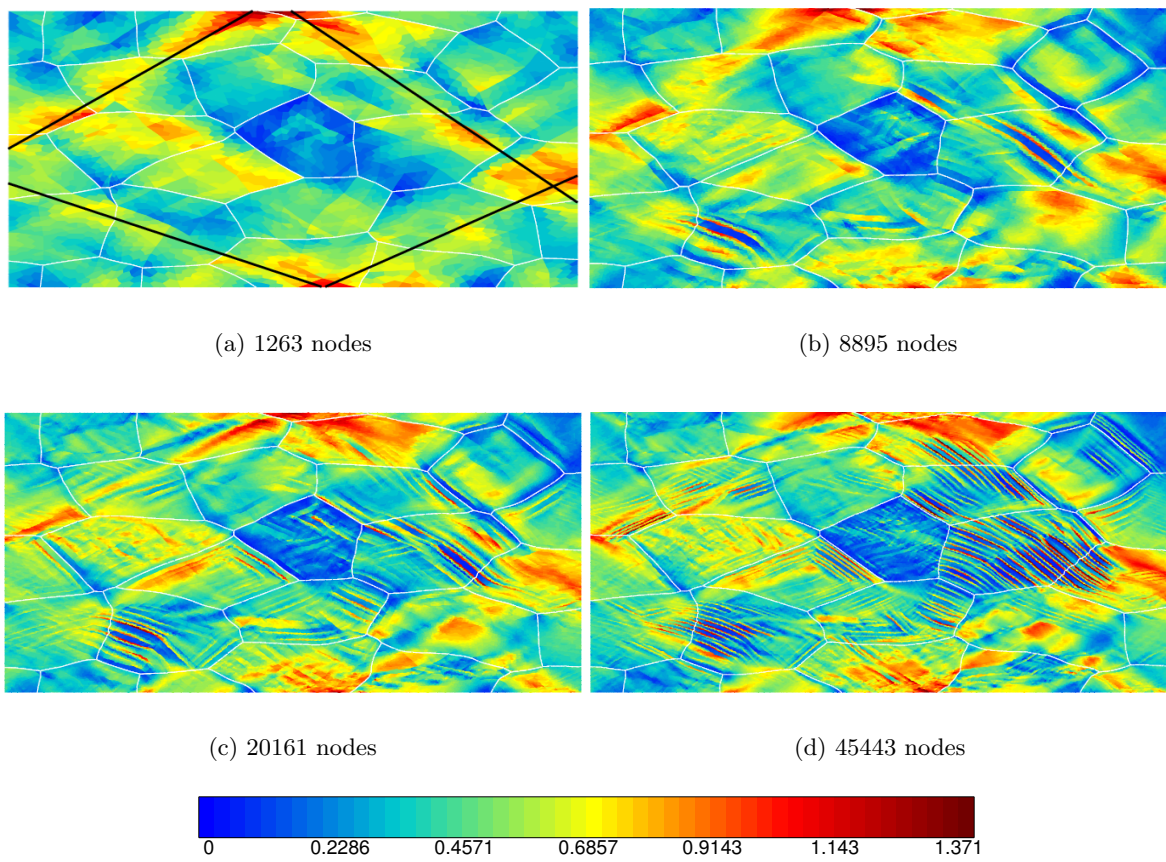
Figure III.36 : Accumulative plastic strain after $30\%s$ height reduction

(a) 1263 nodes

(b) 8895 nodes

(c) 20161 nodes

(d) 45443 nodes
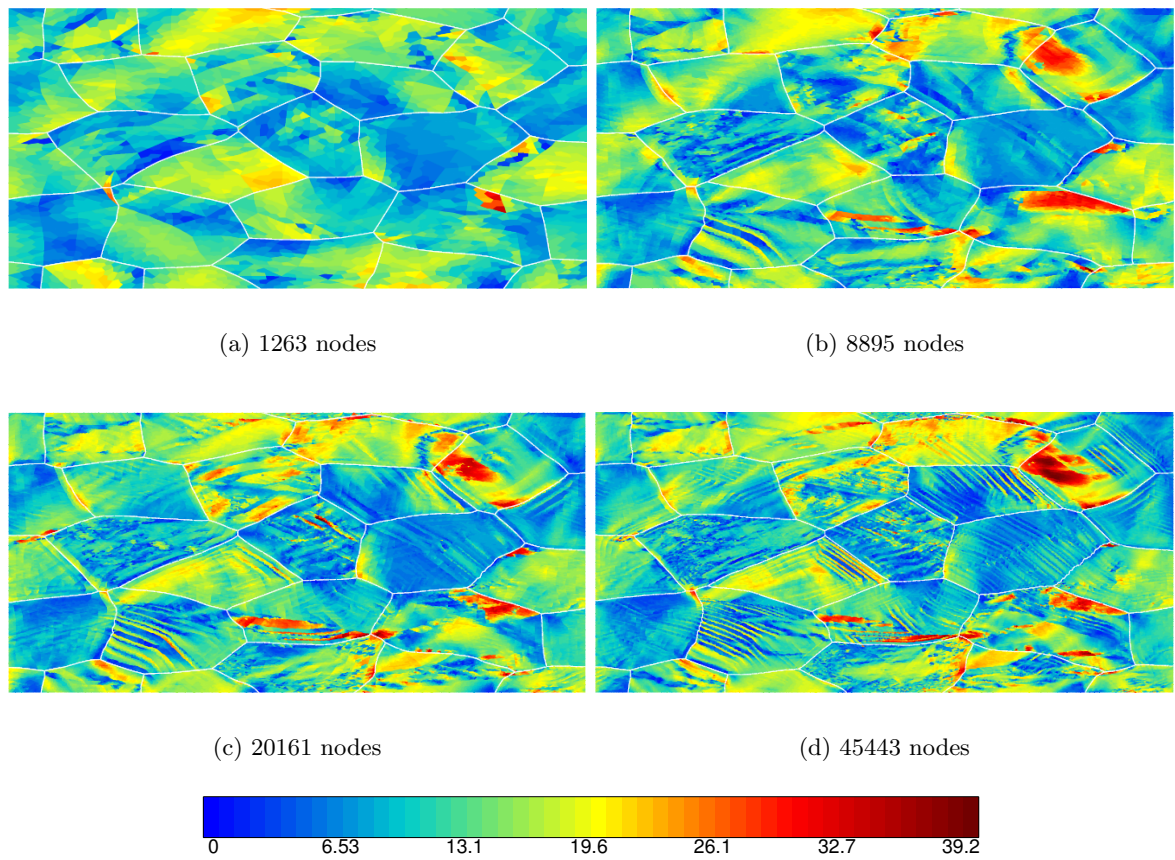
Figure III.37 : Cumulative rotation distribution after $30\%s$ height reduction
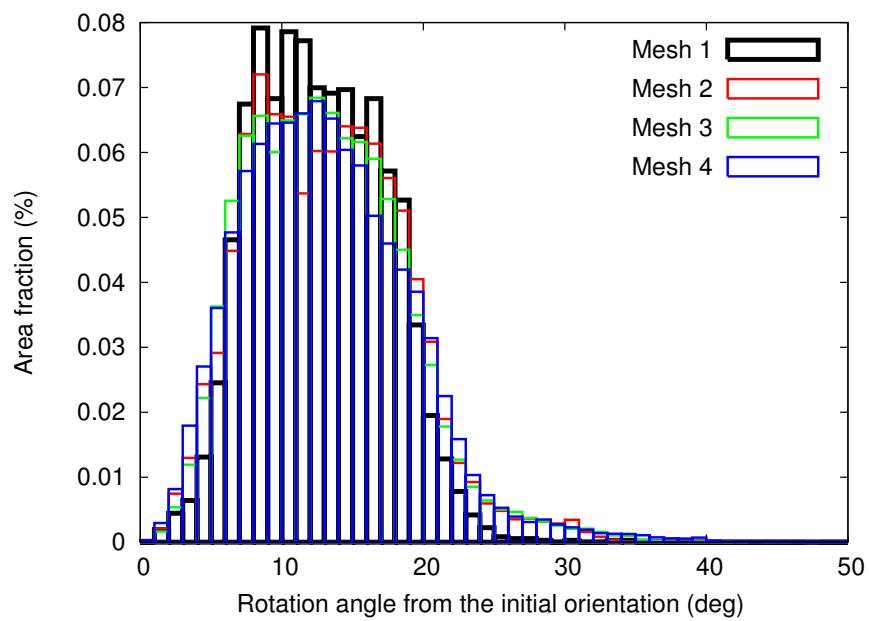
Figure III.38 : Cumulative rotation diagram after 30% height reduction

(a) 8895 nodes

(b) 4358 elements

(c) 20161 nodes

(d) 45443 nodes
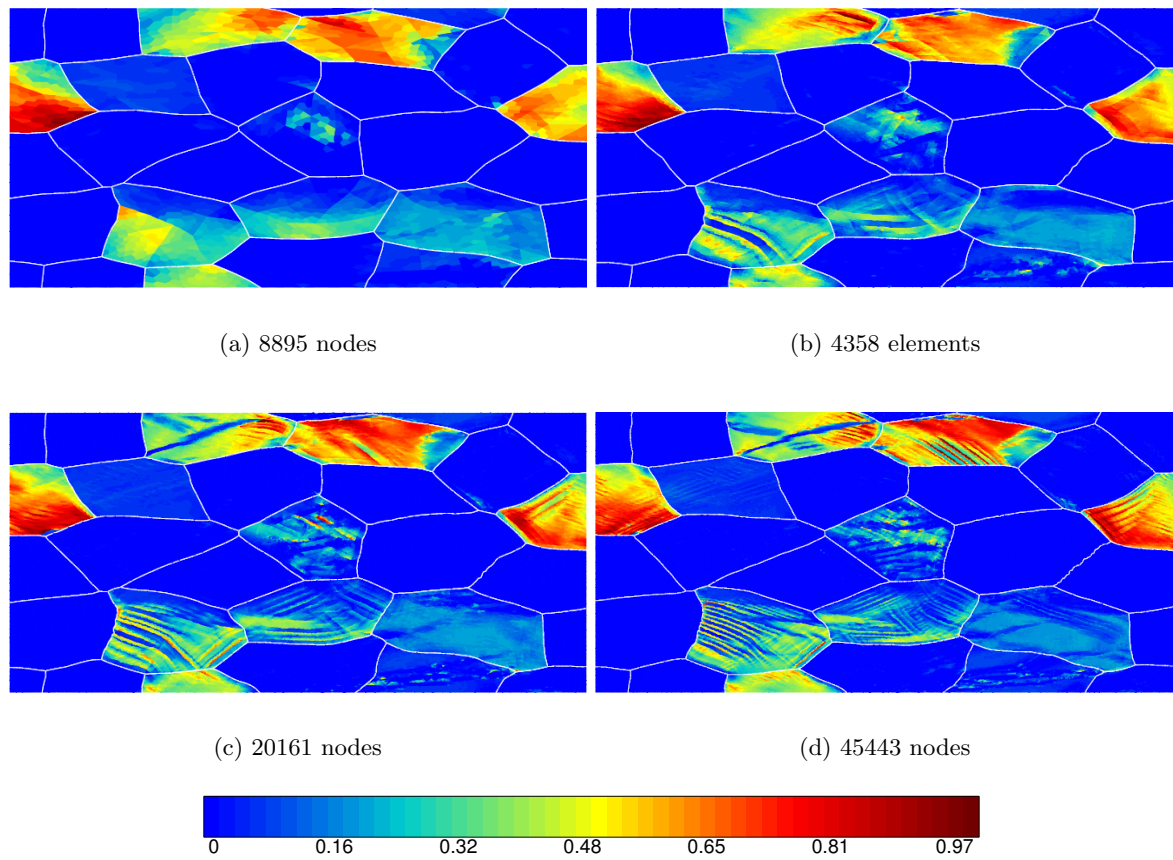
Figure III.39 : Accumulative Slip [1 1 1] {−101} after 30%*s* height reduction
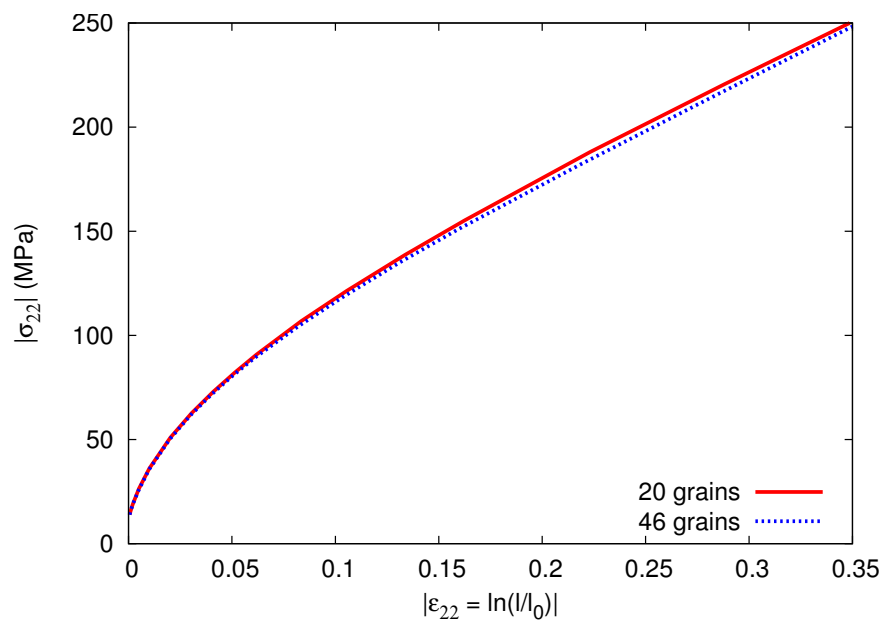
Figure III.40 : Effect of grain number on strain-stress response

(a) 46 grains   (b) 20 grains
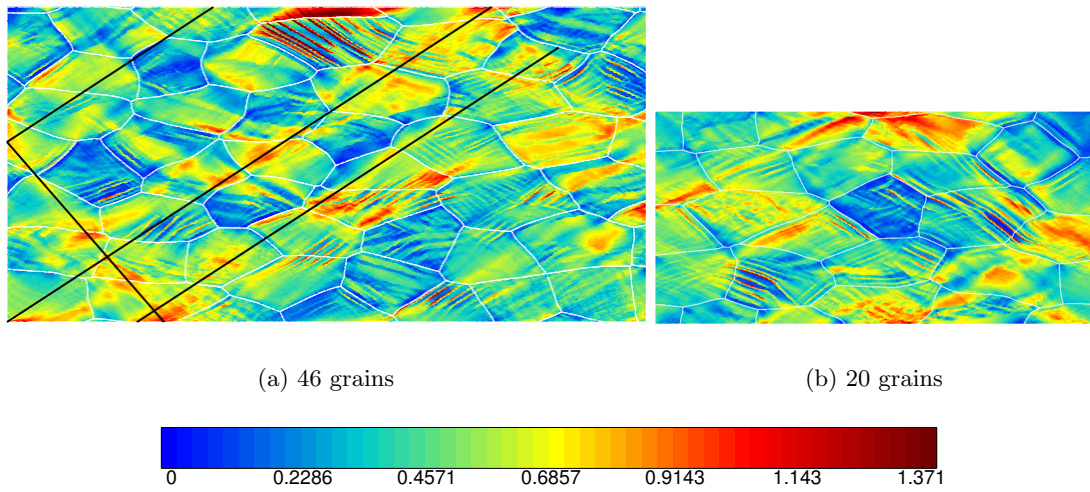
Figure III.41 : Accumulative plastic deformation after 30% height reduction

(a) 46 grains   (b) 20 grains
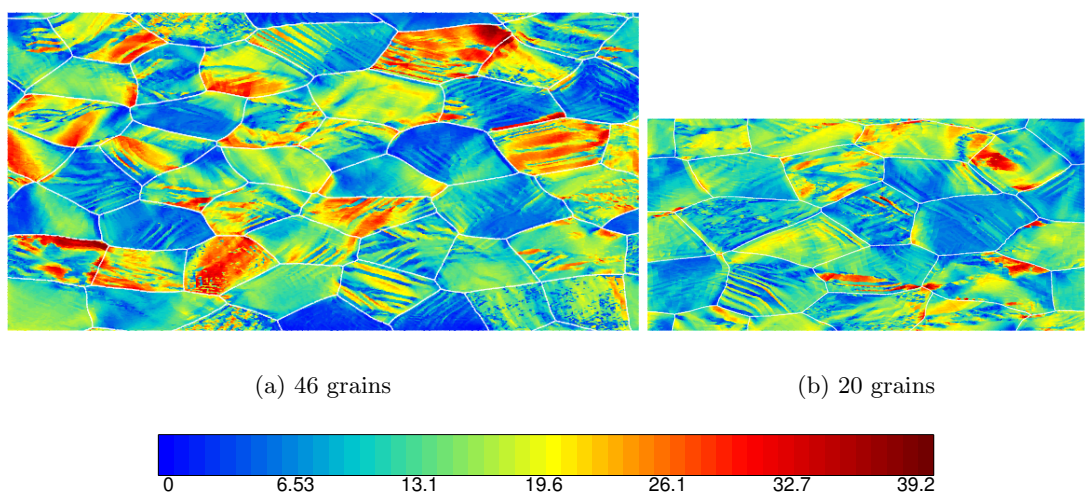
Figure III.42 : Grain rotation from initial orientation after 30% height reduction

III.4.3   Substructures Description

III.4.3.1   Introduction of a Critical Distance in Determination of Slip-Rate Gradients

During deformation, grains rotate and break into subgrains with different slip system activity. As GNDs build-ups are associated with gradients of slip-rate, the number of GNDs increase significantly inside the grains. Contrary to the second gradient and Cosserat theories, no term in the free energy penalizes their development. Therefore, the determination of slip-rate gradients with the method described in section II.4.5, is highly sensible to the mesh size. The main factors increasing this phenomenon are small grain size, large deformation and 2D modelling where strain localisations are accentuated. In order to avoid this phenomenon, a different method for evaluating gradients of slip rate have been proposed. Instead of evaluating slip-rate gradients over one element, an internal distance which defines the neighbouring gauss points included in the determination of slip-rate gradients with the Gauss point of interest has been introduced.

In order to solve the evolutionary laws for the GNDs density, the term $A = \dot{\gamma}^{\alpha} \mathbf{n}^{\alpha} \mathbf{F}^{p}$ is calculated at the Gauss point of interest as well as at neighbouring ones defined by the critical distance. Then, this field of A is then used to compute curl(A) at that point through a linear interpolation in which further gauss points from the gauss point of interest have less weight in interpolation function determination. There is no extrapolation at the nodes using the shape functions of the element. Consequently, the curl(A) is then used to evaluate the evolution of each individual GND as per Eq. II.76.

With this method, the key point is the determination of the critical distance, which is linked to the GNDs spread from the grain boundary (Liang and Dunne, 2009). In a first approach, the critical distance is decided to be the average element size.

III.4.3.2   Inter and Intragranular Heterogeneities

The polycrystal material used in this simulation has been assumed to have a random distribution of grain orientations with two different mesh sizes, 20366 nodes, 45885 nodes, see Figure III.43. The initial texture can be seen in Figure III.33. Only 10 grains are considered with a grain around $100\mu m$ which gives 1 elements, respectively, equal to $4.7\mu m$ and $3.2\mu m$. A 30% height reduction plane strain compression is imposed on the aggregate. Boundary conditions are applied such that the sample deforms by compression along x2 (ND). As few grains are considered, free boundary conditions are considered on left and right sides of the polycrystal.

Figure III.44 shows the effect of mesh refinement on the average strain-stress response of the aggregate with GNDs introduction. The response hardly decrease with mesh refinement. The average strain-stress response converges although the mesh is finer than in the first study. As in the first study, macroscopic bands crossing the grains are seen in Figure III.45 for both cases. Furthermore, the rotation bands are also similar as seen in Figure III.46. Therefore, the predicted microscopic and macroscopic behaviour are independent of the mesh size.

After making sure mesh independency, the same simulation for the finer mesh is run without GNDs introduction. Accumulated grain rotation after 30% height reduction resulting from both simulation are compared in Figure III.47. Grains 1 and 2 exhibited small rotation angle when GNDs are introduced compared to the case where only SSDs are accounted for.

(a) 20366 nodes   (b)   (c) 45885 nodes
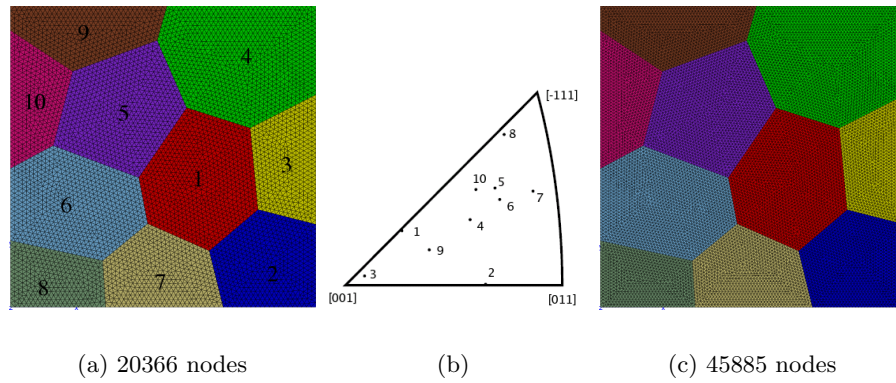
Figure III.43 : Polycrystal aggregate consisting of 10 grains with mesh refinement
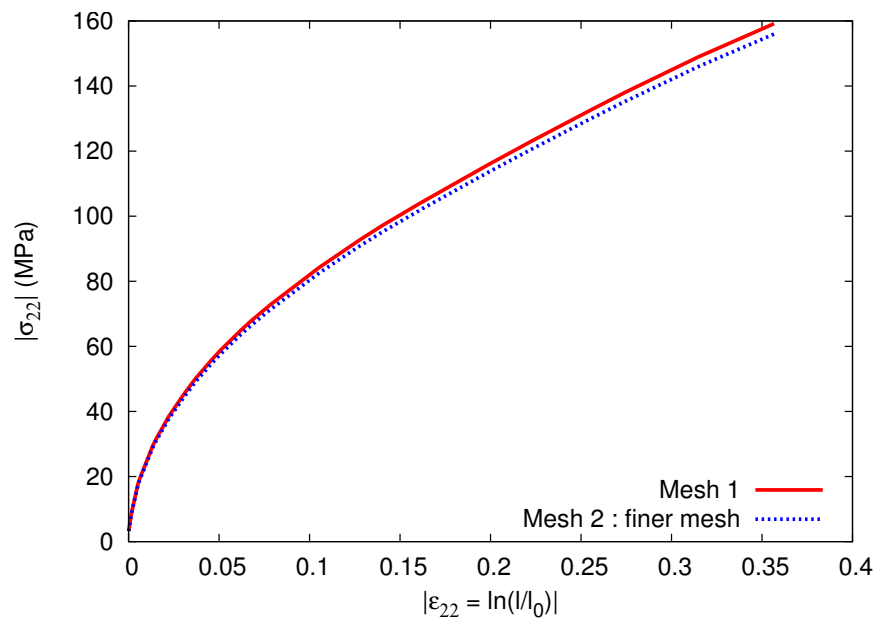
Figure III.44 : Effect of mesh refinement for 10-grain polycrystal on strain-stress response

(a) 20366 nodes   (b) 45885 nodes
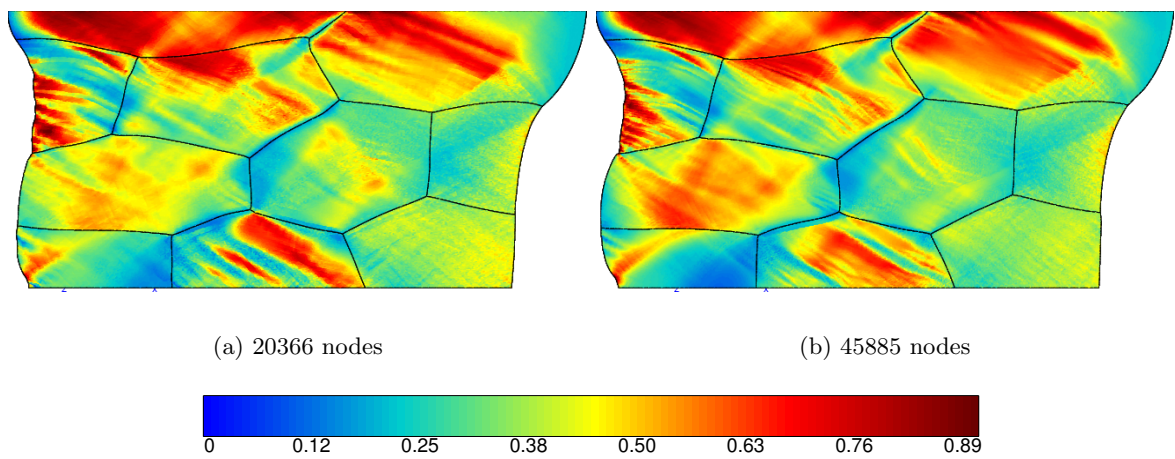
Figure III.45 : Accumulated plastic strain after $30\%s$ height reduction

(a) 20366 nodes   (b) 45885 nodes
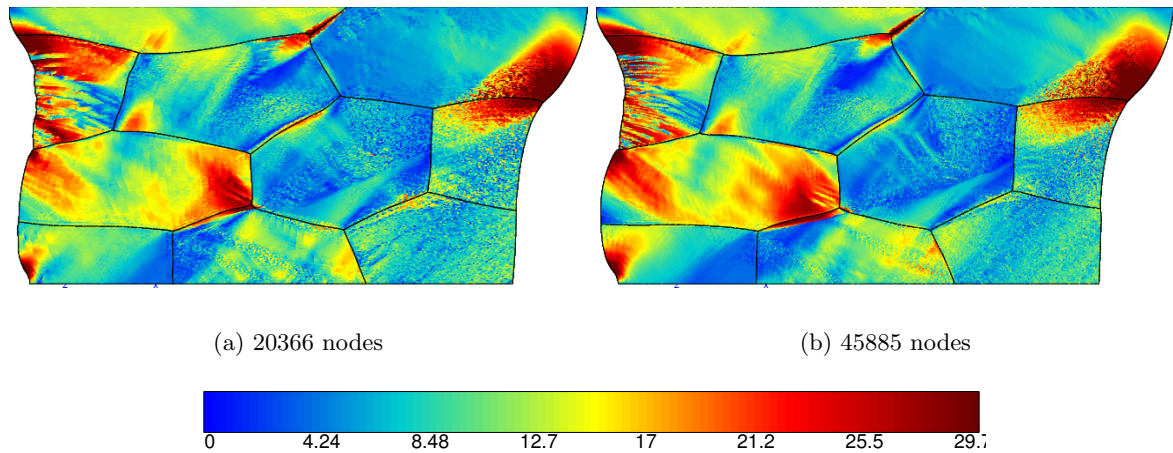
Figure III.46 : Accumulated grain rotation after 30% height reduction

(a) only SSDs   (b) SSDs + GNDs
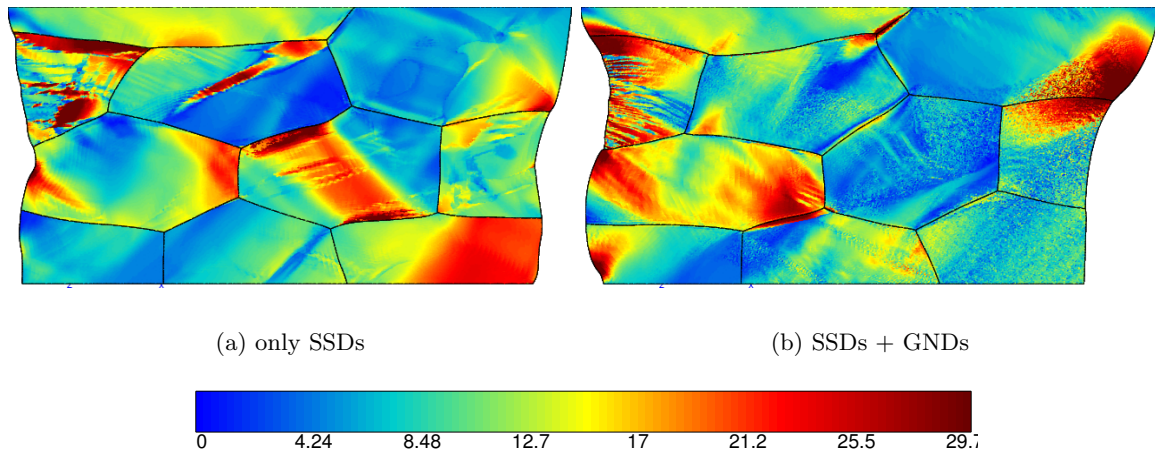
Figure III.47 : Accumulated grain rotation after 30% height reduction

GNDs inibits the misorientation development. This observation is confirmed by the diagram of accumulated grain rotation shown in Figures III.48 (a) (b) where large discrepancies are exhibited for Grains 1 and 2. However, inside other grains, rotation angle is more important when GNDs are taken into account as seen Figure III.48, excepted for Grain 4 where identical results are found in both cases. In addition to the diagram of rotation for each grain, the [001] initial inverse pole figure is shown in Figure III.48 in order to link the initial orientation and the rotation angle observed. No evidence of any relation has been deduced since the neigbhouring grain interaction play a significant role in heterogeneities development.

Inter and intragranular heterogeneities formation such grain fragmentation have been exhibited in this study. However, although the mesh has been refined to leads to GNBs development, no such observation has been done.

III.4.3.3 Cell Size Predictions

As dislocations gather in deformation induced boundaries, the grains become subdivided into smaller regions of different, but similar orientations. The cell size depends on the deformation level, the grain orientation and the loading path. However, in the literature,

(a) Grain 1

(b) Grain 2

(c) Grain 3

(d) Grain 4

(e) Grain 5

(f) Grain 6

(g) Grain 7

(h) Grain 8

(i) Grain 9

(j) Grain 10
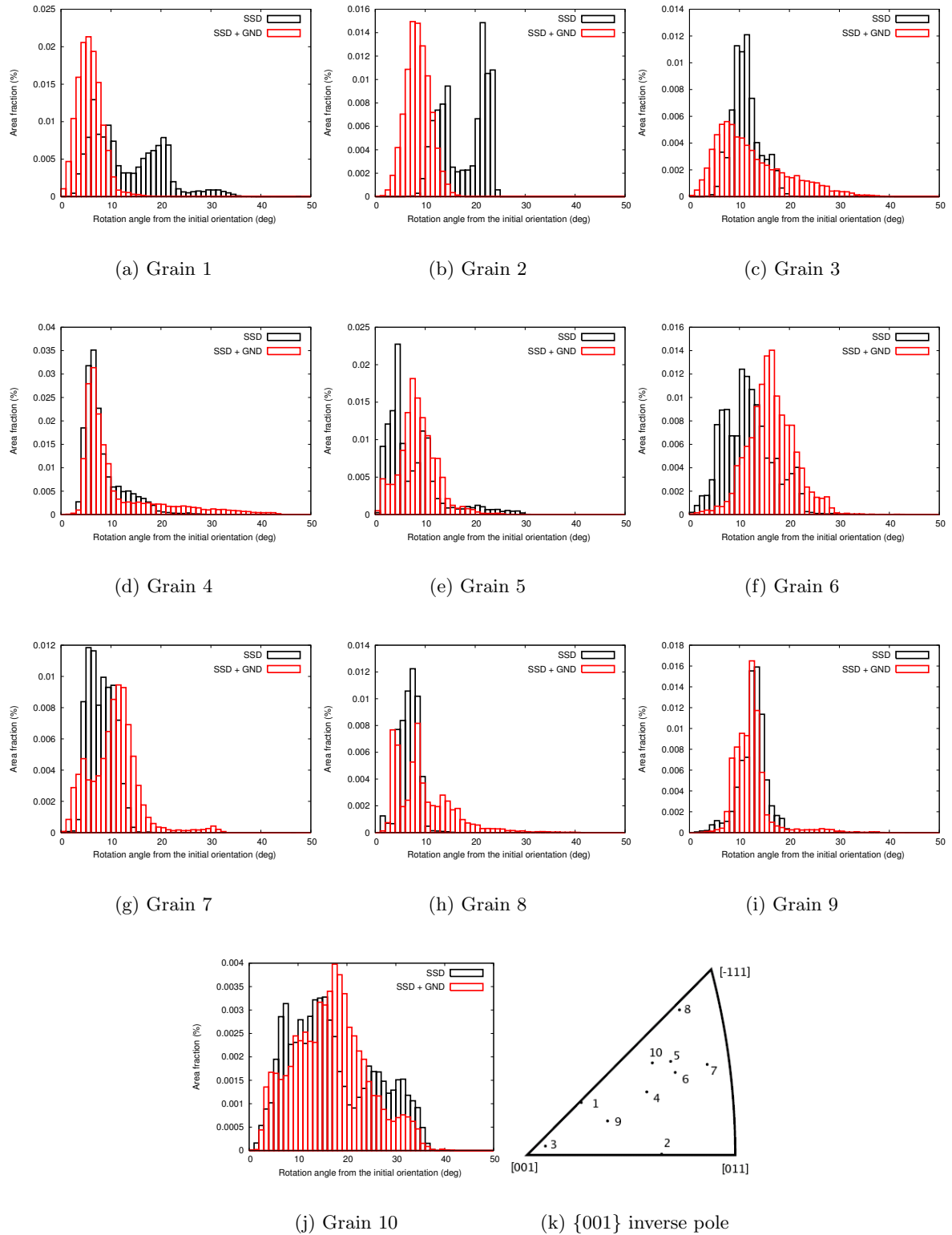
(k) {001} inverse pole

Figure III.48 : Cumulative rotation diagrams after 30% height reduction for each grain
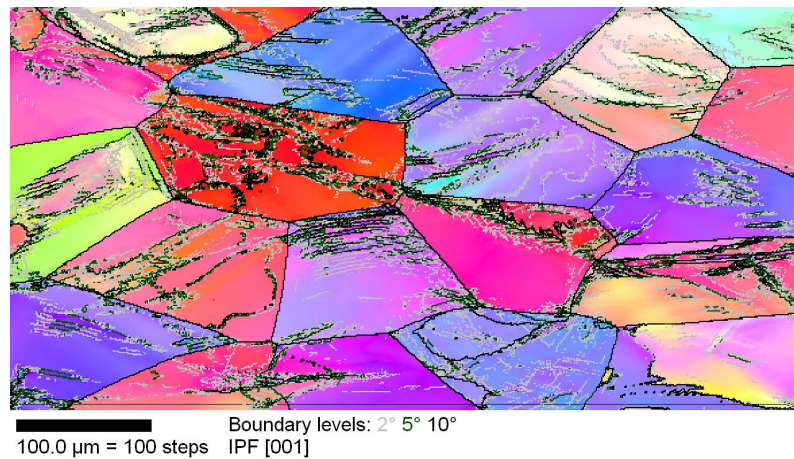
Figure III.49 : Inverse Pole Figure [001] of a 40% height reduction numerical polycrystal
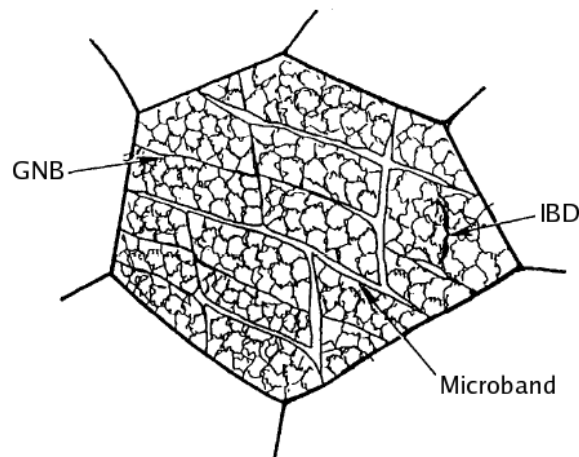
Figure III.50 : Sketch of a grain which is subdivided in cell blocks. Each cell block is further divided in cells (Winther *et al.*, 1997)

for pure aluminium, cell size has always found less than $3\mu m$ while the smallest mesh used in the FE simulation are more than $4\mu m$. Consequently, the cells can not be discretely described in the microstructure as seen in Figure III.50 even if or not the model would take into account the physical phenomena responsible their formation. For instance, no discrete cell is observed in the inverse pole figure of a 40% height reduction numerical polycrystal (without taking into account GNDs), only grain fragmentation are underline through the misorientation line superimposed on the inverse pole figure. Therefore, the cell size will be determined statistically as for dislocations. Cell shape have been found to vary with the grain orientation from TEM observations. However, cell shape will be considered as homogeneous for all grain orientation.

In order to determine the cell size (distance between IDBs, see Figure III.4), the Holt relation is used. Since IDBs form by the random trappings of glide dislocations, only statistically stored dislocation are taken into accounts,

$$d_{IDB} = \frac{K}{\sqrt{\rho_{SSD}}} \qquad \qquad \text{(III.6)}$$

where K is fitted on experimental curves, K=8.5. IDBs distance for each gauss point is plotted
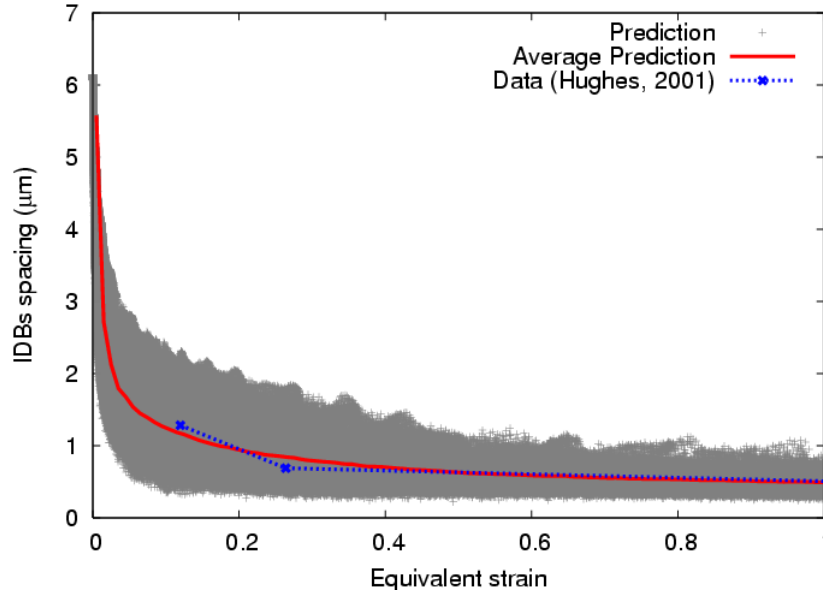
(a)

Figure III.51 : Predicted (mesh 4) and experimental IDBs spacing

in Figure III.51(a). A large range of IDBs distance is found for the same equivalent strain with different grain orientation. The associated average curve is found to have the same shape than the experimental evolution. Since GNBs form between regions with one or more different operating slip systems to accommodate the accompanying difference in lattice rotation, only geometrically necessary dislocations are taken into accounts in the Holt relation,

$$d_{GNB} = \frac{K}{\sqrt{\rho_{GND}}} \tag{III.7}$$

where K = 8.5. In Figure III.52(a), the predicted GNBs distance is in good agreement for equivalent stress higher than 0.25. From experimental data (Hughes, 2001), GNBs distance starts from $3.4\mu m$ for a strain at 0.12 to end at $0.25\mu m$ for a strain at 1.0. Therefore, GNBs distance compared to the mesh size can be considered as a statistical value for low strain.

III.5   Conclusions

Electronic microscopy measurements have been done to quantify the formation of the subgrain structures during deformation. However, substructure formation has not been observed in most of grains. A critical distance has been introduced in the determination of slip rate to avoid mesh dependency. The single crystal model has been employed to predict grain size effect in aluminium 3D polycrystal aggregates. Computations modelling of an aluminium aggregate under plane strain compression deformation, have underlined the formation of different deformation bands morphologies and grain splitting occurrence. The model based on dislocation densities as internal variables, developed in the framework of finite deformation and implemented in the Finite Element Method, is able to capture the main characteristics of different inhomogeneities from the determination of the active and latent slip systems, and also from the quantification of their dislocation densities such as grain fragmentation.
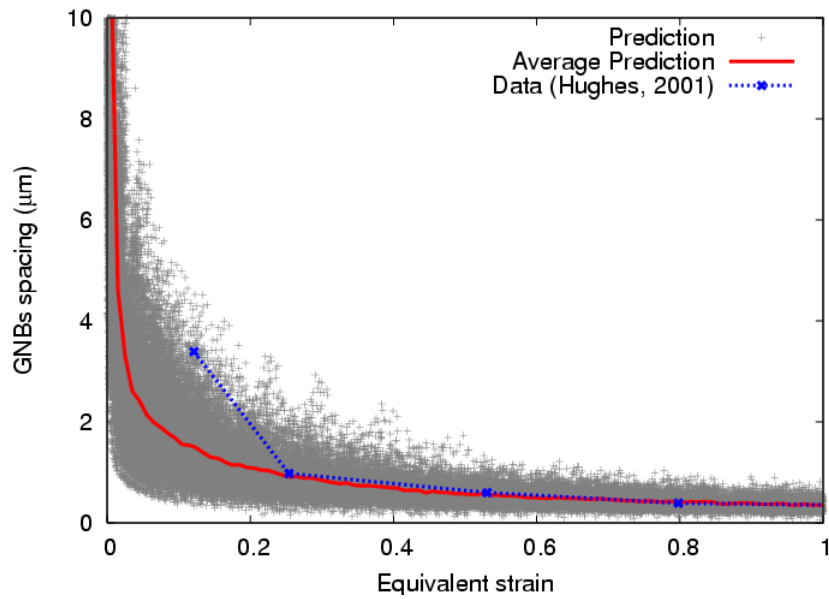
(a)

Figure III.52 : Predicted (mesh 4) and experimental GNBs spacing

The model has not been able to describe explicitly the GNBs and IDBs but statically. Good agreement is found with literature results for cold-rolled aluminium.

References

AKEF A. AND DRIVER J.H. (1991). *Orientation splitting of cube-oriented face-centered cubic-crystals in plane-strain compression.* Materials Science and Engineering A, vol. 132, pp 245–255.

ANANTHAN V.S., LEFFERS T., AND HANSEN N. (1991). *Cell and band structures in cold-rolled polycrystalline copper.* Materials Science and Technology, vol. 7 n° 12, pp 1069–1075.

BALASUBRAMANIAN S. AND ANAND L. (2002). *Elasto-viscoplastic constitutive equations for polycrystalline fcc materials at low homologous temperatures.* Journal of the Mechanics and Physics of Solids, vol. 50 n° 1, pp 101–126.

BARBE F., DECKER L., JEULIN D., AND CAILLETAUD G. (2001a). *Intergranular and intragranular behavior of polycrystalline aggregates. Part 1: F.E. model.* International Journal of Plasticity, vol. 17, pp 513–536.

BARBE F, FOREST S, AND CAILLETAUD G (2001b). *Intergranular and intragranular behavior of polycrystalline aggregates. Part 2: Results.* International Journal of Plasticity, vol. 17 n° 4, pp 537–563.

BECKER R., BUTLER J.F., HU H., AND LALLI L.A. (1991). *Analysis of an aluminum single-crystal with unstable initial orientation (001) [110] in channel die compression.* Metallurgical Transactions A-Physical Metallurgy and Materials Science, vol. 22 n° 1, pp 45–58.

BESSON J., LE RICHE R., FOERCH R., AND CAILLETAUD G. (1998). *Object–Oriented Programming Applied to the Finite Element Method. Part II: Application to Material Behaviors.* Revue Européenne des éléments finis, vol. 7, pp 567–588.

BURGERS W.G. AND SNOEK J.L. (1935). *Lattice distortion and coercive force in single crystals of nickel-iron-aluminium.* Physica, vol. 2, pp 1064–1074.

BUTLER J.F. AND HU H. (1989). *Channel die compression of aluminum single-crystals.* Materials science and engineering a-structural materials properties microstructure and processing, vol. 114, pp L29–L33.

CHEONG K.S., BUSSO E.P., AND ARSENLIS A. (2005). *A study of microstructural length scale effects on the behaviour of FCC polycrystals using strain gradient concepts.* International Journal of Plasticity, vol. 21 n° 9, pp 1797–1814.

CRUSSARD C., AUBERTIN F., FAOUL B., AND WYON G. (1950). *Polygonization in strongly deformed metals.* Progress in Metal Physics, vol. 2, pp 193–202.

DRIVER J. AND CHENAL B. (2000). *Écrouissage d'alliages d'aluminium.* Technical report, Les techniques de l'ingénieur M230.

DRIVER J.H., JENSEN D.J., AND HANSEN N. (1994). *Large-strain deformation in aluminium crystals with rolling texture orientations.* Acta Metallurgica et Materialia, vol. 42 n° 9, pp 3105–3114.

ERIEAU P. (2004). *Étude des hétérogénéités de déformation et leur lien avec la recristallisation d'alliages industriels.* Thèse de Doctorat, Ecole Centrale de Paris.

FAHRAT C. AND ROUX F.-X. (1991). *A Method of Finite Element Tearing and Interconnecting and its Parallel Solution Algorithm.* Int. J. Numer. Meth. Engng, vol. 32, pp 1205–1227.

FEYEL F. (1998). *Application du calcul parall'ele aux mod'eles 'a grand nombre de variables internes.* Thèse de Doctorat, École Nationale Supérieure des Mines de Paris.

GEORGE P.L. (1997). *Improvements on Delaunay-based three-dimensional automatic mesh generator.* Finite elements in analysis and design, vol. 25 n° 3-4, pp 297–317.

GODFREY A., JENSEN D.J., AND HANSEN N. (1998a). *Slip pattern, microstructure and local crystallography in an aluminium single crystal of brass orientation {110}< 112 >.* Acta Materila, vol. 46 n° 3, pp 823–833.

GODFREY A., JENSEN D.J., AND HANSEN N. (1998b). *Slip pattern, microstructure and local crystallography in an aluminium single crystal of copper orientation< 111 >.* Acta Materiala, vol. 46 n° 3, pp 835–848.

GREWEN J. AND HUBER H. *Annealing textures.* Riederer.

HAMMELRATH H., BULTER J.F., HU H., AND LUCKE K. (1991). *Deformation and recrystallization textures of rolled and channel-die compressed high-purity copper.* Textures and Microstructures, vol. 14 n° Part 3-4, pp 629–634. 9th international conf. on textures of materials (ICOTOM 9), Avignon, Sept 17-21, 1990.

HANSEN N. (1977). *Effect of grain-size and strain on tensile flow-stress of aluminium at room-temperature.* Acta Metallurgica, vol. 25 n° 8, pp 863–869.

HANSEN N. AND HUANG X. (1998). *Microstructure and flow stress of polycrystals and single crystals.* Acta Materialia, vol. 46 n° 5, pp 1827–1836.

HOSFORD W.F., FLEISCHER R.L., AND BACKOFEN W.A. (1971). *Tensile deformation of aluminum single crystals at low temperatures.* Acta Metallurgica, vol. 8, pp 187–199.

HUANG X. AND HANSEN N. (1997). *Grain orientation dependence of microstructure in aluminium deformed in tension.* Scripta Materialia, vol. 37 n° 1, pp 1–7.

HUGHES D.A. (2001). *Microstructure evolution, slip patterns and flow stress.* Materials Science And Engineering A-Structural Materials Properties Microstructure And Processing, vol. 319 n° Sp. Iss. SI, pp 46–54.

HUGHES D.A. AND HANSEN N. (1997). *High angle boundaries formed by grain subdivision mechanisms.* Acta Materialia, vol. 45 n° 9, pp 3871–3886.

HUGHES D.A. AND HANSEN N; (2000). *Microstructure and strength of nickel at large strains.* Acta Materialia, vol. 48 n° 11, pp 2985–3004.

HURLEY P.J., BATE P.S., AND HUMPHREYS F.J. (2003). *An objective study of substructural boundary alignment in aluminium.* Acta Materialia, vol. 51 n° 16, pp 4737–4750.

HURLEY P.J. AND HUMPHREYS F.J. (2003). *The application of EBSD to the study of substructural development in a cold rolled single-phase aluminium alloy.* Acta Materialia, vol. 51 n° 4, pp 1087–1102.

KANIT T., FOREST S., GALLIET I., MOUNOURY V., AND JEULIN D. (2003). *Determination of the size of the representative volume element for random composites: statistical and numerical approach.* International Journal of Solids and Structures, vol. 40, pp 3647–3679.

LAUG P. AND BOROUCHAKI H. (2003). *Interpolating and meshing 3D surface grids.* International Journal for Numerical Methods in Engineering, vol. 58 n° 2, pp 209–225. 3rd Symposium on Trends in Unstructured Mesh Generation, Dearborn, Aug 01-04, 2001.

LIANG H. AND DUNNE F. P. E. (2009). *GND accumulation in bi-crystal deformation: Crystal plasticity analysis and comparison with experiments.* International Journal of Mechanical Sciences, vol. 51 n° 4, pp 326–333.

LIU Q., JENSEN D.J., AND HANSEN N. (1998). *Effect of grain orientation on deformation structure in cold-rolled polycrystalline aluminium.* Acta Materialia, vol. 46 n° 16, pp 5819–5838.

MACKENZIE J. K. (1964). *The distribution of rotation axes in a random aggregate of cubic crystals.* Acta Metallurgica, vol. 12, pp 223–225.

MAURICE C., DRIVER J.H., AND TOTH L.S. (1992). *Modelling high-temperature rolling textures of FCC metals.* Textures and Microstructures, vol. 19 n° 4, pp 211–227.

MERRIMAN C.C., FIELD D.P., AND TRIVEDI P. (2008). *Orientation dependence of dislocation structure evolution during cold rolling of aluminum.* Materials Science and Engineering A, vol. 494, pp 28–35.

OSIPOV N. (2007). *Génération et calcul de microstructures bainitiques, approche locale intragranulaire de la rupture.* Thèse de Doctorat, Ecole des Mines de Paris.

SIMMONS G. AND WANG H. (1971). *Single crystal elastic constants and calculated aggregates properties.* The MIT Press.

STANFORD N., DUNNE D., AND FERRY M. (2003b). *Effect of orientation stability on recrystallization textures of deformed aluminium single crystals.* Materials Science and Engineering A, vol. 348 n° 1-2, pp 154–162.

SUE P.L. AND HAVNER K.S. (1984). *Theoretical analysis of the channel die compression test .1. general-considerations and finite deformation of FCC crystals in stable lattice orientations.* Journal of the Mechanics and Physics of Solids, vol. 32 n° 6, pp 417–442.

THEYSSIER M.C., DRIVER J.H., AND CHENAL B. (1995). *Microstructural evolution of aluminum during high-temperature deformation - single-crystals in plane-strain compression.* Journal de Physique IV, vol. 5 n° C3, pp 177–185.

WILKINSON A.J. (2001). *A new method for determining small misorientations from electron back scatter diffraction patterns.* Scripta Materialia, vol. 44 n° 10, pp 2379–2385.

WINTHER G., HUANG X., GODFREY A., AND HANSEN N. (2004). *Critical comparison of dislocation boundary alignment studied by TEM and EBSD: technical issues and theoretical consequences.* Acta Materialia, vol. 52 n° 15, pp 4437–4446.

WINTHER G., JENSEN D.J., AND HANSEN N. (1997). *Dense dislocation walls and microbands aligned with slip planes - Theoretical considerations.* Acta Materialia, vol. 45 n° 12, pp 5059–5068.

ZEGHADI A. (2005). *Effet de la morphologie tri-dimensionnelle et de la taille de grain sur le comportement mécanique d'agrégats polycristallins.* Thèse de Doctorat, Ecole des Mines de Paris.

Chapter -IV-

Stored Energy : Fraction of Plastic Work

Contents

IV.1   Introduction

The mechanical energy W provided to the specimen during deformation can be decomposed into an elastic energy W_e and non-elastic one W_p, expended on plastic deformation. The inelastic energy W_p can also be decomposed into the energy dissipated as a heat Q and a complementary part E_s stored in the material,

$$W = W_e + W_p = W_e + Q + E_s \qquad\qquad\text{(IV.1)}$$

Most of the work expended in deforming a metal is given out as heat and only a small amount remains as energy stored in the material. However, As explained in the following chapter, the stored energy is a key factor in microstructure transformation, it provides the source for recovery and recrystallisation during thermo-mechanical processes and drives the kinetics of grain or subgrain boundaries. For instance, the energy difference between grains supplies a driving force sufficient to overcome the pressure form by the curvature of the boundary, which migrates into the grain with the higher stored energy. Therefore, in order to simulate thermo-mechanical processes, there is a need to identify the stored energy at any local point. In the common case of deformation at ambient temperatures, the stored energy is derived from the point defects and dislocations generated during deformation. Extensive researches have been carried out on the fraction of plastic work converted into heating, commonly, denoted by β and consequently, the fraction into stored energy. The first experiments investigating this issue are (Farren and Taylor, 1937, Taylor and Quinney, 1937). Experimental measures on the stored energy presents a main difficulty; its low amount compared to traditional energy controlling microstructure changes as phase transformation. Various experimental methods have been used to determine the stored energy; calorimetry (Verdier *et al.*, 1997, Scholz *et al.*, 1999), resistivity (Verdier *et al.*, 1997), X-ray diffraction (Rajmohan and Szpunar, 1999, Borbely *et al.*, 2000, Mohamed and Bacroix, 2000). Most of the experimental techniques to measure the stored energy have been compared by (Hodowany *et al.*, 2000). (Taylor and Quinney, 1937) assumed the ratio of plastic work converted into heating is a constant around 0.9 in deformed material while (Bever *et al.*, 1973, Wolfenden and Appleton, 1968) reported the ratio depends on the strain. This chapter is concerned with the fraction of the plastic work converted into stored energy. We examine the status of the common assumption that β is a constant with regard to the thermodynamic foundations and dislocation theory under consideration. Since plastic deformation is heterogeneous in nature, the stored energy distribution in numerically deformed sample is examined.

IV.2   Stored Energy Formulations

IV.2.1   Dislocation-Based Formulation

The final dislocation structure of a cold worked metal is heterogeneous. Dislocations in even moderately worked metals are kinked and jogged and are found in pile-ups and in intricate tangles. The energy of a dislocation depends on its environment and is for example highest in a pile-up and lowest when in a cell or subgrain wall. Therefore, The total energy of a microstructure is discretized in several contribution of the following term (Biermann *et al.*, 1993):

$$E_D = E_{dis} + E_{het} + E_{mean} \qquad\qquad\text{(IV.2)}$$

where E_{dis} is the energy of statistically stored dislocations, E_{het} is the energy arising from their heterogeneous distribution corresponding to the elastic energy associated with the long-range stress fields in cellular dislocation structures and E_{mean} accounts for the polycrystalline

nature of the material. It is well-known that the grain size of a material often affects its mechanical properties. E_{mean} represents the elastic energy contribution of means stresses of the polycrystal due to the heterogeneity of deformation between grains.

First, the energy of a dislocation has been expressed from the dislocation theory. If the energy of the dislocation core is neglected and if isotropic elasticity is assumed, then the energy E^{unit} per unit length of dislocation line is given approximately by (Humphreys and Hatherly, 2004):

$$E_{unit} = \frac{\mu b^2 f(\nu)}{4\pi} ln(\frac{R}{R_0}) \tag{IV.3}$$

where μ is the shear modulus, b is the Burgers vector, R is the upper cut-off radius (usually taken to be the separation of dislocations ($\rho^{-1/2}$)), R_0 is the inner cut-off radius(usually taken as between b and 5b) ans $f(\nu)$ is a function of Poisson's ratio ν.

$$f(\nu) \quad = \quad 1 \quad \text{for screw dislocation} \tag{IV.4}$$

$$f(\nu) \quad = \quad \frac{1}{1-\nu} \quad \text{for edge dislocation} \tag{IV.5}$$

Therefore, for a dislocation density ρ_S the stored energy is then

$$E_{dis} = \rho_S E_{unit} = \rho_S \frac{\mu b^2 f(\nu)}{4\pi} ln(\frac{R}{R_0}) \tag{IV.6}$$

Since E_{mean} accounts for the polycrystalline nature of the material, E_{mean} will be approximated from the geometrically necessary dislocation density as expressed for E_{dis}. Assuming there is no interaction between SSDs and GNDs,

$$E_{mean} = E_G = \rho_G E_{unit} = \rho_G \frac{\mu b^2 f(\nu)}{4\pi} ln(\frac{R}{R_0}) \tag{IV.7}$$

where E_{unit} corresponds to the energy of one dislocation.

Since dislocation theory shows that the energy of a dislocation depends on its environment, $E_{dis} = \rho E_{unit}$ is a significant approximation. E_{het} is introduced to take into account the complex dislocation distribution. For instance, E_{het} is negative in deformed structure associated with wall, cell structure. However, an evaluation of this term is complex. Consequently, in a first approach, the total energy of a microstructure is approximated by

$$E_d = E_{dis} + E_{het} + E_{mean} \approx c\mu b^2(\rho_S + \rho_G) \tag{IV.8}$$

where c is a constant of ≈ 0.5

IV.2.2 Thermodynamic Formulation

IV.2.2.1 Fundamentals of Continuum Thermodynamics

The crystallographic model formulation is expressed within a thermodynamics framework resulting in a expression of the stored energy function only of the internal variables. The local form of the law of thermodynamics requires the verification of the energy balance equation,

$$\rho\dot{e} = \sigma : \mathbf{L} + \rho r - \nabla.\mathbf{q} \tag{IV.9}$$

where e is the internal energy density, L is the strain rate tensor, σ the Cauchy stress tensor, r is the heat supply and $\mathbf{q}$ the heat flux vector. The local form of the second law of thermodynamics gives the entropy principle

$$\rho\dot{s} + \nabla.(\frac{\mathbf{q}}{T}) - \frac{\rho r}{T} \geq 0 \tag{IV.10}$$

Replacing Eq. IV.9 in Eq. IV.10, the Clausius-Duhem inequality is obtained

$$-\rho(\dot{\epsilon} - T\dot{s}) + \sigma : \mathbf{L} - \frac{\mathbf{q}}{T}.\nabla T \geq 0 \tag{IV.11}$$

The Helmholtz free energy density $\psi = \varepsilon - T$ is introduced

$$-\rho(\dot{\psi} + s\dot{T}) + \sigma : \mathbf{L} - \frac{\mathbf{q}}{T}.\nabla T \geq 0 \tag{IV.12}$$

The term $-\rho(\dot{\psi} + \eta\dot{T}) + \sigma : \mathbf{L}$ represent the internal dissipation while $-\frac{\mathbf{q}}{T}.\nabla T$ represents the thermal dissipation.

As explained in chapter II, the gradient of the transformation $\mathbf{F}$ is decomposed in

$$\mathbf{F} = \mathbf{F}^e.\mathbf{F}^p \tag{IV.13}$$

The elastic strain and stress tensor are defined with respect to the isoclinic configuration:

$$\mathbf{E}^e = \frac{1}{2}(\mathbf{F}^e\mathbf{F}^{eT} - \mathbf{I}), \quad \mathbf{T} = det\mathbf{F}^e\mathbf{F}^{e-1}\sigma\mathbf{F}^{e-T} \tag{IV.14}$$

The power power of internal forces makes the link between the different stress tensors:

$$\sigma : \mathbf{L} = \sigma : (\dot{\mathbf{F}}\mathbf{F}^{-1}) = \frac{1}{det\mathbf{F}^e}(\mathbf{T} : \dot{\mathbf{E}}^e + (\mathbf{F}^{eT}.\mathbf{F}^e.\mathbf{T}) : (\dot{\mathbf{F}}^p.\mathbf{F}^{p-1})) \tag{IV.15}$$

The free energy depends on the state variables (E^e, T, additional internal variable s^α) and the Clausius-Duhem inequality takes now the form

$$\rho(\frac{\mathbf{T}}{\rho det\mathbf{F}^e} - \frac{\partial s}{\partial \mathbf{E}^e}) : \dot{\mathbf{E}}^e - \rho(s + \frac{\partial \psi}{\partial T})\dot{T} - \rho(\frac{\partial \psi}{\partial s^\alpha} - S_T^\alpha) : \dot{s}^\alpha - \frac{q}{T}.\nabla T \geq 0 \tag{IV.16}$$

where s are internal variables. The exploitation of the second principle provides the state laws

$$\mathbf{T} = \rho_i \frac{\partial \psi}{\partial E^e} \tag{IV.17}$$

$$S_T^\alpha = \rho_i \frac{\partial \psi}{\partial s^\alpha} \tag{IV.18}$$

$$s = -\frac{\partial \psi}{\partial T} \tag{IV.19}$$

IV.2.2.2 Thermodynamics Single Crystal Framework

In the single crystal model, the critical resolved shear stress in a slip system α is given by

$$\tau^\alpha = S_T^\alpha \tag{IV.20}$$

where S_T^α are internal slip system variables which represent additive slip resistances associated with non-directional hardening mechanisms.

$$S_T^\alpha = \lambda\mu b^\alpha \sqrt{\sum_{\beta=1}^{N} h^{\alpha\beta}(\rho_e^\beta + \rho_s^\beta)} \tag{IV.21}$$

where ρ_e^β, ρ_s^β are respectively the edge and screw dislocation densities. The slip system hardening S_T^α variables can be explicitly expressed in terms of their corresponding thermodynamical state variables, denoted s^α which are adimensional variables.

$$s^\alpha = b^\alpha \sqrt{\sum_{\beta=1}^{N} h^{\alpha\beta}(\rho_e^\beta + \rho_s^\beta)}$$

Consequently,

$$S_T^\alpha = \lambda\mu s^\alpha \tag{IV.22}$$

As underlined in the previous section, the relations between the slip system internal variables and their corresponding state variables, by definition, are linked through the free energy derivatives,

$$S_T^\alpha = \rho\frac{\partial\psi}{\partial s^\alpha} \tag{IV.23}$$

Consequently, the inelastic part of the free energy function can be expressed in terms of s^α as follows:

$$\psi = \frac{1}{2}\rho\lambda\mu s^{\alpha 2} \tag{IV.24}$$

From Eq.IV.12, the intrinsic dissipation is

$$\Phi = -\rho(\dot{\psi} + \eta\dot{T}) + \sigma : \mathbf{L}^p \tag{IV.25}$$

Replacing the expression of ψ in Eq.IV.12

$$\Phi = -\sum_{\alpha=1}^{N}(\lambda\mu s^\alpha \dot{s}^\alpha) - \eta\dot{T} + \sigma : \mathbf{L}^p \tag{IV.26}$$

From Eq. II.21, $\mathbf{L}^p = \sum_{\alpha=1}^{N}\dot{\gamma}^\alpha\mathbf{P}^\alpha$

$$\Phi = -\sum_{\alpha=1}^{N}(\lambda\mu s^\alpha \dot{s}^\alpha) - \eta\dot{T} + \sigma : \sum_{\alpha=1}^{N}\dot{\gamma}^\alpha\mathbf{P}^\alpha \tag{IV.27}$$

which gives, with $\tau^\alpha \approx \sigma : \mathbf{P}^\alpha$

$$\Phi = -\sum_{\alpha=1}^{N}(\lambda\mu s^\alpha \dot{s}^\alpha) - \eta\dot{T} + \dot{\gamma}^\alpha\tau^\alpha \tag{IV.28}$$

$$= -\sum_{\alpha=1}^{N}(S_T^\alpha \dot{s}^\alpha) - \eta\dot{T} + \dot{\gamma}^\alpha\tau^\alpha \tag{IV.29}$$

The intrinsic dissipated energy for an associated crystallographic model is given by the difference between the plastic work and the internal dissipation due to non-directional and directional (i.e. kinematic) hardening mechanisms. Since the plastic work is,

$$E_p = \int_0^t \sum_\alpha (\dot{\gamma}^\alpha\tau^\alpha)dt \tag{IV.30}$$

therefore, the stored energy is expressed as

$$E_t = \int_0^t \sum_\alpha (S_T^\alpha \dot{s}^\alpha)dt \tag{IV.31}$$

Table IV.1 : Euler angles (Bunge notation) with 0.5° misorientation from tensile axis

Orientation	ϕ_1 (deg.)	θ (deg.)	ϕ_2 (deg.)
[111]	54.8	135.01	180.0
[100]	0.4	10.0	0.0
[112]	61.1	69.7	281.0

IV.3   Stored Energy Predictions

Three quantities are proposed to evaluate the stored energy:

- based on dislocation theory:

$$E_d = 0.5\mu b^2 (\rho_S + \rho_G)$$

- based on thermodynamic consideration:

$$E_t = \int_0^t \sum_\alpha (S_T^\alpha \dot{s}^\alpha) dt$$

- based on a ratio of the plastic work:

$$E_p = \int_0^t \sum_\alpha (\dot{\gamma}^\alpha \tau^\alpha) dt$$

### IV.3.1   Stored Energy of Single crystals

Firstly, the three stored energy quantities are calculated for the Al single crystals used in the model calibration (chapter II). Their orientation are recalled in Table IV.3.1. The stored energy evolutions with strain for the three single crystals are shown in Figure IV.1. As seen in this figure, the stored energies and plastic work evolutions are strongly dependent on crystal orientation. Both stored energies and plastic work increase with strain for the three crystal orientation. However, the stored energies seem to saturate with strain while the plastic work rate increases. Fraction of stored energies in the plastic work are shown in Figure IV.2. This fraction decrease in both cases, as found in (Wolfenden and Appleton, 1968) where the ratio of stored to expended energy for all the specimens tested was found to decrease with increasing strain. The fraction calculated from thermodynamic considerations varies between 3% and 26% while in the case where stored energy is evaluated from dislocation theory, it varies between 0.5% and 8%.

IV.3.2   Overall Stored Energy in polycrystal Aggregates

Both stored energies measures and plastic work have been evaluated for the previous simulations of chapter II.

IV.3.2.1   GNDs effects on Stored Energy Distribution

Plastic work and stored energies distributions are shown in Figures IV.3, IV.4 and IV.5. The plastic work and the stored energies do not present the same distribution in the polycrystal aggregate. Stored energies distributions are more localised at the grain boundaries than the plastic work. However, in all cases, the localisations at grain boundaries are more significant when GNDs are included.
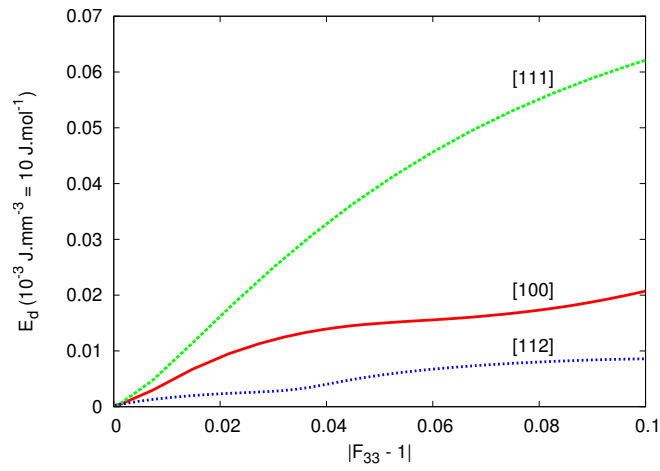
(a) E_d
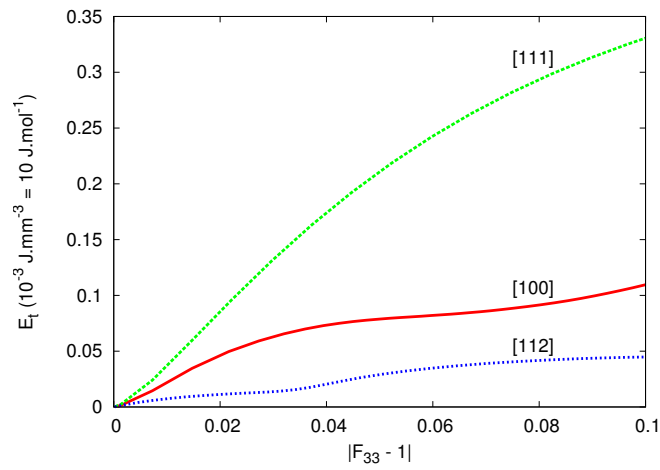
(b) E_t
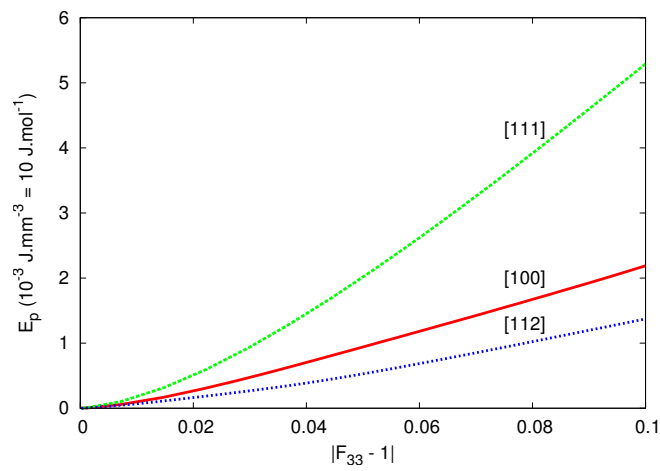
(c) E_p

Figure IV.1 : Stored energy evaluated from (a) the dislocation theory and (b) the thermodynamics formulation and (c) plastic work evaluated during an uniaxial tensile tests, E_p

(a) E_d/E_p

(b) E_t/E_p

Figure IV.2 : Fraction of stored energies in plastic work during an uniaxial tensile tests

(a) with only SSDs   (b) with SSDs and GNDs

0.261   1.2   2.13   3.07   4.01   4.95   5.88   0.328   6.81   13.3   19.8   26.2   32.7   39.2 (Jmm^{-3})

Figure IV.3 : Plastic work distribution after 10% height reduction

(a) with only SSDs   (b) with SSDs and GNDs

0.005933   0.015577   0.02522   0.034864   0.044507   0.054151   0.0637   0.018109   0.088622   0.15913   0.22965   0.30016   0.37067   0.441 (Jmm^{-3})

Figure IV.4 : Stored energy evaluated from dislocation theories distribution after 10% height reduction

| (a) with only SSDs | (b) with SSDs and GNDs |

Figure IV.5 : Stored energy evaluated from the thermodynamics formulation after 10% height reduction

IV.3.2.2 Grain Size Effect on Global Stored Energy

The effect of grain size on the stored energy measures is shown in this section. It can be seen in Figure IV.6 that the stored energy evolutions are non-linear and increase with considering GNDs. A smaller grain size increase all stored energy measures. The stored energy fractions of the plastic work are shown in Figure IV.7. They are also increasing with decreasing the grain size.

IV.3.2.3 Variability of Stored Energy in Microstructure

The annealing behaviour of a deformed metal is dependent not only on the overall stored energy, but more importantly on its spatial distribution. On a local scale, inhomogeneity of stored energy will affect the nucleation of recrystallisation, and larger scale heterogeneity will influence the growth of the new grains. In order to study accurately the stored energy variation in polycrystalline microstructure, the plastic work and stored energy distributions are calculated from a previous study done in the section III.4.3.2 where the mesh size was small. As seen in Figure IV.8, the stored energy and the plastic work distributions exhibit similar features. However, the localisation at grain boundary is more significant in case of the stored energy measure.

The ratio between the average plastic work and stored energy estimated from the dislocation theory and from thermodynamic consideration over the whole structure is shown in Figure IV.9. In both cases, the fractions depend on the strain. Nevertheless, the fraction becomes constant for strain greater than 0.3. In this situation, the stored energy calculated from thermodynamic considerations represent about 5% of the plastic work while the stored energy calculated from dislocation theory only 1%.

(a)

(b)

(c)

Figure IV.6 : Stored energy evaluated from (a) the dislocation theory and (b) the thermodynamics formulation and (c) plastic work evaluated during an uniaxial tensile tests

(a) E_d/E_p

(b) E_t/E_p

**Figure IV.7** : Stored energies fraction of the plastic work during an uniaxial tensile tests

(a) E_p (b) E_t

Figure IV.8 : Plastic work and stored energy distribution after 30% height reduction
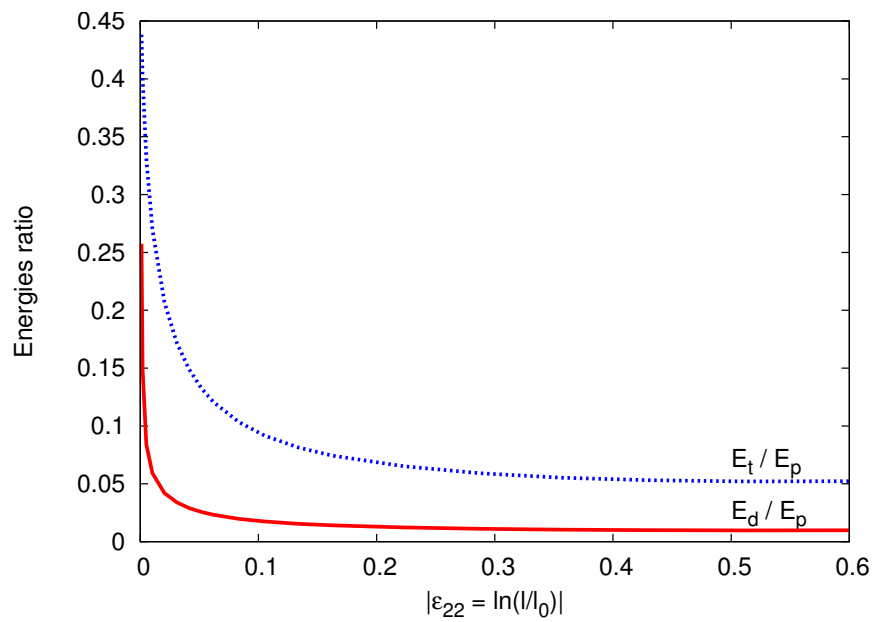

Figure IV.9 : Stored energies fraction of the plastic work during plane stress compression

IV.4   Conclusions

The aim of this chapter is to evaluate the strain energies associated with the dislocation structure and elastic strains of each single crystal grain in the FE model of the RVEs. The model is able of describing the distribution of the stored internal strain energy within the grain. The stored energy of a polycrystal has been evaluated in three ways: (a) the first one from the dislocation density predicted by the FCC single crystal model, (b) the second one from the thermodynamics formulation associated to the single crystal model and (c) the fraction of the plastic work. The measure where the stored energy is defined by a constant fraction of the plastic work is not suitable. Indeed, the results show variations of the fraction with strain. Furthermore, localisations in the stored energy distribution are different than those obtained with plastic work. The measure, proportional to the predicted total dislocation density, is found to be underestimated. The stored energy measure from thermodynamic considerations varies around 10% of the plastic work. Therefore, it seems the more suitable to describe the average stored energy evolution. In addition, since the stored energy is derived from the point defects and dislocations generated during deformation and the distribution of the stored energy measured from thermodynamic considerations is identical to the one obtained from the dislocation theory, it seems to be the more appropriate.

References

BEVER M.B., HOLT D.L., AND TICHENER A.L. (1973). *The stored energy of cold work.* Prog. Mat. Sci., vol. 17, pp 235–274.

BIERMANN H., UNGAR T., PFANNENMULLER T., HOFFMANN G., BORBELY A., AND MUGHRABI H. (1993). *Local variations of lattice-parameter and long-range internal-stresses during cyclic deformation of polycrystalline copper.* Acta Metallurgica et Materialia, vol. 41 n° 9, pp 2743–2753.

BORBELY A., DRIVER J.H., AND UNGAR T. (2000). *An X-ray method for the determination of stored energies in texture components of deformed metals; Application to cold worked ultra high purity iron.* Acta Materialia, vol. 48 n° 8, pp 2005–2016.

FARREN W.S. AND TAYLOR G.I. (1937). *The heat developed during plastic extension of metals.* Proc. Roy. Soc. London, vol. A 107, pp 422–451.

HODOWANY J., RAVICHANDRAN G., ROSAKIS A.J., AND ROSAKIS P. (2000). *Partition of plastic work into heat and stored energy in metals.* Experimental Mechanics, vol. 40 n° 2, pp 113–123.

HUMPHREYS F.J. AND HATHERLY M. (2004). *Recrystallization and Related Annealing Phenomena.* Pergamon.

MOHAMED G. AND BACROIX B. (2000). *Role of stored energy in static recrystallization of cold rolled copper single and multicrystals.* Acta Materialia, vol. 48 n° 13, pp 3295–3302.

RAJMOHAN N. AND SZPUNAR J.A. (1999). *Stored energy in can body aluminium alloy after cold rolling and stress relieving.* Materials Science and Technology, vol. 15 n° 11, pp 1259–1265.

SCHOLZ F., DRIVER J.H., AND WOLDT E. (1999). *The stored energy of cold rolled ultra high purity iron.* Scripta Materialia, vol. 40 n° 8, pp 949–954.

TAYLOR G.I. AND QUINNEY H. (1937). *The latent heat remaining in a metal after cold working.* Proc. Roy. Soc. London, vol. A 163, pp 157–181.

VERDIER M., GROMA I., FLANDIN L., LENDVAI J., BRECHET Y., AND GUYOT P (1997). *Dislocation densities and stored energy after cold rolling of Al-Mg alloys: Investigations by resistivity and differential scanning calorimetry.* Scripta Materialia, vol. 37 n° 4, pp 449–454.

WOLFENDEN A. AND APPLETON A.S. (1968). *The energy stored during the low-temperature deformation of copper and aluminum single crystals.* Acta Metallurgica, vol. 16, pp 915–925.

Chapter -V-

# Grain Boundary Description

Contents

V.1 Introduction

Materials processing, including grain growth and recrystallisation, are affected by the grain boundary properties. Consequently, a short summary of grain boundary properties is first provided in this section. Since the minimisation of stored and grain boundary energies provides the driving force for grain boundary motion, a phase field model taking into account the stored energy distribution is formulated and implemented within the continuum framework to describe the interface motion. Finally, the parameters of the free energy of the phase field model are calibrated based on published Read-Shockley boundary energy data.

V.1.1 Grain Boundary Structure

V.1.1.1 Definition

A grain boundary separates two regions of the same crystal structure but of different orientation. It is made of many crystal lattice defects with a thickness of a few atomic layers, as illustrated in Figure VI.30, where the crystal orientation changes.
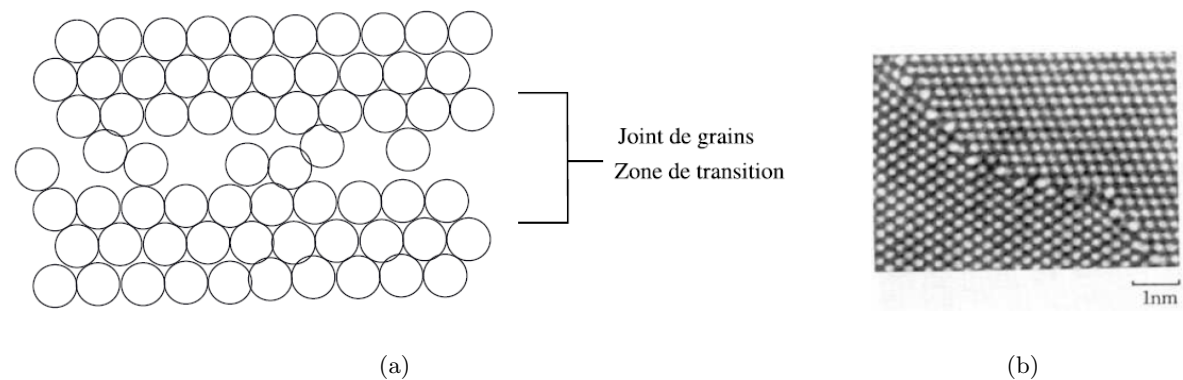
Figure V.1 : (a) Crystal disorder at the grain boundary and (b) grain boundary observed by T.E.M. (Quéré, 1987)

In order to describe mathematically a grain boundary, in a 3D case, eight parameters are necessary : three to describe its misorientation, two parameters to describe its spatial orientation by means of the normal to the grain boundary plane and three components to describe the rigid body translation vector which gives coincidence of the grains separated by the grain boundary. In 2D, the geometry of a boundary is defined by its misorientation $(\Delta\theta)$ (one degree of freedom), the orientation of the boundary plane AB with respect to one of the two crystals (ψ) (one degree of freedom), by rigid body translations parallel and perpendicular to the boundary (two degrees of freedom) required to make the two crystals coincident. There are thus four macroscopic degrees of freedom which define the geometry of the boundary.

Usually, two different types of grain boundaries can be defined: tilt and twist boundaries. A tilt grain boundary plane is parallel to the rotation axis while the twist grain boundary plane is perpendicular to the rotation axis, see Figure V.3. It is also convenient to divide grain boundaries into those whose misorientation is greater than a certain angle - high angle grain boundaries (HAGBs), and those whose misorientation is less than this angle - low angle grain boundaries (LAGBs). The angle at which the transition from low to high angle boundaries
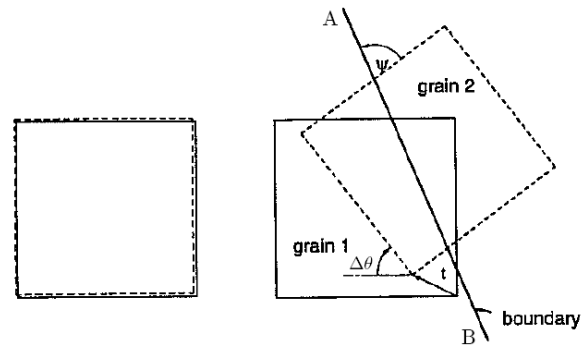
Figure V.2 :   A 2D grain boundary between two crystals misoriented by $\Delta\theta$ (Gottstein and Shvindlerman, 1999)

(a)   (b)
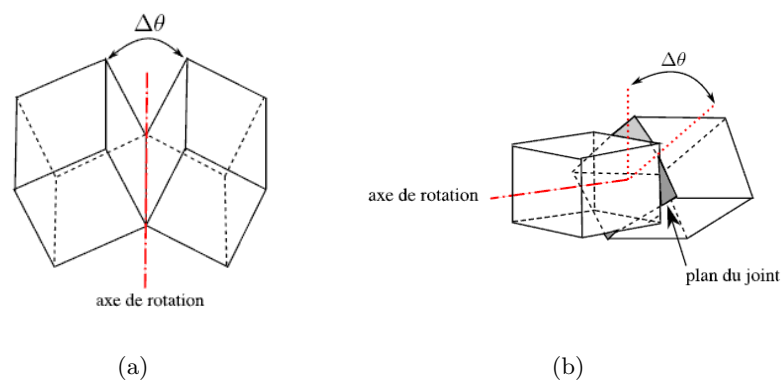
Figure V.3 : (a) a tilt and (b) a twist grain boundary
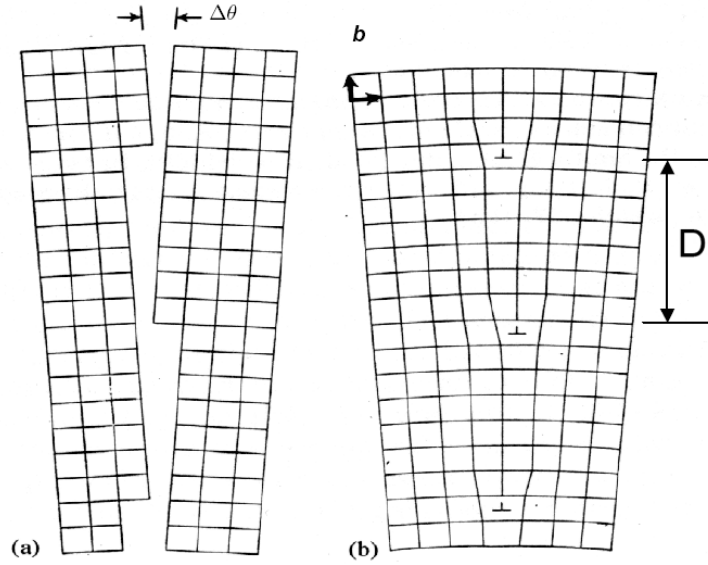
Figure V.4 : A 2D grain boundary between two crystals misoriented by θ

occurs is typically taken between $10°$ and $15°$ for cubic materials. In this work, we will consider only a 2D case. Also, the translation vector is usually not considered.

V.1.1.2 Low Angle Grain Boundaries

If the misorientation between adjacent grains is small, the boundary is entirely comprised of a periodic crystal dislocation arrangements (Burgers, 1939, Shockley and Read, 1949). Each dislocation accommodates the mismatch between the two lattices on either side of the boundary. For example, in Figure V.4, symmetric tilt grain boundaries consist of a single set of parallel edge dislocations of Burgers vector b, where the dislocation spacing D decreases with increasing rotation angle $\Delta\theta$. The corresponding dislocation density is given by:

$$1/D = 2\sin(\Delta\theta/2) \approx \Delta\theta/b \tag{V.1}$$

V.1.1.3 High Angle Grain Boundaries

For grain boundary angle greater than $15°$, the dislocation representation from Equation V.1 is not longer valid. However, there are orientation relationships, where crystallographic planes continue through the grain boundary from one crystal to an other and where there are common atomic positions of both adjacent lattices. Such lattice points are called coincidence sites. Since both crystal lattices are periodic, the coincidence sites must also be periodic, i.e. they also define a lattice, the coincidence site lattice (CSL), see Figure V.5. As a measure of the density of coincidence sites or for the size of the elementary cell of the CSL, the quantity Σ is defined as following:

$$\Sigma = \frac{\text{volume elementary cell of CSL}}{\text{volume elementary cell of crystal lattice}} \tag{V.2}$$

Table V.1 shows a list of Σ boundaries.

Table V.1 :   Rotation axes and angles for coincidence site lattices of Σ < 31 (Humphreys and Hatherly, 2004), Data from Mykura 1980. Column 4, list of frequencies of the occurrence of the boundaries predicted for a random grain assemble (Pan and Adams 1994), using the Brandon criterion

Σ	θ°_{min}	Axis	Frequency %
1	0	Any	2.28
3	60	<111>	1.76
5	36.87	<100>	1.23
7	38.21	<111>	0.99
9	38.94	<110>	1.02
11	50.48	<110>	0.75
13a	22.62	<100>	0.29
13b	27.80	<111>	0.39
15	48.19	<210>	0.94
17a	28.07	<100>	0.20
17b	61.93	<221>	0.39
19a	26.53	<110>	0.33
19b	46.83	<111>	0.22
21a	21.79	<111>	0.19
21b	44.40	<211>	0.57
23	40.45	<311>	0.50
25a	16.25	<100>	0.11
25b	51.68	<331>	0.44
27a	31.58	<110>	0.20
27b	35.42	<210>	0.39
29a	43.61	<100>	0.09
29b	46.39	<221>	0.35
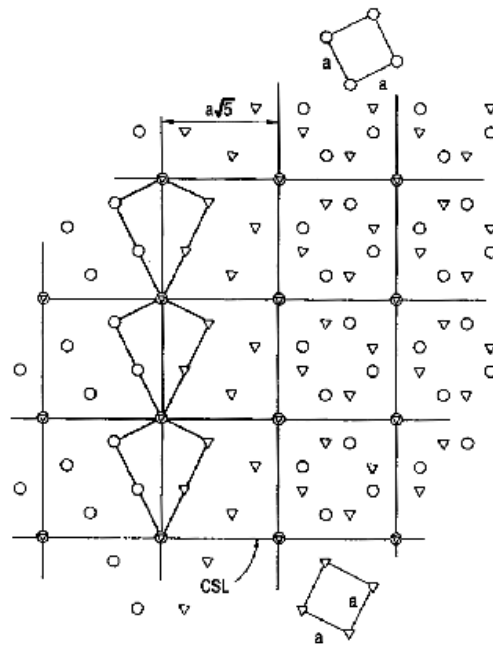
Figure V.5 : Schematic of CSL : $\Sigma 5$ (Gottstein and Shvindlerman, 1999)

V.1.2 Grain Boundary Energy

V.1.2.1 Measurements

The local disorder between two grains creates an excess of energy which depends on the grain characteristics. Figure V.6 shows a summary of methods used to measure grain boundary energies. The method, with dihedral angles at triple lines, is most generally used in the case of LAGB (Yang *et al.*, 2001) as well as the surface grooving method in the case of HAGB (Molodov *et al.*, 1994).

The approach with dihedral angles at triple points relies on measurement of the geometry and crystallography of grain boundary junctions. It is assumed that local equilibrium exists at each triple junction so that the Herring relations may be applied (Herring, 1951). The Herring relations, describing equilibrium at a triple junction, Figure V.7, result from the requirement that a virtual displacement of the triple junction in any direction causes no first order change in energy. If the interface energy is independent of interface orientation, the Herring equations reduce to:

$$\frac{\gamma_1}{\sin \chi_1} = \frac{\gamma_2}{\sin \chi_2} = \frac{\gamma_3}{\sin \chi_3} \tag{V.3}$$

where, γ_i, is the excess free energy of the ith boundary and, χ_i, is the right handed angle of rotation about the triple line of the jth boundary from a reference direction. After characterising a sufficient number of triple junction geometries, relative boundary energies can be extracted as a function of grain boundary misorientation through a statistical analysis, see Equation V.3.

V.1.2.2 Low Angle Grain Boundaries

The free energy of a small angle grain boundary can be calculated from the Read-Shockley theory. As shown by (Shockley and Read, 1949), the stress field of a dislocation core in an
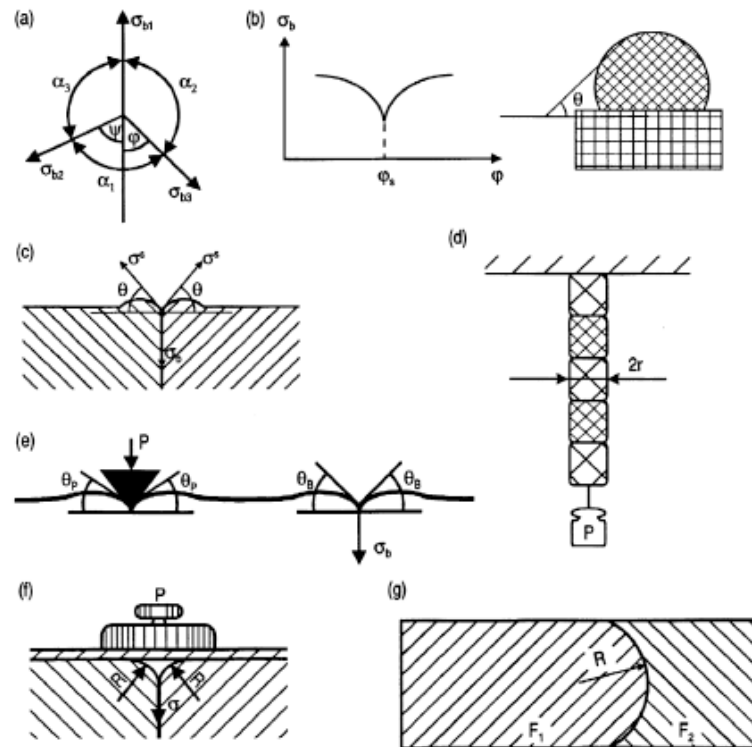
Figure V.6 : Methods of grain boundary surface tension measurement : (a) equilibrium angle at triple function; (b) rotating ball method; sintering of small signal crystal balls to single crystal substrate; (c) thermal groove method; (d) zero creep method; (e) method of a "floating" wedge; (f) hypothetical method of an "equilibrium" grain boundary thermal groove; (g) balance of grain boundary surface tension and volume diving force
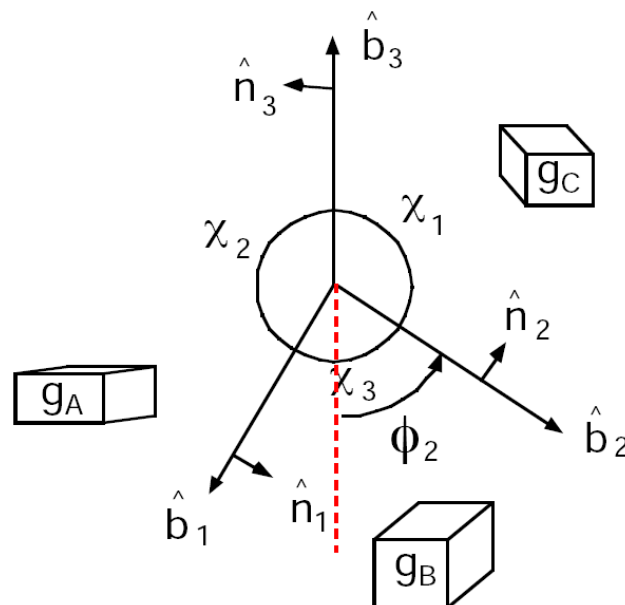
Figure V.7 : Labeling convention for the character of a grain boundary, showing dihedral angles, χ, inclination angles, ϕ, boundary tangent vectors, $\mathbf{b}$, boundary normals, $\mathbf{n}$, and grain orientations, g. Note that the triple junction line is perpendicular to the plane of the diagram (Yang *et al.*, 2001)
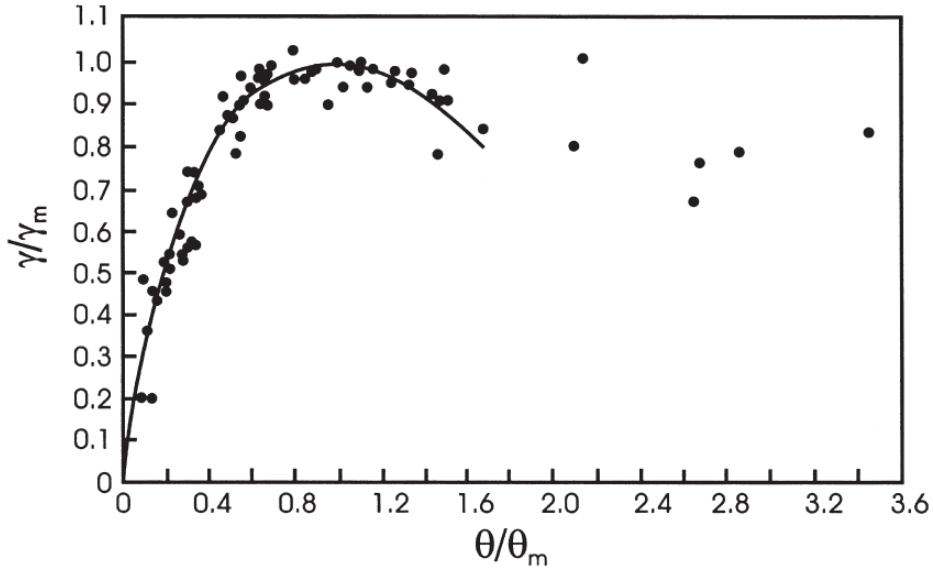
Figure V.8 : Measured (symbols) and calculated (solid line) energy of low angle tilt boundaries as a function of misorientation, for various metals, (Shockley and Read, 1949)

infinite periodic arrangements, is confined to a range in the order of the dislocation spacing, d. The energy of an edge dislocation per unit length is,

$$E_d = \frac{\mu b}{4\pi(1-\nu)} \ln \frac{d}{r_0} + E_c \tag{V.4}$$

where μ is the shear modulus, ν, the Poisson ratio, $r_0 \approx b$, radius of dislocation core and E_c, the energy of dislocation core. For a symmetrical tilt boundary with a tilt angle $\Delta\theta$ (infinite array of edge dislocations), the number of dislocations per unit length is $n \approx 1/d = \Delta\theta/b$, and thus, the grain boundary energy per unit area is:

$$\gamma = \frac{\Delta\theta}{b}\Big(\frac{\mu b}{4\pi(1-\nu)} \ln \frac{1}{\Delta\theta} + E_c\Big) = \Delta\theta(A - B \ln \Delta\theta) \tag{V.5}$$

where $A = E_c/b$ and $B = \mu/4\pi(1-\nu)$. It is often convenient to use the above equation in a form where the boundary energy and misorientation are normalised with the parameters γ_m and θ_m. The parameters γ_m and θ_m are constant values of γ and θ when the boundary becomes a high angle boundary (i.e. $\sim 15°$), see Figure V.8. Thus,

$$\gamma = \gamma_m \frac{\Delta\theta}{\Delta\theta_m}\Big(1 - \ln \frac{\Delta\theta}{\Delta\theta_m}\Big) \tag{V.6}$$

According to Equation V.6, the grain boundary energy γ increases with the misorientation, $\Delta\theta$.

V.1.2.3 High Angle Grain Boundaries

For low angle boundaries, the Read-Shockley model with a logarithmic dependence has been well established both experimentally and theoretically. For misorientations in excess of 15°, measurements of grain boundary energy reveal no further change with increasing rotation angle. Dislocation cores tend to overlap, the dislocations lose their identity as individual lattice defects, so the dislocation model fails. For instance, in Figure V.9, the grain boundary energy is plotted for aluminium for a twist boundary with a <110> boundary plane. Deep
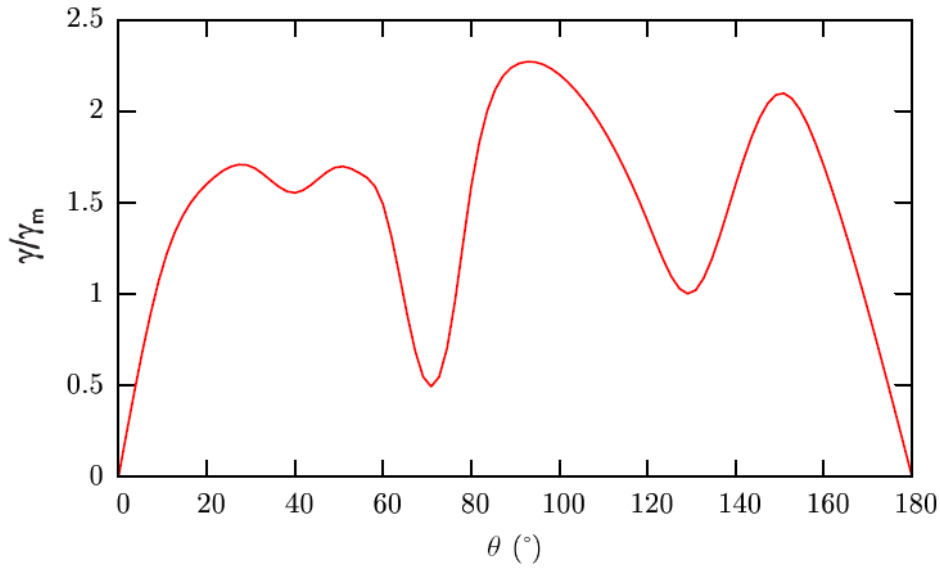
Figure V.9 : Measured energies at 650° for symmetrical <110> tilt boundaries in aluminium (Hasson and Goux, 1971)

Table V.2 : Measured grain boundary energies (mJm^{-2})(Murr, 1975)

Material	High angle grain boundary energy	Coherent twin boundary energy	Incoherent twin boundary energy
Ag	375	8	126
Al	324	75	-
Au	378	15	-
Cu	625	24	498
Ni	866	43	-

cusp exist for a few <110> CSL types in FCC (Σ3, Σ11). No universal theory exists to describe the energy of HAGBs. Based on a disordered atomic structure for general high angle boundaries, it is expected that the grain boundary energy should be at a maximum and approximately a constant. Otherwise, on the basis of the CSL structural models, it might be expected that the energy of the boundary would see a minimum for an exact coincidence relationship and that it would increase as the orientation deviates from this, due to the energy of the network of accommodating boundary dislocations. However, the correlation between the geometry and the energy of a grain boundary is more complicated. Practically, high angle boundaries energy is chosen in general constant. Typical values of grain boundary energies for Al is taken as $0.32J.m^{-2}$, see Table V.2.

V.1.3   Grain Boundary Mobilities

The mechanism of boundary migration depends on several parameters including the boundary structure. It also depends, in particular, on the temperature and the nature and magnitude of the forces acting on the boundary. It is also strongly influenced by point defects in the material such as solutes and vacancies. Lows angle grain boundary migration occurs during

recovery and during the nucleation of recrystallisation while high angle boundary migration occurs during and after primary recrystallisation.

V.1.3.1   Measurements

Extracting grain boundary motion data from the temporal evolution of grain size during recrystallisation or grain growth data is very complicated. In order to succeed in estimating grain boundary mobility, measurements are made by determining the velocity of a boundary in response to a well defined driving force. The boundaries move in response to a driving force (P) which generally arises from stored dislocations or from the energy of the boundaries in the material. In most cases (Humphreys and Hatherly, 2004), it is expected that the velocity of the moving boundary (v) is given by

$$v = MP \tag{V.7}$$

where, M is the boundary mobility, usually assumed to vary with temperature according to

$$M = M_0 \exp(-\frac{Q}{RT}) \tag{V.8}$$

where M_0 is a constant, T the absolute temperature, Q the activation energy for boundary migration and R is the universal gas constant.

In the case of motion due to grain boundary geometry, research on boundary mobilities has been carried out using bicrystal sample. In contrast to polycrystal experiments, bicrystal experiments provide reliable and reproducible physical data on grain boundary mobility. (Gottstein and Shvindlerman, 1992, Molodov *et al.*, 1994) have extracted the mobility of grain boundary of bicrystal under a capillary driving force. Figure V.10 shows the bicrystal geometry with a constant curvature during the grain boundary motion. The main advantage of this technique is a simple relation between the driving force P and the macroscopic grain dimension (radius of curvature), R. Here,

$$P = \frac{\gamma_{gb}}{R} \tag{V.9}$$

where γ_{gb} is the grain boundary energy. Therefore, the grain boundary mobility is deduced from the measurement of velocity.

The driving force arising from the boundary geometry is very low in comparison to the driving force arising from the minimisation of stored energy. In order to determine the grain mobility in this situation, microstructural evolution has been followed by imaging with backscattered electrons and a U-matic video recorder during annealing by (Huang and Humphreys, 1999). Using this technique enables subgrain sizes and misorientations in well recovered materials to be determined quite accurately. Furthermore, they assumed that in the recovered microstructures, the density of free dislocations was negligible and that the stored energy was entirely due to the subgrain boundaries of energy, γ_s. For subgrains of diameter, D, the stored energy is given by, (Hurley and Humphreys, 2003),

$$E_D = \frac{3\gamma_s}{D} \tag{V.10}$$

The driving pressure is calculated from Equation V.10 and EBSD measurements and grain boundary mobility is deduced from Equation V.7,.
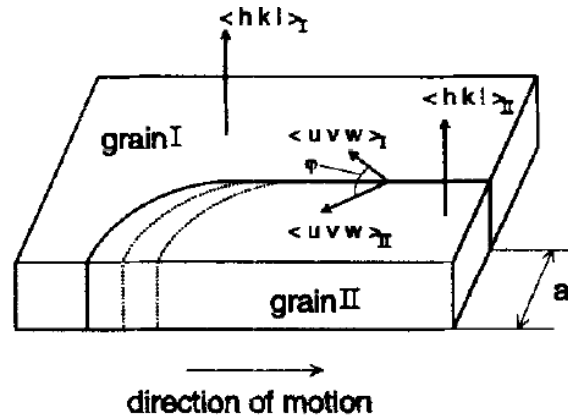
Figure V.10 : Bicrystal geometry for grain boundary motion measurement under a constant driving force (Molodov *et al.*, 1995)

V.1.3.2   Low Angle Grain Boundaries

Low angle grain boundaries migrate through climb and glide of dislocations. Therefore, many aspects of LAGB migration may therefore be interpreted in terms of the theory of dislocations. However, an empirical relationship is commonly used to describe the mobilities of boundaries in dilute aluminium alloys,

$$M = M_m\{1 - \exp[-B(\Delta\theta/\Delta\theta_m)^N]\} \tag{V.11}$$

where M_m is the mobility of a high angle boundary and generally N = 4 and B = 5.

V.1.3.3   High Angle Grain Boundaries

The fundamental process during the migration of high angle boundaries is the transfer of atoms to and from the grains which are adjacent to the boundary. No relation exists to describe the grain boundary mobility, see Figure VI.8, and highest grain boundary mobilities are not necessary for Σ grain boundaries.

V.1.4   Existing Theories to Model Mobile Grain Boundaries

Efforts directed at modeling the evolution of grain boundaries have used a variety of approaches, e.g., Monte Carlo (Srolovitz, 1986, Tavernier and Szpunar, 1991, Rollett *et al.*, 1992), cellular automaton (Marx *et al.*, 1999, Gottstein and Sebald, 2001, Geiger *et al.*, 2001), Vertex method (Soares *et al.*, 1985, Gill and Cocks, 1996), level set method (Osher and Sethian, 1988, Bernacki *et al.*, 2008), finite element (Serre, 2007) and phase field approach (Chen and Fan, 1996, Steinbach *et al.*, 1996, Ubachs *et al.*, 2005). In this section, only main phase field approaches will be detailed.

The phase field method has been successfully employed both as a tool to model heterogeneous materials and as a numerical method for calculating the motion of interfaces and phase boundaries without explicitly tracking those interfaces. In phase-field theories, the underlying idea is to replace sharp grain-boundaries by interfacial layers associated with rapid changes in variables that have a continuous spatial variation along the interface. The grain boundary is considered as a layer of defined thickness comprising a phase with a specific atomic arrangement. The first phase field models were developed to describe the evolution of a dual phase (Chen and Fan, 1996, Khachaturyan, 1996, Chen and Wang, 1996), and multiphase
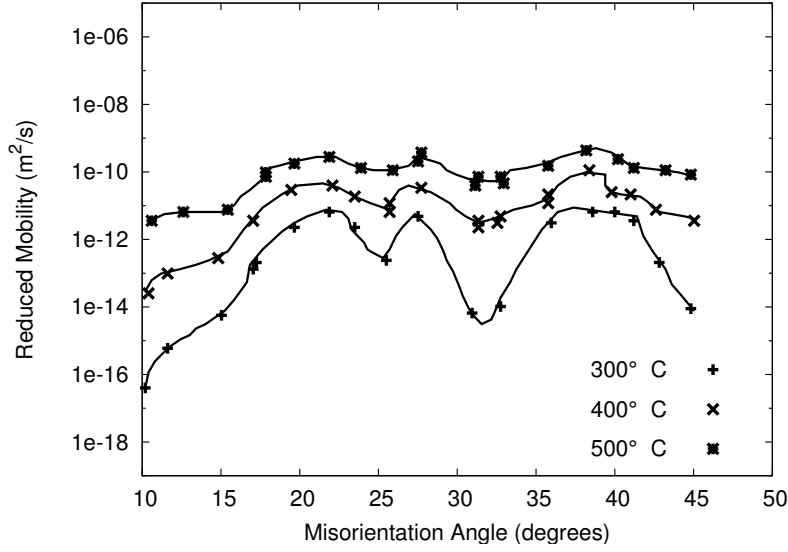
Figure V.11 : Experimental variation of relative boundary energy with misorientation angle (Gottstein and Shvindlerman, 1992)

problems (Steinbach *et al.*, 1996, Nestler and Wheeler, 1998). The kernel of phase field theories is the functional of the local free energy density, which depends on non-conserved field variables (or order parameter fields) of the system and its spatial derivatives. In order to apply these models to describe recrystallisation phenomena, each order parameter has been used for defining grains instead of phases (Suwa *et al.*, 2007, Takaki *et al.*, 2009).

In the theory proposed by (Chen and Fan, 1996, Suwa *et al.*, 2007), the microstructure of polycrystalline materials is described by a set of orientation field variables, $\eta_1(\mathbf{r}, t)$, $\eta_2(\mathbf{r}, t)$, ..., $\eta_q(\mathbf{r}, t)$, that distinguish different grain orientations and are defined at a given time and at each position $\mathbf{r}$ where q is the number of possible orientations. Within a grain labeled by η_1, $\eta_1(\mathbf{r}, t)$ equals 1 or -1, while all other field variables equal 0. At a grain boundary, all $\eta_i(\mathbf{r}, t)$ vary continuously between their equilibrium values in each neighbouring grain. From the diffuse-interface theory (Cahn and Hilliard, 1959), the total free energy of an inhomogeneous system can be written as :

$$\mathcal{F} = \int_{\mathcal{V}} \Big[f_0(\eta_1(\mathbf{r}, t), \eta_2(\mathbf{r}, t), ..., \eta_Q(\mathbf{r}, t) + \sum_{i=1}^{Q} \frac{\kappa_i}{2} (\nabla \eta_i(\mathbf{r}, t))^2 \Big] d^3 r \qquad (V.12)$$

where f_0 is local free energy density which is a function of the field variables, η_i and κ_i is the gradient coefficient energy. The smaller the gradient energy coefficient κ_i, the thinner the boundary region is. Note that $\nabla \eta_i^2$ is the gradient energy term, namely, the origin of the grain boundary energy. The spatial and temporal evolution of orientation field variables is described by the Ginzburg-Landau equations :

$$\frac{d\eta_i(\mathbf{r}, t)}{dt} = -L_i \frac{\delta \mathcal{F}}{\delta \eta_i(r, t)} = -L_i \Big(\frac{\partial f_0}{\partial \eta_i} - \kappa_i \nabla^2 \eta_i \Big), \qquad i = 1, 2, ..., p \qquad (V.13)$$

where L_i is a kinetic coefficient related to grain boundary mobility, t is the time and $\mathcal{F}$ is the total free energy of the system. To simulate grain growth kinetics, the following simple free

energy density functional is assumed:

$$f_0(\eta_1(\mathbf{r}, t), \eta_2(\mathbf{r}, t), ..., \eta_p(\mathbf{r}, t)) = \sum_{i=1}^{p} \left(-\frac{\alpha}{2}\eta_i^2 + \frac{\beta}{4}\eta_i^4 \right) + \gamma \sum_{i=1}^{p} \sum_{j \neq i}^{p} \eta_i^2 \eta_j^2, \qquad \text{(V.14)}$$

where α, β and γ are phenomenological parameters. The only requirement for f_0 is that it has 2q minima with equal well depth at η_1, η_2, ..., η_p = (1, 0, ..., 0), (0, 1, ...,0), ..., (0, 0, ..., 1), (-1, 0, ..., 0), (0,-1, ..., 0), ..., (0,0, ..., -1). The existence of the minima guarantees that finite regions will be stabilized and separated by boundaries.

When L and κ are assumed to be constant, the above equations describe isotropic grain growth. The mobility anisotropy is incorporated by making L misorientation-dependent (Ma *et al.*, 2004). The energy anisotropy can be introduced by making κ misorientation-dependent. According to (Ma *et al.*, 2004), the misorientation field corresponding to an arbitrary distribution for grain boundary in system is characterised as

$$\theta(r, t) = \frac{\sum_{i,j \neq i}^{Q} \eta_i(r, t)^2 \eta_j(r, t)^2 \theta_{ij}}{\sum_{i,j \neq i}^{Q} \eta_i(r, t)^2 \eta_j(r, t)^2} \qquad \text{(V.15)}$$

where, θ_{ij}, is the misorientation angle between grain i and grain j with orientations η_i and η_j. Equation V.15 assigns a constant misorientation angle in the grain-boundary region between grain i and grain j with value of the angle θ_{ij}, and yields a weighted-mean misorientation for the junction.

In multi-phase-field models (Steinbach *et al.*, 1996, Takaki *et al.*, 2009), the free energy functional takes the form of,

$$F = \int_V \epsilon a(\phi, \nabla\phi) + \frac{1}{\epsilon} w(\phi) dV \qquad \text{(V.16)}$$

where, $a(\phi, \nabla\phi)$, is the gradient free energy density, $w(\phi)$, the potential and ϕ the N-component phase field vector $(\phi_1, ..., \phi_\alpha, ..., \phi_N)$ representing N different grain orientations. The state variables satisfy

$$\sum_\alpha \phi_\alpha = 1 \quad and \quad 0 \leq \phi_\alpha \leq 1 \quad (\alpha \in \{1...N\}) \qquad \text{(V.17)}$$

The energy density contribution is chosen to be

$$w(\phi) = \frac{16}{\pi^2} \sum_{\alpha < \beta} \gamma_{\alpha\beta} \phi_\alpha \phi_\beta + \sum_{\alpha < \beta < \delta} \gamma_{\alpha\beta\delta} \phi_\alpha \phi_\beta \phi_\delta \qquad \text{(V.18)}$$

where $\gamma_{\alpha\beta}$ is the surface energy. The gradient free energy density, $a(\phi, \nabla\phi) = \sum_{\alpha < \beta} \gamma_{\alpha\beta} |\vec{q}_{\alpha\beta}|^2$, is formulated as a function of generalised gradient vectors $\vec{q}_{\alpha\beta} = \phi_\alpha \nabla\phi_\beta - \phi_\beta \nabla\phi_\alpha$. This allows different grain boundary energies depending on the misorientation angle between neighbouring grains. The evolution of the grain structure is given by a set of N kinetic equations for the phase fields, ϕ_α, which are derived from the variational derivative of the free energy. This,

$$\tau\epsilon \frac{\partial\phi_\alpha}{\partial t} = -\frac{\delta F}{\delta\alpha} - \lambda \qquad \text{(V.19)}$$

$$= \epsilon(\nabla.a_{,\nabla\phi_\alpha}(\phi, \nabla\phi) - a_{,\phi_\alpha}(\phi, \nabla\phi) - \frac{1}{\epsilon} w_{,\phi_\alpha}(\phi) - \lambda, \qquad \text{(V.20)}$$

where $\lambda = 1N \sum_\alpha [\epsilon(\nabla.a_{,\nabla\phi_\alpha}(\phi, \nabla\phi) - a_{,\phi_\alpha}(\phi, \nabla\phi) - \frac{1}{\epsilon}w_{,\phi_\alpha}(\phi)]$, accounts for the restriction $\sum_\alpha \phi_\alpha = 1$. Note that the parameters ϵ, $\gamma_{\alpha\beta}$ and τ are related to physical grain boundary properties.

In both models, a large set of non-conserved phase fields is used to represent the different grain orientations. In the first model, the field variables are treated as being independent while in the second, the phase fields are interpreted as volume fractions which are subject to the constraint that the sum of the phase fields must equal one at each material position. Furthermore, the thermodynamic free energy in the continuum-field model has multiple degenerate minima, one for each grain orientation. The free energy of multi-phase-field models has a single minimum for all phase fields equal to zero. From a mathematical point of view, the evolution equations obtained in the two approaches, have different solutions. Both models give essentially the same results, except for differences in the structure near small shrinking grains which are most often locally and temporary for large grain structures (Moelans *et al.*, 2009).

These models have been shown to be effective at representing interfacial migration and describing recrystallisation simulations (Suwa *et al.*, 2007, Takaki *et al.*, 2009). However, these models are not invariant by rotation. In real materials, the number of orientations is infinite ($q = \infty$). Even if it was shown that a finite number for q might be sufficient to realistically simulate grain growth, it requires one phase field variable by orientation which results in a lot of variables. In addition, these models prohibit grain rotation, a phenomenon which has been observed experimentally, see V.12.
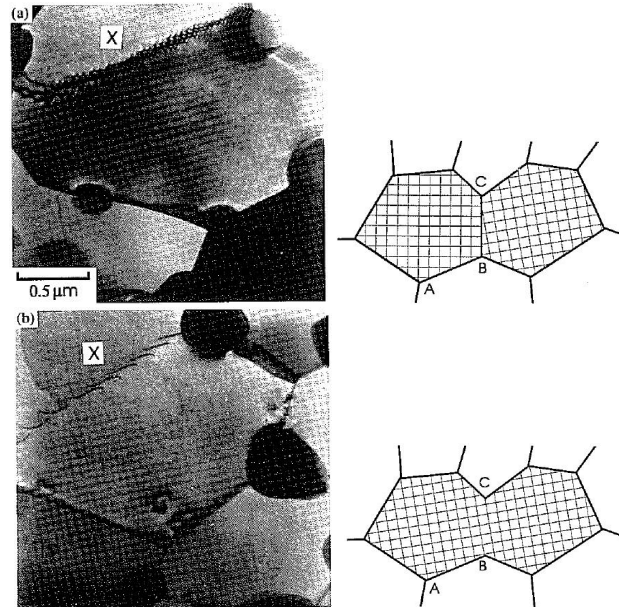
Figure V.12 : In-situ annealing of a thin $Al - 6\%Ni$ foil (Chan and Humphreys, 1984)

(Kobayashi *et al.*, 2000) (KWC) proposed an alternative phase field model describing the evolution of a collection of nearly perfect crystalline grains via a gradient flow using a phenomenological free energy. The crystalline phase field model has two fields variables: orientation, θ, and crystallinity (measure of the degree of the crystalline order at the macro-scale), η. An upper bound, $\eta = 1$, is assigned to perfect crystallinity and a lower bound, $\eta = 0$, implies no crystalline order on a coarse-grained scale. η may take values less than 1

near a grain boundary, and, for certain configurations, there will be an equilibrium bicrystal structure with $\eta = \eta_{min}$ within the grain boundary. The field parameter, θ, that measures the local orientation of crystal with respect to a fixed coordinate system is sufficient for an isotropic two-dimensional case. All crystals have a N-fold symmetry, thus all θ should lie in the irreducible domain. In addition, the presence of mirror symmetries further reduces the possible misorientations. The phenomenological free energy is

$$\mathcal{F}(\eta, \theta) = \int_\Omega \frac{\alpha^2}{2} |\nabla \eta|^2 + f(\eta) + g(\eta) s |\nabla \theta| + h(\eta) \frac{\epsilon^2}{2} |\nabla \theta|^2 dV \qquad \text{(V.21)}$$

where α, ϵ and s are positive constants.

The first term describes the penalty for gradients in the order parameter (grain boundaries cost energy). The free energy density $f(\eta)$ is chosen to be a single well with the minimum at $\eta = 1$ and f(1) = 0 reflecting the fact that a disordered material has a higher free energy. The third and fourth terms introduced in the free energy are functions of the gradient in the orientation, θ, and account for grain boundary energy misorientation penalties. These terms, in $|\nabla \theta|$, are coupled to η with the positive definite functions $g(\eta)$ and $h(\eta)$. The linear dependence on $|\nabla \theta|$ introduces a cusp into the total free energy density at $|\nabla \theta| = 0$. The presence of the linear term $|\nabla \theta|$ (as opposed to higher order powers $|\nabla \theta|$) is required for grain boundaries that are localised at equilibrium. Note that without this linear term, the grain boundary regions (where θ is spatially varying) spread. In other words, stable grain boundaries of finite width do not exist in the model unless the free energy density depends, to lowest order, linearly on $|\nabla \theta|$ (Kobayashi *et al.*, 2000). At least one higher order term is essential for the dynamics of grain boundaries, that is why $|\nabla \theta|^2$ is included in the free energy. Here, orientation term is not included in the homogeneous part of the free energy because the free energy must be invariant with respect to orientation in the laboratory frame. Assuming the relaxational dynamics for a non conserved set of order parameters, KWC finds the following gradient flow equations:

$$Q(\eta, \nabla \theta) \tau_\eta \frac{\partial \eta}{\partial t} = -\frac{\delta \mathcal{F}}{\delta \eta} = \alpha^2 \nabla^2 \eta - f_\eta - g_\eta s |\nabla \theta| - h_\eta \frac{\epsilon^2}{2} |\nabla \theta|^2 \qquad \text{(V.22)}$$

$$P(\eta, \nabla \theta) \tau_\theta \eta^2 \frac{\partial \theta}{\partial t} = -\frac{\delta \mathcal{F}}{\delta \theta} = \nabla . [h \epsilon^2 \nabla \theta + g s \frac{\nabla \theta}{|\nabla \theta|}] \qquad \text{(V.23)}$$

The kinetic scaling factors τ_η and τ_θ are specified to be uniform and constant, while the inverse mobility functions, P and, Q contain all the information concerning functional dependence of the kinetic coefficients on the order parameters and anisotropy. Equation V.23 introduces the possibility of grain rotation whereas θ can change as a function of time. The term $\frac{\nabla \theta}{|\nabla \theta|}$ yields a singularity in the dynamic equations. The mobility functions P and Q must be positive definite, continuous at $|\nabla \theta| = 0$, but are otherwise unrestricted.

Also, $f(\eta)$ is a single well with a minimum at $\eta = 1$, f(1)=0 reflecting the fact that disordered materials have higher free energy. A simple choice for f is

$$f(\eta) = \frac{\omega^2}{2} (1 - \eta)^2 \qquad \text{(V.24)}$$

(a)   (b)
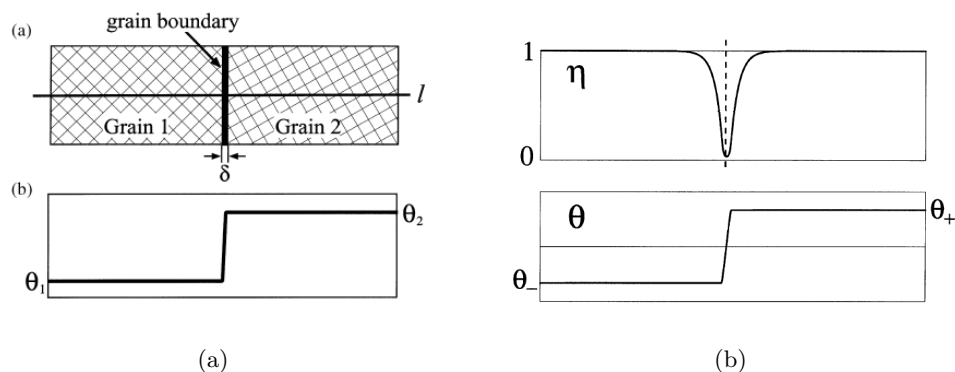
Figure V.13 : (a) Schematic drawing of a bicrystal and (b) typical profile of the equilibrium
solution η and θ
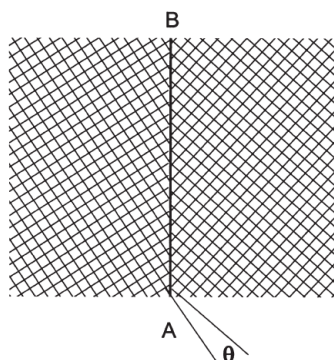
Figure V.14 : Schematics of a 2D grain boundary

V.2 Polycrystalline Microstructure Description Using a Phase Field Approach

V.2.1 Review of the Kobayashi-Warren-Carter model

The KWC model is two dimensional, which considerably simplifies the description of a grain
boundary. In 2D cases, a grain boundary has only two geometrical degrees of freedom:
the inclination angle of the boundary plane between two crystals, and the crystallographic
misorientation $\Delta\theta$. Here, the free energy is independent of the grain boundary orientation,
see Figure V.14. Finally, the KWC phase field model has two field variables: orientation θ
and crystallinity η. Before deformation, we consider that the crystal lattice is perfect inside
the grains; the crystal order (measure of the degree of the crystalline order at the macro-
scale), η, is constant and equal to 1. At the grain boundary, the crystallinity varies with the
misorientation between grains, therefore between 0 and 1. The phenomenological free energy
invariant by rotation is expressed as:

$$\mathcal{F}(\eta, \theta) = \int_{\Omega} \frac{\alpha^2}{2}|\nabla\eta|^2 + f(\eta) + g(\eta)|\nabla\theta| + h(\eta)|\nabla\theta|^2 dV \qquad (V.25)$$

where α, ϵ and s are positive constants.

V.2.2   Introduction of Stored Energy in the Free Energy

During the deformation process, the dislocation density increases inside the grains giving a non periodic crystal lattice, and therefore, a lattice order $\eta < 1$. However, even in the large strain regime, the lattice disorder inside the grain due to deformation remains smaller than the disorder inside the high angle grain boundaries. Otherwise, the polycrystal will only be one grain boundary phase. A measure of the lattice disorder due to deformation is the stored energy. Therefore, to measure this phenomenon, the stored energy due to deformation is introduced in the free energy. As the high angle grain boundary is the highest disorder area in the polycrystal, we considered the stored energy due to deformation always less than the high angle grain boundary energy. The stored energy density, E_{st}, is normalized by a high angle grain boundary energy, E_{gb} in order to introduce it in the free energy formulation, where the grain boundary energy between two grains of high misorientation is taken constant (the Σ grain boundaries are not considered). The phenomenological free energy, an invariant of the rotation, is expressed as follows:

$$\mathcal{F}(\eta, \theta) = \int_\Omega \rho\psi dV \tag{V.26}$$

$$\mathcal{F}(\eta, \theta) = \int_\Omega \frac{\alpha^2}{2}|\nabla\eta|^2 + f(\eta) + C_e \frac{E_{st}}{E_{gb}}\eta + g(\eta)|\nabla\theta| + h(\eta)|\nabla\theta|^2 dV \tag{V.27}$$

where α, ω and C_e are positive constants.

The second term in Equation V.27 is chosen so as to yield a single well with the minimum at $\eta = 1$. This reflects the fact that disordered materials have higher free energies, $f(\eta) = \frac{\omega^2}{2}(1 - \eta)^2$. The third term represents the additional stored energy due to deformation. The constant C_e is calibrated from experimental data.

V.2.3   Balance of Generalised Stresses

V.2.3.1   Principle of Virtual Power

A continuum-mechanics framework to describe dynamic problems has been proposed in (Fried and Gurtin, 1996, Gurtin and Lusk, 1999, Ammar *et al.*, 2009) based on a balance law for generalised forces associated with the equilibrium of defect-structures. In the case of recrystallisation, the short-range transport of atoms between adjacent mismatched lattices occurring at the lattice length-scales is introduced via dissipative generalized forces that perform work over the macroscopic motion of grain boundaries at continuum length-scales. In this section, the same approach is used to determine the balance and constitutive laws associated with the free energy. As explained in the previous paragraph, the microstructure is represented by the phase-field variables η, the crystallinity, and θ, the crystal orientation. The generalised forces associated with both fields are characterised by micro-stresses and by micro-forces. Here, $\underline{\xi}_\eta$ is the micro-stress associated to η and π_η and π_η^{ext} are, respectively, the internal and external micro-forces associated to η. $\underline{\xi}_\theta$ is the microstress associated to θ and π_θ and π_θ^{ext} are, respectively, the internal and external microforces associated to θ. The method of virtual powers due to the work performed by the forces is used to determine the balance law equations. The virtual power of internal forces is expressed as :

$$\begin{aligned}\mathcal{P}^{(i)} &= \int_\mathcal{D} (\pi_\eta \dot\eta - \underline{\xi}_\eta.\nabla\dot\eta + \pi_\theta\dot\theta - \underline{\xi}_\eta.\nabla\dot\theta)d\mathcal{V}, \tag{V.28}\\ &= \int_\mathcal{D} \big((\nabla.\underline{\xi}_\eta + \pi_\eta)\dot\eta + (\nabla.\underline{\xi}_\theta + \pi_\theta)\dot\theta\big)d\mathcal{V} - \int_{\partial\mathcal{D}} \big((\underline{\xi}_\eta.\mathbf{n})\dot\eta + (\underline{\xi}_\theta.\mathbf{n})\dot\theta\big)d\mathcal{S}. \tag{V.29}\end{aligned}$$

The virtual power of external forces including distance and contact forces is given by :

$$\mathcal{P}^{(e)} = \int_{\mathcal{D}} (\pi_\eta^{ext}\dot{\eta} + \pi_\theta^{ext}\dot{\theta})d\mathcal{V}, \tag{V.30}$$

$$\mathcal{P}^{(c)} = \int_{\partial\mathcal{D}} (\pi_\eta^c\dot{\eta} + \pi_\theta^c\dot{\theta})d\mathcal{S}. \tag{V.31}$$

The principle of virtual power then states (power of inertial microforces are neglected, $\mathcal{P}^{(a)}$) that

$$\forall\mathcal{D} \in V, \quad \forall(\dot{\eta},\dot{\theta}), \quad \mathcal{P}^{(i)} + \mathcal{P}^{(e)} + \mathcal{P}^{(c)} = 0 \tag{V.32}$$

Therefore,

$$\forall\mathcal{D} \in V, \quad \forall(\dot{\eta},\dot{\theta}), \quad \int_{\mathcal{D}} (\nabla.\underline{\xi}_\eta + \pi_\eta + \pi_\eta^{ext})\dot{\eta} + (\nabla.\underline{\xi}_\theta + \pi_\theta + \pi_\theta^{ext})\dot{\theta}d\mathcal{V} = 0 \tag{V.33}$$

Assuming that the quantities, θ and η are continuous on V , the local equilibrium equations are derived

$$\nabla.\underline{\xi}_\theta + \pi_\theta + \pi_\theta^{ext} = 0 \quad \text{on} \quad \mathcal{V} \tag{V.34}$$

$$\nabla.\underline{\xi}_\eta + \pi_\eta + \pi_\eta^{ext} = 0 \quad \text{on} \quad \mathcal{V} \tag{V.35}$$

When external forces are neglected, the equations become

$$\nabla.\underline{\xi}_\theta + \pi_\theta = 0 \quad \text{on} \quad \mathcal{V}, \tag{V.36}$$

$$\nabla.\underline{\xi}_\eta + \pi_\eta = 0 \quad \text{on} \quad \mathcal{V}. \tag{V.37}$$

As a result, the principle of virtual power can be expressed as

$$\forall\mathcal{D} \in V, \quad \forall(\dot{\eta},\dot{\theta}), \quad \int_{\partial\mathcal{D}} \left((\underline{\xi}_\eta.\mathbf{n} - \pi_\eta^c)\dot{\eta} + (\underline{\xi}_\theta.\mathbf{n} - \pi_\theta^c)\dot{\theta}\right)d\mathcal{S}, \tag{V.38}$$

from which the boundary conditions are deduced

$$\underline{\xi}_\eta.\mathbf{n} = \pi_\eta^c \quad \text{on} \quad \partial\mathcal{V}, \tag{V.39}$$

$$\underline{\xi}_\theta.\mathbf{n} = \pi_\theta^c \quad \text{on} \quad \partial\mathcal{V}. \tag{V.40}$$

V.2.3.2 Constitutive Phase Field Equations

Neglecting power of acceleration, the energy conservation principle is written:

$$\dot{E} = P_{ext} + Q. \tag{V.41}$$

Using the power principle,

$$\dot{E} = -P_i + Q. \tag{V.42}$$

Let e be the internal energy per unit mass, $\underline{q}$ the heat flux vector, ρ the current density. The energy balance equation reads

$$\rho\dot{e} = \underline{\xi}_\eta.\nabla\dot{\eta} + \underline{\xi}_\eta.\nabla\dot{\theta} - \pi_\eta\dot{\eta} - \pi_\theta\dot{\theta} - \text{div}\,\underline{q}; \tag{V.43}$$

According to the thermodynamics of irreversible processes, the entropy principle is given by

$$\rho\dot{s} + \text{div}\,\frac{q}{T} \geq 0 \tag{V.44}$$

where T denotes the absolute temperature and, s, the entropy per unit mass.

Introducing the free energy, $\psi = e - sT$, and combining the energy and entropy equations, one derives the Clausius-Duhem inequality

$$-\rho(s\dot{T} + \dot{\psi}) - p^i - \frac{q}{T}.(\nabla T) \geq 0 \tag{V.45}$$

$$-\rho(s\dot{T} + \dot{\psi}) + \underline{\xi}_\eta.\nabla\dot{\eta} + \underline{\xi}_\eta.\nabla\dot{\theta} - \pi_\eta\dot{\eta} - \pi_\theta\dot{\theta} - \frac{q}{T}.(\nabla T) \geq 0 \tag{V.46}$$

The free energy and entropy are only dependent on $\eta, \nabla\eta, \nabla\theta$. Therefore,

$$\dot{\psi}(\eta, \theta, \nabla\eta, \nabla\theta) = \frac{\partial\psi}{\partial\eta}\dot{\eta} + \frac{\partial\psi}{\partial\nabla\eta}\nabla\dot{\eta} + \frac{\partial\psi}{\partial\theta}\dot{\theta} + \frac{\partial\psi}{\partial\nabla\theta}\nabla\dot{\theta} \tag{V.47}$$

The Clausius-Duhem inequality gives:

$$(-\rho\frac{\partial\psi}{\partial\eta} - \pi_\eta)\dot{\eta} + (-\rho\frac{\partial\psi}{\partial\theta} - \pi_\theta)\dot{\theta} + (-\rho\frac{\partial\psi}{\partial\nabla\eta} + \underline{\xi}_\eta).\nabla\dot{\eta} + (-\rho\frac{\partial\psi}{\partial\nabla\theta} + \underline{\xi}_\theta)\nabla\dot{\theta} - (\rho s + \rho\frac{\partial\psi}{\partial T}) - \frac{q}{T}.(\nabla T) \geq 0 \tag{V.48}$$

The microstresses $\underline{\xi}_\eta$ and $\underline{\xi}_\theta$ are assumed independent of $\dot{\eta}$ and $\dot{\theta}$ and satisfy

$$\underline{\xi}_\eta = \rho\frac{\partial\psi}{\partial\nabla\eta} \tag{V.49}$$

$$\underline{\xi}_\theta = \rho\frac{\partial\psi}{\partial\nabla\theta} \tag{V.50}$$

$$s = \frac{\partial\psi}{\partial T} \tag{V.51}$$

Therefore,

$$(-\frac{\partial\psi}{\partial\eta} - \pi_\eta)\dot{\eta} + (-\frac{\partial\psi}{\partial\theta} - \pi_\theta)\dot{\theta} \geq 0 \tag{V.52}$$

$$\pi_\eta = \frac{\partial\psi}{\partial\eta} + \pi_\eta^{non} \tag{V.53}$$

$$\pi_\theta = \pi_\theta^{non} \tag{V.54}$$

The functions π_η^{non} and π_θ^{non} represent non-equilibrium contributions to the internal forces, π_η and π_θ. To be consistent with the second thermodynamic principle, π_η^{non} and π_θ^{non} should satisfy the following condition,

$$\pi_\eta^{non}\dot{\eta} + \pi_\theta^{non}\dot{\theta} \leq 0 \tag{V.55}$$

V.2.3.3 Evolutionary Equations of the Field Variables η and θ

From the free energy expression, we deduce the constitutive equations:

$$\underline{\xi}_\eta = \rho\frac{\partial\psi}{\partial\nabla\eta} = \alpha^2\nabla\eta, \tag{V.56}$$

$$\underline{\xi}_\theta = \rho\frac{\partial\psi}{\partial\nabla\theta} = g(\eta)\frac{\nabla\theta}{|\nabla\theta|} + h(\eta)\nabla\theta, \tag{V.57}$$

$$\pi_\eta = -\rho\frac{\partial\psi}{\partial\eta} + \pi_\eta^{non} = -f'(\eta) - g'(\eta)|\nabla\theta| - h'(\eta)|\nabla\theta|^2 + \pi_\eta^{non}, \tag{V.58}$$

$$\pi_\theta = -\rho\frac{\partial\psi}{\partial\theta} + \pi_\theta^{non} = \pi_\theta^{non}, \tag{V.59}$$

where

$$\pi_\eta^{non} = -\tau_\eta \exp(\frac{Q}{kT})\dot{\eta}, \tag{V.60}$$

$$\pi_\theta^{non} = -\tau_\theta f_m(\eta) \exp(\frac{Q}{kT}) f_r(\eta, \nabla\eta)\dot{\theta}. \tag{V.61}$$

Here, $f_m(\eta)$ is an increasing positive function of η which controls the grain boundary migration rate. Equation V.61 introduces the possibility of grain rotation. Since the multiplicative term of $\dot{\eta}$ and $\dot{\theta}$ are the inverse boundary mobility, the term $\exp(\frac{Q}{kT})$ is introduced in non-equilibrium contributions to include the temperature dependence shown in section V.1.3.1. The kinetic constant, τ_η, should be less than τ_θ in order to avoid grain rotations due to the absence of mechanical stress. To prevent this phenomenon, the inverse mobility function $f_r(\eta, \nabla\eta)$ is chosen to cancel grain rotations when the crystallinity variation is small that is inside the grains. Also, f_r is chosen so as to not affect the grain boundary migration rate. Thus,

$$f_r(\eta, \nabla\eta) = 1 + \beta_r(1 - \exp(-\beta_s \frac{\eta}{\nabla\eta})). \tag{V.62}$$

Replacing the stress and force expressions in the balance laws, the evolutionary equations for the crystal order, η, and the crystal orientation, θ, become

$$\tau_\eta \exp(\frac{Q}{kT})\dot{\eta} = \alpha^2 \nabla^2 \eta - f'(\eta) - C_e \frac{E_{st}}{E_{gb}} - g'(\eta)|\nabla\theta| - h'(\eta)|\nabla\theta|^2 \tag{V.63}$$

$$\tau_\theta f_m(\eta) \exp(\frac{Q}{kT}) f_r(\eta, \nabla\eta)\dot{\theta} = \nabla.[2h(\eta)\nabla\theta + g(\eta)\frac{\nabla\theta}{|\nabla\theta|}] \tag{V.64}$$

By considering the equilibrium solution inside the grains, namely where $\nabla\eta = 0$ and $\nabla\theta = 0$, Equation V.63 gives

$$0 = -f'(\eta) - C_e \frac{E_{st}}{E_{gb}} = \omega^2(1 - \eta) - C_e \frac{E_{st}}{E_{gb}} \tag{V.65}$$

which yields the lattice order value inside the grain (see Figure V.15),

$$\eta = 1 - \frac{C_e}{\omega^2} \frac{E_{st}}{E_{gb}} \tag{V.66}$$

Since $0 \leq \eta \leq 1$, Equation V.66 raises the following condition on the model parameters,

$$\frac{C_e}{\omega^2} \frac{E_{st}}{E_{gb}} < 1 \tag{V.67}$$

### V.2.3.4 Evolutionary Equations of the Stored Energy for Recrystallisation

In this section, the evolution of the stored energy is only considered for the recrystallisation phenomena. During primary recrystallisation, the grain boundary migration rearranges the crystal lattice, dislocations are annihilated, and after grain boundary motion, the stored energy decreases, see Figure V.16. During deformation, stored energy increases inside the grains and the metastable solution of η is deduced from Equation V.66: η decreases from 1, the perfect lattice order, to $\frac{C_e}{\omega^2} \frac{E_{st}}{E_{gb}}$, the disturbed lattice order. Consequently, the stored energy E_{st} must be constant when $\dot{\eta} \leq 0$. Since η is minimal at the grain boundaries, after

(a)   (b)
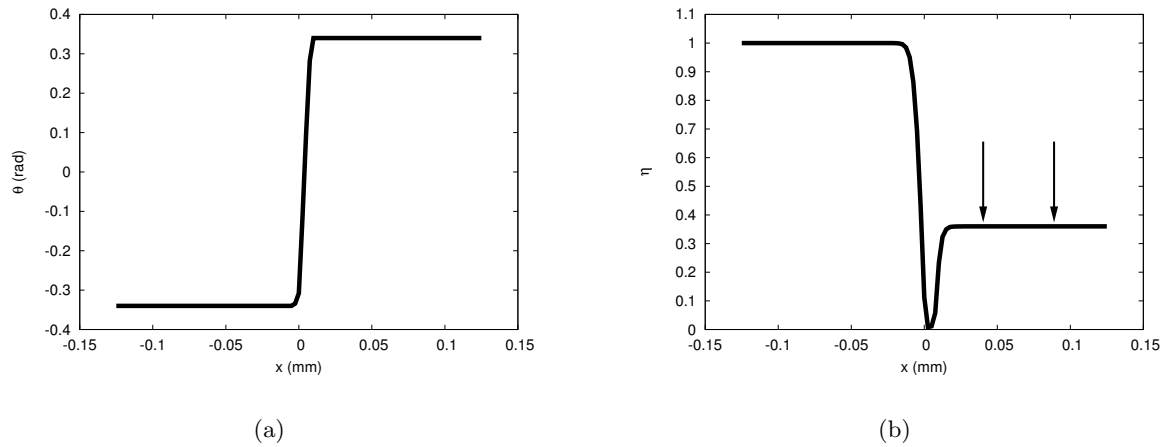
Figure V.15 : Profiles of (a) orientation and (b) lattice order with an initial constant stored energy distribution
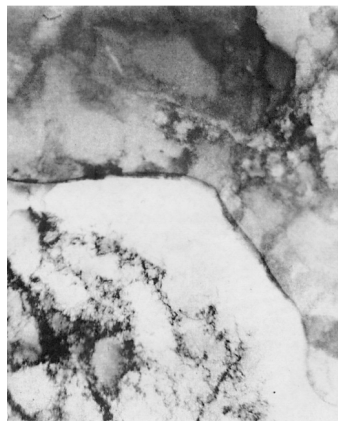
Figure V.16 : Migration of an existing grain boundary. The boundary between grains, in the middle of the photo, has moved upwards leaving in its wake a region relatively free of dislocation substructures (Gurtin and Lusk, 1999)
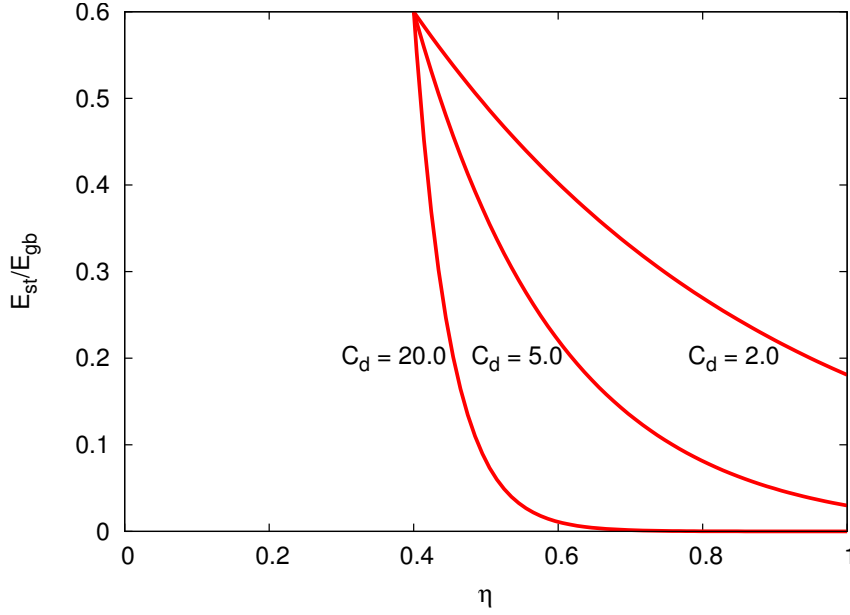
Figure V.17 : Stored energy evolution with an initial value of $E_0 = 0.6$

grain boundary motion, η increases to reach the stable state, $1 - \frac{C_e}{\omega^2}\frac{E_{st}}{E_{gb}}$, which implies that $\dot{\eta} > 0$. Finally, the evolutionary equations for the stored energy is expressed in a simple form as,

$$\dot{E}_{st} = -C_d E_{st}\dot{\eta}A(|\nabla\theta|) \quad if \quad \dot{\eta} > 0 \tag{V.68}$$
$$\dot{E}_{st} = 0 \quad if \quad \dot{\eta} \leq 0 \tag{V.69}$$

where C_d is a fitting parameter. The introduction of $A(|\nabla\theta|)$ in Equation V.68 is necessary to localise stored energy annihilation in the grain boundary regions. Thus,

$$A(|\nabla\theta|) = \tanh(|\nabla\theta|^2) = \begin{cases} 0 & if \quad |\nabla\theta| = 0 \\ 1 & if \quad |\nabla\theta| \neq 0 \end{cases}$$

In order to study the stored energy evolutionary equation, we considered $A(|\nabla\theta|) = 1$ which gives,

$$\dot{E}_{st} = -C_d E_{st}\dot{\eta} \quad if \quad \dot{\eta} > 0 \tag{V.70}$$

Integrating Equation V.70, the stored energy evolution is

$$E_{st} = B \exp(-C_d\eta) \tag{V.71}$$

where B is a constant. With the initial conditions, $E_{st}/E_{gb} = E_0/E_{gb}$, and therefore, $\eta = 1 - E_{st}/E_{gb}$, Thus, Equation V.71 becomes

$$E_{st} = E_0 \exp(C_d(1 - E_0 - \eta)) \tag{V.72}$$

Figure V.17 shows the stored energy evolution with an initial stored energy. The stored energy evolves towards 0 at the same time as η tends to 1 (the slope is decreasing). It should be noted that the stored energy annihilation rate increases with C_d.

V.3 Implementation of the Phase-Field Equations into the Finite Element Method

The method is detailed in (Ammar *et al.*, 2009) for phase transformation problem.

V.3.1   Variational Formulation

The variational formulation of the phase field partial differential equations directly follows from the formulated principle of virtual power, detailed in Section V.2.3.1. Here,

$$\mathcal{F}(\eta^*, \mathcal{V}) = \int_{\mathcal{V}} (\pi_\eta \eta^* - \underline{\xi}_\eta . \nabla \eta^*) d\mathcal{V} + \int_{\partial \mathcal{V}} (\zeta_\eta \eta^*) d\mathcal{S} \quad = \quad 0 \qquad (V.73)$$

$$\mathcal{F}(\theta^*, \mathcal{V}) = \int_{\mathcal{V}} (\pi_\theta \theta^* - \underline{\xi}_\theta . \nabla \theta^*) d\mathcal{V} + \int_{\partial \mathcal{V}} (\zeta_\theta \theta^*) d\mathcal{S} \quad = \quad 0 \qquad (V.74)$$

The phase field problem to solve in FE admit the initials conditions at t = 0,

$$\eta(\mathbf{x}, 0) \quad = \quad \eta_0(\mathbf{x}) \qquad (V.75)$$

$$\theta(\mathbf{x}, 0) \quad = \quad \theta_0(\mathbf{x}) \qquad (V.76)$$

and at each instant, t>0,

$$\int_{\mathcal{V}} (\pi_\eta \eta^* - \underline{\xi}_\eta . \nabla \eta^*) d\mathcal{V} + \int_{\partial \mathcal{V}} (\zeta_\eta \eta^*) d\mathcal{S} \quad = \quad 0 \qquad (V.77)$$

$$\int_{\mathcal{V}} (\pi_\theta \theta^* - \underline{\xi}_\theta . \nabla \theta^*) d\mathcal{V} + \int_{\partial \mathcal{V}} (\zeta_\theta \theta^*) d\mathcal{S} \quad = \quad 0 \qquad (V.78)$$

V.3.2   FE Discretisation

In order to obtain a finite element solution, the spatial domain in discretised into N elements. The nodal degrees of freedom are the values at the nodes of the lattice order and the crystal orientation. The fields η and θ are approximated within each element and at every time, t, in terms of nodal values by means of interpolation functions within each element. Here,

$$\eta(\underline{x}, t) = \sum_{i=1}^{n} N_i^e(\underline{x}) \eta_i(t), \qquad \theta(\underline{x}, t) = \sum_{i=1}^{n} N_i^e(\underline{x}) \theta_i(t) \qquad (V.79)$$

$$\eta^*(\underline{x}, t) = \sum_{i=1}^{n} N_i^e(\underline{x}) \eta_i^*(t), \qquad \theta^*(\underline{x}, t) = \sum_{i=1}^{n} N_i^e(\underline{x}) \theta_i^*(t) \qquad (V.80)$$

$$\nabla \eta(\underline{x}, t) = \sum_{i=1}^{n} B_i^e(\underline{x}) \eta_i(t), \qquad \nabla \theta(\underline{x}, t) = \sum_{i=1}^{n} B_i^e(\underline{x}) \theta_i(t) \qquad (V.81)$$

where n is the number of nodes in the element, e, containing, $\underline{x}$, and the shape functions are denoted by N_i^e. The matrix, B_i^e, is defined by the first derivative of the shape functions, which in 2D case, is

$$[B^e] = \begin{bmatrix} \frac{\partial N_1^e}{\partial x} & \frac{\partial N_2^e}{\partial x} & \cdots & \frac{\partial N_n^e}{\partial x} \\ \frac{\partial N_1^e}{\partial y} & \frac{\partial N_2^e}{\partial y} & \cdots & \frac{\partial N_n^e}{\partial y} \end{bmatrix}$$

An implicit Euler scheme is applied for the time discretisation. Using the notation, $\eta(t)$ and $\theta(t)$, for the known values of the current time step, t, $\eta(t + \delta t)$ and $\theta(t + \delta t)$ at time, $t + \delta t$, are estimated by solving the following equations:

$$\eta(t + \Delta t) \quad = \quad \eta(t) + \Delta t \dot{\eta}(t + \phi \Delta t) \qquad (V.82)$$

$$\theta(t + \Delta t) \quad = \quad \theta(t) + \Delta t \dot{\theta}(t + \phi \Delta t) \qquad (V.83)$$

$$\eta(0) = \eta_0 \qquad \theta(0) = \theta_0 \qquad (V.84)$$

Δt is the time increment, and η_0, θ_0 are the initial conditions for the lattice order and the crystal orientation. We deduce the element residual after substituting the nodal approximations in Equation V.77. Then,

$$\{R^e(\eta, \theta)\} = \left\{ \begin{array}{c} R^e_\eta(\eta, \theta) \\ R^e_\theta(\eta, \theta) \end{array} \right\}$$

where R^e_η and R^e_θ are, respectively, the element residuals for the variational formulation of the lattice order and crystal orientation,

$$(R^e_\eta)_i = \int_{\mathcal{V}^\rceil} N^e_i(\underline{x})\pi_\eta d\mathcal{V} - \int_{\mathcal{V}^\rceil} [B^e(\underline{x})]_{ij}.\underline{\xi}_{\eta j} d\mathcal{V} + \int_{\partial\mathcal{V}^\rceil} N^e(\underline{x})\zeta_\eta d\mathcal{S} = 0 \qquad (V.85)$$

$$(R^e_\theta)_i = \int_{\mathcal{V}^\rceil} N^e_i(\underline{x})\pi_\theta d\mathcal{V} - \int_{\mathcal{V}^\rceil} [B^e(\underline{x})]_{ij}.\underline{\xi}_{\theta j} d\mathcal{V} + \int_{\partial\mathcal{V}^\rceil} N^e(\underline{x})\zeta_\theta d\mathcal{S} = 0 \qquad (V.86)$$

The global residual vector can be obtained by assembling the element residuals for all elements using the matrix assembly $[A^e]$:

$$\{R(\eta)\} = \sum_{e=1}^{N} [A^e].\{R^e(\eta)\} = \{0\} \qquad (V.87)$$

Given a known set of nodal degrees of freedom at time, t, and assuming that the residual vanishes at the next time step, $t + \Delta t$, a set of non-linear equations result for the nodal degrees of freedom at $t + \Delta t$. It is solved with the Newton-Raphson method in an iterative method. This requires the computation of the generalised stiffness matrix which is obtained by derivation of the residual vector with respect to the degrees of freedoms (η, θ):

$$[K^e_t] = \left[\begin{array}{cc} [K^e_{\eta\eta}] & [K^e_{\eta\theta}] \\ [K^e_{\theta\eta}] & [K^e_{\theta\theta}] \end{array} \right]$$

Finally, the element generalised matrix is divided in four sub-matrix,

$$(K^e_{\eta\eta})ij = -\frac{\partial(R^e_1)i}{\partial\eta^e_j} = \int_{\mathcal{V}^\rceil} N^e_i.(\frac{\pi_\eta}{\partial\eta^e})_j d\mathcal{V} - \int_{\mathcal{V}^\rceil} [B^e(\underline{x})]_{ik}.[\frac{\partial\underline{\xi}_\eta}{\partial\eta^e}]_{kj} d\mathcal{V} \qquad (V.88)$$

$$(K^e_{\eta\theta})ij = -\frac{\partial(R^e_1)i}{\partial\theta^e_j} = \int_{\mathcal{V}^\rceil} N^e_i.(\frac{\pi_\eta}{\partial\theta^e})_j d\mathcal{V} - \int_{\mathcal{V}^\rceil} [B^e(\underline{x})]_{ik}.[\frac{\partial\underline{\xi}_\eta}{\partial\theta^e}]_{kj} d\mathcal{V} \qquad (V.89)$$

$$(K^e_{\theta\eta})ij = -\frac{\partial(R^e_2)i}{\partial\eta^e_j} = \int_{\mathcal{V}^\rceil} N^e_i.(\frac{\pi_\theta}{\partial\eta^e})_j d\mathcal{V} - \int_{\mathcal{V}^\rceil} [B^e(\underline{x})]_{ik}.[\frac{\partial\underline{\xi}_\theta}{\partial\eta^e}]_{kj} d\mathcal{V} \qquad (V.90)$$

$$(K^e_{\theta\theta})ij = -\frac{\partial(R^e_2)i}{\partial\theta^e_j} = \int_{\mathcal{V}^\rceil} N^e_i.(\frac{\pi_\theta}{\partial\theta^e})_j d\mathcal{V} - \int_{\mathcal{V}^\rceil} [B^e(\underline{x})]_{ik}.[\frac{\partial\underline{\xi}_\theta}{\partial\theta^e}]_{kj} d\mathcal{V} \qquad (V.91)$$

V.3.3   Validation of the FE Implementation

In order to compare analytical solution and FE results, cases where $h(\eta) = 0$ are considered, that is $|\nabla\theta|^2$ is not included in the free energy.

V.3.3.1   Example of a Bicrystal

If we consider two semi-infinite grains with orientations indicated by θ_+ and θ_-, the free energy of the bicrystal with $h(\eta)) = 0$ takes the following form :

$$\mathcal{F}(\eta, \theta) = \int_\Omega (\frac{\alpha^2}{2}|\nabla\eta|^2 + f(\eta) + g(\eta)|\nabla\theta|)dV \qquad (V.92)$$

Simple choices for $f(\eta)$ and $g(\eta)$, which satisfy the criteria stated above, are

$$f(\eta) = \frac{1}{2}(1 - \eta)^2 \tag{V.93}$$

$$g(\eta) = \eta^2 \tag{V.94}$$

The form for $g(\eta)$ is chosen for mathematical convenience. The resulting equations of motion are

$$P_\eta \dot{\eta} = \alpha^2 \Delta \eta + 1 - \eta - 2\eta|\nabla\theta| \tag{V.95}$$

$$P_\theta \eta^2 \dot{\theta} = \nabla.[\eta^2 \frac{\nabla\theta}{|\nabla\theta|}], \tag{V.96}$$

where P_η and P_θ are inverse mobilities. For the one-dimensional case, the equilibrium grain boundary solutions, $\eta(x)$ and $\theta(x)$ for a bicrystal, must satisfy the following equations :

$$0 = \alpha^2 \eta_{,xx} + 1 - \eta - 2\eta|\theta_{,x}| \tag{V.97}$$

$$0 = \nabla.[\eta^2 \frac{\theta_{,x}}{|\theta_{,x}|}]_{,x}, \tag{V.98}$$

where the subscripts, x indicates derivation with respect to x. Dirichlet boundary conditions $\theta(\pm\infty) = \theta_\pm$ are applied as well as the condition, $0 \leq \eta(x) \leq 1$. Without loss of generality, the center of the grain boundary is located at x = 0. If $\eta(x)$ has only one minimum, it can be shown that the solution for $\theta(x)$ is a step function at the point, where η takes minimum :

$$\theta(x) = \begin{cases} \theta_-, & -\infty < x < 0, \\ \theta_+, & 0 < x < \infty \end{cases}$$

Note that $|\theta_{,x}| = \Delta\theta\delta(x)$, where $\Delta\theta = |\theta_+ - \theta_-|$ and that $\delta(x)$ is the Dirac delta function. Integrating Equation V.97 gives

$$\eta(x) = 1 - (1 - \eta_0)\exp\left\{-\frac{|x|}{\alpha}\right\} \tag{V.99}$$

where, $\eta_0 = \eta(0)$, and should be determined by integration of Equation V.98 through the discontinuity in θ:

$$\alpha^2[\eta_{,x}]_{x=0^-}^{x=0^+} = 2\eta_0\Delta\theta, \tag{V.100}$$

which gives

$$\eta_0 = \frac{1}{1 + \Theta} \tag{V.101}$$

where $\Theta = \frac{\Delta\theta}{\alpha}$ is a scaled misorientation.

The mesh used in the FE simulation is described in Figure V.18a. Boundary conditions and the initial orientation, θ, are imposed as in the analytical study while the lattice order, η is assumed to be constant ($\eta = 1$). Figure V.18b shows the equilibrium contour of η. In Figure V.19, profiles of the lattice order and the crystal orientation obtained analytically and FE are identical for several values of the parameter α. As $h(\eta) = 0$, $\nabla\theta$ is singular.

(a)   (b)
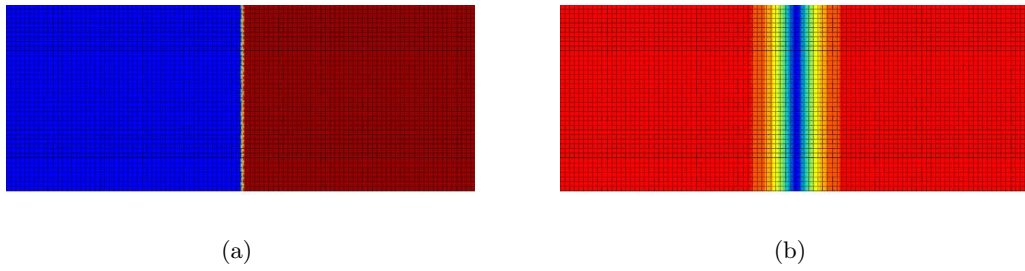
Figure V.18 : Stable grain boundary of a bicrystal. Contour of (a) the lattice order (η) and (b) the crystal orientation (θ)

(a)   (b)
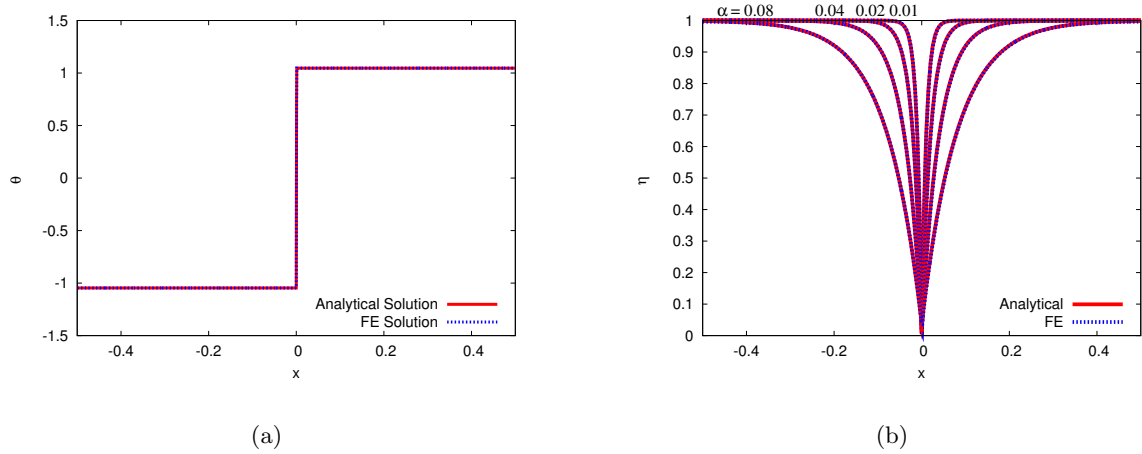
Figure V.19 : Superposition of the analytical and FE solutions for (a) the lattice order (η) and (b) the crystal orientation (θ)
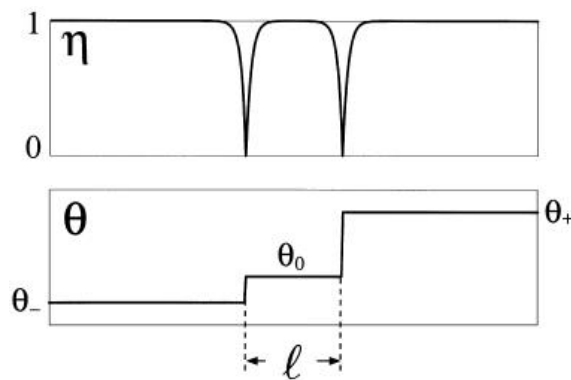
Figure V.20 : Analytical profiles of (a) the lattice order (η) and (b) the crystal orientation (θ) (Kobayashi *et al.*, 2000)

(a) t=0s

(b) t=150s

(c) t=400s

(d)
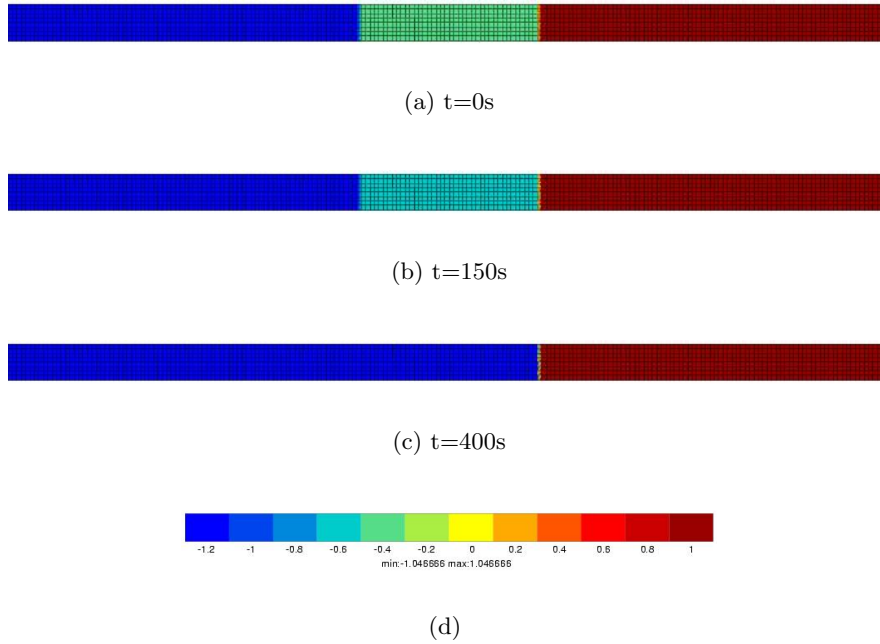
Figure V.21 : Rotation of three grain crystals at different times. Contour of the crystal orientation (θ)

V.3.3.2   Example of a Three Grain Polycrystal

We considered the case where a narrow band-shaped interior grain with thickness, l, lies between two semi-infinite grains with orientations indicated by θ_+ and θ_-. Let the orientation of the interior grain be θ_0, and assume that $l >> \alpha$. Then the system is described by η and θ as shown in Figure V.20. The system can eliminate the interior grain by two independent mechanisms: by moving the boundaries towards each other at fixed misorientations and by adjusting the orientation(s) of the interior grain(s) at fixed boundary spacing. Since the grain boundary is flat, there is no driving force due to the curvature. Therefore rotation should be the dominant process to decrease the energy.

Assuming that $\theta_- < \theta_0 < \theta_+$, (Kobayashi *et al.*, 2000) proposed an analytical solution to this problem with the evolution of θ which is plotted in Figure V.22. The unconstrained grain(s) rotate to lower the energy by adjusting the two boundary misorientations until the equilibrium solution is attained. The mesh used in FE simulation is described in Figure V.21a. Dirichlet boundary conditions and initial orientation, θ, are imposed as in the analytical study while the lattice order, η is assumed constant ($\eta = 1$). Figures V.21b, c show the evolution of the contour of θ where the middle grain is vanishing. Profiles of crystal orientation obtained by the FE simulation for several mesh sizes and by analytical study are superimposed in Figure V.22. As $h(\eta) = 0$, the change of the crystal orientation through the grain is in one element for each boundary. Therefore, the size of the grain boundary decrease with decreasing the mesh size and the FE simulation is highly mesh dependent. However, the rotation velocity of the middle grain tends to the analytical solution with mesh decreasing size.
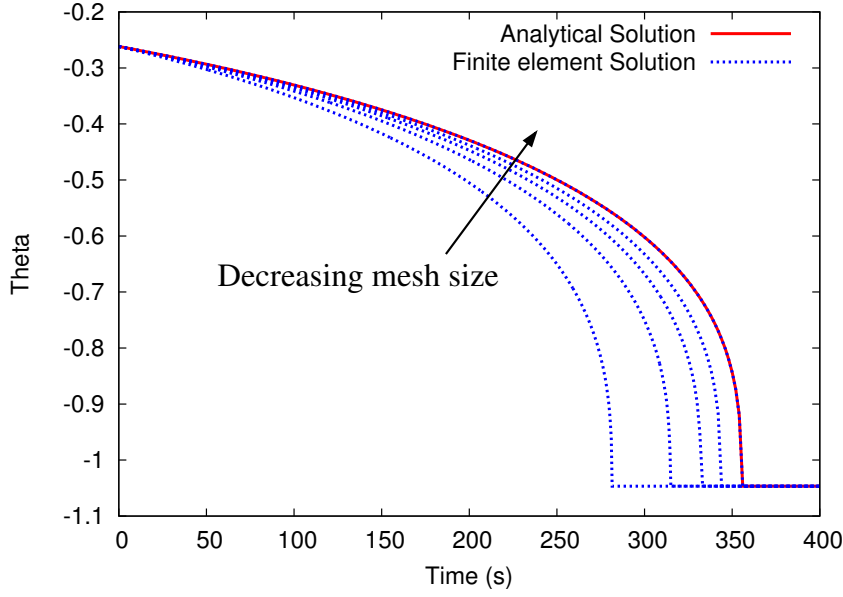
Figure V.22 : Superposition of the analytical and FE solutions for (a) the lattice order (η) and (b) the crystal orientation (θ)

V.4   Calibration of the Free Energy Parameters

The materials used for the simulation is Al. The Read-Shockley model is used to fit the energy for small misorientation angles. For high misorientation angles, the grain boundary energy is assumed to be independent of the misorientation and of the boundary plane. For an aluminium foil, (Yang *et al.*, 2001) found the grain boundary energy to be $0.37 Jm^{-2}$. Apart from special low Σ boundaries, the boundary properties remain effectively independent of misorientation. Here,

$$\gamma = \gamma_m \frac{\Delta\theta}{\Delta\theta_m}(1 - \ln(\frac{\Delta\theta}{\Delta\theta_m})) \quad for \quad \Delta\theta \leq 15°, \tag{V.102}$$

$$\gamma = \gamma_m \quad for \quad \Delta\theta \geq 15, \tag{V.103}$$

where γ_m is the grain boundary energy if $\theta_m \geq 15°$.

The change of θ and ϕ through the interface creates energy; the grain boundary energy. The surface energy (for the $h(\eta) = 0$ case) for a bicrystal can be expressed analytically. Note that the energy is localized in the α-neighbourhood of the grain boundary, the surface excess or grain boundary energy, and will be referred to as γ_{gb}. The total free energy can be separated into two terms: the contribution due to disordering, E_{dis} (deviation of η from 1), and the contribution from the singular incompatibility at $x = 0$ (the jump in θ), E_{inc}. There is no stored energy, $E_{st} = 0$. The equilibrium grain boundary solution (θ and η) of a one dimensional bicrystal centered in $x = 0$ must satisfy the following evolutionary equations :

$$\alpha^2 \eta_{,xx} - f'(\eta) - sg'(\eta)|\theta_{,x}| = 0, \tag{V.104}$$

$$s[g(\eta)\frac{\theta_{,x}}{|\theta_{,x}|}]_{,x} = 0. \tag{V.105}$$

In the regions where x > 0 or x < 0,

$$0 = \alpha^2 \eta_{,xx} - f'(\eta) \tag{V.106}$$

Integrating,

$$\frac{\alpha^2}{2}\eta_{,x}^2 = f(\eta) \tag{V.107}$$

$$\alpha\eta_{,x} = +\sqrt{2f(\eta)} \quad for \quad x > 0, \quad \alpha\eta_{,x} = -\sqrt{2f(\eta)} \quad for \quad x < 0 \tag{V.108}$$

and through the discontinuity in θ leaves:

$$\frac{s\Delta\theta}{\alpha} = \frac{2\sqrt{2f(\eta_0)}}{g'(\eta_0)} \tag{V.109}$$

Furthermore,

$$E_{dis} = \int_{-\infty}^{\infty} [\frac{\alpha^2}{2}\eta_{,x}^2 + f(\eta)]dx \tag{V.110}$$

$$E_{dis} = 2\int_0^{\infty} 2f(\eta)dx = 2\alpha\int_0^{\infty}\sqrt{2f(\eta)}\eta_{,x}dx = 2\alpha\int_{\eta_0}^1\sqrt{2f(\eta)}d\eta \tag{V.111}$$

$$E_{inc} = \int_{-\infty}^{\infty} [sg(\eta)|\theta_{,x}|]dx = sg(\eta_0)\Delta\theta \tag{V.112}$$

The energy can be expressed as a function of the misorientation. Then,

$$\gamma_{gb} = 2\alpha\int_{\eta_0}^1\sqrt{2f(\eta)}d\eta + g(\eta_0)\Delta\theta. \tag{V.113}$$

As chosen by KWC, the function f exhibits a single well in 1, thus

$$f(\eta) = \frac{\omega^2}{2}(1-\eta)^2, \tag{V.114}$$

Therefore,

$$\gamma_{gb} = \alpha\omega(1-\eta_0)^2 + g(\eta_0)\Delta\theta \tag{V.115}$$

To fit the Read-Shockley curve, we take $g(\eta)$ as a polynomial function of third order,

$$g(\eta) = a|\eta| + b\eta^2 + c|\eta|^3 \tag{V.116}$$

By replacing $g(\eta)$ in Equation V.115, we found that

$$\eta_0 = \frac{\alpha\omega}{3c\Delta\theta}\Big(-(\frac{b\Delta\theta}{\alpha\omega}+1) + \sqrt{(\frac{b\Delta\theta}{\alpha\omega}+1)^2 - \frac{6c\Delta\theta}{\alpha\omega}(\frac{a\Delta\theta}{2\alpha\omega}-1)}\Big) \tag{V.117}$$

Replacing η_0 in equation V.109, the analytical solution of the energy is obtained, see Figure V.23. As we can see in the expression of η_0, the parameters α and ω appears only in the product $\alpha\omega$. To be independent of the mesh size, the θ change through the interface can't be sharp. To have a smooth interface, the term $h(\eta)|\nabla\theta|^2$ is taken into account in the free energy.

$$h(\eta) = d\eta^2 + e \tag{V.118}$$

Adding $h(\eta)$ to the free energy increases significantly the grain boundary energy as seen in Figure V.24.
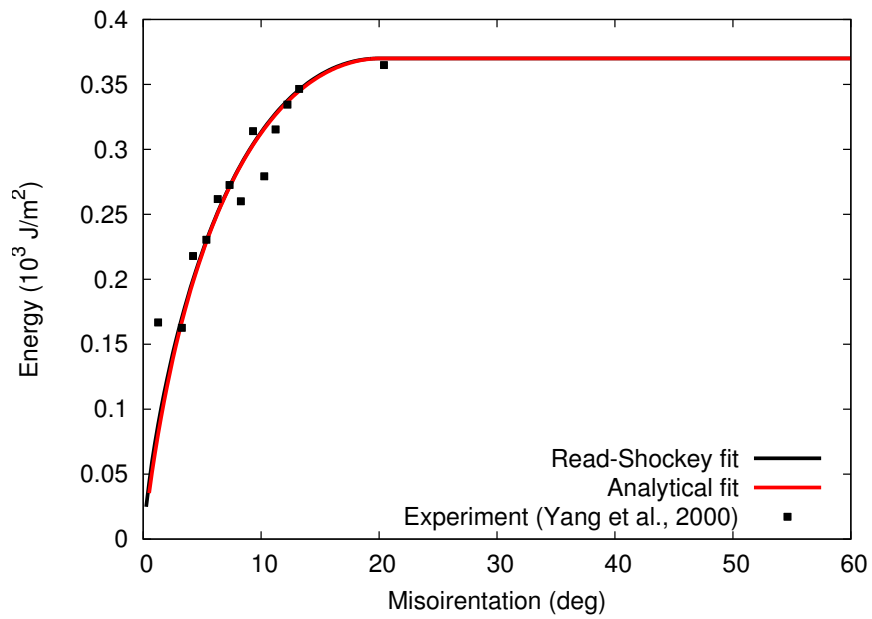
Figure V.23 : Grain boundary energy calibration with $\alpha = 0.04$, $a = 2.10$, $b = 0.95$, $c = 1.35$, $\omega = 7.50$
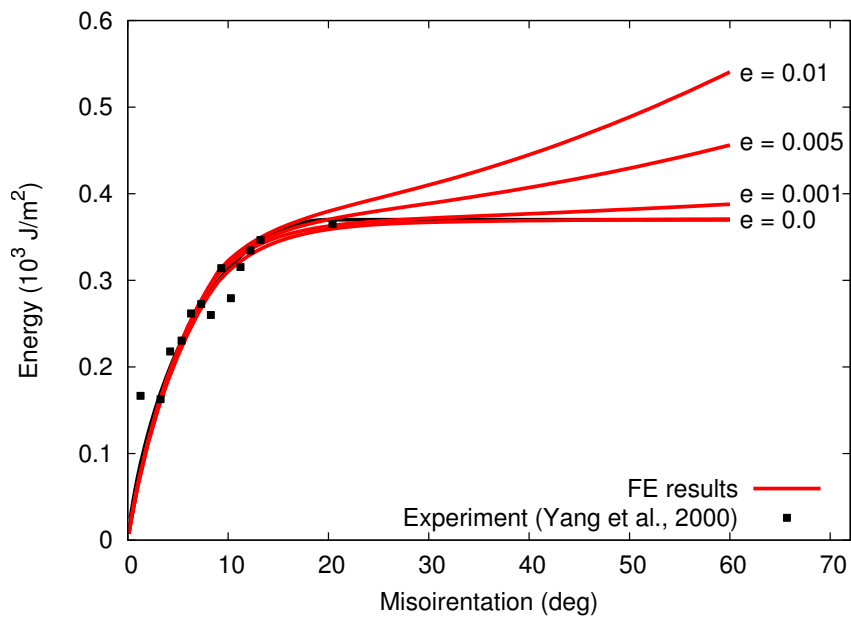

Figure V.24 : Grain boundary energy calibration with $\alpha = 0.04$, $a = 1.00$, $b = 0.95$, $c = 1.35$, $d = 0.45$, $\omega = 7.50$

V.5   Conclusions

The phase field model is based on two continuous field variables, the grain orientation, θ and the lattice order, η, to describe the microstructure. The stored energy has been introduced in the free energy of the phase field model to take into account its influence on grain boundary motion. A finite element formulation for the phase field model has been presented, based on the introduction of generalized stresses and their balance, and the framework of the thermodynamics of irreversible processes. Three evolutionary equations, for the grain orientation, θ, the lattice order, η, and the stored energy have been developed. The parameters of the free energy have been calibrated on the Read-Shockley energy for low angle grain boundaries.

References

AMMAR K., APPOLAIRE B., CAILLETAUD G., FEYEL F., AND FOREST S. (2009). *Finite element formulation of a phase field model based on the concept of generalized stresses.* Comput. Mat. Sci., vol. 45 n° 3, pp 800–805. 17th International Workshop on Computational Mechanics of Materials, Paris, FRANCE, AUG 22-24, 2007.

BERNACKI M., CHASTEL Y., COUPEZ T., AND LOGE R. E. (2008). *Level set framework for the numerical modelling of primary recrystallization in polycrystalline materials.* Scripta Materialia, vol. 58 n° 12, pp 1129–1132.

BURGERS J.M. (1939). *Some considerations on the fields of stress connected with dislocation in a regular crystal lattice I.* Proceedings of the Koninklijke Nederlandse Akad. Wetenschappen, vol. 42, pp 293–325.

CAHN J.W. AND HILLIARD J.E. (1959). *On the equilibrium segregation at a grain boundary.* Acta Metallurgica, vol. 7, pp 219–221.

CHAN H.M. AND HUMPHREYS F.J. (1984). *The recrystallisation of aluminium-silicon alloys containing a bimodal particle distribution.* Acta Metallurgica, vol. 32 n° 2, pp 235–243.

CHEN L.Q. AND FAN D.A. (1996). *Computer simulation model for coupled grain growth and Ostwald ripening-application to Al2O3-ZrO2 two-phase systems.* Journal of the american ceramic society, vol. 79 n° 5, pp 1163–1168.

CHEN L.Q. AND WANG Y.Z. (1996). *The continuum field approach to modeling microstructural evolution.* Jom-journal of the minerals metals & materials society, vol. 48 n° 12, pp 13–18.

FRIED E. AND GURTIN M.E. (1996). *A phase-field theory for solidification based on a general anisotropic sharp-interface theory with interfacial energy and entropy.* Physica D, vol. 91 n° 1-2, pp 143–181.

GEIGER J., ROOSZ A., AND BARKOCZY P. (2001). *Simulation of grain coarsening in two dimensions by cellular-automaton.* Acta Materila, vol. 49 n° 4, pp 623–629.

GILL S.P.A. AND COCKS A.C.F. (1996). *A variational approach to two dimensional grain growth .2. Numerical results.* Acta Materila, vol. 44 n° 12, pp 4777–4789.

GOTTSTEIN G. AND SEBALD R. (2001). *Modelling of recrystallization textures.* Journal of Materials Processing Technology, vol. 117 n° 3, Sp. Iss. SI, pp 282–287.

GOTTSTEIN G. AND SHVINDLERMAN L.S. (1992). *On the orientation dependence of grain-boundary migration.* Scripta Metallurgica et Materialia, vol. 27 n° 11, pp 1515–1520.

GOTTSTEIN G. AND SHVINDLERMAN L.S. (1999). *Grain boundary migration in metals, thermodynamics, kinetics, applications.* CRC Press.

GURTIN M.E. AND LUSK M.T. (1999). *Sharp-interface and phase-field theories of recrystallization in the plane.* Physica D, vol. 130 n° 1-2, pp 133–154.

HASSON G.C. AND GOUX C. (1971). *Interfacial energies of tilt boundaries in aluminium. Experimental and theoretical determination.* Scripta Metallurgica, vol. 5, pp 889–894.

HERRING C. (1951). *Some theorems on the free energies of crystal surfaces.* Physical Review, vol. 82, pp 87–93.

HUANG Y. AND HUMPHREYS F.J. (1999). *Measurements of grain boundary mobility during recrystallization of a single-phase aluminium alloy.* Acta Materialia, vol. 47 n° 7, pp 2259–2268.

HUMPHREYS F.J. AND HATHERLY M. (2004). *Recrystallization and Related Annealing Phenomena.* Pergamon.

HURLEY P.J. AND HUMPHREYS F.J. (2003). *The application of EBSD to the study of substructural development in a cold rolled single-phase aluminium alloy.* Acta Materialia, vol. 51 n° 4, pp 1087–1102.

KHACHATURYAN A.G. (1996). *Long-range order parameter in field model of solidification.* Philosophical magazine a-physics of condensed matter structure defects and mechanical properties, vol. 74 n° 1, pp 3–14.

KOBAYASHI R., WARREN J.A., AND CARTER W.C. (2000). *A continuum model of grain boundaries.* Physics D, vol. 140, pp 141–150.

MA N., KAZARYAN A., DREGIA D., AND WANG Y. (2004). *Computer simulation of texture evolution during grain growth: effect of boundary properties and initial microstructure.* Acta Mater., vol. 52, pp 3869–3879.

MARX V., REHER F.R., AND GOTTSTEIN G. (1999). *Simulation of primary recrystallization using a modified three-dimensional cellular automaton.* Acta Materialia, vol. 47 n° 4, pp 1219–1230.

MOELANS N., WENDLER F., AND NESTLER B. (2009). *Comparative study of two phase-field models for grain growth.* Computational Materials Science, vol. 46 n° 2, pp 479–490.

MOLODOV D.A., CZUBAYKO U., GOTTSTEIN G., AND SHVINDLERMAN L.S. (1995). *Mobility of 111 tilt grain-boundaries in the vicinity of the special misorientation sigma=7 in bicrystals of pure aluminum.* Scripta Metallurgica et Materialia, vol. 32 n° 4, pp 529–534.

MOLODOV D.A., SWIDERSKI J., GOTTSTEIN G., LOJKOWSKI W., AND SHVINDLERMAN L.S. (1994). *Effect of pressure on grain-boundary migration in aluminum bicrystals.* Acta Metallurgica et Materialia, vol. 42 n° 10, pp 3397–3407.

MURR L.E. (1975). *Interfacial phenomena in metals and alloys.* Addison-Wesley.

NESTLER B. AND WHEELER A.A. (1998). *Anisotropic multi-phase-field model: Interfaces and junctions.* Physical review e, vol. 57 n° 3, Part A, pp 2602–2609.

OSHER S. AND SETHIAN J.A. (1988). *Fronts propagating with curvature-dependent speed - algorithms based on hamilton-jacobi formulations.* Journal of Computational Physics, vol. 79 n° 1, pp 12–49.

QUÉRÉ Y. (1987). *Physique des Matériaux.* Ellipses.

ROLLETT A.D., LUTON M.J., AND SROLOVITZ D.J. (1992). *Microstructural simulation of dynamic recrystallization.* Acta Metallurgica et Materialia, vol. 40 n° 1, pp 43–55.

SERRE B. (2007). *Simulation numérique 3D de la croissance de grains par la méthode des éléments finis.* Thèse de Doctorat, Ecole des Mines de Saint Etienne.

SHOCKLEY W. AND READ W.T. (1949). *Quantitative predictions from dislocation models of crystal grain boundaries.* Physical Review, vol. 75, pp 692.

SOARES A., FERRO A.C., AND FORTES M.A. (1985). *Computer-simulation of grain-growth in a bidimensional polycrystal.* Scripta Metallurgica, vol. 19 n° 12, pp 1491–1496.

SROLOVITZ D.J. (1986). *Grain-growth phenomena in films - a Monte-Carlo approach.* Journal of Vacuum Science & Technology A, vol. 4 n° 6, pp 2925–2931.

STEINBACH I., PEZZOLLA F., NESTLER B., SEESSELBERG M., PRIELER R, SCHMITZ GJ, AND REZENDE JLL (1996). *A phase field concept for multiphase systems.* Physica D, vol. 94 n° 3, pp 135–147.

SUWA Y., SAITO Y., AND ONODERA H. (2007). *Phase field simulation of stored energy driven interface migration at a recrystallization front.* Materials science and engineering A, vol. 457 n° 1-2, pp 132–138.

TAKAKI T., HISAKUNI Y., HIROUCHI T., YAMANAKA A., AND TOMITA Y. (2009). *Multi-phase-field simulations for dynamic recrystallization.* Computational Materials Science, vol. 45 n° 4, pp 881–888.

TAVERNIER P. AND SZPUNAR J.A. (1991). *A Monte-Carlo simulation applied to the modeling of nucleation of texture.* Acta Metallurgica et materialia, vol. 39 n° 4, pp 557–567.

UBACHS R.L.J.M., SCHREURS P.J.G., AND GEERS M.G.D. (2005). *Phase field dependent viscoplastic behaviour of solder alloys.* International Journal of Solids and Structures, vol. 42 n° 9-10, pp 2533–2558.

YANG C.-C., ROLLET A.D., AND MULLINS W.W. (2001). *Measuring relative grain boundary energies and mobilities in an aluminium foil from triple junction geometry.* Scripta materialia, vol. 44, pp 2735–2740.

Chapter -VI-

Grain Boundary Migration

Contents

VI.1   Introduction

A driving force for grain boundary migration arises when a boundary displacement leads to a reduction of the total energy. In recrystallisation phenomena, two kinds of energy are responsible for the grain boundary motion; an excess of energy due to grain boundary itself and a free energy difference between the adjacent grains due to the energy stored during deformation. Both driving forces participate in the recrystallisation process. First, at the early beginning, when the recrystallisation nuclei appear, their kinetics are controlled by curvature, then by stored energy. This is the primary recrystallisation. After leaving the crystal free of dislocations, the microstructure is made of small grains. To reduce its energy due to the large grain boundary quantity, grain growth occurs driven by curvature effects.

## VI.1.1   Nucleation of Recrystallization

Nucleation is a major factor in determining both the size and orientation of the grains of final microstructure. Two phenomena have been identified for describing the nucleation process; the classical nucleation and the strain induced boundary migration (SIBM). In the classical nucleation, nuclei originates from small volumes which pre-exist in the deformed microstructure (Humphreys and Hatherly, 2004). Nuclei are highly misoriented from the deformed matrix while in SIBM, the new grains have similar orientations to the old grains from which they have grown, see Figure VI.1. SIBM involves the bulging of part of a pre-existing grain boundary, leaving a region behind the migrating boundary with a lower dislocation content as shown schematically in Figure VI.2. The SIBM mechanism identified first by (Beck and Sperry, 1950) is essentially at low strain and is replaced by the classical nucleation at higher strain. For instance, SIBM phenomena are observed only at reductions $< 40\%$ in pure aluminium.
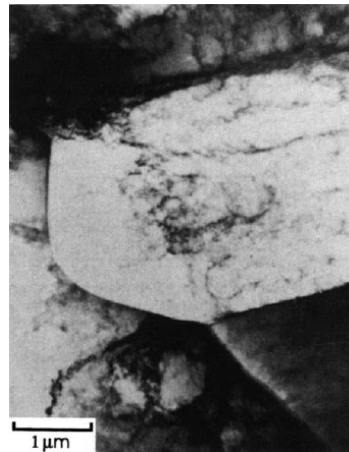
Figure VI.1 : TEM micrograph of SIBM in copper deformed 14% in tension and annealed 5 min at $234°C$, (Bailey and Hirsch, 1962)

VI.1.2   Growth of Nuclei

As explained in the chapter IV, the boundary velocity (v) which arises from stored dislocations or the grain boundary geometry was found to be proportional to the driving force (P).

$$v = MP \tag{VI.1}$$
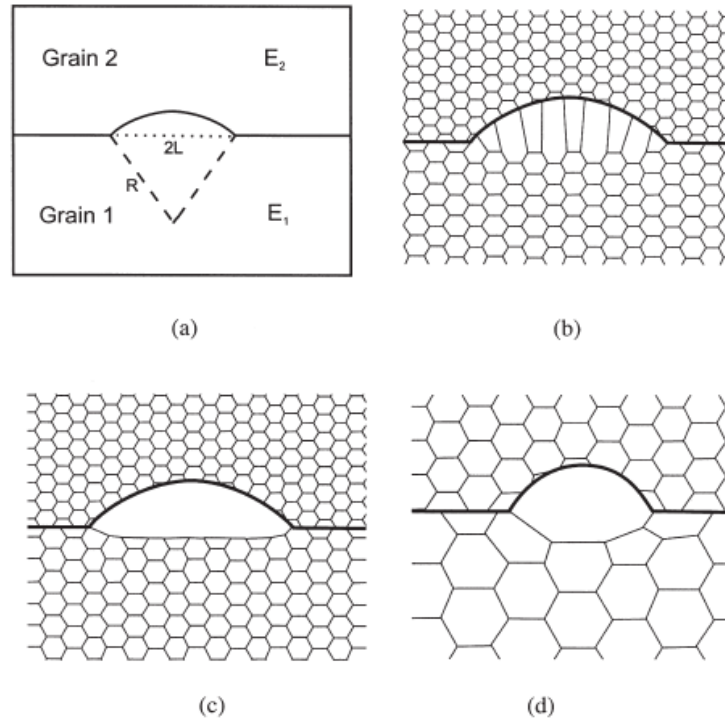
Figure VI.2 : (a) SIBM of a boundary separating a grain of low stored energy (E1) from one of higher energy (E2), (b) dragging of the dislocation structure behind the migrating boundary, (c) the migrating boundary is free from the dislocation structure, (d) SIBM originating at a single large subgrain (Humphreys and Hatherly, 2004)

where the boundary mobility, M, is a quantitative measure of the kinetic properties of a grain boundary. It is generally assumed that boundary mobility is controlled by a single activated process with an Arrhenius relation,

$$M = M_0 \exp(-Q/k_B T) \tag{VI.2}$$

where Q is the activation energy (enthalpy) for migration, k_B is Boltzmann's constant and M_0 is a temperature independent factor and T is the temperature.

The driving force due to stored energy provided by the dislocation density responsible for the growth of new grains is given by

$$P = \Delta E_{st} \tag{VI.3}$$

where ΔE_{st} is the difference of energy between new grains and deformed grains. The stored energy of the new grains is considered null. However, these new grains of radius R create grain boundary energy due to their expansion. Therefore, an opposing driving force is arising from the curvature of their boundary,

$$P \approx \frac{\gamma}{R}. \tag{VI.4}$$

where γ is the grain boundary energy. Therefore, below a critical grain size there would be no net driving force for recrystallisation.

VI.1.3 Kinetics of Primary Recrystallization

The progress of recrystallisation with time during isothermal annealing is commonly represented by a plot of the volume fraction of material recrystallized (X_v) as a function
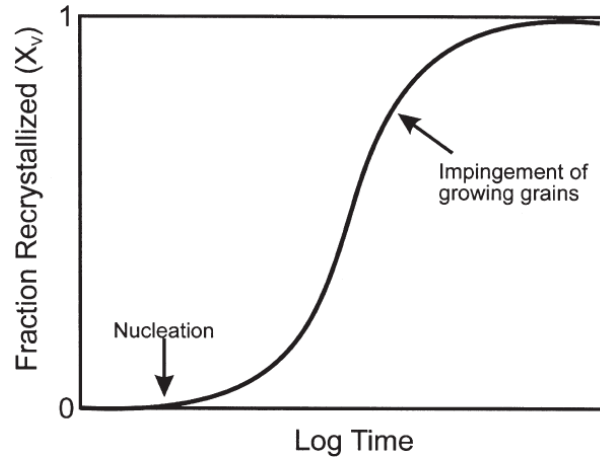
Figure VI.3 : Typical recrystallisation kinetics during isothermal annealing

of log(time), see Figure VI.3. Johnson-Mehl-Avrami-Kolmogorov proposed a model based on randomly distributed nucleation sites to describe the curve in Figure VI.3. A more generally relationship between the volume fraction of material recrystallized (X_v) and the time (t), called usually the JMAK equation, is obtained from their model,

$$X_v = 1 - \exp(-Bt^n) \tag{VI.5}$$

where B and n are fitting parameters. Numerous investigations found values of n of the order of 1 for aluminium.

VI.1.4   Grain Growth Following Recrystallization

After recrystallisation process, most of dislocations have been annihilated, stored energy has vanished. However, the microstructure is not stable because of the large of grain boundary. Grain growth may occur in order to reduce this excess of grain boundary area. Assuming that the radius of curvature is proportional to the mean radius ($\overline{R}$) of an individual grain and the grain boundary energy γ_{gb} is the same for all boundaries, (Burke and Turnbull, 1952) proposed a parabolic law to describe the mean grain size evolution,

$$\overline{R} = Bt^{1/n} \tag{VI.6}$$

where n, the grain growth exponent is theoretically 2.
Experimentally, (Gordon and El-Bassyouni, 1965) found the grain growth exponent to be 4 for isothermal grain growth in high purity aluminium.

In this chapter, the kinetics of grain boundary motion due to both phenomena, curvature and stored energy, are studied. In both cases, variation of the grain boundary mobility with grain boundary misorientation is examined. Since motion of grain boundary systems are also controlled by junctions (Mattissen *et al.*, 2005), triple and quadruple junction will be explored. Finally, the phase field model is applied to a microstructure. Parameters are scrutinized to see the effect on the grain morphology, the misorientation and the grain size evolution.

(a)   (b)   (c)   (d)
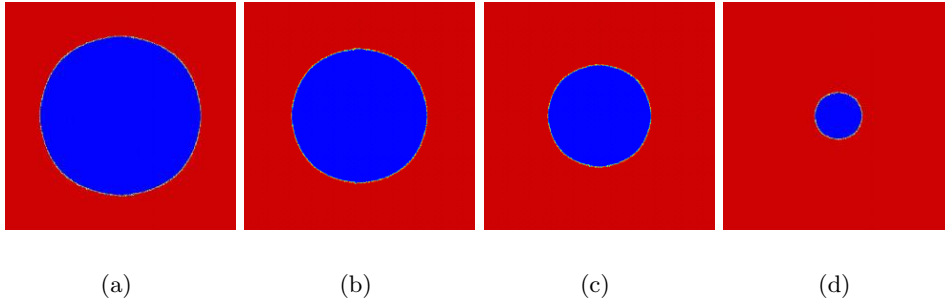
Figure VI.4 : Shrinking of a grain ($\theta = -\frac{\pi}{4}$) embedded in a large grain ($\theta = \frac{\pi}{4}$)

VI.2 Curvature as a Driving Force

VI.2.1 Grain Boundary Mobility

VI.2.1.1 Misorientation Dependency

In the applications to be described in the section, there is no stored energy. Since grain boundary motion does not occur in bicrystal with planar grain boundary, curvature is introduced in order to investigate grain boundary motion dependency on misorientation. In numerical simulations, in order to drive the grain boundary due to geometrical curvature, the cusp profile of η and the discontinuous profile of θ have to be smoothed, and this is achieved by inclusion of higher order terms in $|\nabla\theta|$ in Equation V.27. Thus, in addition to the terms already described, $h(\eta) \neq 0$. The introduction of the higher order term, $|\nabla\theta|^2$, induces finite gradients in θ in contrast to the step profile found in the analytical solutions presented in the chapter IV.

To analyse the motion, we consider a grain embedded in a large grain. The curvature is considered as the only driving force for grain boundary motion. The initial grain size is $1mm$. Neumann boundary conditions is imposed on η and Dirichlet on θ. The results of the circular grain motion is shown in Figure VI.4. The grain shrinks and therefore, reduction in grain boundary area is found. In Figure VI.5, the velocity of the interface between the grains associated with the decrease in the free energy of the system by a reduction in grain boundary area was found to be proportional to the curvature of the interface which is coherent with experimental observations (Upmanyu *et al.*, 1999),

$$\dot{R} = \frac{M\gamma_{gb}}{R} \tag{VI.7}$$

where R is the radius of a circular grain, M is the mobility and γ_{gb} is the grain boundary energy (per unit area). While the curvature of the grain boundary is a purely geometrical variable, the mobility M and the grain boundary energy γ_{gb} are intrinsic material parameters. Grain boundary energy γ_{gb} has been studied in chapter V and high angle grain boundary energy was found to be constant when the term $|\nabla\theta|^2$ is not included and does not vary more than a factor of two when it is introduced.

To see the effect of misorientation on grain boundary kinetics, several grain embedded in a large grain are considered with different misorientations. Since the grain boundary energy γ_{gb} is difficult to extract from experimental measures, reduced mobility defined by the product

(a)

(b)
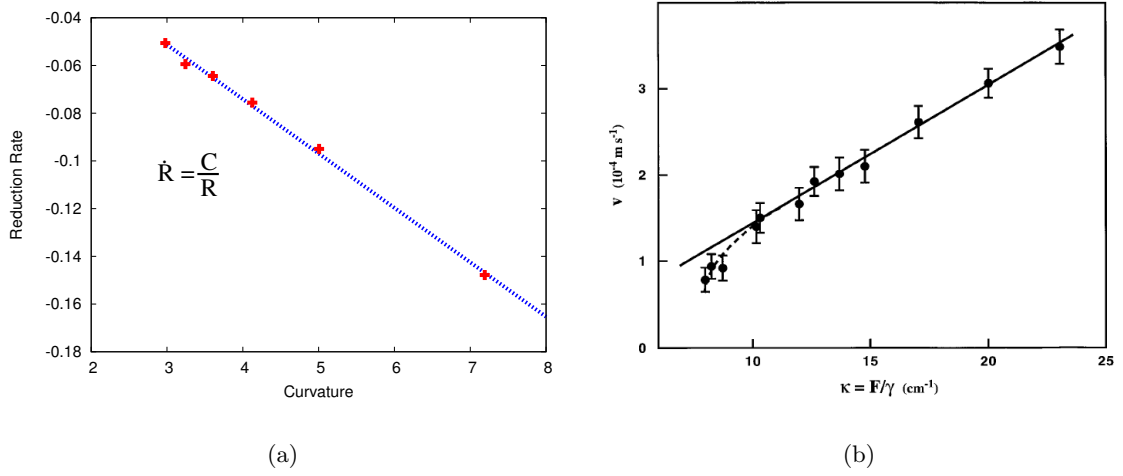
Figure VI.5 : (a) Numerical and (b) Experiment measurements (Upmanyu *et al.*, 1999) of grain boundary velocity vs boundary curvature for a general grain boundary in high purity Al,

of the mobility and the grain boundary energy $A_m = M\gamma_{gb}$ is introduced. Eq.VI.7 becomes

$$\dot{R} = \frac{A_m}{R}. \tag{VI.8}$$

The reduced mobility which is calculated by taking the slope of the curve $\dot{R} - 1/R$ shown in Figure VI.5 for each misorientation, is plotted in Figure VI.6. The ability of grain boundaries (GB) to move has been found to be strongly dependent on misorientation of the adjacent grains as in experimental observation (Yang *et al.*, 2001, Gottstein and Sebald, 2001). The reduced mobility is increasing with the misorientation and approaches a constant.

LAGBs are distinguished from HAGBs in order to compare more in detailed FE and experimental results. Figure VI.7 shows relative boundary mobility of LAGBs over HAGBs mobility. In both cases, there is a misorientation value where the mobility increases significantly, 11° in experimental and 6° in FE results. The LAGBs mobility over HAGBs mobility have similar values with a more significant gap at the transition misorientation in the numerical predictions. In both cases, the grain boundary mobility evolves in a non-monotonic way with respect to the misorientation angle. However, the model does not describe the cusps observed in Figure VI.8 for Σ grain boundaries.

VI.2.1.2   Parameter Study of the Model

The previous results have been obtained from specific parameters, $e = 0.015(J/m)$ and $\beta_\eta = 10^{-4}(s)$. Several grain embedded in a large grain with the same previous boundary conditions are considered with different misorientations for different values of the parameter e (term in front of $|\nabla\theta|^2$). Results are in Figure VI.9. The reduced mobility approaches a constant value with increasing e and the dependency of the reduced grain boundary mobility on misorientation angle decreases.

The parameter e controls the interface size and therefore the grain boundary energy. As
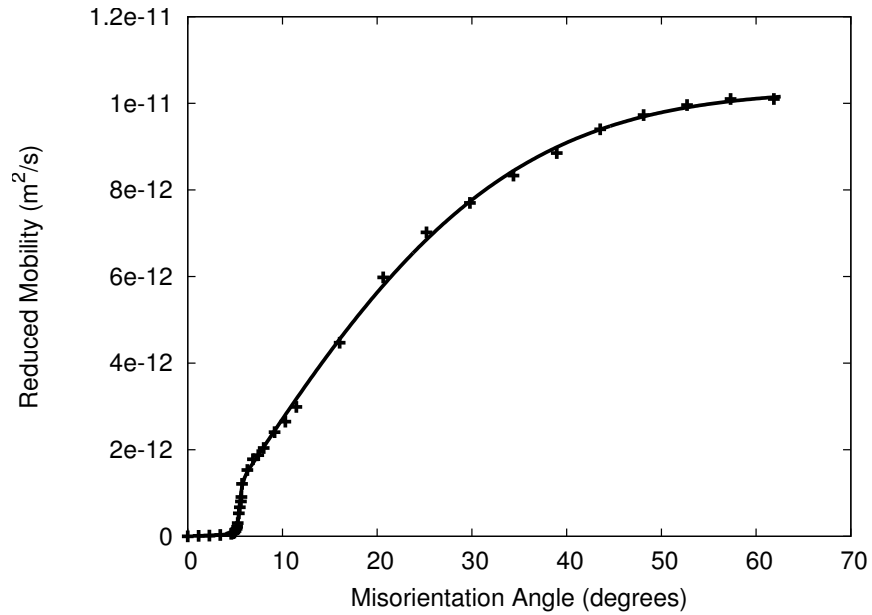
Figure VI.6 : Reduced mobility dependency on grain boundary misorientation
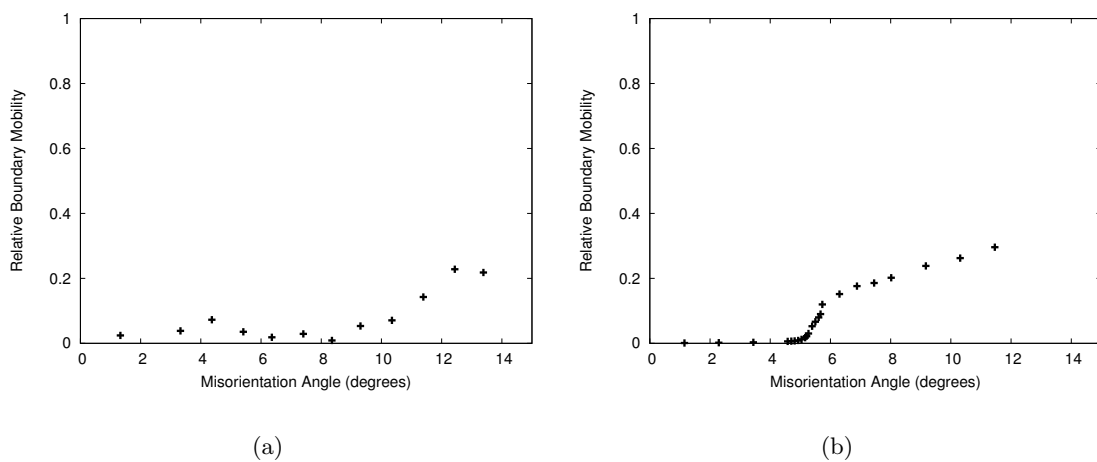
Figure VI.7 : (a) Experimental (Yang *et al.*, 2001) and (b) numerical variation of relative boundary mobility with misorientation angle
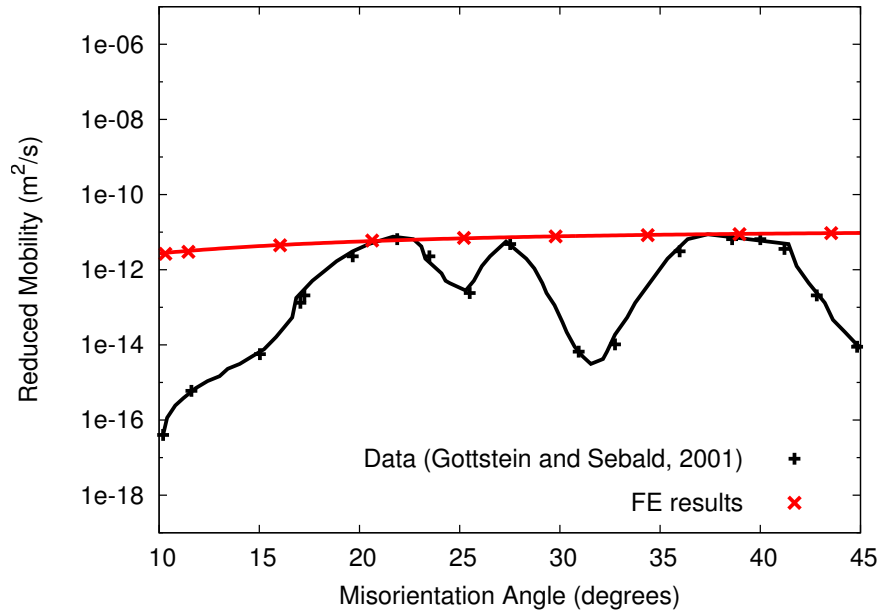
Figure VI.8 : Experimental and Numerical reduced mobility dependency on grain boundary misorientation at 300° C
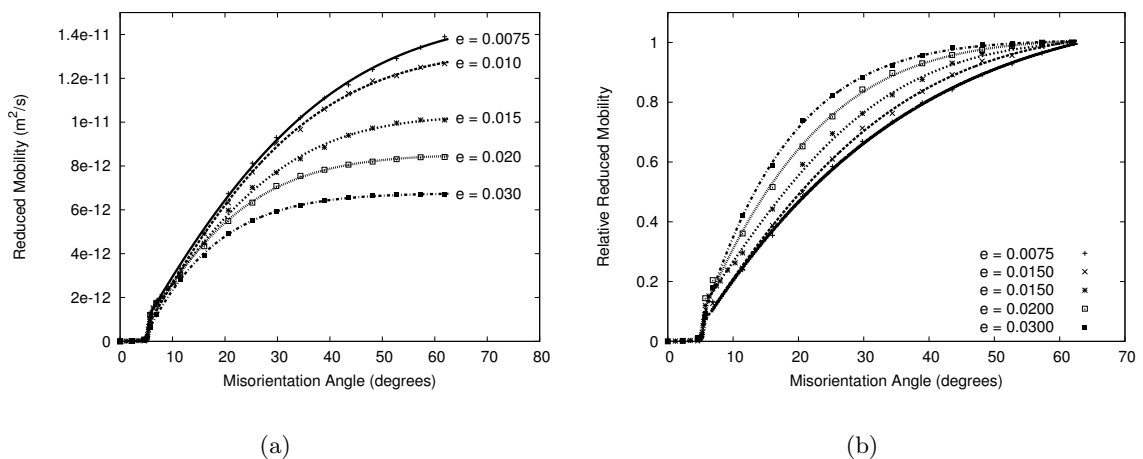
Figure VI.9 : Interface size variation: (a) reduced mobility (b) relative reduced mobility dependency on grain boundary misorientation
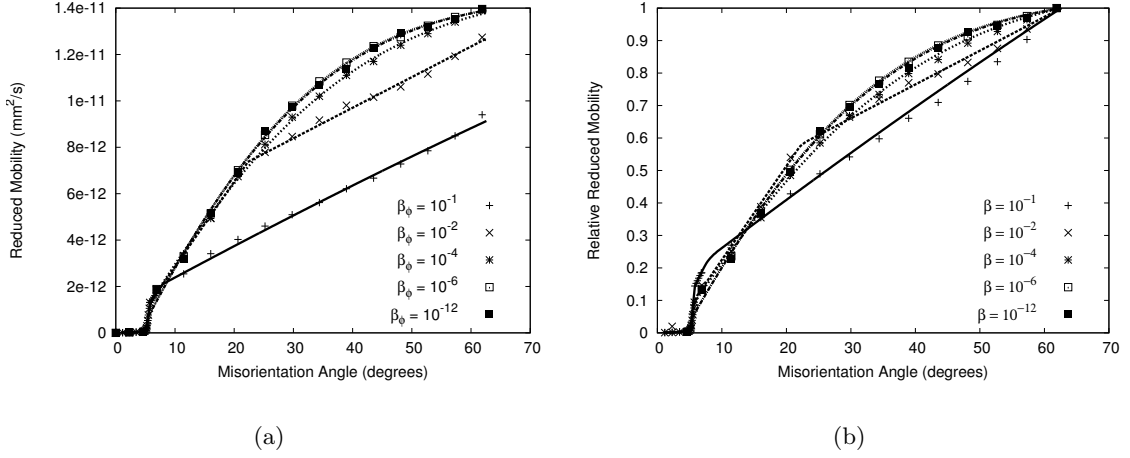
Figure VI.10 : β_θ variation : (a) reduced mobility (b) relative reduced mobility dependency on grain boundary misorientation

the grain boundary energy is responsible for the grain boundary motion, the parameter e has an impact on the grain boundary velocity. However, without changing the grain boundary energy, the relaxation parameters, β_η and β_θ, play a role in the grain boundary mobility. In order to avoid grain rotation, $\beta_\theta > \beta_\eta$ is imposed. To see the effect of β_η on the grain boundary mobility, several grains embedded in a large grain are considered with different misorientations for $e = 0.0075$ and $\beta_\theta = 100.0$. By taking $\beta_\theta > \beta_\eta$, the relaxation parameter, β_θ controls the average mobility of the grain boundary while, β_η, controls the mobility dependency on the misorientation, see Figure VI.10. However, the fluctuation of the reduced mobility on misorientation angle keeps less than a factor 10 while in experimental data, fluctuations greater than 100 are observed, see Figure VI.8.

VI.2.1.3 Temperature Effect

In the evolutionary equations V.63 and V.64, temperature dependencies have been introduced in the inverse boundary mobility. Under the conditions described previously, several grains embedded in a large grain are considered with $35°$ misorientation under different temperatures with parameters $Q = 1.7eV$ and $M_0 = 4.0^3 m^2 s^{-1}$. Predicted reduced mobilities with respect to the inverse temperature are shown in Figure VI.11. The predicted reduced mobilities show a linear dependency on inverse T and verify the experimental relation

$$M\gamma = M_0\gamma \exp(\frac{Q}{RT}) \tag{VI.9}$$

However, in the model the activation enthalpy Q and the pre-exponential factor M_0 are constant while for special misorientations ($low - \Sigma$ boundaries), they assume minima. The experimental misorientation dependence of these parameters is exhibited in Figure VI.12. Since the predicted high angle grain boundary mobility does not take into account the cusp due to ($low - \Sigma$ boundaries), an average value of the reduced mobility in Figure VI.12 is chosen for fitting the parameters ($M_0\gamma = 4.0^3$ and $Q = 1.7$).
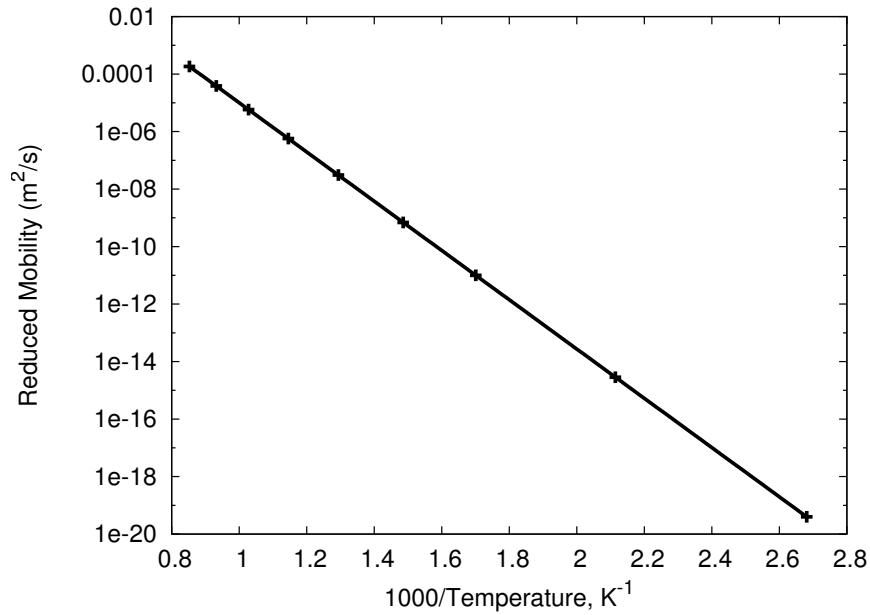
Figure VI.11 : Reduced mobility vs inverse temperature for a series of simulations corresponding to misorientation angle of 35°

(a)   (b)
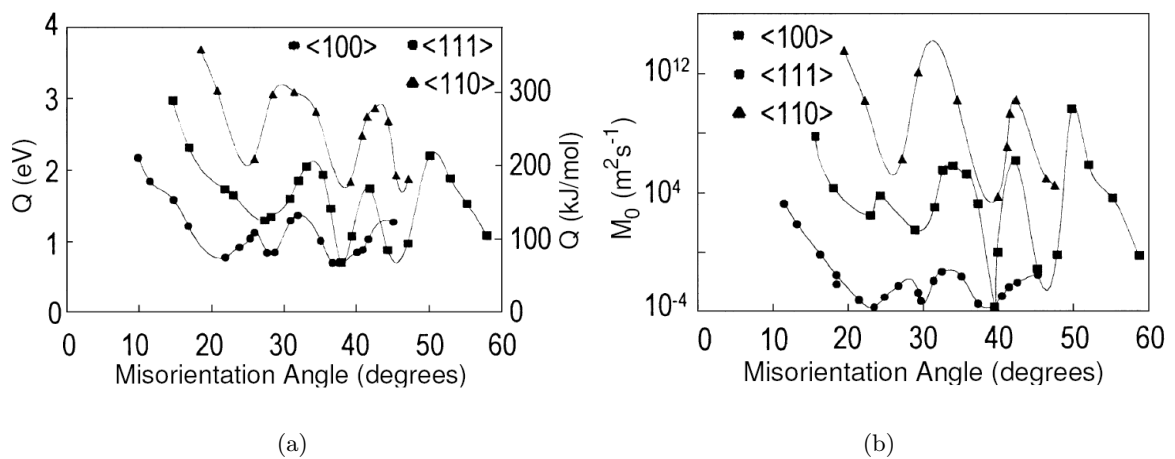
Figure VI.12 : Experimental dependency of the activation enthalpy Q and the pre-exponential factor M_0 with misorientation angle (Gottstein *et al.*, 2001)
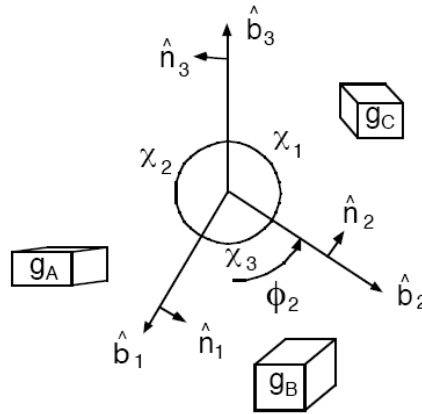
Figure VI.13 : Triple junction description with dihedral angle definition

VI.2.2 Triple Junction

The interfacial energies at the triple junctions of boundaries, see Figure VI.13, affect the dihedral angles as described in Herring's equation (Herring, 1951),

$$\frac{\gamma_1}{\sin \chi_1} = \frac{\gamma_2}{\sin \chi_2} = \frac{\gamma_3}{\sin \chi_3}. \tag{VI.10}$$

If the grain boundary energies are equal on the 3 grains boundaries, independent of the misorientation and the crystallographic orientations, then the triple point will be in equilibrium when the boundaries make angles of 120°, $\chi_1 = \chi_2 = \chi_3 = 120°$.

Let us consider three grains with identical misorientation between neighbours. Since the grain orientation is 2π periodic, 120° misorientation gives equal energies for the three grain boundary. The grain boundaries are initial set to form two dihedral angles of 90° and one of 180° as shown in Figure VI.14 (a), and do not verify the Herring equation. Neumann boundary conditions are applied. Figure VI.14 shows the evolution of the triple junction. First, the triple junction tends to local equilibrium configuration with curved grain boundaries where dihedral angles are identical and equal to 120°, and, consequently, verify Herring's equation. Then, the triple junction moves so as to reduce one of the grain boundary surface keeping dihedral angles equal to 120°. As expected by the variational formulation, the free energy of the system is decreasing by eliminating grain boundaries. Finally, all grain boundaries disappeared to leave only one grain.

The difference with the theoretical results is the curved moving grains. As seen in Figure VI.15, after reaching the local equilibrium with curved grain boundary, the grain boundary shape tends to a straight line. The Neumann boundary conditions are assumed not to be correct and are replaced by Dirichlet boundary conditions. Therefore, grain boundary can not move on the mesh boundary. Triple junction evolution shown in Figure VI.16 corresponds to the theoretical analysis.

VI.2.3 Quadruple Junction

Let us consider four grains with different initial orientations, G1 (5.0°), G2 (34.0°), G3 (63.0°) and G4 (92.0°). They form initially a quadruple junction with equal dihedral angles (90°) and with 2 kinds of grain boundary, three with misorientation angle of 29.0° and one with 87°, as shown in Figure VI.17. Figure VI.17 shows the four grain evolution for three different values

(a) t=0.0s   (b) t=5.5s   (c) t=9.9s   (d) t=10.4s
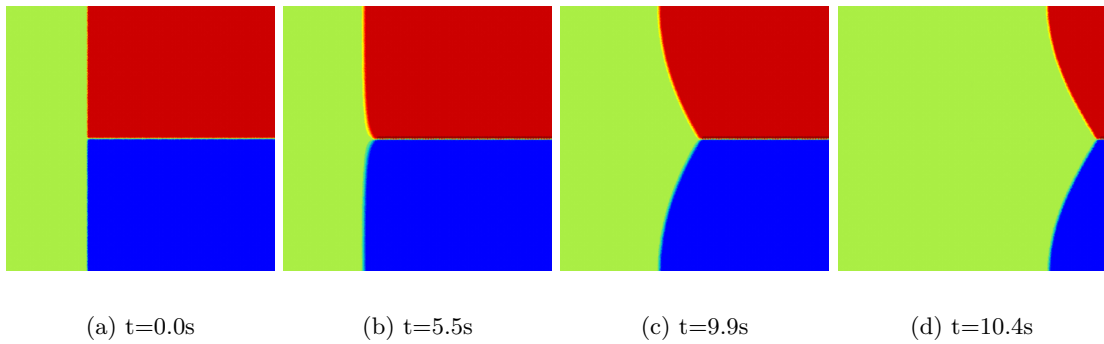
Figure VI.14 : Evolution of a triple junction formed with grains of equal boundary energies (Neumann boundary conditions)
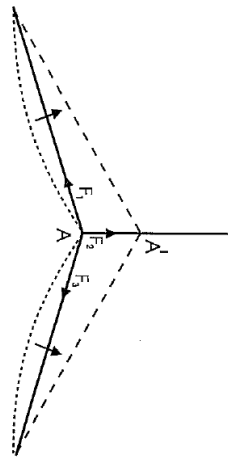

Figure VI.15 : Schematic motion of triple junction to reach equilibrium position

(a) t=0.0s   (b) t=10s   (c) t=90s   (d) t=120s
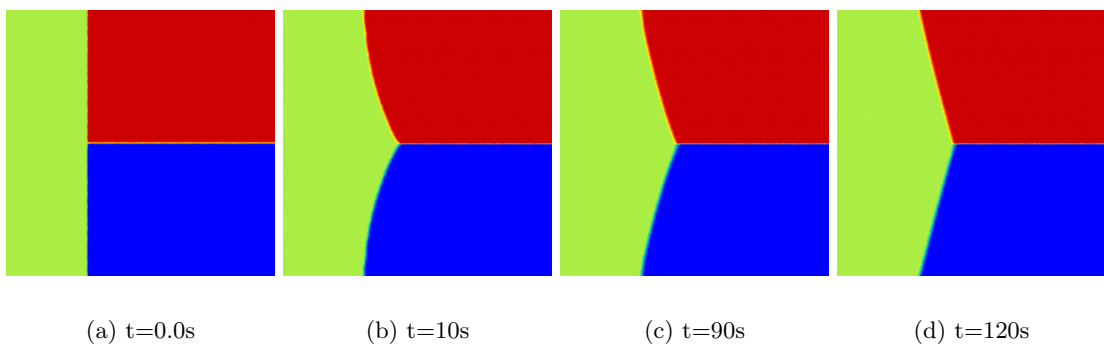
Figure VI.16 : Evolution of a triple junction formed with grains of equal boundary energies (Dirichlet boundary conditions)
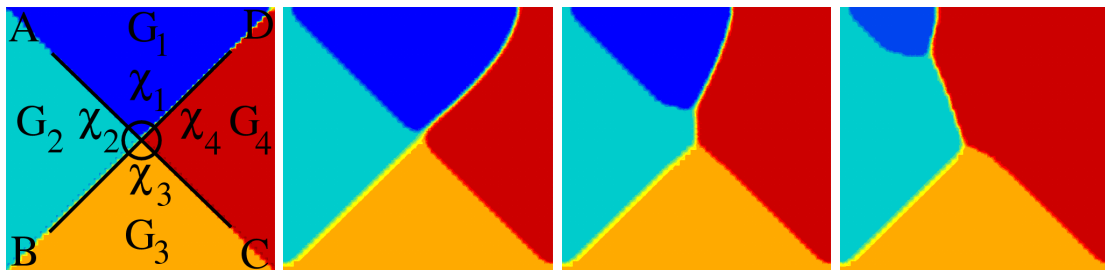
(a) e = 0.001
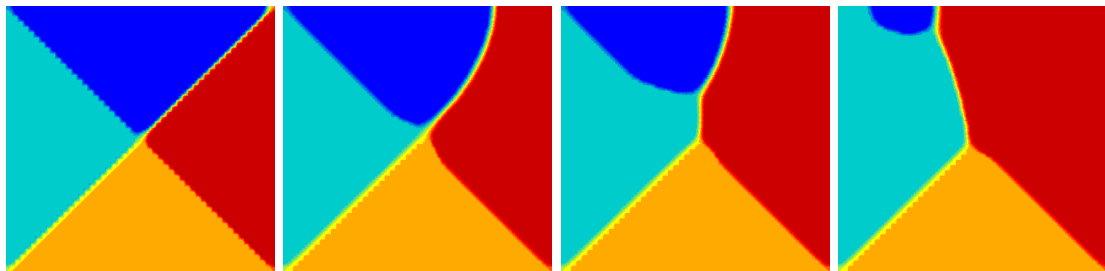
(b) e = 0.0025
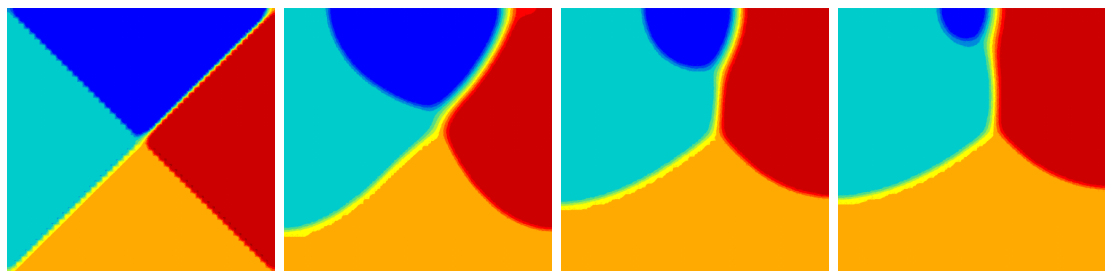
(c) e = 0.01

Figure VI.17 : Evolution of a quadruple junction for three values of parameter e (term $|\nabla\theta|^2$)
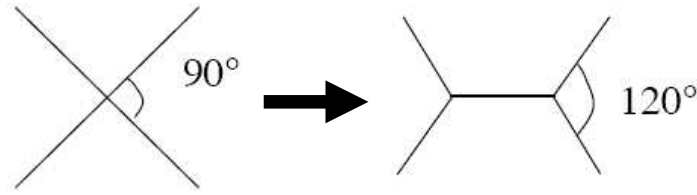
Figure VI.18 : Schematic evolution of quadruple junction formed with equal grain boundary energies

of parameter e (term of $|\nabla\theta|^2$), e=0.001, 0.002 and 0.01 (J/m). First, the quadruple junction splits into two triple-fold junctions. Therefore, the total grain boundary length decreases so does the free energy of the system, as expected for a quadruple junction with isotropic grain boundary energies, see Figure VI.18. Since one of the grain boundary mobility is higher than this other, an asymmetry appears; the length of the highest grain boundary energy (0D) decreases more quickly than the other ones.

When the parameter $e = 0.001$, only the grain boundary (0D) is moving significantly while the grain boundaries (0A), (0B) and (0C) keep their initial position. The length of the grain boundaries (0A) is decreasing due to the triple junction migration imposed by the grain boundary (0D). This results a significant higher mobility for (0D) illustrated in Figure VI.6 in which grain boundary mobility increases with grain boundary misorientation. After comparing the figures for different parameters e, motion of grain boundaries (0A), (0B) and (0C) is more important with increasing the parameter e. For instance, in Figure VI.17 a, the size of grains G1 is reduced by the motion of the grain boundary (0D) while in Figure VI.17 c, both grain boundaries (0A) and (OD) participate in its reduction. The difference between the grain boundary mobility of (0A), (0B) and (OC) and these of (0D) (higher misorientation), namely the grain boundary mobility dependency on misorientation, is decreasing when increasing the parameter e, as underlined in Figure VI.10.

Let invert the grain orientation of G1 and G2, two kinds of grain boundaries are formed; two grain boundaries 58° misoriented and two grain boundaries 29° misoriented. In Figure VI.19, comparison of the quadruple junction are done w.r.t. the grain orientation distribution. In the second case, the highest grain boundaries misoriented (0B) and (0D) controlled the microstructure evolution while only one in the first case. This confirms the previous results where the grain boundaries mobility dependency on misorientation has be shown.

VI.2.4   Microstructure

VI.2.4.1   Topological Aspects

We follow now the evolution of 2D polycrystals. The initial microstructure consists of 100 grains obtained according to a Voronoi algorithm and assuming periodic boundary conditions. Initial grain orientations have been chosen randomly with a misorientation angle between 12° and 62° for each neighbouring grains as found for isotropic FCC polycrystal (Mackenzie, 1964). The mesh is made of 200×200 quadratic elements. The annealing temperature is 315°. The parameters are listed in Table VI.1. Figure VI.20 shows the evolution of the microstructure by representing the lattice orientation θ and lattice order η. As expected, some grains grow, others vanish to end up with higher average grain size.

The evolution of individual grains in these microstructures is compared to the initial
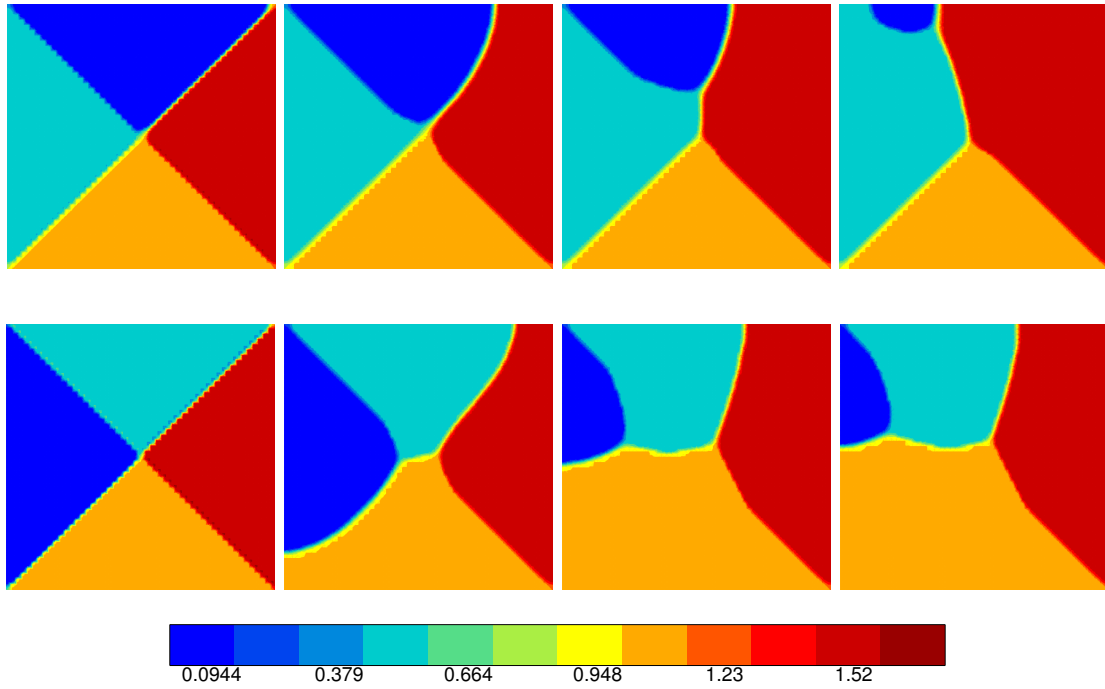
Figure VI.19 : Evolution of a quadruple junction formed by grains with identical orientation with two different distributions ($e = 0.001$)

Table VI.1 : Phase field model parameters

$\alpha(J/m)^{1/2}$	$\omega(J/m^3)$	$a(J/m^2)$	$b(J/m^2)$	$c(J/m^2)$	$d(J/m)$	β_θ (s)	β_η (s)
0.04	7.50	1.00	0.95	1.35	0.45	100.0	0.01
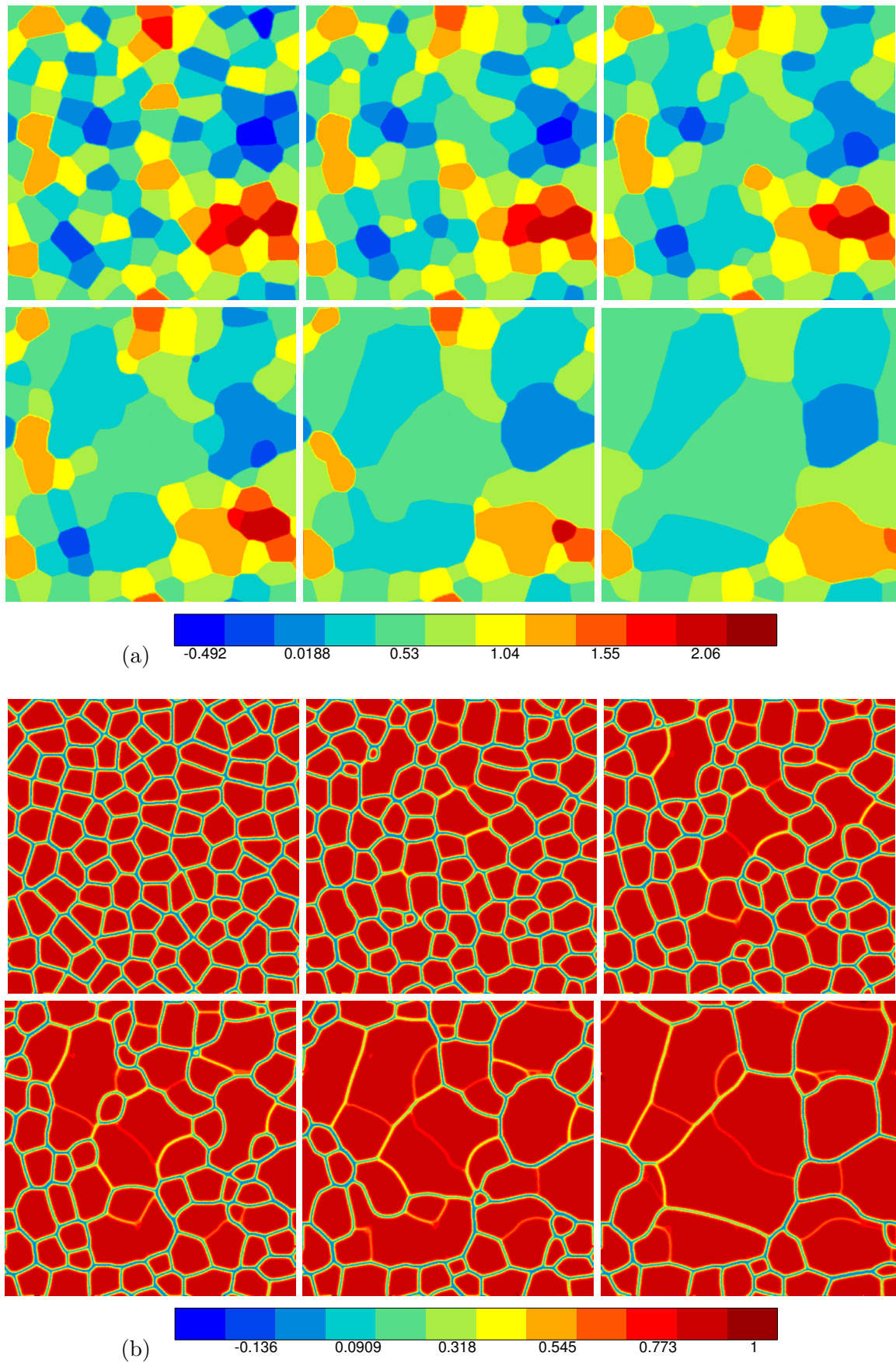
Figure VI.20 : Evolution of (a) grain orientation θ and (b) lattice order η distributions. From left to right, from top to bottom: t=0, 89, 18., 295, 553, 2770s

distribution of the lattice order η. In order to analyse the topological variation, Figure VI.21 shows microstructure evolution by representing η (red lines) superimposed with the initial distribution (white lines). First, the triple junctions drag the boundaries when they are close to equilibrium. Most of the grains move slightly from their initial position to reach a pseudo-equilibrium respecting the dihedral law detailed in the triple junction section. The dihedral angle obtained from this adjustment are not necessary 120° because of different grain boundaries energies. Once the triple junctions have a configuration close to that required for thermodynamic equilibrium and the boundaries have obtained their curvature, growth mechanism begins with two grains (G2, 4 sides and G3, 5 sides) which vanish quickly as seen in the third picture. Then, during microstructure evolution, generally, grains with less than 6 sides disappear as observed in the classical approach. Indeed, Von Neumann-Mullins relation (Von Neumann, , Mullins, 1956) predicts for 2D polycrystals that grains with less than six neighbours (n<6) (generally the smallest one) will shrink while those with n>6 will grow, where n is the topological class. However, this theory is based on equal mobilities and surface tensions for all grain boundaries. In our case, the grain boundary mobility gap between low and high angle grain boundary interferes in the classical approach and, for instance, grains with n=6 are not necessary stable grains (G4). Finally, for the last picture, they is no superposition between the white lines and the red lines, all grain boundaries have left their initial position. We should note that only one grain, marked as G1, kept its initial position until the sixth picture. It can be noticed that it is a grain with 6 edges and with closed 120° dihedral angle. The use of orientations as a variable allow coalescence as seen from the disappearance of junction Q1 and Q2 which gives a new grain formed by two grains of closed initial lattice orientation.

As seen in the section VI.2.1.1, the parameter e (term $|\nabla\theta|^2$) plays a significant role in the grain boundary reduced mobility. Two additional microstructures identical as the first one are run with two values of parameter e, $e = 0.0075(J/m)$ and $e = 0.015(J/m)$. Figure VI.22 shows the lattice orientation θ and the lattice order η for the three parameters at different time. These times have been chosen such that microstructure showed similar size for the reddest grain. The grain shapes show significant differences, with increasing parameter e, grains are more curved. The number of neighbours per grain appears similar in all three cases. It can be observed that there is a greater proportion of smaller and larger grains when the difference between low and high angle grain boundary is higher ($e = 0.0025$). This is reminiscent of the abnormal grain growth where a few grains grow in the microstructure and consume the matrix of smaller grains.

VI.2.4.2 Macroscopic Evolution

The number of grains considered in the simulations is probably too small to obtain reliable grain growth statistics. However, some macroscopic properties and average values will be extracted from the three microstructures in order to compare the influence of parameter e. Figure VI.23 shows the evolution of the average grain radius, $\overline{R}$, with time, t. The growth rate of average radius of the grains is approximated by a simple power law by

$$\overline{R} = Bt^{1/n} \tag{VI.11}$$

The growth exponents were found to be n = 3.3 for e=0.015 and e=0.0075, and n = 3.7 for e = 0.0025, which is far from the classical grain growth exponent (n = 2.0). The classical grain growth exponent is obtained from a theory based on equal grain boundary energy and mobility for misorientations. However, the growth exponents for pure aluminium is approximately n = 4.0 which is closer to the predicted growth exponents. In pure
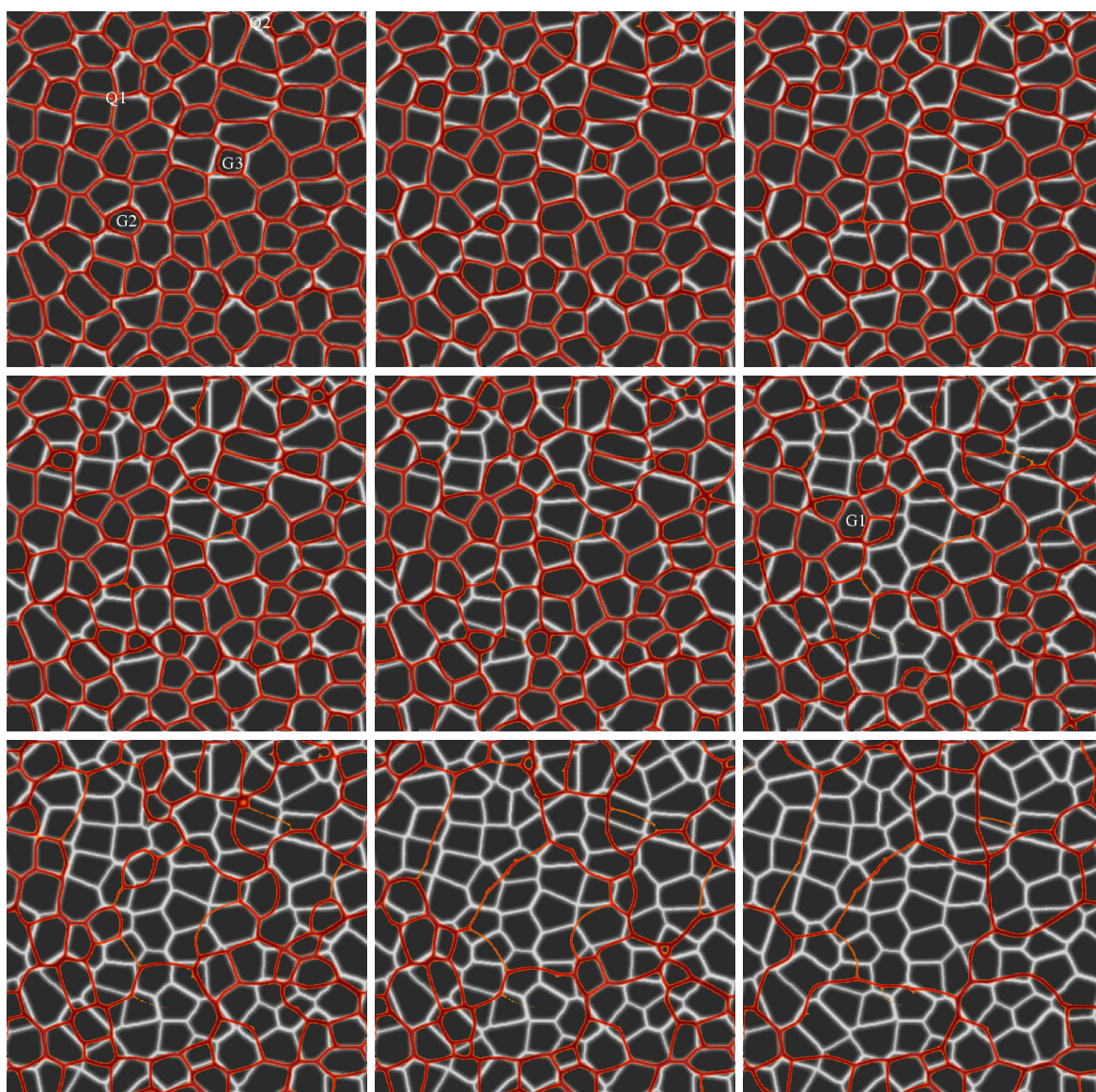
Figure VI.21 : Superposition of the current (red line) and initial (white line) lattice order η distributions where η is closed to 0. From left to right, from top to bottom: t=0, 21, 44, 61, 81, 108, 189, 242, 428, 956s

(a) e=0.0025, t=553s (b) e=0.0075, t=112s (c) e=0.0150, t=220s

(d) e=0.0025, t=553s (e) e=0.0075, t=112s (f) e=0.0150, t=220s
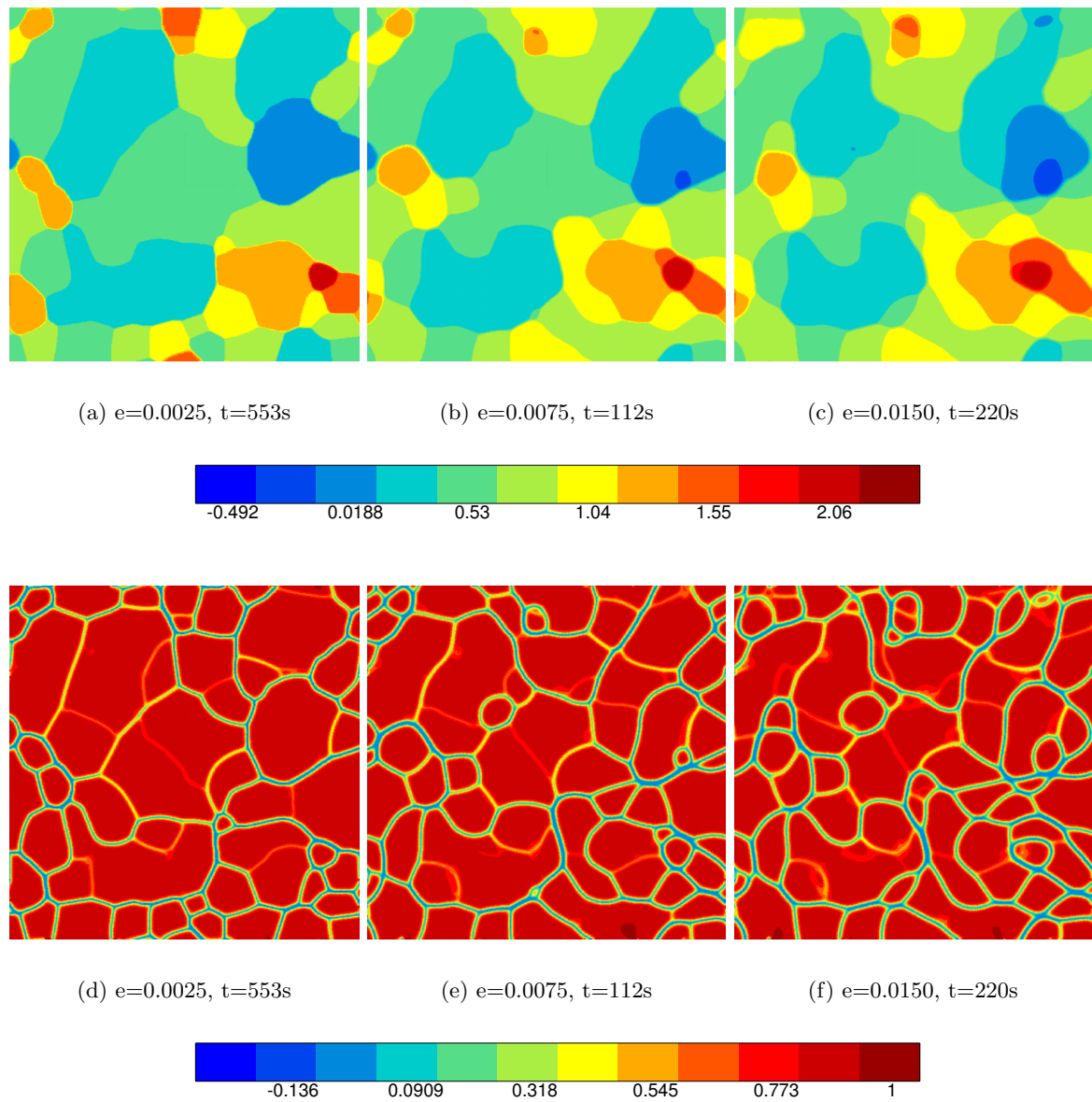
Figure VI.22 : Evolution of (a-c) grain orientation θ and (d-e) lattice order η distributions
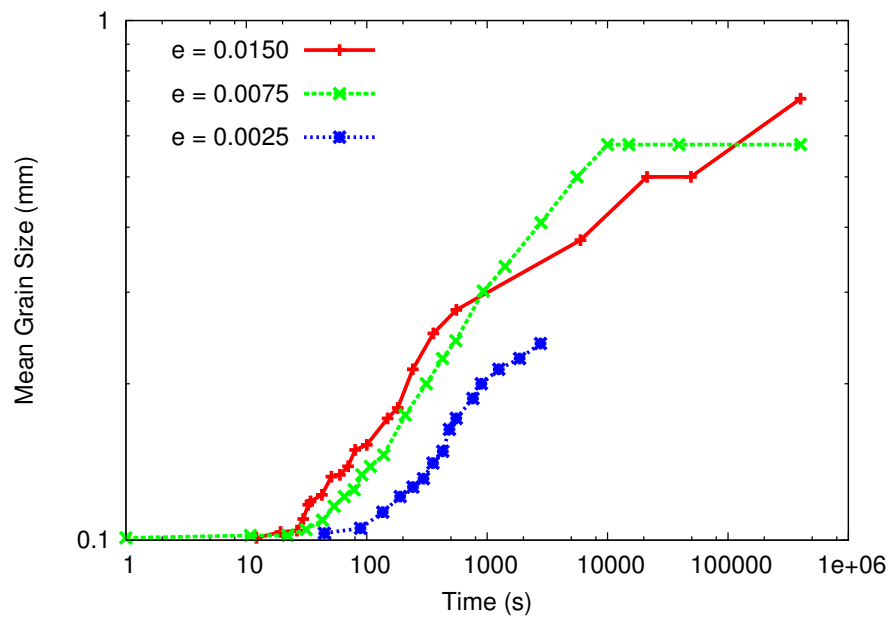
Figure VI.23 : Mean grain size evolution
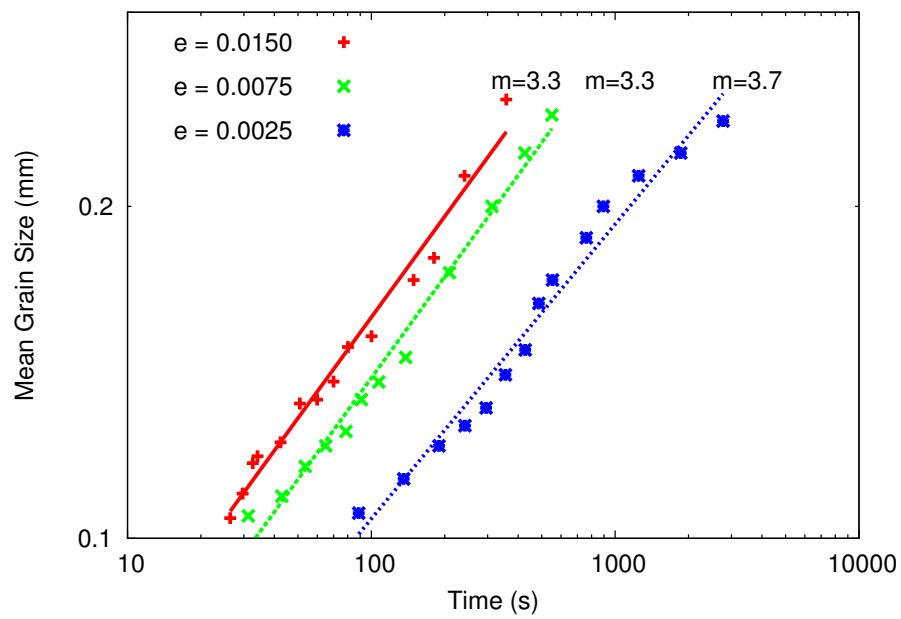
**Figure VI.24** : Linear interpolation of mean grain size
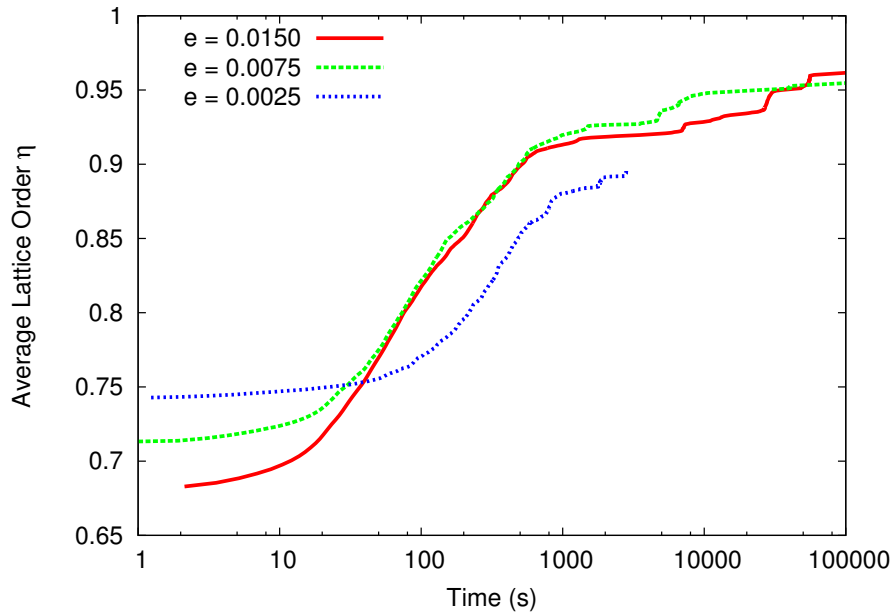
Figure VI.25 : Average lattice order evolution

aluminium as many other materials, grain boundary energy and mobility strongly depends on misorientation due to the presence of low misorientations and Σ grain boundary and the classical grain growth theory can not be applied. As seen in Figure VI.6, the grain boundary mobility is misorientation dependent especially for low misorientation and also for increasing misorientation between grains. We also note that the misorientation dependency increases by decreasing the parameter e. This can explain the higher value of the growth exponents for $e = 0.0025$ which increases grain boundary mobility dependency on misorientation. For identical relaxation parameters, β_θ and β_η, growth mechanism is retarded for $e = 0.0025$.

Figure VI.25 shows the average value of the lattice order of microstructure. As expected, the thickness of the grain boundary increases with the parameter e, and therefore the grain boundary area (average value of η decreases). The grain boundaries vanish and the average value of the lattice order get closer to 1. In the same way, see Figure VI.26, the initial free energy of the microstructure is higher for higher value of the parameter e and then tends toward 0 with time.

The average grain orientation follows the same evolution for the three cases, as seen in Figure VI.27. First, the lattice orientation increases then decreases with only 5° variation. However, the decreasing part of the curve occurs sooner with decreasing parameter e. In order to have more accurate idea on grain orientation evolution, grain orientation distributions are shown in Figure VI.28. The orientation distribution is plotted when the three microstructures have eighteen grain left. The initial grain orientation distribution is mainly comprised between 0° and 90° because of initial imposed misorientation between grains. The resulting microstructure obtained with $e = 0.015$ is centering in $\theta = 40°$ while with decreasing e, more discrepancy between orientations is observed in the distribution. The resulting microstructure obtained with $e = 0.0025$ is more heterogeneous as seen by the superimposition of the four distributions, Figure VI.29.
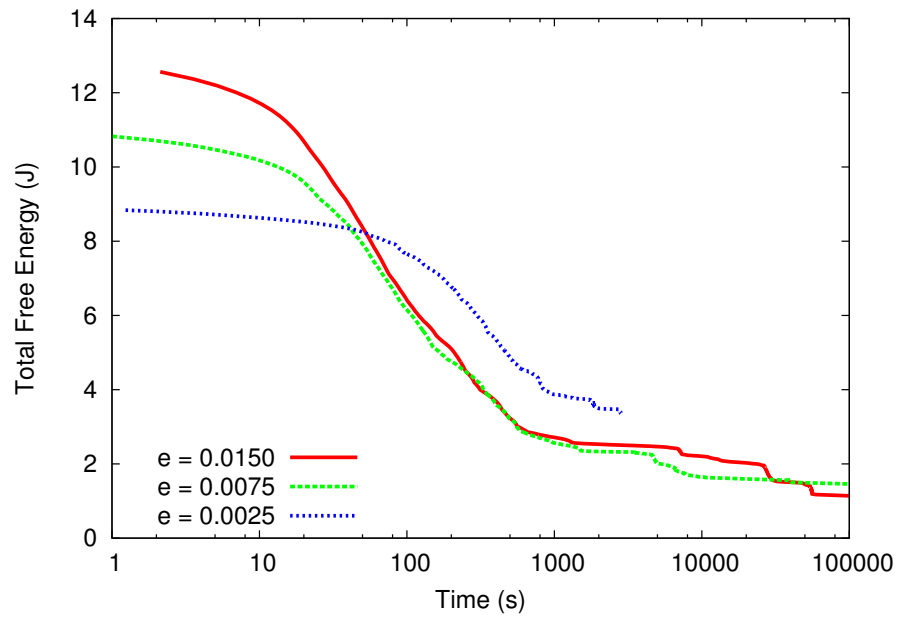
Figure VI.26 : Total microstructure free energy evolution
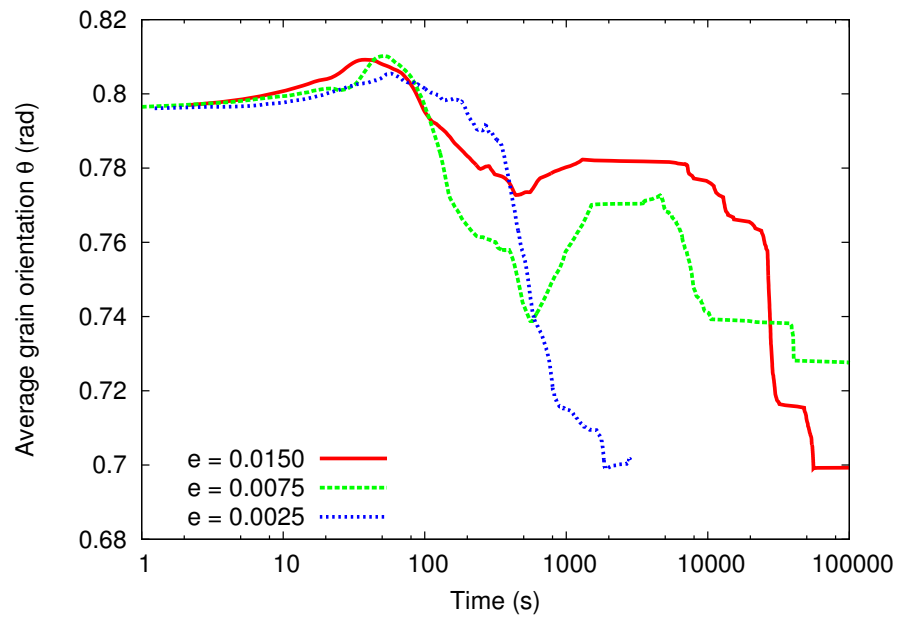
Figure VI.27 : Average lattice orientation evolution

(a) t=0

(b) e=0.0025, t=2768s

(c) e=0.0075, t=328s

(d) e=0.0150, t=225s
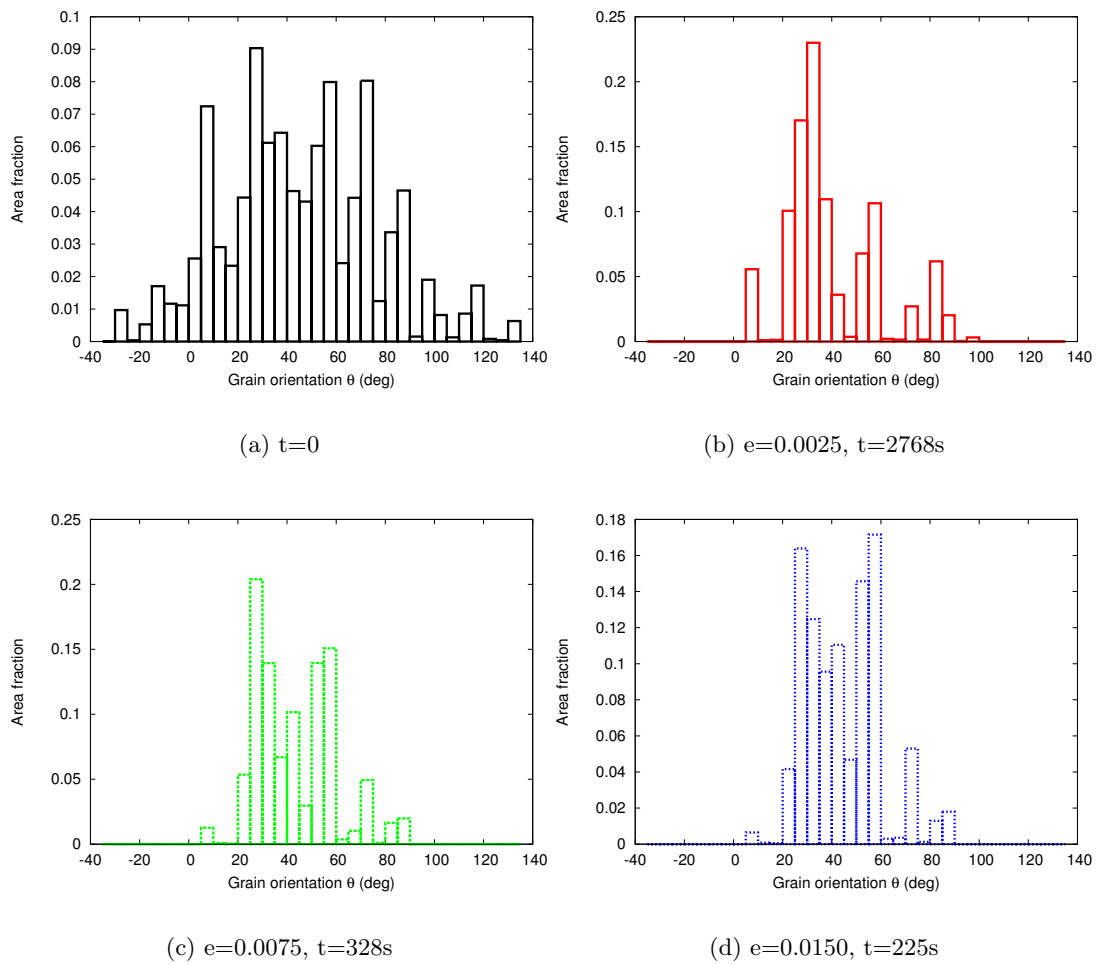
Figure VI.28 : Grain orientation distribution when 18 grains are left
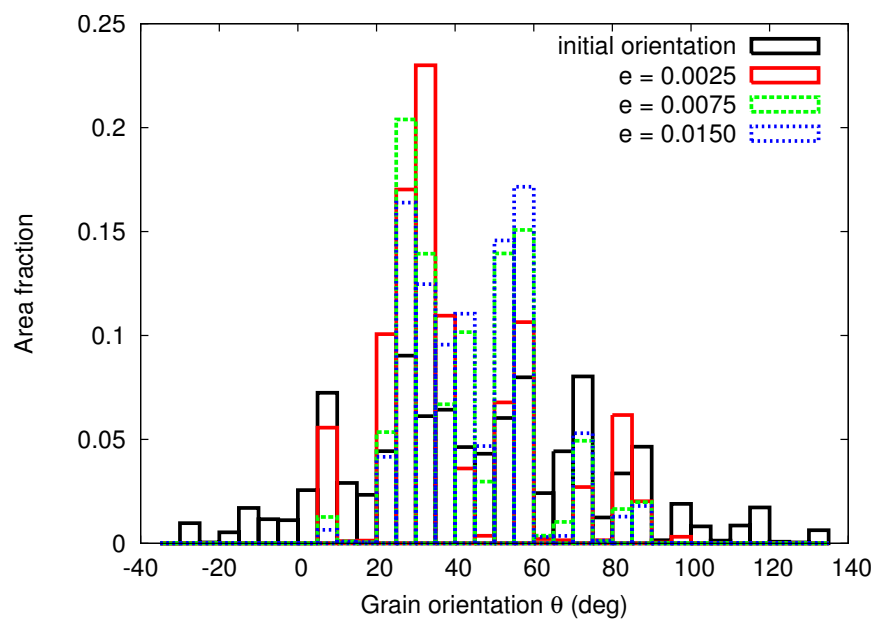

**Figure VI.29** : Superposition of grain orientation distribution
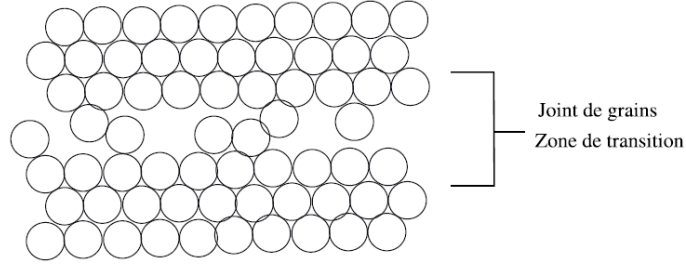
Figure VI.30 : Schematic thickness of a grain boundary

VI.3   Stored Energy as a Driving Force

VI.3.1   High Angle Grain Boundary Energy as a Maximal Energy

As explained in the section V.2.2, the stored energy density, E_{st}, is normalized by the grain boundary energy of high angle misorientation, E_{gb} in the free energy formulation, where the grain boundary energy between two grains of high misorientation is assumed constant (the Σ grain boundaries are not considered). In 3D space, the stored energy density, E_{st}, is expressed in Jm^{-3} while the grain boundary energy is described at the surface and therefore, expressed in Jm^{-2}. However, as seen in Figure VI.30, the thickness of a grain boundary is around three-four atom layers. In pure FCC crystals, the distance between two atom centers is about

$$a \approx \frac{4R}{\sqrt{2}} \tag{VI.12}$$

where R is the atom radius with R = 125 pm for aluminium. Therefore, the grain boundary energy density with a grain boundary thickness about 3 - 4 atoms is

$$E_{gb} \approx \frac{\gamma_{gb}}{\delta} \approx 50 Jm^{-3} \tag{VI.13}$$

where $\delta = 3.5a = 600pm$ and $\gamma_{gb} = 0.37 Jm^{-2}$.

VI.3.2   Stored Energy Effect on Grain Boundary Velocity

In a first step, a bicrystal is studied with a flat grain boundary in order to suppress the curvature effect in interface motion. A stored energy distribution due to deformation is initially introduced. Both grains, 40° misoriented, have a constant stored energy but different in order to introduce an energy gradient between both grains. Figure VI.31 illustrates that the grain boundary evolves in the direction of the grain of higher stored energy. After the grain boundary motion, it leaves the way free of stored energy, $E_{st} = 0$ and $\eta = 1$.

To study the effect of the stored energy gradient on the grain boundary velocity, several flat grain boundaries with different stored energy gradients and with different relaxation parameters β_η, are simulated. Results are given in Figure VI.33. A phenomenon of saturation is observed for all relaxation parameters β_ϕ. The saturation part is suppressed to obtain the curve in Figure VI.33. A linear relationship between the driving force arising from stored dislocations and the velocity is found as in the experimental work of (Huang and Humphreys, 1999), see Figure VI.34,

$$v = MP \propto M\Delta E_{st} \tag{VI.14}$$

where the grain boundary mobility M increases with decreasing inverse mobility parameter β_ϕ. This relation applies only under a critical value of the stored energy. After this critical

(a)

(b)

(c)
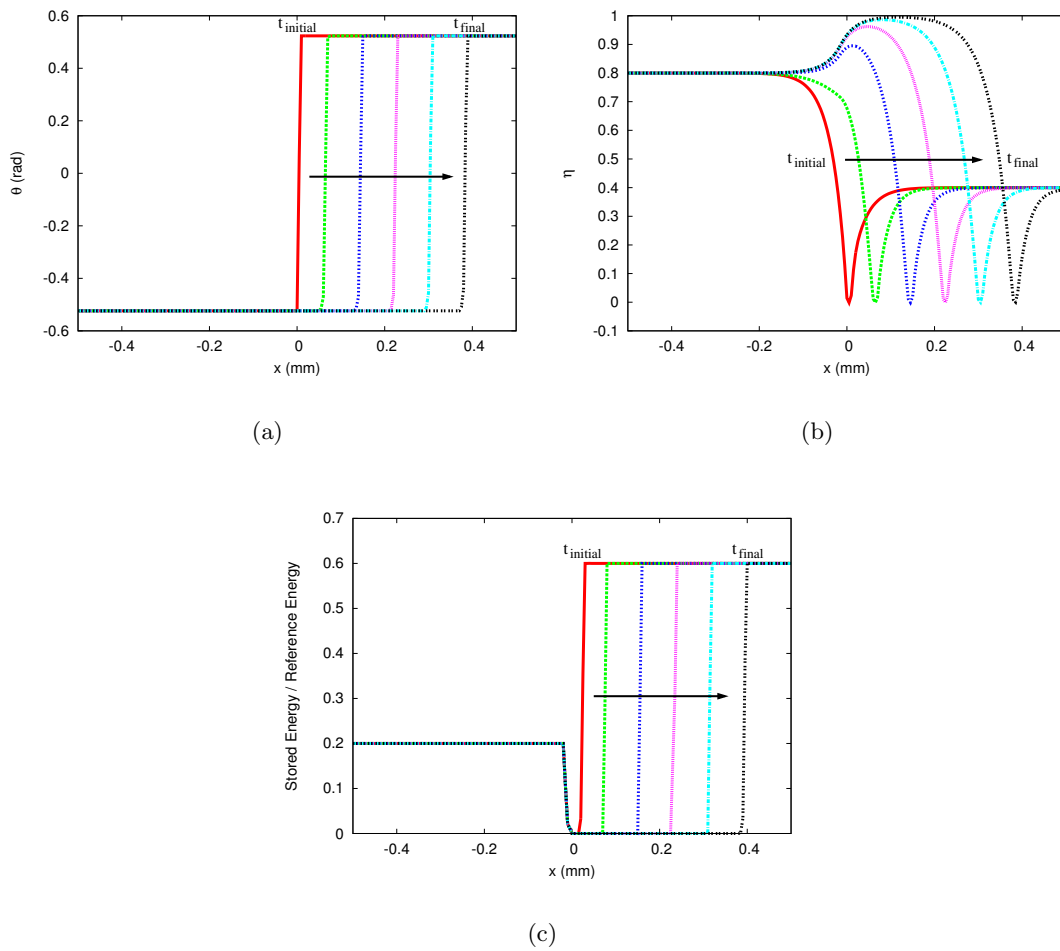
Figure VI.31 : Profile of bicrystal with stored energy : (a) orientation , (b) crystallinity and (c) stored energy
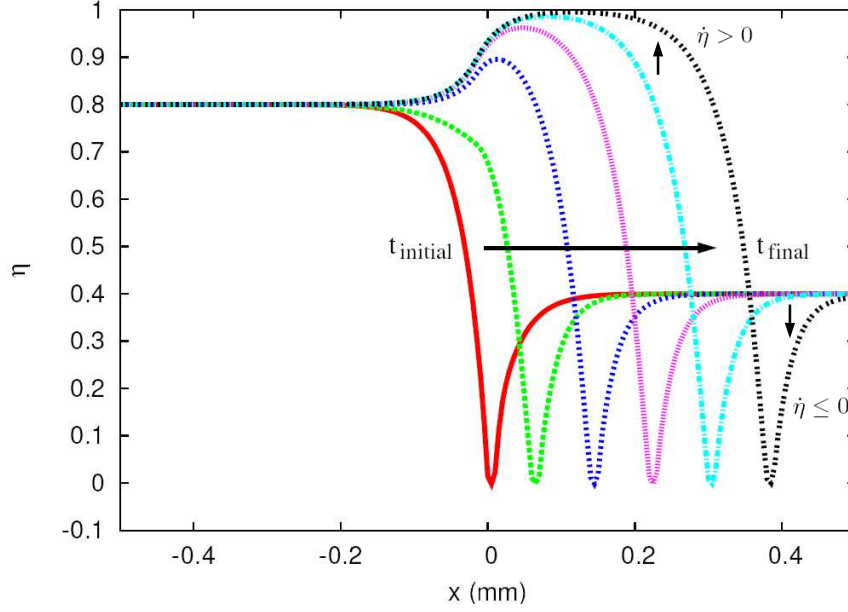
Figure VI.32 : Profile of bicrystal with stored energy : (a) orientation , (b) crystallinity and (c) stored energy

value, the velocity of the grain boundary stops increasing with additional stored energy and fluctuates closed to the maximum velocity as if the additional stored energy was not taking into account. In order to explained this phenomenon, we recall the annihilation equation,

$$\dot{E}_{st} = -C_d E_{st} \dot{\eta} A(|\nabla \theta|) \quad if \quad \dot{\eta} > 0 \qquad (VI.15)$$

$$\dot{E}_{st} = 0 \quad if \quad \dot{\eta} \leq 0 \qquad (VI.16)$$

illustrated by Figure VI.32. Ahead of the grain boundary, $\dot{\eta} < 0$, no annihilation of the stored energy occurs while after its motion, $\dot{\eta} > 0$, stored energy level decreases. However, numerically, positive variation of η may occur ahead of the grain boundary due to the rapid change of the η profile. This phenomenon is more pronounced above a critical value of stored energy due to a crystal order, η, closer to 0.

We note that the critical stored energy value is higher for the inverse mobility parameter $\beta_\eta = 10^{-1}$s. Indeed, since β_η controls the mobility of the variable η, its variation affects the annihilation rate. However, as seen in Figure VI.33, $\beta_\eta = 10^{-2}$ and $\beta_\eta = 10^{-6}$ gave similar curves. Under a key value linked to β_θ, β_η does not affect the grain boundary velocity. Furthermore, we must have $\beta_\theta >> \beta_\eta$s for preventing from grain rotation. Therefore, the range of possible β_η values affecting the velocity of the grain boundary and inhibiting rotation is narrow and, for instance, comprised between 10^{-1} and 10^{-2} for $\beta_\theta = 100$s. Consequently, the inverse mobility parameter β_η impact on the velocity is limited while the inverse mobility parameter β_θ serves as the main adjusting parameter to the experimental data.

Figure VI.35 shows the linear curves obtained by changing the parameter e in the free energy (increasing e increases the thickness of the grain boundary). First, the figure depicts an increasing in the slope with reducing the parameter e. It also emphasises an activation stored energy difference between both grains for getting grain boundary motion. The activation value is lower with increasing parameter e. For instance, it is found to be 0.03 for $e = 0.0075 (J/m)$ while it is 0.23 for $e = 0.0025 J/m)^{1/2}$

Curves obtained by changing C_d, parameter which controls the annihilation of stored energy,
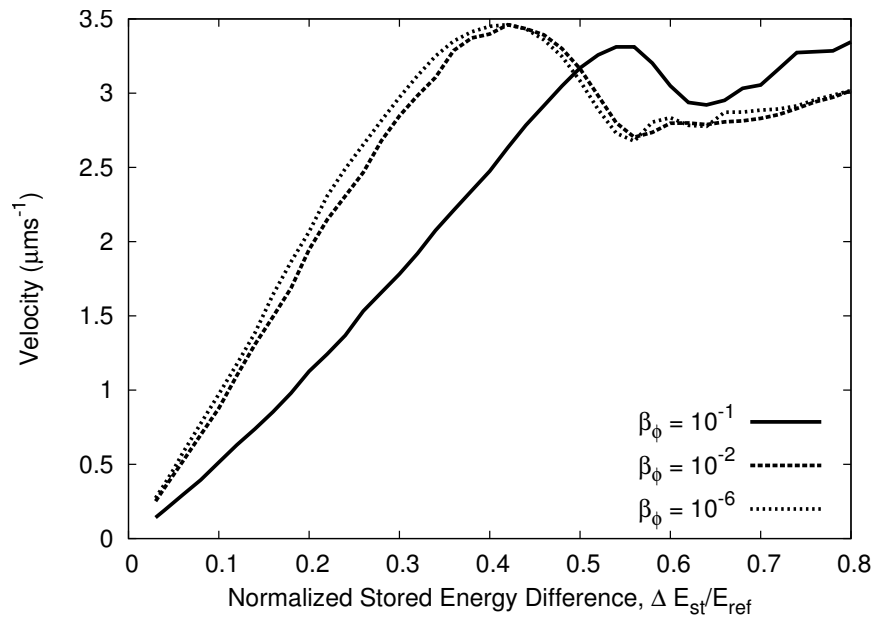
(a)
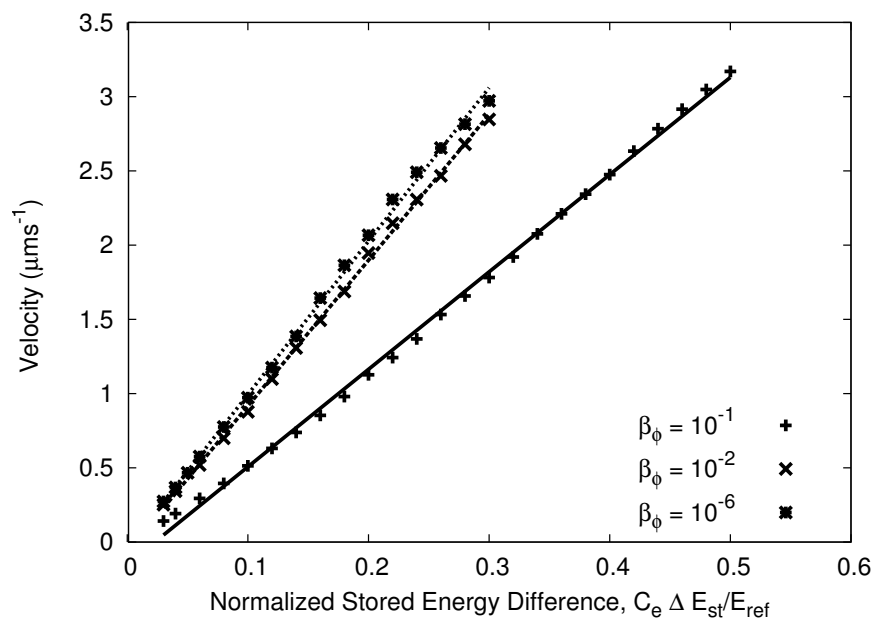
(b)

Figure VI.33 : (a) Predicted dependence of the boundary velocity as a function of the driving force, (b) its linear interpolation : variation of the relaxation parameter β_η
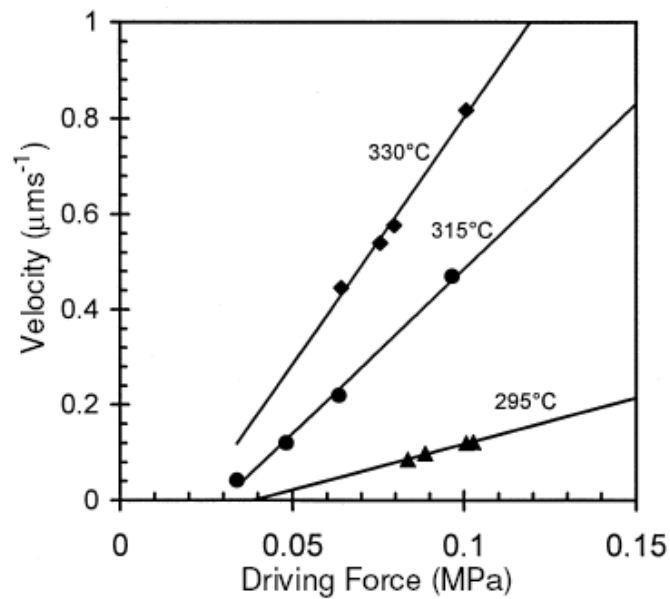
Figure VI.34 : Experimental dependence of the boundary velocity as a function of driving force (Huang and Humphreys, 1999)
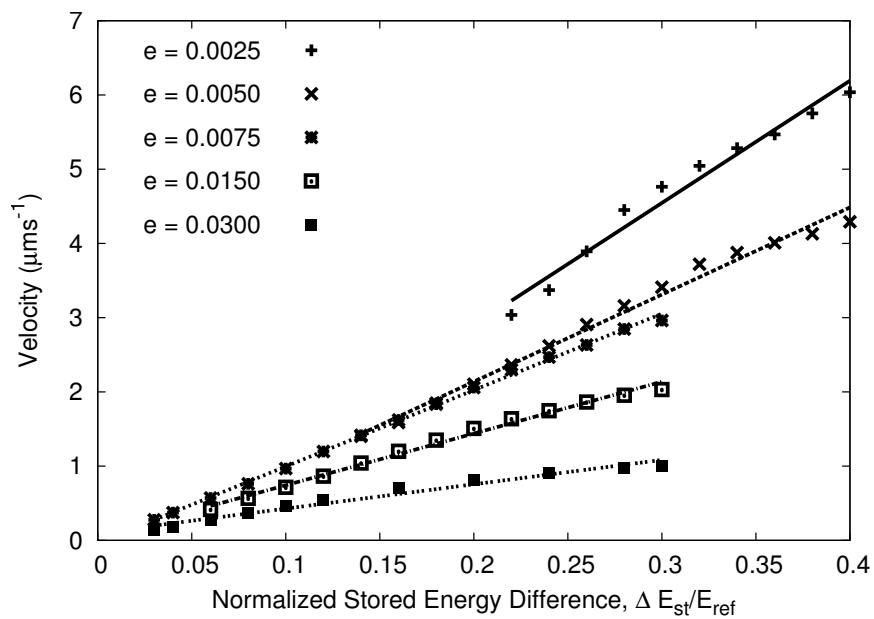
Figure VI.35 : Predicted dependence of the boundary velocity as a function of driving force: variation of e (term $|\nabla\theta|^2$)

are shown in Figure VI.36. The velocity of the grain boundary increases with the parameter C_d to reach a maximal value, then varies in a non-monotonic way. The maximal velocity of grain boundary motion with $C_d = 50$, 2 and 1 is respectively obtained for the normalized stored energy difference, $\Delta E_{st}/E_{ref} = 0.45$, 0.7 and 0.78. This phenomenon is more pronounced for higher value of C_d since a raise parameter C_d increases the annihilation rate of stored energy.

Figs.VI.37 (a) and (b) show the boundary velocity as a function of misorientation angle for two different initial stored energy gradients and two values of parameters e. In both cases, the boundary velocity increases until the misorientation angle reaches 20° as seen for the grain boundary energy. Then, from 20° misorientation, the boundary velocity is approximately constant. Some high angle grain boundaries do not move for the smallest value of e with a small amount of stored energy differences.

VI.3.3 Nuclei Growth: Curvature vs Stored Energy

In a previous section, we considered a grain embedded in a large grain. In all events, the interior grain reduced then vanished due to the driving force arising from the curvature and grain boundary energy. Nevertheless, even with their small radius, nuclei grow inside the deformed microstructure. This is due to the driving force arising from the stored energy difference between the nuclei, free of dislocation and the deformed matrix, full of dislocations. Let us consider a small grain free of dislocation, $E_{st} = 0$, embedded a deformed grain, $E_{st}/E_{ref} = 0.8$. Dirichlet boundary conditions are used on the top side and right side. Nucleus growth is shown in Figure VI.38a by representing grain orientation distribution θ. The associated stored energy evolution is shown in Figure VI.38b. After moving toward higher stored energy area, the grain boundary leaves in its wake a region considered as a deformed matrix free of energy.

The previous results have been obtained under specific conditions. The nuclei growth occurs only with a sufficient amount of stored energy depending on the initial nucleus size. The previous simulation has been run several times with different amounts of stored energy and initial grain sizes in order to determine the critical amount of stored energy to obtain grain growth. The critical curve with an exponential shape is shown in Figure VI.39 for two parameters e (term $|\nabla\theta|^2$). Obviously smaller the initial grain size, the higher the amount of stored energy is necessary to have grain growth. We note that the initial grain size is large, between $10\mu m$ and $100\mu m$. However, these numbers depend of the grain boundary size parameter e and the associated mesh size. In the simulation, the element size is $5\mu m$. For instance, in the Figure VI.38, an initial size of $10\mu m$ has been used which corresponds to 2 elements.

VI.3.4 A First Step toward Strain Induced Boundary Migration (SIBM)

A bicrystal is studied with a flat grain boundary. A stored energy distribution due to deformation is initially introduced. Both grains, 40° misoriented, have a constant stored energy but different in order to introduce an energy gradient between both grains. In addition to the case detailed in section VI.3.2, initial dislocation cells (or subgrains) are imposed with an higher cell size for the grain with the lowest stored energy as described in Figure VI.40a. Figure VI.40(a) shows the evolution of the microstructure by representing the lattice orientation θ. A schematic theoretical evolution is also in the figure. Contrary to the results of section VI.3.2 where the grain boundary remains flat, in this case, the grain boundary motion is influenced by the substructure network. The figure specially displays the
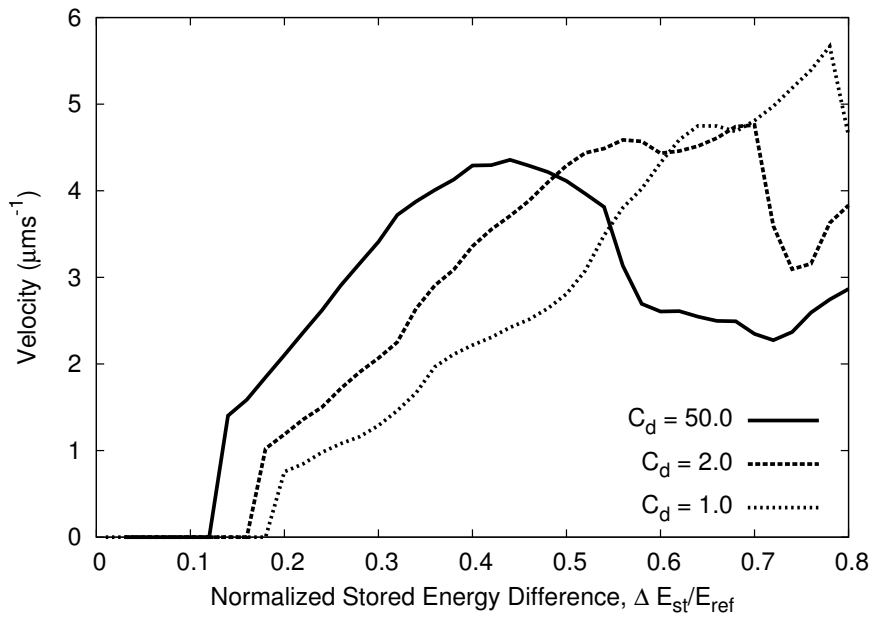
(a)
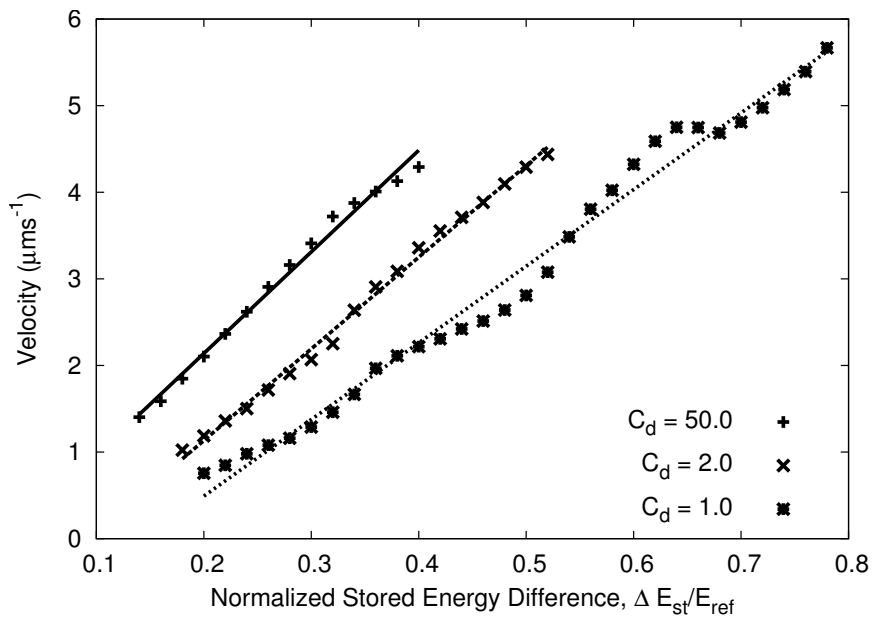
(b)

Figure VI.36 : (a) Predicted dependence of the boundary velocity as a function of driving force, (b) its linear interpolation: Variation of C_d (annihilation term)
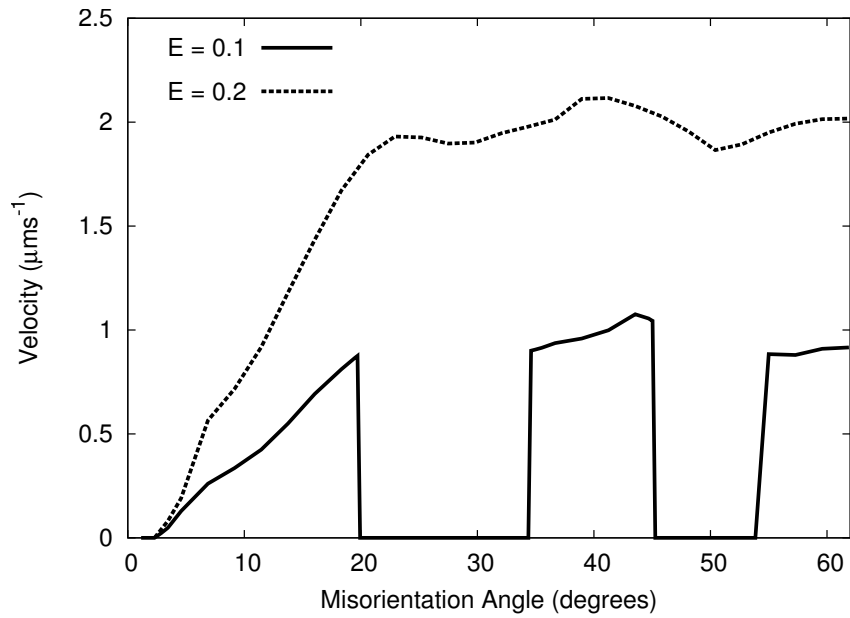
(a) e=0.0075
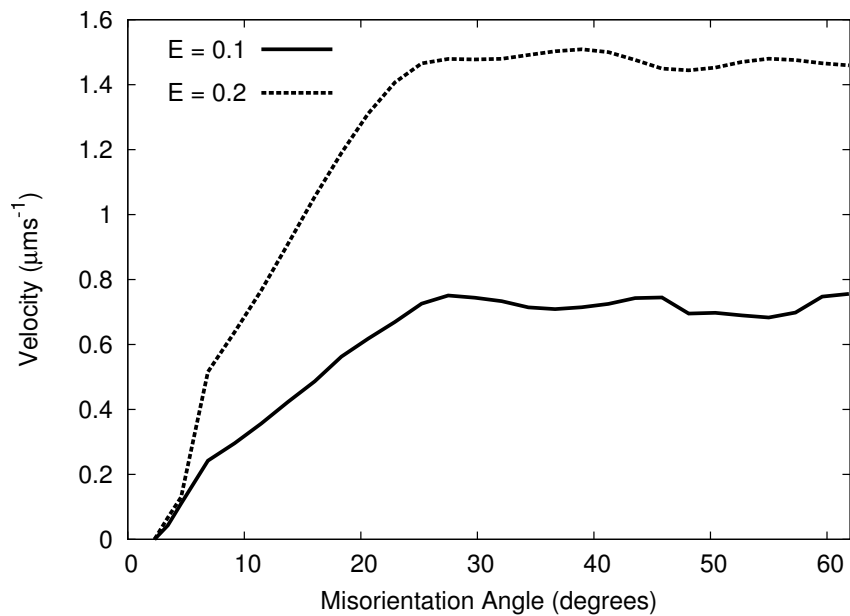
(b) e=0.0150

Figure VI.37 : Predicted dependence of the boundary velocity as a function of misorientation angle for two different initial stored energy difference ($E = 0.1$ and $E = 0.2$

(a)

(b)
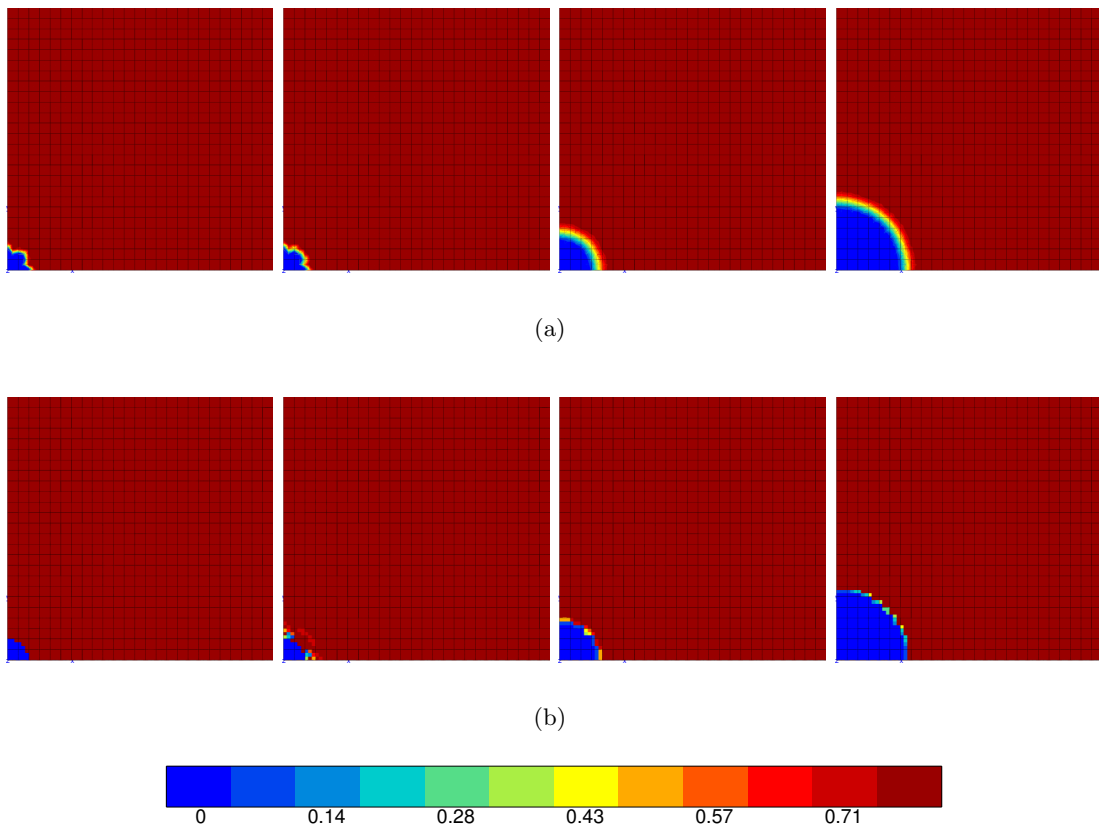
Figure VI.38 : Grain growth evolution $(\theta = -\frac{\pi}{9})$ embedded in a large grain $(\theta = \frac{\pi}{9})$: (a) grain orientation θ, (b) stored energy E_{st}/E_{gb}
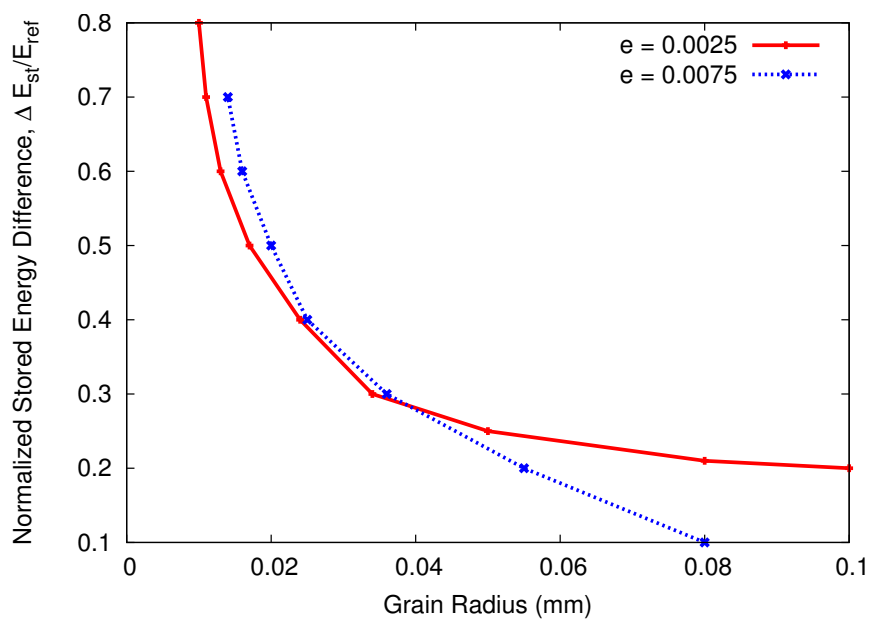
**Figure VI.39** : Critical stored energy for grain growth with respect to its initial size
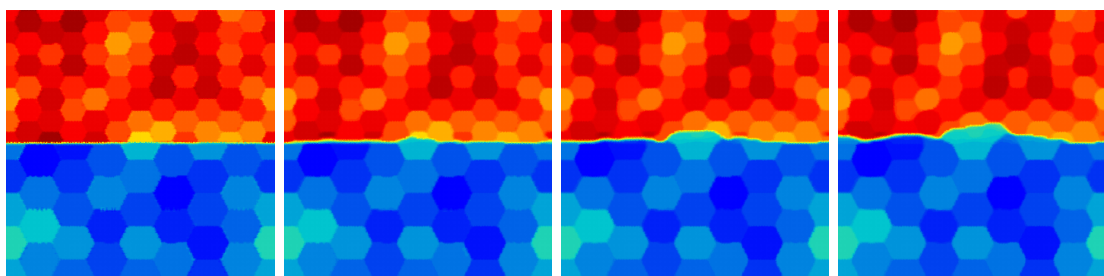
(a)
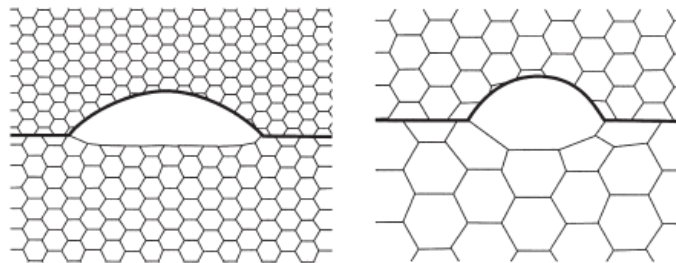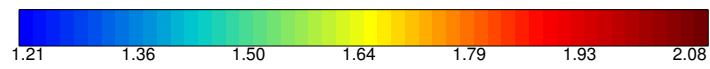
(b)

Figure VI.40 : (a) Predicted grain boundary motion in substructure network with a initial stored energy difference, (e) schematic SIBM mechanism

curved grain boundary shape evolving non homogeneously in the microstructure as for SIBM mechanism, described schematically in Figure VI.40(e).

VI.3.5   Microstructure

VI.3.5.1   Stored Energy Effect on Distribution

As explained in chapter III, the energy stored in grains after deformation depends on the lattice orientation which is non homogeneous inside grains. However, we assume a weakly deformed microstructure (around 15%) where the orientation is approximately constant inside grain. In this case, we consider SIBM as the single active recrystallisation mechanism; the classical nucleation process does not occur. Since, in SIBM mechanism, the new grains have orientations similar to those of the old grains from which they have grown, a simple approach is to consider the new grains with similar orientations to the old grains where they grow. Therefore, the new grains will be merely an extension of the old ones.

In order to study the stored energy effect on the microstructure, two initial distributions of the stored energy were assumed. They vary between 0 and 0.4 (arbitrary unit) and depend on grain orientations. Arbitrarily, in the first case, the higher value of grain orientation is assumed to store more energy than the lower value of grain orientation. In a second case, we study the opposite situation. We distinguish both cases by case 1 and case 2. Stored energy distributions are depicted in the first map of Figure VI.42(a) and (b). Initial lattice order distribution takes the stored energy due to deformation into account by having value less than 1 inside grains. Initial lattice order is set up to verify Eq.V.66 ($\eta = 1 - \frac{C_e}{\omega^2}\frac{E_{st}}{E_{gb}}$). The first map of Figure VI.41 shows the lattice order distribution where lighter color grains (yellow) stored more energy than the darker one (red). Initial orientation distribution is identical to the grain growth case. The parameter e is taken as 0.0025. All other parameters and boundary conditions are the same than those applied in grain growth case.

Six figures, three for each case, summarize the results by following the variables evolution through six distribution maps. Figs.VI.41(a) and (b) describe the grain orientation, θ and the lattice order, η evolution for case 1. First, two grains, G1 and G3 vanish and 6 grains, G2, G4, G5, G6, G7 and G8 shrink. In the microstructure, G1, G2, G3, G4 and G5 have the highest stored energy (yellow). Since they are the first to vanish, the shrink rate is assumed higher for G1 and G3 than for G2, G4 and G5. However, G3 is surrounded by G2, G4 and G5. Therefore, their common sides move to shrink G3 while their other sides move toward their center. As a result the three grains translate with a global reduction. Then, all grains with higher stored energy vanish (only red and back red grains left). The resulting shape is contorted, especially until map 4, since the driving force arising from curvature of grain boundary is less than the stored energy driving force. Figure VI.42 (a) describes the associated stored energy evolution. The grain boundaries move first through the area where stored energy is greater. In order to compare stored energy distribution, its evolution for case 2 is exhibited in Figure VI.42(b). As observed in case 1, grain boundaries move first through the highest area of stored energy. Figure VI.43 shows the microstructure evolution for case 2, by representing θ and η. Same previous comments apply for microstructure evolution in case 2.

The significant difference is about the grain orientation distribution. The orientation maps clearly exhibits a larger amount of blue color in case 1 than in case 2. Indeed, in case 1, low values of orientation are promoted while in case 2 is high values of orientation are favoured. This is merely due to the initial choice of associated higher energy for high value of orientation
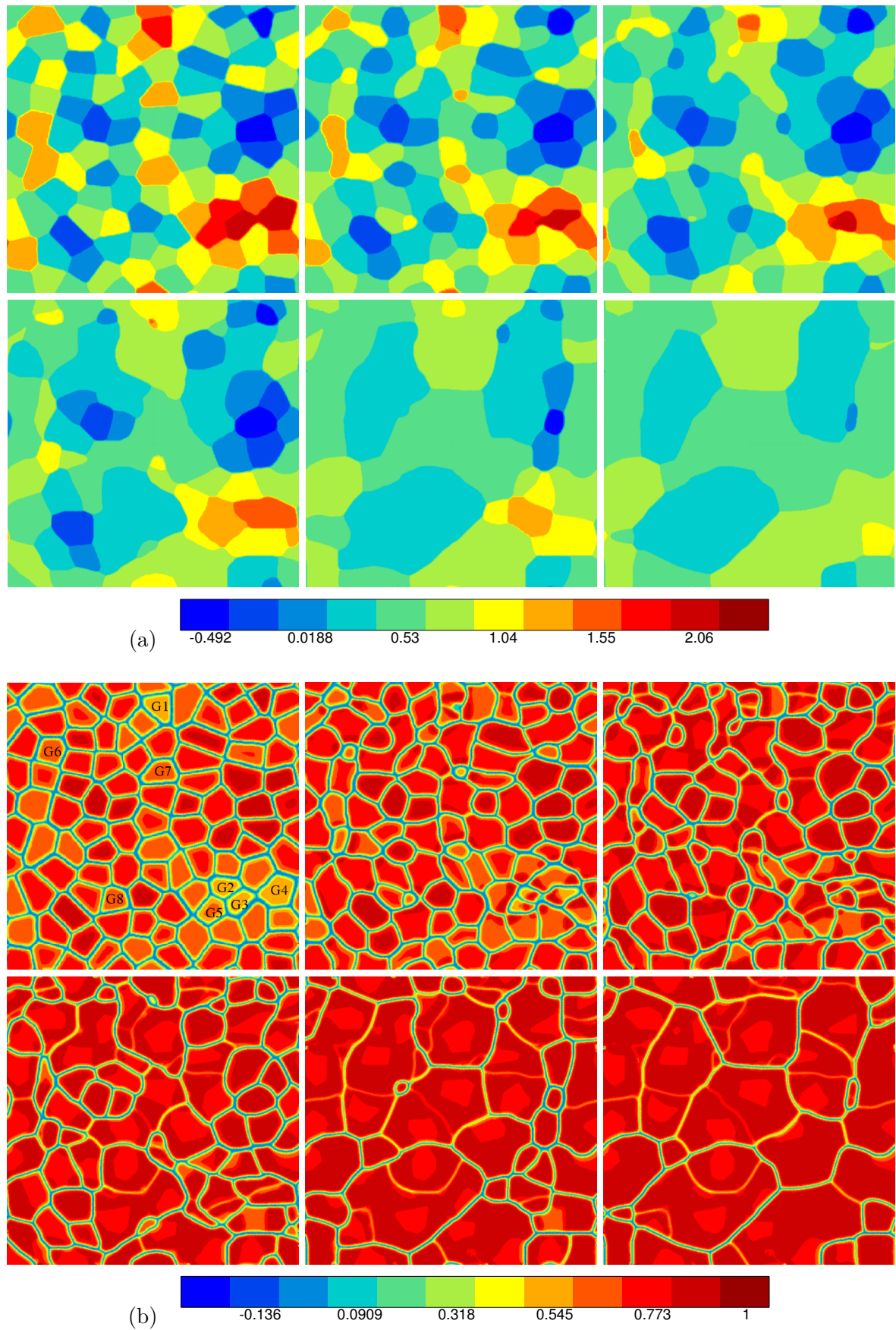
Figure VI.41 : (a) Grain orientation θ, (b) lattice order η evolutions : case 1 (increase of the initial stored energy from blue to red grains). From left to right, from top to bottom: t=0, 10, 28, 55, 209, 453s
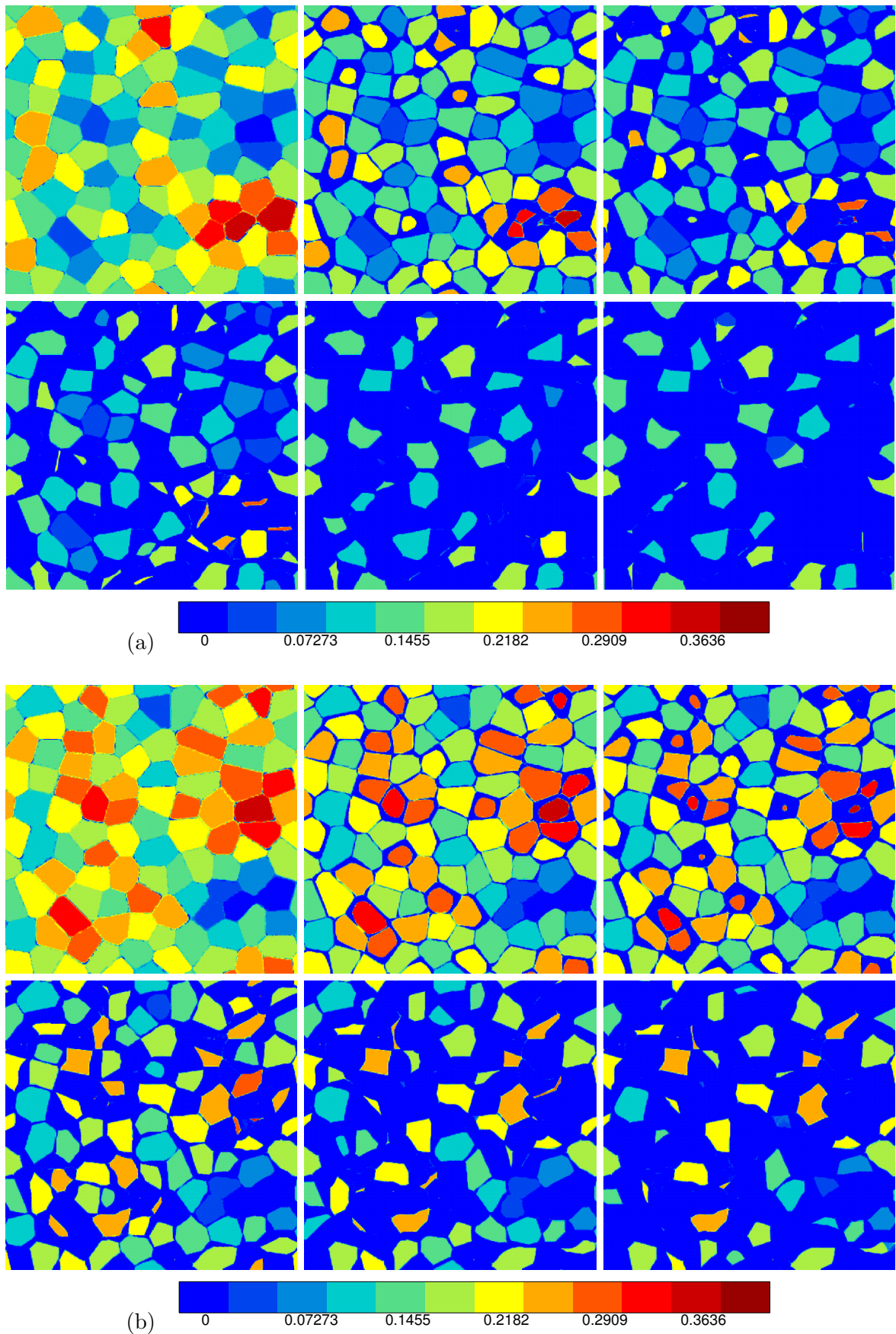
Figure VI.42 : Stored energy evolution : (a) case 1 : higher initial stored energy in high value of θ, (b) case 2 : higher initial stored energy in low value of θ
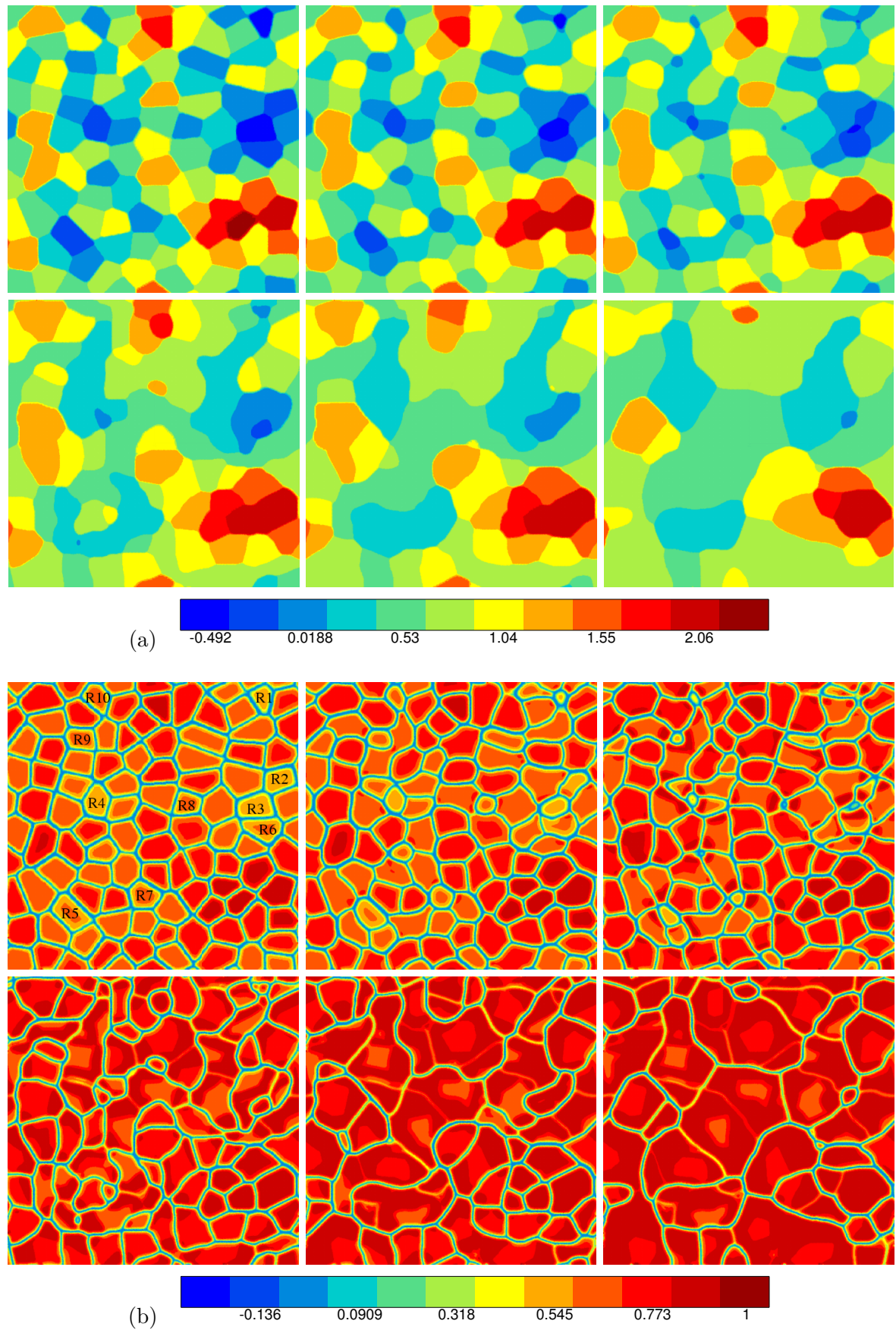
Figure VI.43 : (a) Grain orientation θ, (b) lattice order η evolutions : case 2 (increase of the initial stored energy from red to blue grains). From left to right, from top to bottom: t=0, 4, 9, 28, 60, 167s

in case 1 and inversely in case 2. In order to confirm this observation, microstructure orientation distributions superimposed with the one obtained with only curvature as a driving force are shown in Figure VI.44. We notice both diagrams are translated from the grain growth case; to lower value of orientation in case 1 and higher value of orientation in case 2. The additional term in stored energy in the free energy allows to promote the grain orientations with the lowest value of stored energy.

VI.3.5.2   Stored Energy Effect on Average Values

Figure VI.45 describes the evolution of the stored energy for both cases. As expected, the total stored energy in the microstructure decreases slowly at the beginning, then faster tends to 0. We note that the initial stored energy is higher in case 2. However, the gap between both curves decreases quickly and both curves are quite similar after 10s. Obviously, same observation are done for the average lattice order plotted in Figure VI.46. In Figure VI.47, the average value of the grain orientation θ is plotted for case 1, case 2 and without initial stored energy. As explained in a previous section, average variation of θ with no stored energy is low, about 2° until t=100s, then about 5° due to only few grains left. In case 1 and 2, the average orientation vary about 10° to reach a minimal or maximal value around 35s. Then, the average orientation evolves in a opposite way. Therefore, two steps are distinguished: the first step where the microstructure is driven by the stored energy, then the second step where it is driven by curvature. The maximal or minimal values of orientation depicted in Figure VI.47 clearly underline the end of the stored energy effect on the microstructure evolution.

VI.3.5.3   Kinetics

We define the recrystallized area by the region where there is no stored energy left. Recrystallized areas evolution is shown for case 2 in Figure VI.48. They are represented by a red color while blue zones represent deformed matrix. One grain had been chosen initially with no stored energy, and therefore already considered as recrystallized (red grain in map 1). First, recrystallized zones begin at grain boundary, then, spreads out toward grains center. Some grains are quickly recrystallized compared to other ones. In the last map, some grains are still not recrystallized which means that there is still stored energy left; no grain boundary moves through them. By comparing with Figure VI.41(b), these grains correspond to low values of stored energy. Therefore, the stored energy difference required to activate the grain boundary motion is not reached in these grains.

In order to have an idea on transformation kinetics, the curve representing the volume fraction of material recrystallized (X_v) as a function of log(time) is plotted in Figure VI.49 a. The curve have a standard shape of kinetics transformation. The JMAK equation is usually used to describe the recrystallisation kinetics,

$$X_v = 1 - \exp(-Bt^n). \tag{VI.17}$$

The JMAK equation is fitted on the FE results by extracting the linear part of Figure VI.49a. The results are highlighted in Figure VI.49b. The coefficient n is found to be 0.86 for case 1 and 0.88 for case 2. Considering all the assumptions which have been done, the results are surprisingly close to the experimental value for aluminum, n=1.
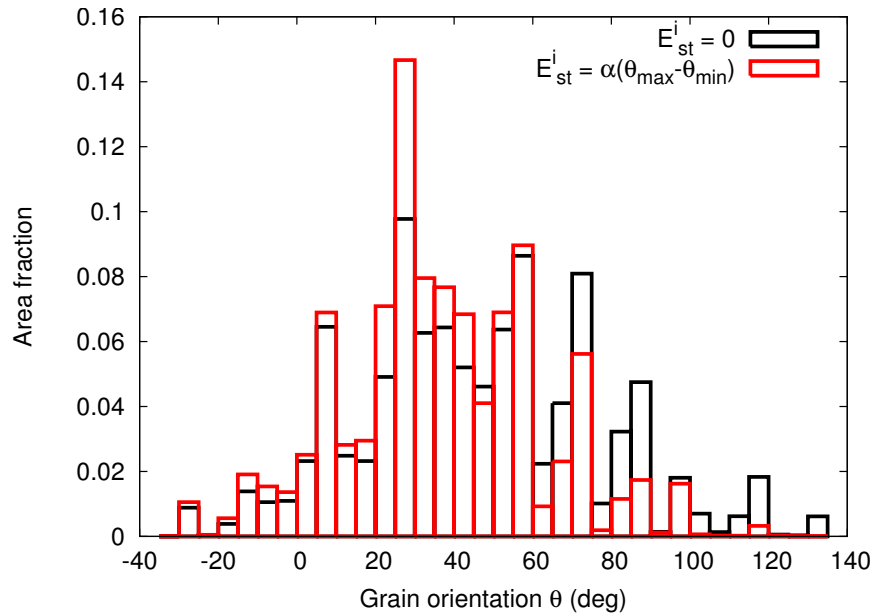
(a)
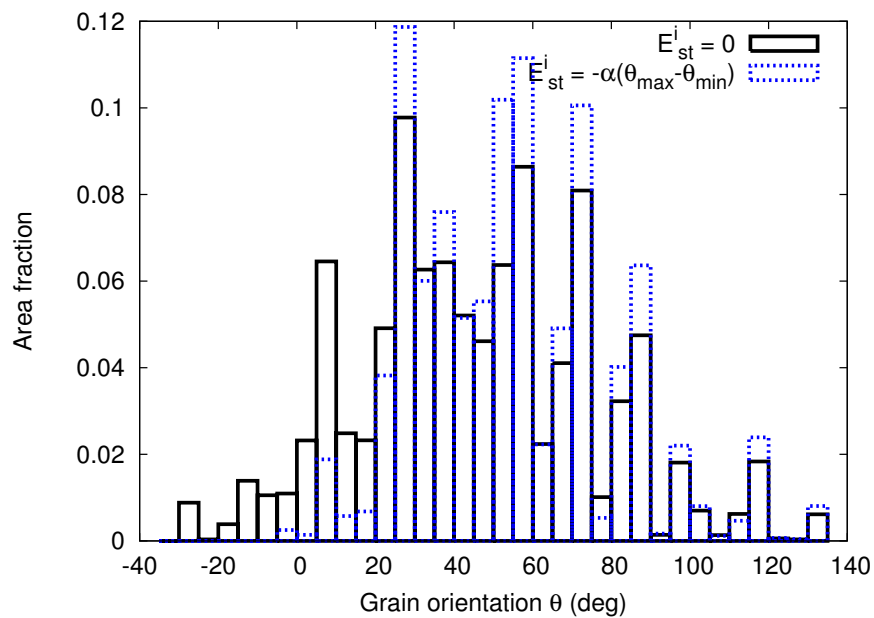
(b)

Figure VI.44 : Diagram of grain orientation distribution: superposition between results obtained without initial stored energy and results obtained (a) in case 1 (b) in case 2 at t = 34s
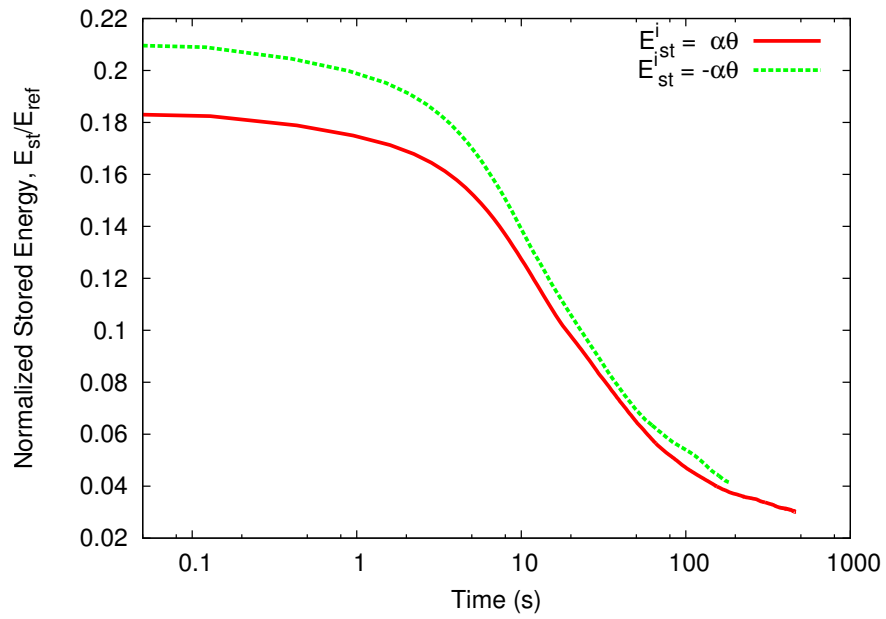
Figure VI.45 : Total stored energy evolution for both distributions
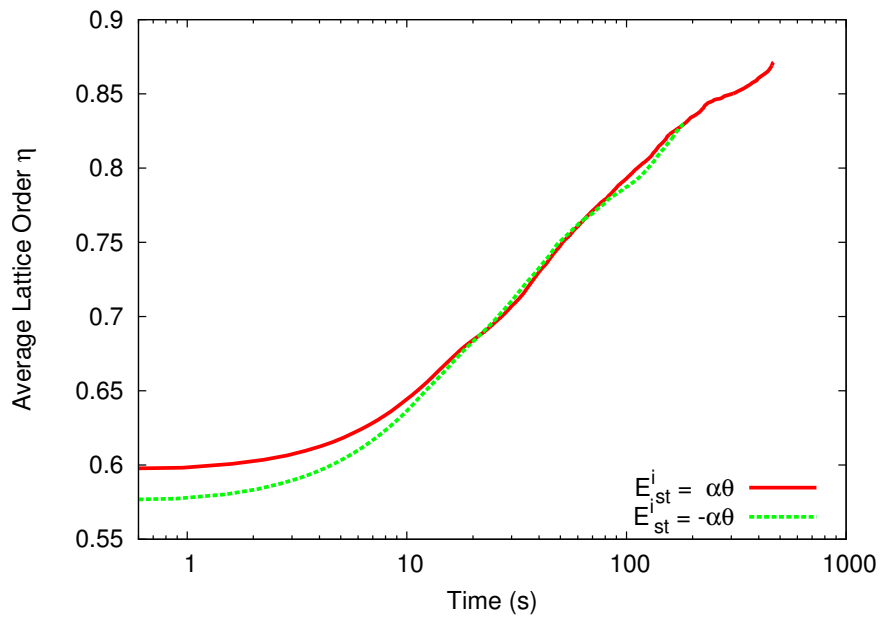

Figure VI.46 : Average value of lattice order η evolution for both distributions
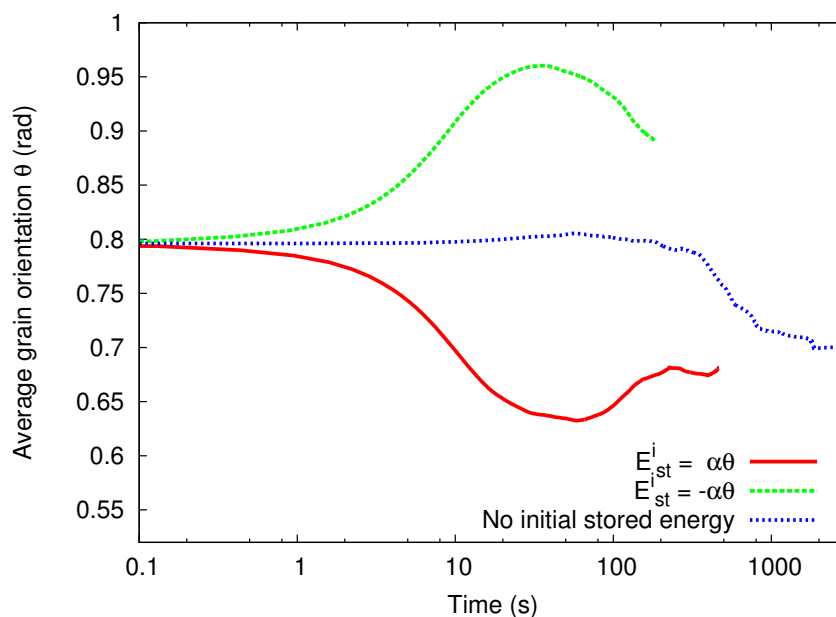
Figure VI.47 : Average grain orientation θ evolution

VI.4 Weak Coupling Between Mechanics and Grain Boundary Kinetics Motion

VI.4.1 Method

A weak coupling between the grain boundary kinematics and the crystal plasticity model is made through the stored energy and the grain orientations. The schematics of the method is done in Figure VI.50.

In the classical FE method, grains of polycrystalline aggregates are defined by groups of elements where each group of elements has a different orientation. In the phase field method, grain orientations of polycrystalline aggregates are defined by the variation of one phase field variable, θ. The first coupling consists of describing the orientation of the grains for mechanical calculations by the phase field variable, θ. Therefore, instead of having sharp grain boundaries, grain boundaries have a finite thickness. Furthermore, the deformed shape of the grains obtained from the mechanical deformation are also taken into account in the grain boundary curvature, which is a driving force for grain boundary motion in the phase field. We note that a finite thickness for the grain boundary is not more physical than a sharp grain boundary given that the physical thickness of a grain boundary is about 4 atoms layers.

As detailed in the previous sections, the stored energy is introduced in the phase field free energy to drive the grain boundary motion. The second coupling consists of using the stored energy obtained from the single crystal plasticity to drive the grain boundary migration

VI.4.2 Application to a Polycrystalline Aggregate

In a preliminary study, the coupling method is used for a 2D polycrystalline aggregate made of 10 grains under 1% height reduction. In this simulation, GNDs are not included in the single crystal model. The microstructure evolution is shown in Figure VI.51 by representing the
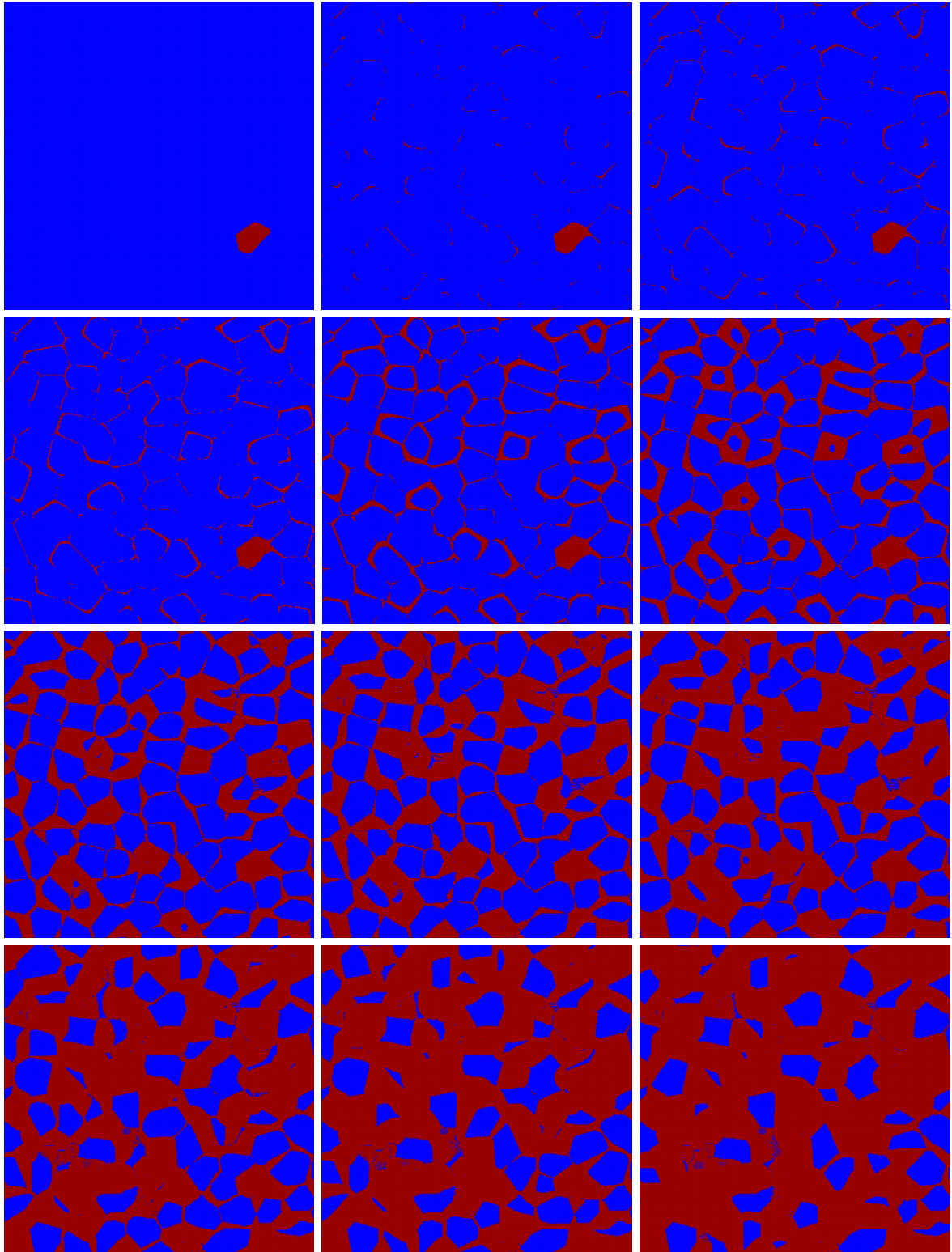
Figure VI.48 : Recrystallized area evolution : deformed area in color blue and recrystallized area in color red. From left to right, from top to bottom: t=0, 0.4, 0.9, 1.5, 4, 9, 14, 21, 33, 60, 105, 182s
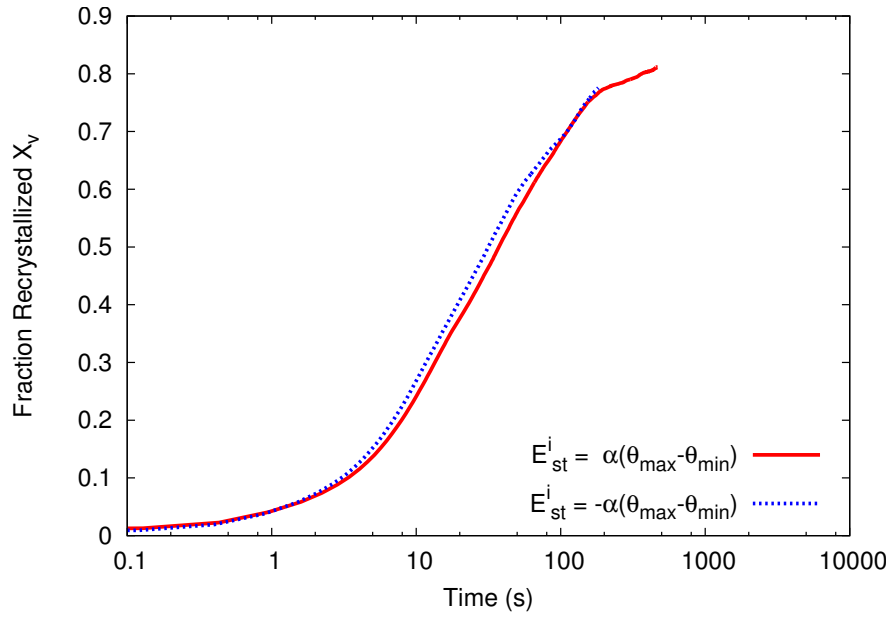
(a)
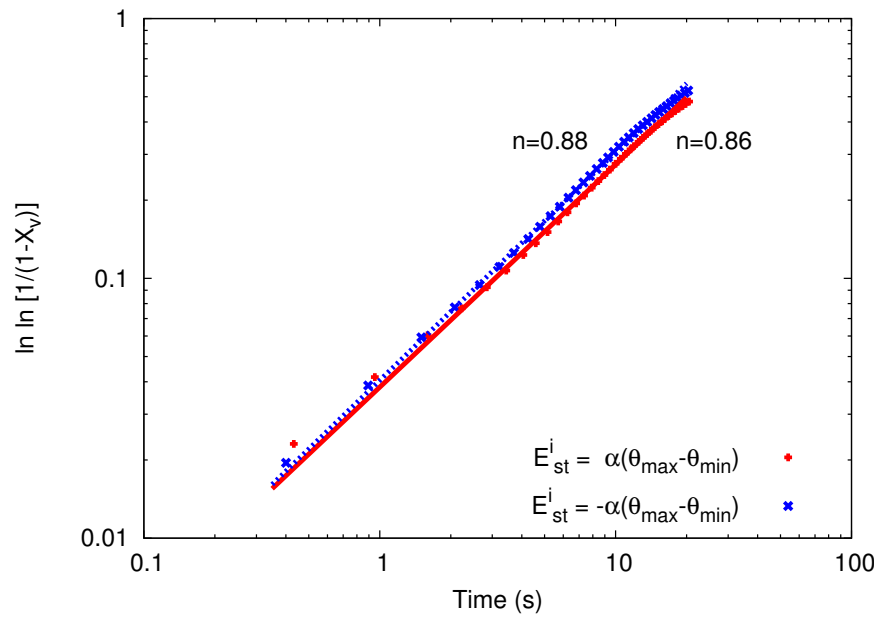
(b)

Figure VI.49 : Fraction recrystallized X_v evolution and its linear interpolation on JMAK
equation
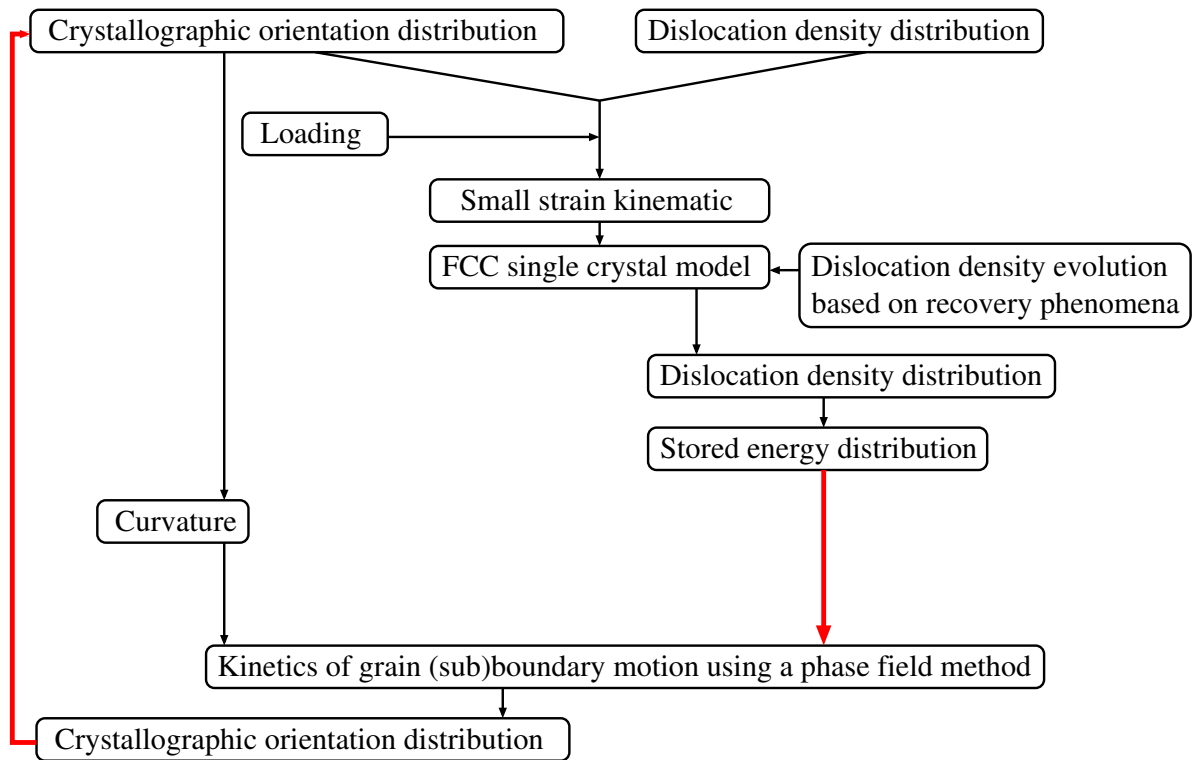
Figure VI.50 : Schematics of the coupling between mechanics and grain boundary kinetics motion

grain orientation, θ. In addition to the phase field variable, the Von Mises stresses evolution is also shown. In this study, we note especially the effect of the grain boundary thickness on the stresses. A stress localisation is found at the grain boundaries similar to the results obtained when GNDs are introduced. Therefore, the term $|\nabla\theta|^2$ in the free energy may be a measure of the GNDs density. Thus, the GNDs introduction by the gradient of the slip rate as estimated in the first chapters may not be necessary.

VI.5   Conclusions

This chapter gives an overview of the possibilities of a phase-field model. Phase field simulations of grain growth and recrystallisation require only two order parameters while a large number of order parameters are necessary to describe the individual grains in usual phase field model. In addition to the curvature, the stored energy has been introduced in the phase field model as a driving force for grain boundary motion. The grain boundary energy has been calibrated on Read-Shockley energy. Simulations were performed for simple two- and three-grain structures, for structures with a limited number of grains, and for different values of the grain boundary energies. The effect of the diffuse interface width on the numerical results was studied as well. Increasing the term $|\nabla\theta|^2$ diminishes the grain mobility dependency on misorientation and decreases also the growth rate. This term is rate-controlling and thus, affects microstructure evolution and resulting grain orientation. Furthermore, the phase field model has been able to predict basic features of recrystallisation, such as the nuclei growth and the SIBM mechanism in a bicrystal. Finally, a weak coupling formulation between single crystal model and phase field model has been proposed. It consists of describing the polycrystalline aggregate by the phase field variable θ and using the stored energy obtained from the single crystal plasticity to drive the grain boundary migration.
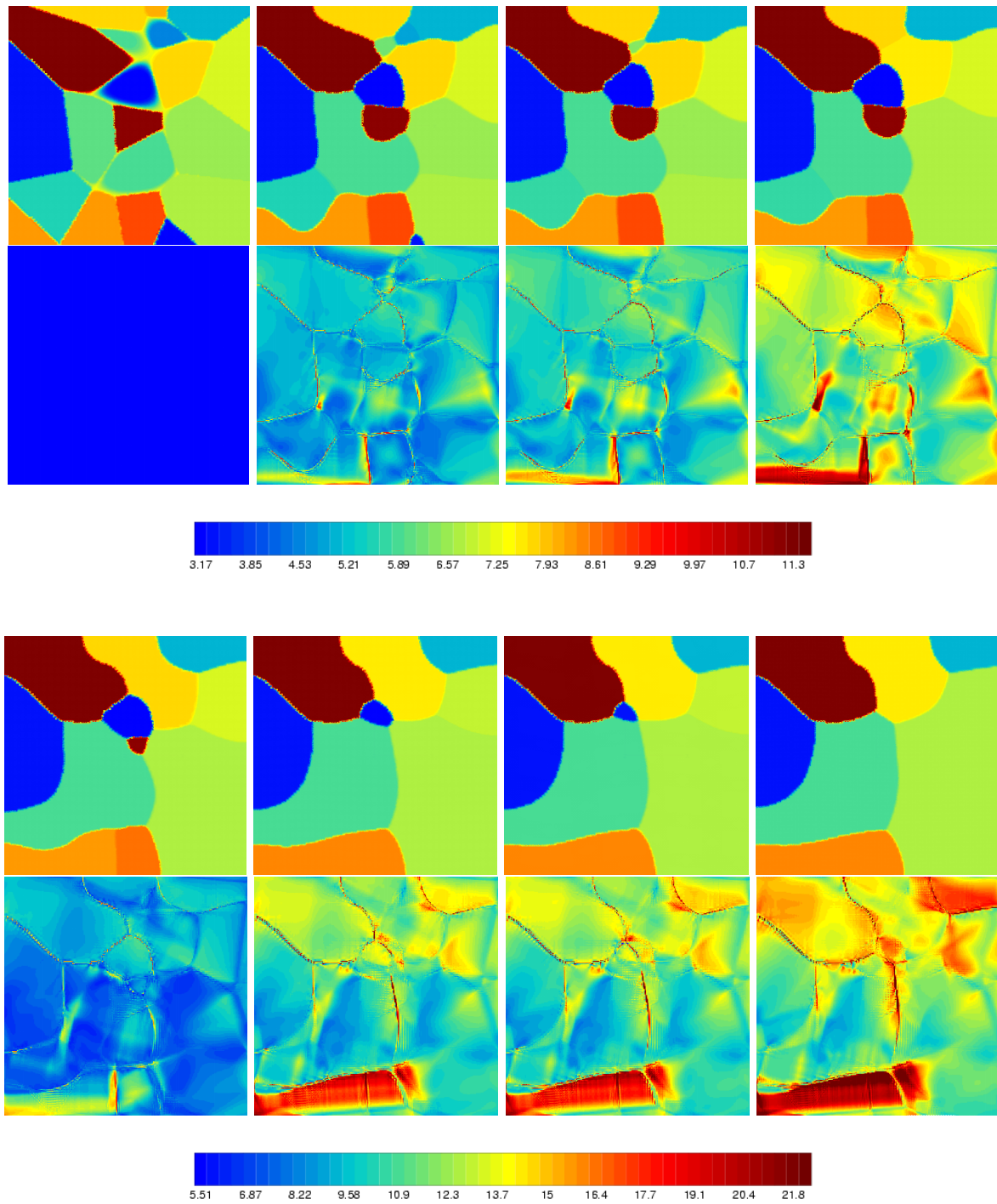
Figure VI.51 : Microstructure 2D under 1% deformation: θ and σ_{mises}. From left to right, from top to bottom: t=0, 0.4, 1.3, 1.8, 3.0, 4.4, 5.5, 9.2, 10.4, 13.0s

References

Bailey J.E. and Hirsch P.B. (1962). *Recrystallization process in some polycrystalline metals.* Proc. Roy. Soc. London, vol. A267, pp 11–30.

Beck P.A. and Sperry P.R. (1950). *Strain induced grain boundary migration in high purity aluminum.* Journal of Applied Physics, vol. 21, pp 150–152.

Burke J.E. and Turnbull D. (1952). *Recrystallization and grain growth.* Progress in Metal Physics, vol. 3, pp 220–292.

Gordon P. and El-Bassyouni T.A. (1965). *The effect of purity on grain growth in aluminum.* Transactions of the Metallurgical Soc. AIME, vol. 223, pp 391–397.

Gottstein G., Molodov D.A., Shvindlerman L.S., Srolovitz D.J., and Winning M. (2001). *Grain boundary migration : misorientation dependence.* Current Opinion in Solid State & Materials Science, vol. 5 n° 1, pp 9–14.

Gottstein G. and Sebald R. (2001). *Modelling of recrystallization textures.* Journal of Materials Processing Technology, vol. 117 n° 3, Sp. Iss. SI, pp 282–287.

Herring C. (1951). *Some theorems on the free energies of crystal surfaces.* Physical Review, vol. 82, pp 87–93.

Huang Y. and Humphreys F.J. (1999). *Measurements of grain boundary mobility during recrystallization of a single-phase aluminium alloy.* Acta Materialia, vol. 47 n° 7, pp 2259–2268.

Humphreys F.J. and Hatherly M. (2004). *Recrystallization and Related Annealing Phenomena.* Pergamon.

Mackenzie J. K. (1964). *The distribution of rotation axes in a random aggregate of cubic crystals.* Acta Metallurgica, vol. 12, pp 223–225.

Mattissen D., Molodov D.A., Shvindlerman L.S., and Gottstein G. (2005). *Drag effect of triple junctions on grain boundary and grain growth kinetics in aluminium.* Acta Materialia, vol. 53 n° 7, pp 2049–2057.

Mullins W.W. (1956). J Appl Phys, vol. 27, pp 900.

Upmanyu M., Srolovitz D.J., Shvindlerman L.S., and Gottstein G. (1999). *Misorientation dependence of intrinsic grain boundary mobility : simulation and experiment.* Acta Materialia, vol. 47 n° 14, pp 3901–3914.

Von Neumann J. In: Metal interfaces, ed. C. Herring.

Yang C.-C., Rollet A.D., and Mullins W.W. (2001). *Measuring relative grain boundary energies and mobilities in an aluminium foil from triple junction geometry.* Scripta materialia, vol. 44, pp 2735–2740.

Conclusions – Prospects

During thermo-mechanical processing, the strain energy stored during deformation in the microstructure of a FCC polycrystalline aggregate is generally reduced by physical mechanisms which rely, at least partially, on mechanisms such as dislocation cell formation or grain boundary motion which occur during recovery and recrystallisation. The microstructure resulting from the previous process is full of small grains, and consequently a large quantity of grain boundary. Therefore, grain growth occurs to reduce the grain boundary energy driven by grain boundary curvature. The first objective of this work is to quantitatively predict the development of the stored energy just before the onset of thermal recrystallisation using a dislocation based single crystal constitutive framework. The second objective is to describe, from these predicted distributions, grain growth phenomena driven by stored and grain-boundary energies, using a phase field model.

Main results

A successful prediction of the mechanical behavior depends on an accurate characterization of the microstructure and its evolution (plastic deformation and lattice rotation). The model based on dislocation densities as internal variables has shown to be able to describe development of microstructural inhomogeneities during deformation. The single crystal elasto-viscoplastic model has been applied for 3D polycrystalline aggregates. The GNDs have been generally found to develop near the grain boundaries. However, it is shown that they can also accumulate inside grains due to the complex interaction between neighbouring grains. For all grain sizes, the GNDs generation has strengthened the polycrystal. The single crystal elasto-viscoplastic model has also been applied for 2D polycrystalline aggregates under channel die compression test. It allows to use plane strain compression conditions and finer mesh to capture intragranular heterogeneities with a competitive computational time. It has been underlined that the plane strain compression conditions in 2D promote localisations compared to usual compression test by exhibiting kind of micro-bands inside the grains. These sharp micro-bands are only observed with the GNDs introduction. The micro-bands size is limited to the element size and thus, decreases with mesh refinement. Furthermore, stress-strain response is diverging with mesh refinement due the multiplication of gradients and consequently, GNDs. In order to avoid this phenomenon, a different method for evaluating gradients of slip rate has been proposed. Instead of evaluating gradients over one element, a critical distance have been introduced to define the neighbouring gauss points included in the gradients evaluation with the Gauss point of interest. With this method, the stress-strain curves is converging with mesh refinement. Dislocation density concentrates near the grain boundary.

Since stored energy is of prime importance for an accurate prediction of the recrystallisation phenomenon, specific care have been taken for its evaluation. Three measures of stored internal strain energy have been obtained from the single crystal elasto-viscoplastic model. The first measure based on dislocation theory is calculated from the dislocation densities defined as internal variables in the single crystal model. The second one is obtained from the thermodynamic formulation associated to the single crystal model. The third one which is usually employed is defined as a fraction of the plastic work. Formulations based on dislocation density and thermodynamics exhibited the same tendency, namely, decreasing with respect the deformation while the plastic work amount increases with the deformation. The partition of the plastic work between heat and stored energy is not constant. The fraction of stored energy based on thermodynamic formulation decreases with strain up to a minimum value between 5% and 10% reached for strain large than 0.3. Identical tendency is observed for stored energy based on dislocation theory with a ratio ten time smaller which

seems to be too low compared to experimental data. The stored energy obtained from a thermodynamic formulation is the most accurate measure. Furthermore, differences in distributions are observed between the plastic work and both stored energy formulations. The introduction of GNDs increases the total stored energy in the polycrystal for the three formulations. They also influence the stored energy distribution for the three grain sizes. The stored energy increases with reducing the grain size, more significant the stored energy increase is. However, the stored energy distribution based on plastic work was seen to be less affected by the GNDs introduction than the one based on dislocation density as confirmed by the fraction of the stored energy increases with the grain size.

Once the stored energy has been evaluated, a constitutive framework capable of describing the microstructural evolution driven by grain boundary curvature and/or stored energy has been developed using a phase field method. The model uses only two phase field variables to represent the microstructure which continuously changing at the interfaces. However, in reality the grain boundary is only the location of a discontinuity of crystal orientation. A finite element formulation for the phase field model has been presented, based on the introduction of generalized stresses and their balance, and the framework of the thermodynamics of irreversible processes. The finite element implementation has been validated by comparing FE results with analytical solution for simple cases. The phase-field model contains a large number of phenomenological parameters, which have to be determined in order to obtain quantitative results. The parameters of the free energy are calibrated based on published Read-Shockley boundary energy data for aluminium.

An extensive study has been carried on the model. With only curvature as a driving force, reduced grain boundary mobility has been found dependent on temperature and on grain misorientation by distinguishing high and low angle grain boundaries. Furthermore, increasing the parameter in front of $|\nabla\theta|^2$ in the free energy, reduces slightly the high grain boundary mobility and therefore, the misorientation dependency. Triple and quadruple junctions evolution follows the Hearing's equation. The model has been applied to simulate grain growth phenomena with periodic boundary conditions in pure aluminium. Although 100 initial grains may not be considered as statistically representative, transformation kinetics has been found in good agreement with experiment. In a second step, the stored energy differences is considered as introduced in bicrystal with flat grain boundary. A linear relation has been predicted between the velocity and the stored energy difference as observed experimentally. Finally, curvature and stored energy are introduced as opposing driving forces in the case where a grain free of energy grows in a deformed grain. The stored energy necessary to obtain grain growth is found to increase with the initial grain curvature in a non-linear way. In materials having high stacking fault energy such as Al, the formation of new orientations by recrystallisation twinning does not play an important role. Thus, the sources of nuclei are the existing subgrains or cells in the deformed microstructure. A qualitative study has been done in a bicrystal case with substructure network for modelling strain induced boundary migration. The model has been applied on a simplified recrystallisation study. It has shown that grains with the lowest stored energy are dominant at the end of the process. In spite of all the assumptions, the predicted recrystallised material volume fraction evolution with respect to time was found to be surprisingly closed to experimental data.

Since microstructural features such as the grain size and orientation determine the mechanical properties of the material, a weak coupling between the grain boundary kinematics and the crystal plasticity model is made through the stored energy and the grain orientations. It allows to predict the evolution of stress distribution in the polycrystalline aggregate. The
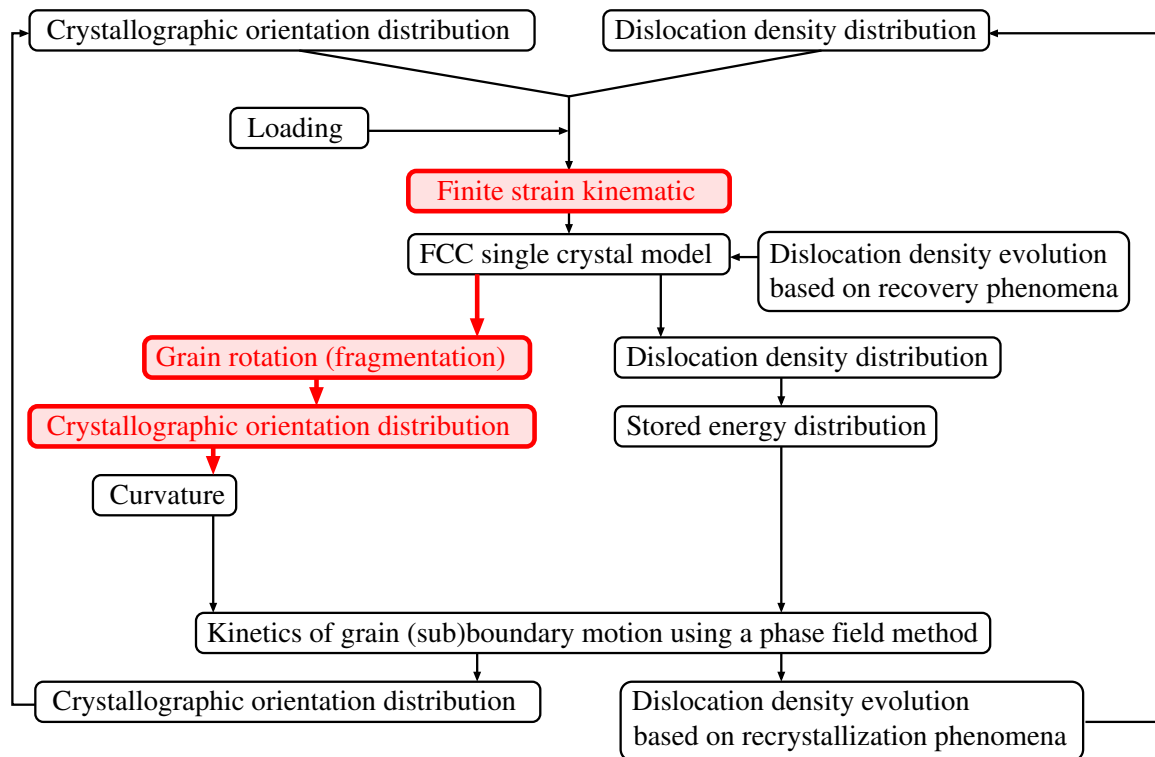
Figure VI.52 : Schematics: introduction of finite strain kinematics in the phase field model

main result of the preliminary study is the possible measure of the GNDs effect through the term $|\nabla\theta|^2$ in the free energy.

Prospects

First, additional studies need to be carried out to validate the previous results.
• In chapter II, we assumed that a channel die compression test can be modelled by a 2D plane strain compressions based on (Erieau, 2004). In order to verify this assumption, macroscopic behaviour, texture, inter and intragranular heterogeneities characteristics obtained for 2D calculations should be compared with those obtained for 3D calculations in the case of aluminium.
• The calculated strain energy needs to be compared with experimental data through overall values and distributions. The comparison has to be done with single crystal data and with polycrystal aggregates with a given crystallographic texture.
• Concerning the phase field model, a mesh size and types of elements study need to be done to insure the results independent of the element and have convergence solution with mesh refinement.

Then, the model needs some improvement in order to model recrystallization phenomena.
• The weak coupling between single crystal model and phase field model needs to be extended to finite strain kinematics in order to take into account subgrain formation for the SIBM mechanism, see Figure VI.
• The nucleation phenomenon has to be included in the model to have a full description of the "classical" recrystallisation as seen in Figure VI.
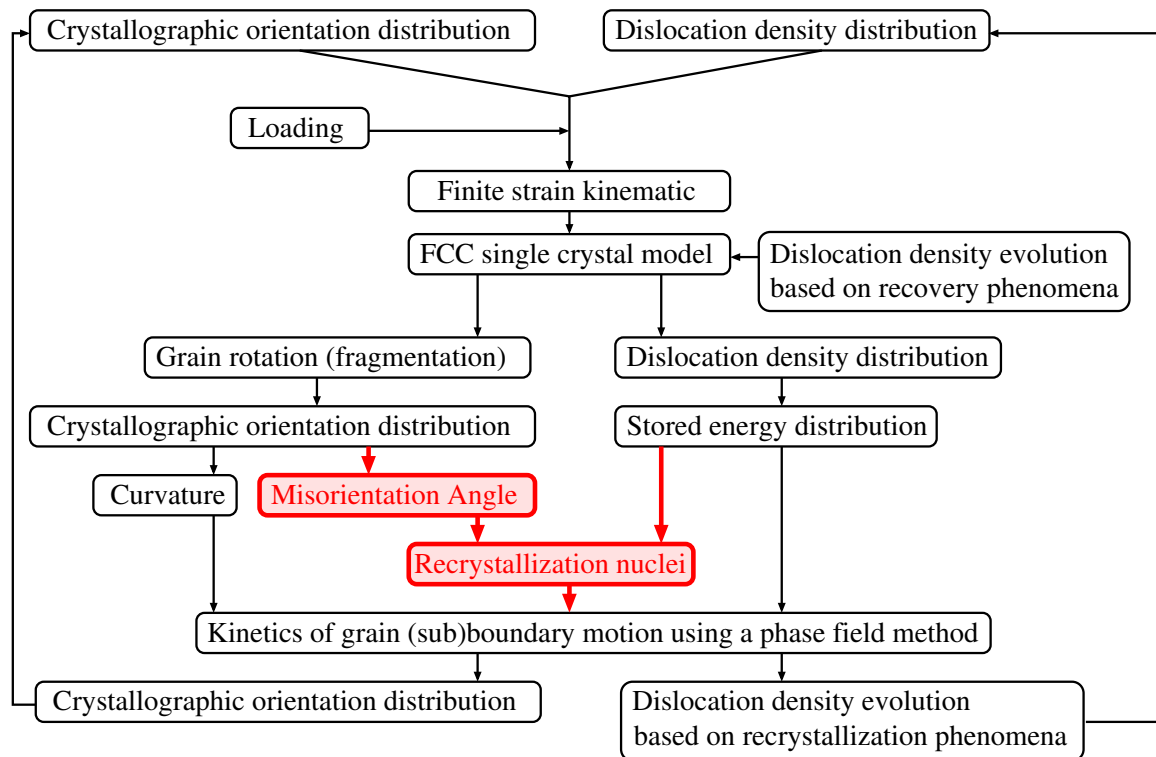
Figure VI.53 : Schematics: introduction of nucleation in the phase field model

The numerical solution and implementation of phase-field equations is, in principle, relatively simple, as there is no need to track the interfaces. However, the resolution of the numerical technique must be very fine to catch the steep transitions of the phase-field variables at interfaces. Simulations for realistic system sizes and time scales necessitate excessive computation times. An adaptive mesh has to be applied for simulating microstructure evolution. Thus, the mesh is taken extremely fine at grain boundaries, to resolve the transition of the phase-field variables, and coarse within the grains. For instance, the variable η varying between 0 (grain boundary) and 1 (inside the grains) could be a suitable variable to control the mesh size.

The model has to be extended to 3D description to describe accurately microstructure evolutions.
• For instance, the main influences on texture development during recrystallisation are the orientation of the nuclei or new grains, the growth rate of the new grains, the location of new grains belonging to a given texture component relative to one another, the stored energy of the grain into which the new grains grow. Therefore, the phase field model should be extended from two to three dimensions (3D). θ must be replaced with a model which describes 3D orientation.
• The grain boundary direction needs to be included in the model in order to predict the cusp of Σ grain boundaries in the grain boundary energy, and thus, account for grain boundary energy anisotropy. It is important because the anisotropic nature of most material properties leads to anisotropic behaviour in textured polycrystals.

In the present coupled model, displacement and lattice orientation are degrees of freedom, therefore, lattice rotation is also a degree of freedom. As in the Cosserat theories where displacement and lattice orientation are regarded as independent degrees of freedom,

(Forest and Sievert, 1997), we suggest to connect the displacement and the lattice rotation on the constitutive level and by the balance equation in order to describe non-local effect in the model without including explicitly GNDs.

In the thesis, we focused in particular on recrystallisation and grain growth. However, there are two ways to reduce the stored strain energy associated with dislocations, recrystallisation and recovery. Contrary to recrystallisation, recovery results in an annihilation or rearrangement of dislocations in low energy dislocation structures to reduce the dislocation density. Significant improvement needs to be done in the mechanical model through the development of a non local approach describing explicitly the formation of substructures at the grain scale.

References

Erieau P. (2004). *Étude des hétérogénéités de déformation et leur lien avec la recristallisation d'alliages industriels.* Thèse de Doctorat, Ecole Centrale de Paris.

Forest, S. Cailletaud G. and Sievert R. (1997). *A Cosserat theory for elastoviscoplastic single crystals at finite deformation.* Archives of Mechanics, vol. 49, pp 705–736.

Appendix

Appendix I.A : Implicit Implementation

The resolved shear stress can be expressed as:

$$\tau^\alpha = (\underset{\sim}{\boldsymbol{F}}^{eT}\underset{\sim}{\boldsymbol{F}}^e \Lambda \underset{\sim}{\boldsymbol{E}}^e) : \underset{\sim}{\boldsymbol{N}}^\alpha \tag{.18}$$

However, since the elastic stretch for metallic materials is unsignificant, we can simplify the resolved shear stress as:

$$\tau^\alpha = (\Lambda \underset{\sim}{\boldsymbol{E}}^e) : \underset{\sim}{\boldsymbol{N}}^\alpha \tag{.19}$$

Calcul steps : Zebulon Architecture

- PreStep at the beginning of each increment :

$$\underset{\sim}{\boldsymbol{F}}^* = \underset{\sim}{\boldsymbol{F}}_{n+1}\underset{\sim}{\boldsymbol{F}}_n^{p-1} \tag{.20}$$

$$\underset{\sim}{\boldsymbol{E}}^* = \frac{1}{2}(\underset{\sim}{\boldsymbol{F}}^{*T}\underset{\sim}{\boldsymbol{F}}^* - \underset{\sim}{\boldsymbol{I}}) \tag{.21}$$

At the beginning of the step, the plastic deformation gradient is used in order to obtain the elastic strain. $\underset{\sim}{\boldsymbol{F}}^p$ need to be conserved during the increment, it is an auxiliary variable.

- StrainPart in order to calculate Cauchy Stress and to update the auxialiary variables after convergence:

$$\underset{\sim}{\boldsymbol{F}}_{n+1}^p = \underset{\sim}{\boldsymbol{F}}_n^p \exp(\Delta\gamma^\alpha \underset{\sim}{\boldsymbol{N}}^\alpha) \tag{.22}$$

$$\underset{\sim}{\boldsymbol{F}}_{n+1}^e = \underset{\sim}{\boldsymbol{F}}_{n+1}\underset{\sim}{\boldsymbol{F}}_{n+1}^{p-1} \tag{.23}$$

$$\underset{\sim}{\boldsymbol{T}}_{n+1} = \Lambda : \underset{\sim}{\boldsymbol{E}}_{n+1}^e \tag{.24}$$

$$\sigma_{n+1} = (1/J)\underset{\sim}{\boldsymbol{F}}_{n+1}^e \underset{\sim}{\boldsymbol{T}}_{n+1}\underset{\sim}{\boldsymbol{F}}_{n+1}^{eT} \tag{.25}$$

- CalcGradF enables the resolution by Newton's method :

First, we calculate:

$$C_{n+1}^e = 2\underset{\sim}{\boldsymbol{E}}_{n+1}^e + \underset{\sim}{\boldsymbol{I}} \tag{.26}$$

$$\underset{\sim}{\boldsymbol{T}}_{n+1} = \Lambda : \underset{\sim}{\boldsymbol{E}}_{n+1}^e \tag{.27}$$

Second, we calculate all the partial derivatives for each integration variables :
∗ elastic strain:

$$\frac{\partial r_e}{\partial \Delta \underset{\sim}{\boldsymbol{E}}^e} = \underset{\sim}{\boldsymbol{I}} + 2\sum_{\alpha=1}^N \left\{ N^\alpha \underset{\sim}{\boldsymbol{I}} \right\} \Delta\gamma^\alpha \tag{.28}$$

$$\frac{\partial r_e}{\partial \Delta\gamma^\alpha} = \left\{ N^\alpha C_{n+1}^e \right\} \tag{.29}$$

$$\frac{\partial r_e}{\partial \Delta\rho_{Se}^\alpha} = 0 \tag{.30}$$

$$\frac{\partial r_e}{\partial \Delta \rho_{Ss}^\alpha} = 0 \tag{.31}$$

$*$ slip:

$$\frac{\partial r_{\gamma^\alpha}}{\partial \Delta \gamma^\gamma} = \delta_{\alpha\gamma} \tag{.32}$$

$$\frac{\partial r_{\gamma^\alpha}}{\partial \Delta \underset{\sim}{\boldsymbol{E}}^e} = - \dot{\gamma}_0 \exp\left[-\frac{F_0}{kT} \left\{ 1 - \left\langle \frac{|\tau_{n+1}^\alpha| - S_{n+1}^\alpha}{\widehat{\tau}} \right\rangle^p \right\}^q \right] \frac{F_0 pq}{kT} \left\{ 1 - \left\langle \frac{|\tau_{n+1}^\alpha| - S_{n+1}^\alpha}{\widehat{\tau}} \right\rangle^p \right\}^{q-1} sgn(\tau^\alpha)$$
$$\times \quad \left\langle \frac{|\tau_{n+1}^\alpha| - S_{n+1}^\alpha}{\widehat{\tau}} \right\rangle^{p-1} \frac{sgn(\tau^\alpha)}{\widehat{\tau}} \frac{\partial \tau^\alpha}{\partial \Delta \underset{\sim}{\boldsymbol{E}}_{n+1}^e} \Delta t \tag{.33}$$

$$\frac{\partial r_{\gamma^\alpha}}{\partial \Delta \rho_{Se}^\gamma} = - \dot{\gamma}_0 \exp\left[-\frac{F_0}{kT} \left\{ 1 - \left\langle \frac{|\tau_{n+1}^\alpha| - S_{n+1}^\alpha}{\widehat{\tau}} \right\rangle^p \right\}^q \right] \frac{F_0 pq}{kT} \left\{ 1 - \left\langle \frac{|\tau_{n+1}^\alpha| - S_{n+1}^\alpha}{\widehat{\tau}} \right\rangle^p \right\}^{q-1} sgn(\tau^\alpha)$$
$$\times \quad \left\langle \frac{|\tau_{n+1}^\alpha| - S_{n+1}^\alpha}{\widehat{\tau}} \right\rangle^{p-1} \frac{1}{\widehat{\tau}} \frac{\partial \Delta S_T^\alpha}{\partial \Delta \rho_{Se}^\gamma} \Delta t \tag{.34}$$

$$\frac{\partial r_{\gamma^\alpha}}{\partial \Delta \rho_{Ss}^\gamma} = - \dot{\gamma}_0 \exp\left[-\frac{F_0}{kT} \left\{ 1 - \left\langle \frac{|\tau_{n+1}^\alpha| - S_{n+1}^\alpha}{\widehat{\tau}} \right\rangle^p \right\}^q \right] \frac{F_0 pq}{kT} \left\{ 1 - \left\langle \frac{|\tau_{n+1}^\alpha| - S_{n+1}^\alpha}{\widehat{\tau}} \right\rangle^p \right\}^{q-1} sgn(\tau^\alpha)$$
$$\times \quad \left\langle \frac{|\tau_{n+1}^\alpha| - S_{n+1}^\alpha}{\widehat{\tau}} \right\rangle^{p-1} \frac{1}{\widehat{\tau}} \frac{\partial \Delta S_T^\alpha}{\partial \Delta \rho_{Ss}^\gamma} \Delta t \tag{.35}$$

We define the following variables:

$$glis = \dot{\gamma}_0 \exp\left[-\frac{F_0}{kT} \left\{ 1 - \left\langle \frac{|\tau_{n+1}^\alpha| - S_{n+1}^\alpha}{\widehat{\tau}} \right\rangle^p \right\}^q \right] sgn(\tau^\alpha) \tag{.36}$$

$$deriv = glis \frac{F_0 pq}{kT} \left\{ 1 - \left\langle \frac{|\tau_{n+1}^\alpha| - S_{n+1}^\alpha}{\widehat{\tau}} \right\rangle^p \right\}^{q-1} \left\langle \frac{|\tau_{n+1}^\alpha| - S_{n+1}^\alpha}{\widehat{\tau}} \right\rangle^{p-1} \Delta t \tag{.37}$$

We get:

$$\frac{\partial r_{\gamma^\alpha}}{\partial \Delta \underset{\sim}{\boldsymbol{E}}^e} = -deriv \frac{sgn(\tau^\alpha)}{\widehat{\tau}} \frac{\partial \tau^\alpha}{\partial \Delta \underset{\sim}{\boldsymbol{E}}_{n+1}^e} \tag{.38}$$

$$\frac{\partial r_{\gamma^\alpha}}{\partial \Delta \gamma^\gamma} = \delta_{\alpha\gamma} \tag{.39}$$

$$\frac{\partial r_{\gamma^\alpha}}{\partial \Delta \rho_{Se}^\gamma} = \frac{deriv}{\widehat{\tau}} \frac{\partial \Delta S_T^\alpha}{\partial \Delta \rho_{Se}^\gamma} \tag{.40}$$

$$\frac{\partial r_{\gamma^\alpha}}{\partial \Delta \rho_{Ss}^\gamma} = \frac{deriv}{\widehat{\tau}} \frac{\partial \Delta S_T^\alpha}{\partial \Delta \rho_{Ss}^\gamma} \tag{.41}$$

With:

$$\frac{\partial \tau^\alpha}{\partial \Delta \underset{\sim}{\boldsymbol{E}}_{n+1}^e} = \Lambda \underset{\sim}{\boldsymbol{N}}^\alpha \tag{.42}$$

$$\frac{\partial \Delta S_T^\alpha}{\partial \Delta \rho_{Se}^\gamma} = \frac{\lambda \mu b h^{\alpha\gamma}}{2\sqrt{\sum_{\beta=1}^N h^{\alpha\beta}(\rho_{Se_{n+1}}^\beta + \rho_{Ss_{n+1}}^\beta)}} \tag{.43}$$

$$\frac{\partial \Delta S_T^\alpha}{\partial \Delta \rho_{Ss}^\gamma} = \frac{\lambda \mu b h^{\alpha\gamma}}{2\sqrt{\sum_{\beta=1}^N h^{\alpha\beta}(\rho_{Se_{n+1}}^\beta + \rho_{Ss_{n+1}}^\beta)}} \tag{.44}$$

∗ edge dislocation density :

$$\frac{\partial r_{\rho_{Se}^\alpha}}{\partial \Delta \underset{\sim}{\boldsymbol{E}}^e} = 0 \tag{.45}$$

$$\frac{\partial r_{\rho_{Se}^\alpha}}{\partial \Delta \gamma^\gamma} = -\frac{C_e}{b^\alpha}\left[K_e\sqrt{\sum_{\beta=1}^N \rho_{T_{n+1}}^\beta} - 2d_e\rho_{Se_{n+1}}^\alpha\right]\delta_{\alpha\gamma}sgn(\tau^\alpha) \tag{.46}$$

$$\frac{\partial r_{\rho_{Se}^\alpha}}{\partial \Delta \rho_{Se}^\gamma} = -\frac{C_e K_e}{b^\alpha}\frac{\Delta\gamma^\alpha sgn(\tau^\alpha)}{2\sqrt{\sum_{\beta=1}^N \rho_{T_{n+1}}^\beta}} + \left(1 + \frac{2C_e d_e}{b^\alpha}\Delta\gamma^\alpha sgn(\tau^\alpha)\right)\delta_{\alpha\gamma} \tag{.47}$$

$$\frac{\partial r_{\rho_{Se}^\alpha}}{\partial \Delta \rho_{Ss}^\gamma} = -\frac{C_e K_e}{b^\alpha}\frac{\Delta\gamma^\alpha sgn(\tau^\alpha)}{2\sqrt{\sum_{\beta=1}^N \rho_{T_{n+1}}^\beta}} \tag{.48}$$

∗ screw dislocation density:

$$\frac{\partial r_{\rho_{Ss}^\alpha}}{\partial \Delta \underset{\sim}{\boldsymbol{E}}^e} = 0 \tag{.49}$$

$$\frac{\partial r_{\rho_{Ss}^\alpha}}{\partial \Delta \gamma^\gamma} = -\frac{C_s}{b^\alpha}\left[K_s\sqrt{\sum_{\beta=1}^N \rho_{T_{n+1}}^\beta} - \rho_{Ss_{n+1}}^\alpha(\pi d_s^2 K_s\sqrt{\sum_{\beta=1}^N \rho_{T_{n+1}}^\beta} + 2d_s\right]\delta_{\alpha\gamma}sgn(\tau^\alpha) \tag{.50}$$

$$\frac{\partial r_{\rho_{Ss}^\alpha}}{\partial \Delta \rho_{Se}^\gamma} = -\frac{C_s}{b^\alpha}\left[\frac{K_s}{2\sqrt{\sum_{\beta=1}^N \rho_{T_{n+1}}^\beta}} - \rho_{Ss}^\alpha\frac{\pi d_s^2 K_s}{2\sqrt{\sum_{\beta=1}^N \rho_{T_{n+1}}^\beta}}\right]\Delta\gamma^\alpha sgn(\tau^\alpha) \tag{.51}$$

$$\frac{\partial r_{\rho_{Ss}^\alpha}}{\partial \Delta \rho_{Ss}^\gamma} = -\frac{C_s}{b^\alpha}\left[\frac{K_s}{2\sqrt{\sum_{\beta=1}^N \rho_{T_{n+1}}^\beta}} - \rho_{Ss_{n+1}}^\alpha\frac{\pi d_s^2 K_s}{2\sqrt{\sum_{\beta=1}^N \rho_{T_{n+1}}^\beta}}\right]\Delta\gamma^\alpha sign(\tau^\alpha) +$$
$$\left[1 + \frac{C_s}{b^\alpha}\left(\pi d_s^2 K_s\sqrt{\sum_{\beta=1}^N \rho_{T_{n+1}}^\beta} + 2d_s\right)\Delta\gamma^\alpha sign(\tau^\alpha)\right]\delta_{\alpha\gamma} \tag{.52}$$